

Design and Applications of Anisotropic Magnetic Hybrid Microgels

Von der Fakultät für Mathematik, Informatik und Naturwissenschaften der
RWTH Aachen University zur Erlangung des akademischen Grades eines
Doktors der Naturwissenschaften genehmigte Dissertation

vorgelegt von

Dominik Lukas Braunmiller, M.Sc.

aus

Oberndorf bei Salzburg, Österreich

Berichter: Jun.-Prof. Dr. rer. nat. Jérôme Crassous
Univ.-Prof. Dr.-Ing Laura De Laporte

Tag der mündlichen Prüfung: 28.03.2025

Diese Dissertation ist auf den Internetseiten der Universitätsbibliothek online
verfügbar.

Die vorliegende Arbeit wurde im Zeitraum November 2019 bis Juni 2024 am Institut für Physikalische Chemie der Rheinisch-Westfälischen Technischen Hochschule Aachen (RWTH Aachen University) angefertigt.

“Die Neugier ist die mächtigste Antriebskraft im Universum, weil sie die beiden größten Bremskräfte im Universum überwinden kann: die Vernunft und die Angst.”

Die Stadt der Träumenden Bücher (Walter Moers)

Abstract

Magnetic nanoparticles (MNPs) are extensively researched and utilized in various applications, including biomedicine, sensors, and materials science. In some cases, there is a preference for soft materials over rigid particles, leading to an increased interest in magnetic soft matter materials, such as magnetic hybrid microgels (MMGs). This thesis explores the preparation, characterization, and applications of MMGs with different sizes, shapes, and compositions by using ellipsoidal maghemite MNPs as the foundation for incorporating specific magnetic properties into microgels.

The first focus is on the synthesis of small anisotropic MMGs utilizing a precipitation polymerization method. These microgels feature a single MNP core surrounded by a thermoresponsive microgel shell. The nanoscale structures exhibit tunable dipolar interactions and anisotropic properties, making them ideal tracers in dense microgel systems. By utilizing these MMGs to investigate complex phase behaviors and dynamics, the findings provide valuable insights into the relationship between microgel dimensions, softness, and dynamic phase behavior.

Additionally, emphasis is placed on the development of rod-shaped MMGs as pre-programmable building blocks for tissue engineering applications. Using the PRINT technique, rod-shaped MMGs are created with adjustable magnetic properties by incorporating and pre-aligning MNPs during synthesis. This approach allows for precise control over magnetic behavior, enabling the design of multi-directional scaffolds that guide cell growth. This positions pre-programmed rod-shaped MMGs as promising materials for advanced tissue engineering applications, such as wound healing, regenerative medicine, and drug testing platforms.

Finally, the exploration of larger MMGs focuses on their potential role as microactuators in active microfluidic devices. The fabrication of complex-shaped MMGs is achieved using stop-flow lithography in combination with a magnetic field, allowing for the creation of intricate 3D geometries with precise nanoparticle pre-alignment. These MMGs exhibit strong magnetic properties, making them suitable for actuator applications.

Kurzzusammenfassung

Magnetische Nanopartikel (MNP) werden ausgiebig erforscht und in verschiedenen Anwendungen eingesetzt, darunter in der Biomedizin, der Sensorik und der Materialwissenschaft. In einigen Fällen werden weiche Materialien gegenüber starren Partikeln bevorzugt, was zu einem gesteigerten Interesse nach magnetischen Materialien wie magnetischen Kompositmikrogelen (MMGs) führt. Diese Arbeit erforscht die Herstellung, Charakterisierung und Anwendung von MMGs mit verschiedenen Größen, Formen und Zusammensetzungen durch die Verwendung von ellipsoiden MNPs als Grundlage für die Entwicklung spezifischer magnetischer Eigenschaften in unterschiedlichen Mikrogele.

Der erste Schwerpunkt dieser Dissertation liegt auf der Synthese von kleinen anisotropen MMGs. Diese Mikrogele weisen einen einzelnen MNP-Kern auf, der von einer thermoresponsiven Mikrogel-Hülle umgeben ist. Die Strukturen weisen kontrollierbare dipolare Wechselwirkungen und anisotrope Eigenschaften auf, was sie zu idealen Tracern in dichten Mikrogelsystemen macht. Die Verwendung dieser MMGs zur Untersuchung des komplexen Phasenverhaltens liefert wertvolle Einblicke in die Beziehung zwischen Mikrogeleigenschaften, Konzentration und dynamischem Phasenverhalten.

Ein weiterer Schwerpunkt ist die Entwicklung stäbchenförmiger MMGs als programmierbare Bausteine für Tissue-Engineering-Anwendungen. Mithilfe der PRINT-Technik werden stäbchenförmige MMGs mit einstellbaren magnetischen Eigenschaften hergestellt, indem MNPs während der Synthese vorausgerichtet eingebaut werden. Dieser Ansatz ermöglicht eine präzise Kontrolle des magnetischen Verhaltens und damit die Entwicklung von multidirektionalen Gerüsten, die das zielgerichtete Zellwachstum fördert. Dies positioniert vorprogrammierte MMGs als vielversprechende Materialien für fortschrittliche Tissue-Engineering-Anwendungen wie Wundheilung und Medikamententestplattformen.

Abschließend wurden größere MMGs auf ihre potenzielle Rolle als Mikroaktuatoren in aktiven mikrofluidischen Geräten untersucht. Die Herstellung komplex geformter MMGs erfolgt mittels Stop-Flow-Lithographie in Kombination mit einem Magnetfeld, was die Produktion komplexer 3D-Formen mit einer präzisen Vorausrichtung der Nanopartikel ermöglicht. Diese MMGs weisen starke magnetische Eigenschaften auf, wodurch sie sich für Aktuatoranwendungen eignen.

List of Publications

Parts of Chapter 4 and 6 were previously published in:

- Braunmiller, D. L., Babu, S., Gehlen, D. B., Seuß, M., Haraszti, T., Falkenstein, A., Eigen, J., De Laporte, L., & Crassous, J. J. Pre-Programmed Rod-Shaped Microgels to Create Multi-Directional Anisogels for 3D Tissue Engineering. *Advanced Functional Materials* **2022**, 32(50), 2202430.

The experiments were designed by me and the other authors. I prepared and characterized the nanoparticles with the help of Andreas Falkenstein for the TGA experiments. The microgels were prepared by Susan Babu, David Gehlen, and Max Seuß, and the SEM images were recorded by Julian Eigen and analyzed by me. The Matlab and ImageJ routine I used to analyze the rotation of rod-shaped microgels was written by myself based on ImageJ plugins. Susan Babu conducted the preparation of the Anisogel and the cell culture experiments. Haraszti developed a code and performed the orientation analysis of cells and microgels in images of Anisogels. I wrote the manuscript jointly with Susan Babu, who focused on the parts concerning anisogels. The manuscript was revised and corrected by all co-authors.

Parts of Chapter 4 and 7 were previously published in:

- Steinbeck, L., Braunmiller, D. L., M. Wolff, H. J., Huettche, V., Wang, J., Wessling, M., Crassous, J. J., & Linkhorst, J. Magnetically Actuable Complex-Shaped Microgels for Spatio-Temporal Flow Control. *Advanced Materials Technologies* **2023**, 8(14), 2300044.

The experiments were designed by me and the other authors. I prepared and characterized the nanoparticles with the help of Andreas Falkenstein for the TGA. The microgels were prepared by Lea Steinbeck, Hanna Wolff, and Vincent Huettche, and the SEM images were recorded by Julian Eigen and analyzed by me. The Matlab and ImageJ routine Julia Wang and I used to analyze the rotation of the microgels was written by myself based on ImageJ plugins. The fabrication of in-chip actuators was conducted and analyzed by Lea Steinbeck, Hanna Wolff, and Vincent Huettche. I wrote the manuscript jointly with Lea Steinbeck and Hanna Wolff, with them focussing on the fabrication of the microgels and in-chip systems. The manuscript was revised and

corrected by all co-authors.

Further Publications:

- Hagemans, F., Hazra, N., Lovasz, V. D., Awad, A. J., Frenken, M., Babenyshev, A., Laukkanen, V., Braunmiller, D., Richtering, W., & Crassous, J. J. Soft and Deformable Thermoresponsive Hollow Rod-Shaped Microgels. *Small*, 2401376.
- Saadli, M., Braunmiller, D. L., Mourran, A., & Crassous, J. J. (2023). Thermally and Magnetically Programmable Hydrogel Microactuators. *Small*, 19(16), 2207035.
- Riegert, J., Töpel, A., Schieren, J., Coryn, R., Dibenedetto, S., Braunmiller, D., Zajt, K., Schalla, C., Rütten, S., Zenke, M., Pich, A., & Sechi, A. Guiding cell adhesion and motility by modulating cross-linking and topographic properties of microgel arrays. *PLOS ONE*, 16(9), e0257495.

Contents

1	Introduction	1
2	Scientific Background	3
2.1	Hybrid Microgels	3
2.2	Magnetic Nanoparticles	5
2.3	Magnetic Microgels	8
2.3.1	Synthesis of Magnetic Microgels	8
2.3.2	Anisotropic Magnetic Microgels as Model Systems . .	10
2.4	Magnetic Microactuators	11
2.5	Biomedical Applications	13
2.6	Scope of the Thesis	16
3	Methods	19
3.1	Thermogravimetric Analysis (TGA)	19
3.2	Scattering Methods	20
3.2.1	Dynamic Light Scattering (DLS)	21
3.2.2	Small-Angle X-Ray Scattering (SAXS)	22
3.2.3	Differential Dynamic Microscopy (DDM)	24
3.3	Microscopy	26
3.3.1	Confocal Microscopy	26
3.3.2	Electron Microscopy	27
4	Characterization and Self-Assembly of Anisotropic Hybrid Magnetic Microgels	29
4.1	Introduction	29
4.2	Experimental Section	31
4.2.1	Materials	31
4.2.2	Hematite Synthesis	31
4.2.3	Silica Coating	31
4.2.4	Transformation from Hematite to Maghemite	32
4.2.5	Disolution of the Silica Shell	33

4.2.6	Microgel Synthesis	33
4.2.7	Preparation Dipolar Chains	34
4.2.8	Scanning Electron Microscopy	34
4.2.9	Transmission Electron Microscopy	34
4.2.10	X-ray Diffractometry	35
4.2.11	Dynamic Light Scattering	35
4.2.12	Differential Dynamic Microscopy	35
4.2.13	Small-Angle X-Ray Scattering	36
4.3	Results and Discussion	36
4.3.1	Hematite Particles and Conversion to Maghemite . . .	36
4.3.2	Dipolar Interactions	44
4.3.3	Microgel Synthesis	48
4.3.4	Magnetic Field directed Assembly	51
4.4	Summary and Outlook	53
5	Structure and Dynamics of Concentrated Magnetic Microgels under Static and Rotating Fields	57
5.1	Introduction	57
5.2	Experimental Section	59
5.2.1	SAXS	59
5.2.2	Drying Cell	60
5.2.3	Experiments at the Air/Water Interface	61
5.2.4	Confocal Microscopy	61
5.2.5	SEM	62
5.2.6	AFM	62
5.3	Results and Discussion	62
5.3.1	Nematic Phases, Plastic Crystals and "Spin" Glasses . .	62
5.3.2	Structural Evolution of Anisotropic Microgels under Unidirectional Drying	67
5.3.3	Static Magnetic Fields	72
5.3.4	Dynamic Magnetic Fields	75
	Response to Rotating Magnetic Field	75
	90° Relaxation Experiments	80
5.3.5	Arrangement of Magnetic Microgels at the Air/Water Interface	83
5.4	Conclusion	85

6	Static and Dynamic Control of Rod-shaped Pre-programmed Magnetic Microgels	89
6.1	Introduction	89
6.2	Experimental Section	92
6.2.1	Synthesis of the Ellipsoidal Magnetic Nanoparticles . .	92
6.2.2	Preparation of Magnetic Rod-Shaped Microgels	92
6.2.3	Scanning Electron Microscopy	93
6.2.4	Magnetic Response Experiments	93
6.2.5	Cell Culture in Anisogels	94
6.2.6	Confocal Microscopy	96
6.3	Results and Discussion	98
6.3.1	Ellipsoidal Maghemite Nanoparticles	98
6.3.2	Preparation and Characterization of the Magnetic Microgel Rods via PRINT	98
6.3.3	Static Control	100
6.3.4	Dynamic Control	102
6.3.5	Cell Culture in Anisogels	109
6.4	Summary and Outlook	113
7	Complex-Shaped Magnetic Microgel Microactuators	115
7.1	Introduction	115
7.2	Experimental Section	117
7.2.1	Synthesis and Characterization of Ellipsoidal Maghemite Nanoparticles	117
7.2.2	Fabrication of Microfluidic Chips	118
7.2.3	Preparation of the Precursor Solution	118
7.2.4	Fabrication of Magnetic Microgels using SFL	118
7.2.5	Analysis of the Magnetic Response of Microgels	119
7.2.6	Particle Tracking for Flow Manipulation	120
7.2.7	Scanning Electron Microscopy	120
7.3	Results and Discussion	121
7.3.1	Magnetic Microgel Fabrication	121
7.3.2	Magnetic Responsiveness of Microgels	124
7.3.3	Influence of Microgel Shape, MNP Content, and Magnetic Field Strength on the Magnetic Responsiveness .	127
7.3.4	Flow Manipulation with Actuated Microgels	130
7.3.5	In-Chip Microactuator	134
7.4	Summary and Outlook	135

8 Summary and Outlook	137
8.1 Summary	137
8.2 Outlook	141
Bibliography	i
Acknowledgements	xxix

List of Abbreviations

AFM	Atomic Force Microscopy
BIS	N,N'-methylene BISacrylamide
DDM	Differential Dynamic Microscopy
DLS	Dynamic Light Scattering
EM	Electron Microscopy
KPS	Potassium PeroxydiSulfate
MNP	Magnetic Nanoparticles
MMG	Magnetic Microgels
PBS	Phosphate-Buffered Saline
PDMS	Poly(DiMethylSiloxane)
PEG(-DA)	Poly(Ethylene Glycol) / Poly(Ethylene Glycol) DiAcrylate
PET	Poly(ethylene terephthalate)
PNIPAm	Poly(N-IsoPropylacrylAmide)
PRINT	Particle Replication In a Non-wetting Template
PVP	Poly(VinylPyrrolidone)
SAXS	Small-Angle X-ray Scattering
SEM	Scanning Electron Microscopy
SFL	Stop-Flow Lithography
SPION	Superparamagnetic Iron Oxide Nanoparticles
(EF)TEM	Energy-filtered Transmission Electron Microscopy
TEOS	Tetraethyl OrthoSilicate
TGA	Thermogravimetric Analysis
TMAH	TetraMethylAmmonium Hydroxide
TPM	3-(Trimethyloxysilyl)-PropylMethacrylate
UV	UltraViolet
VPTT	Volume Phase Transition Temperature

List of Symbols

A	Amplitude
\vec{B}	Magnetic Field
d	Distance
d_{eq} / d_{pol}	Equatorial / Polar Diameter
D	Diffusion Coefficient
E_d	Interaction Energy
$f(p)$	Friction Coefficient
$f(q, \tau)$	Intermediate Scattering Function
$g(q, \tau)$	Correlation Function
I	Intensity
k_B	Boltzmann Constant
m	Mass
N	Number Density
\vec{q}	Scattering Vector
p	Aspect Ratio
$P(q)$	Form Factor
Q	Swelling Ratio
R_H	Hydrodynamic Radius
S_1	Orientational Order Parameter
$S(q)$	Structure Factor
t	Time
T	Temperature
V	Volume
\dot{V}	Flow Rate
α	Particle Orientation with Respect to the Magnetic Field
β	Rod Orientation
γ	Drag Coefficient
η_0	Solvent Viscosity
θ	Scattering Angle
λ	Wave Length

XVIII

μ	Magnetic Moment
μ_0	Magnetic Permeability in Vacuum
ξ	Cell Alignment Angle
$\Delta\rho$	Scattering Contrast
σ_S	Saturation Magnetisation
τ	Lag Time
φ	Cumulative Anglur Change
ω	Angular frequency

Chapter 1

Introduction

Starting from a young age, most of us learn playfully how to use magnets, whether as compasses to find our way (or at least the north) or as magnetic tiles to build our dream castles. As we grow older, this curiosity often translates into a deeper interest in the scientific and technological realm of magnetic systems with similar concepts. Magnets are extensively utilized across various fields, including robotics, nanotechnology, material science, and biomedicine [1–3].

At the micro- to nanometer scale, colloidal systems present exciting opportunities for magnetic applications, especially when non-magnetic materials are combined with magnetic systems. Magnetic nanoparticles, in particular, have been widely studied for their potential applications in tracking tools, magnetic tweezers, and cancer treatment [4, 5]. Despite significant research on hard magnetic materials, the creation of magnetically functionalized soft matter remains a unique challenge. Soft matter refers to materials that exhibit large deformations in response to small external forces, typically governed by a balance of weak to moderate intermolecular interactions. These materials often exhibit self-organization, particularly in systems like liquid crystals and colloids, though not all soft materials exhibit this behavior. Examples for soft matter include polymers, gels, liquid crystals, colloids, foams, and emulsions [6, 7].

Introducing magnetism into soft materials requires a delicate balance between incorporating magnetic components while maintaining the desirable properties of the soft material. In this thesis, a specific class of soft magnetic materials will be explored: magnetic hybrid microgels. These materials are formed by combining non-magnetic polymer networks with magnetic nanoparticles [8–10]. A primary challenge in creating these materials lies in

the synthesis process. Various methods have been employed for the preparation of magnetic hybrid microgels, such as polymerization in the presence of magnetic nanoparticles or post-modification of pre-synthesized microgel particles [8, 9]. Hybrid magnetic microgels offer significant advantages in diverse applications, such as targeted drug delivery, environmental remediation, and microactuation [1, 11]. The integration of magnetic responsiveness with the inherent softness of microgels enables precise control over their behavior in response to external stimuli, such as magnetic fields. This makes them ideal for use in applications like magnetic separation or biosensing [12]. Moreover, their magnetic properties can be harnessed for controlled drug release, where the microgel structure is engineered to respond to both pH variations and magnetic fields, enabling targeted and efficient drug delivery [5]. The multifunctionality of magnetic hybrid microgels thus opens up new possibilities for advanced biomedical and environmental applications.

Despite the significant progress in creating and characterizing magnetic hybrid microgels, there are still open questions and challenges that need to be addressed. For instance, understanding the interactions between magnetic nanoparticles and their response to magnetic fields is critical for improving and fine-tuning the properties of these materials. This thesis will consider different synthesis methods for differently sized and shaped microgels applicable for different properties, starting on a colloidal level on the same size scale as the MNP cores up to non-diffusive microgels suitable for microactuation.

Chapter 2

Scientific Background

2.1 Hybrid Microgels

In recent research developments, soft materials have gained a large focus as they harbor significant benefits for many applications, for example, in medicine and other life sciences. In these fields, hydrogels and especially their smaller brethren, micro- or nanogels, stand out. They combine softness from a swollen polymer network, leading to human tissue-like properties, with the possibility of introducing "smart" properties into the system [13].

Nano- and microgels are sized in the nano to micrometer range and are defined as intermolecularly cross-linked polymer networks. They can be considered "smart" materials as they can respond to external stimuli, including a wide variety of external forces like temperature or pH changes, external magnetic or electric fields, or light pulses leading to changes in size, shape or softness, the release of cargo, or translational or rotational motion [13]. There are various ways of introducing stimuli-responsiveness into microgels, starting from the monomers used either as a pure monomer (e.g., *N*-isopropyl acrylamide) or as comonomers (mixture of two or more monomers), different types of cross-links (e.g. photo- or enzymatically degradable), or the integration of nanoparticles creating hybrid materials [13, 14].

Depending on the type of nanoparticle (NP) used, the hybrid microgels can react to different stimuli such as light (gold NPs) [15], electrical (silica NPs) [16, 17] or magnetic fields (MNPs) [18, 19]. Gold nanoparticles are often used in combination with poly(*N*-isopropyl acrylamide) (PNIPAm) microgels, as these undergo a volume phase transition (VPT) at 32 °C due to the properties of the used monomer. This causes the microgels to shrink when heated above the VPT temperature (VPTT). By introducing gold either as nanoparticles inside the network [20] or as a layer on the surface of the microgel [21], local

heating with a laser enables local changes in the size, shape and softness of the system via plasmon effects.

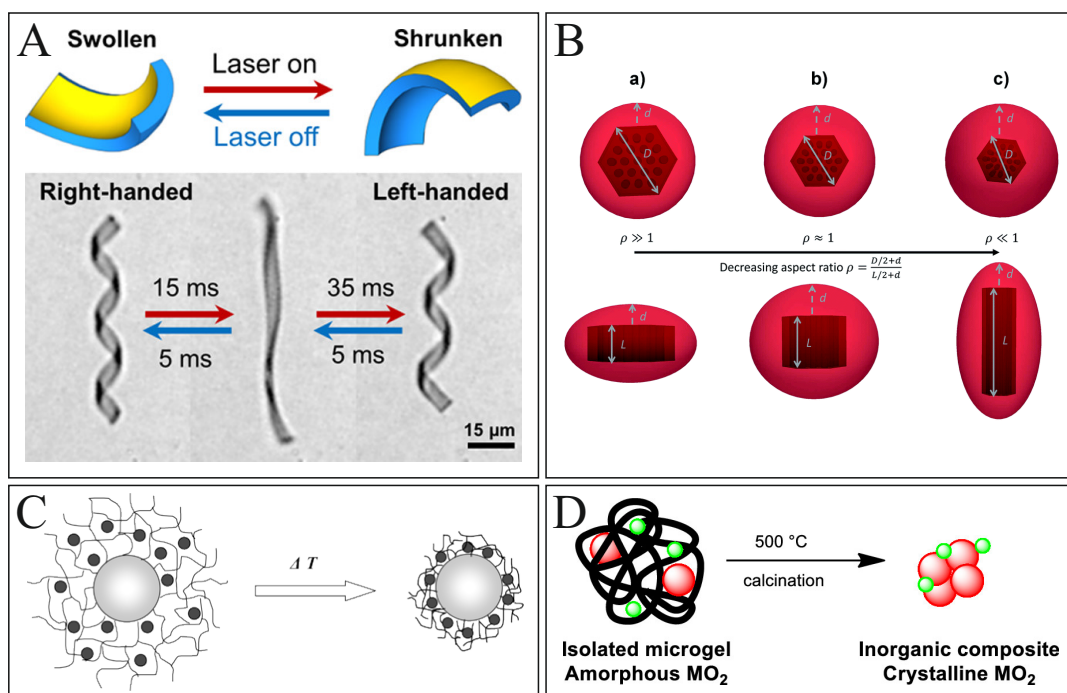


FIGURE 2.1: Schematic overview of hybrid microgels: A) PNIPAm ribbons with a one-sided gold coating, bending depending on the swelling degree of the microgel part. Reprinted with permission from American Chemical Society, Nano Letters [21]. B) Silica nanoparticles can be used as an anisotropic template for synthesizing anisotropic microgels. Reprinted with permission from Royal Society of Chemistry, RSC Advances [16]. C) PNIPAm microgels with a polystyrene core and silver nanoparticles integrated as switchable catalytic "nanoreactors." Reprinted with permission from American Chemical Society, The Journal of Physical Chemistry B [22]. D) Hybrid microgels used as a precursor for metal nanoparticle fabrication. Reprinted with permission from American Chemical Society, ACS Applied Nano Materials [23].

Zhang et al. used this principle to produce PNIPAm ribbons coated on one side with a layer of gold. In this way, they created a hybrid material that behaves like a bimetallic strip that bends depending on the swelling of the microgel part. The gold layer enables the microgel to de-swell through local laser-induced heating of the sample [21].

Silica nanoparticles can serve as core templates for synthesizing microgels and enable the production of microgels in different sizes and shapes. Schmitt et al. used mesoporous SBA-15 nanoparticles with varying aspect ratios as templates to obtain microgel particles with disk- and rod-like shapes [16]. Hybrid microgels are also being developed as carriers or "nanoreactors" for

catalytic purposes. If the metal nanoparticles (the catalytic centers) are integrated into a thermoresponsive network, the catalytic activity of such a system can be modulated by temperature changes since the accessibility of the catalytic centers changes in the collapsed state [22]. Vescovo et al. fabricated hybrid microgels as a precursor for the fabrication of noble metal/metal oxide nanoparticles. They used microgels as scaffolds for nanoparticle synthesis [23], forming the nanoparticle centers via precipitation and removing the microgel scaffold via calcination at 500 °C.

Building on the discussion of hybrid microgels with different nanoparticle materials, the following sections focus on the specific case of magnetic hybrid microgels.

2.2 Magnetic Nanoparticles

Magnetism is one of the fundamental physical forces. Magnets or magnetized materials exert an attractive or repulsive force on magnetic objects in their vicinity. This force is expressed through interactions between magnetic dipoles and charges. The introduction of the general principles of magnetism and the different types is based on the work of N. Wiberg, "Lehrbuch der Anorganischen Chemie" [24]. Magnetic fields surrounding magnetic materials are responsible for the attractive and repulsive forces. The strength and direction of these forces depend on factors such as the magnitude and orientation of the magnetic moments involved and their separation distance. Generally, one can distinguish different types of magnetism depending on the orientation of the spins inside the material.

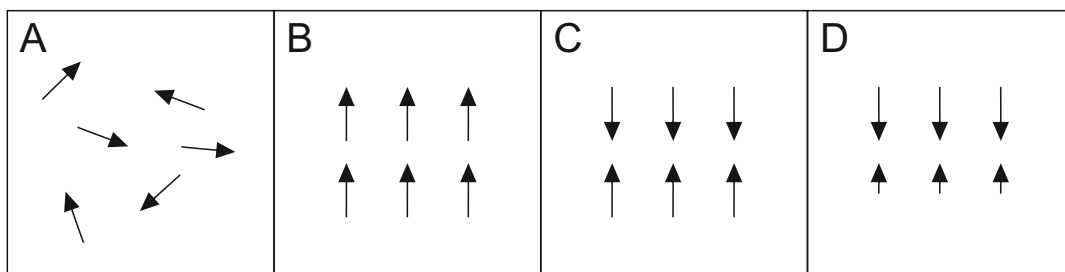


FIGURE 2.2: Schematic representation of the magnetic spin orientation for A) paramagnetism, B) ferromagnetism, C) antiferromagnetism and D) ferrimagnetism. Reproduced from "Lehrbuch der Anorganischen Chemie" [24].

Diamagnetism is characterized by the fact that no magnetic moments are present in these materials without an external magnetic field. The magnetic moments are only temporarily induced by the influence of an external magnetic field on fully occupied electron shells. Although all materials can exhibit diamagnetism, its effect is negligible compared to other types of magnetism within materials with another kind of magnetism.

In paramagnetism, the materials possess inherent magnetic moments even without an external magnetic field. This magnetic behavior arises from unpaired spins of electrons. As the orientation of these magnetic moments is randomly distributed in a material, no overall magnetic moment of the material can be observed. Within a magnetic field, these molecular magnets align themselves and create a macroscopic magnetization of the material. As soon as the external magnetic field is removed, the movement of molecular magnets (induced by the ambient temperature) randomizes the orientation again, and the macroscopic magnetization is gone. Paramagnetic materials only display weak magnetic properties compared to ferromagnets.

Ferromagnets exhibit spontaneous magnetization below their Curie temperature. In this state, permanent magnetic moments align parallel to one another. However, it is essential to note that the coupling of spins only extends over small areas, known as "magnetic domains." In the absence of an external magnetic field, these randomly oriented domains result in no observable macroscopic magnetization in ferromagnets. Nevertheless, when exposed to an external magnetic field, the magnetic moments of the magnetic domains align with the field, producing a macroscopic magnetization that does not entirely disappear upon removal of the magnetic field, a phenomenon referred to as remanence or residual magnetism. This behavior distinguishes ferromagnets from paramagnets, where the macroscopic effect vanishes entirely without an external field (Figure 2.2).

Ferrimagnetism shares many similarities with Ferromagnetism. However, the main distinction lies in the presence of two different magnetic centers. If these centers have unequal strengths and their magnetizations point in opposing directions, the net magnetic force is reduced, but the magnetic domains maintain a uniform magnetization. Consequently, Ferrimagnetism exhibits behaviors that are comparable to Ferromagnetism.

Lastly, Antiferromagnetism describes a material with two magnetic centers of equal strength that spontaneously align in an antiparallel fashion, resulting in the extinction of net magnetic moments. The antiparallel alignment is perfect at absolute zero (0 K), leading to a Diamagnetic material. However,

as the temperature rises, the material exhibits ferrimagnetic properties. For nanoparticles made of ferro- or ferrimagnetic materials, there is a unique magnetic property known as superparamagnetism [25]. In their bulk state, these materials transition to a paramagnetic state when heated above the Curie temperature. However, when the particle size is smaller than the magnetic domain size, these materials can be considered macroscopically paramagnetic even below the Curie temperature. This property results in a material that does not exhibit magnetic remanence. According to the "macrospin approximation", individual nanoparticles behave as if they are macroscopic magnetic spins, with thermal fluctuations allowing for Brownian relaxation (rotational diffusion) and Neel relaxation (reorientation of the magnetic moment) after the magnetic field is removed.

Magnetic nanoparticles (MNPs) are typically produced from various materials, sizes, and shapes, and the type of magnetism they exhibit depends on the material composition and size.

For instance, most iron oxides demonstrate ferromagnetic or superparamagnetic behavior when scaled below a specific size, while manganese MNPs are paramagnetic [26]. Depending on the application, different magnetic properties might be desired. Two primary approaches are utilized for MNP synthesis: top-down and bottom-up methods [12]. Top-down strategies entail reducing bulk materials into smaller fragments. Common techniques include ball milling, laser abrasion and thermal evaporation. In contrast, bottom-up approaches involve targeted synthesis of nanoparticles from scratch through self-assembly or chemical reactions. The choice of fabrication method depends on the requirements for the synthesized MNPs, such as size, shape or polydispersity. Overall, bottom-up methods can be regarded as more targeted and precise, while top-down methods tend to have high throughput.

Among MNPs, iron oxides such as magnetite (Fe_3O_4) and maghemite ($\gamma\text{-Fe}_2\text{O}_3$) are the most commonly used, but variety of non-iron oxide materials have been explored for magnetic nanoparticle synthesis, such as ferrites (e.g. CoFe_2O_4 or CuFe_2O_4) [27, 28] or paramagnetic manganese [26]. Among iron oxide nanoparticles, spherical superparamagnetic iron oxide nanoparticles (SPIONs) are the most widely studied type of MNPs due to their tunable size and highly magnetic properties [5]. They can be synthesized using a variety of bottom-up techniques, such as co-precipitation or thermal decomposition of organometallic compounds. Recently, there has also been

increasing interest in synthesizing nonspherical iron oxide nanoparticles, including rods, wires, platelets, and nanocubes [29]. These anisotropic structures exhibit unique magnetic properties that can be harnessed for various applications.

The incorporation of magnetic nanoparticles is essential for synthesizing hybrid magnetic microgels. In this thesis, we utilize single crystal α -Fe₂O₃ hematite nanoparticles, which possess a distinctive ellipsoidal shape and exhibit a weak magnetic moment oriented perpendicular to their long axis [30, 31]. We transform these nanoparticles into the stronger magnetic γ -Fe₂O₃ maghemite. Ellipsoidal maghemite nanoparticles have a magnetic moment oriented along their long axis, making them particularly suitable for introducing defined magnetic properties into hybrid microgel materials [10].

2.3 Magnetic Microgels

Introducing magnetic properties into microgel systems is essential for various applications, especially in medicine, where a significant challenge lies in regenerating specialized tissue such as nerves or cartilage. These tissues require scaffolds to guide cell growth in a specific direction, i.e. connecting separated nerves. Magnetic microgels can be employed for bottom-up assembly of these scaffolds, thereby promoting cellular growth and maintaining biocompatibility, depending on the monomer utilized for microgel synthesis [18, 32]. Additionally, magnetic microgels are researched, among others, for applications in drug delivery. Their magnetic properties enable targeted transportation of microscale containers to desired locations, where the encapsulated drugs are subsequently released [32]. Moreover, magnetic microgels can act as local heaters upon exposure to an alternating magnetic field, triggering drug release [33], or functioning as magnetic actuators.

2.3.1 Synthesis of Magnetic Microgels

There are different possibilities for introducing magnetic properties into a microgel system. The magnetic nanoparticles (MNP) can, for example, be dispersed into the precursor solution [18] and physically trapped inside the network, can be formed inside the microgel [34], or a microgel shell can be grafted on top of the nanoparticles leading to single core microgels [9, 35]. All of these methods lead to magnetic hybrid microgels varying in size, nanoparticle loading and magnetic responsiveness.

However, the most straightforward approach involves mixing pre-fabricated microgels with dispersions of MNPs [8]. This method is well suited for incorporating small, spherical MNP into microgels with large pore sizes. Still, microgels created in this manner are sensitive to the leaking of the MNP over time or inhomogeneous distribution inside the microgels due to diffusion limitations. The uptake of charged MNPs into oppositely charged microgels is more pronounced and can prevent leaking.

A variation of this method was reported by Zhang et al. using functionalized microgels and MNPs, effectively coating only the outside of microgels with covalently bonded nanoparticles (Figure 2.3 A, [36]).

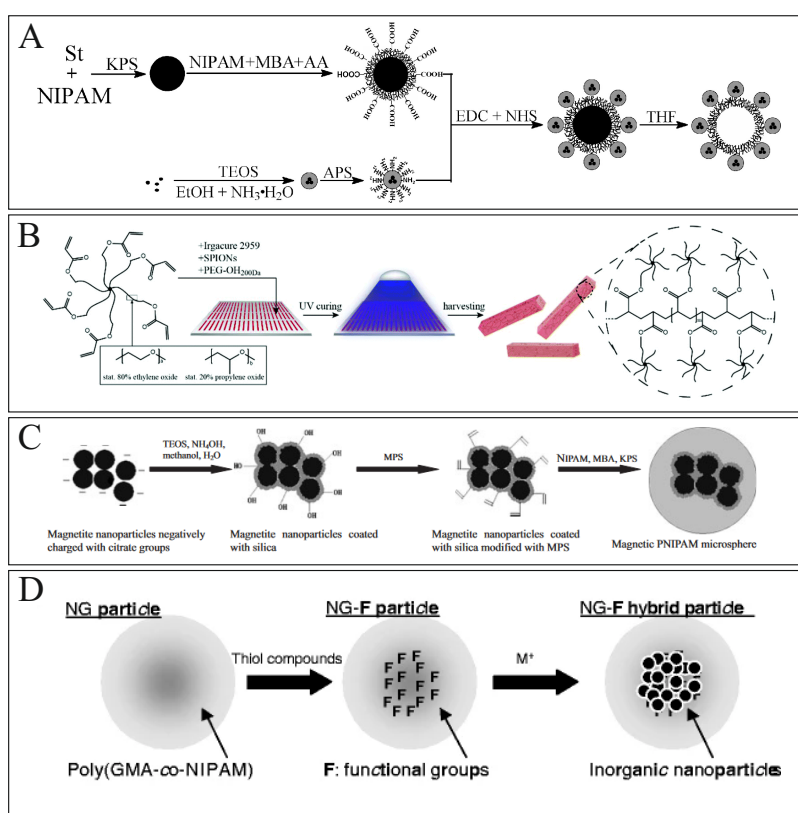


FIGURE 2.3: Synthesis options for magnetic microgels include: A) coating of the microgels with covalently bond MNPs (Reprinted with permission from American Chemical Society, Langmuir [36]), B) trapping of the nanoparticles inside the network during the microgel synthesis (Reprinted with permission from Royal Society of Chemistry, Polymer Chemistry [37]), C) grafting of microgel networks on functionalized MNP cores (Reprinted with permission from John Wiley and Sons, Advanced Materials [9]) and D) in situ synthesis of iron oxide MNPs inside a NIPAM-co-GMA (NG) microgel matrix (Reprinted with permission from Springer Nature, Colloid and Polymer Science [38]).

Incorporating larger MNPs into a microgel with this method can be challenging due to the mesh size of microgels. Therefore, another option is to disperse the nanoparticles into the precursor solution, which consists of an initiator, monomer, and crosslinker, and fabricate the microgel structure around the nanoparticles. This can be done without modification of MNP, leading to homogeneously trapped nanoparticles inside the microgel (Figure 2.3 B) [37, 39]. It is also possible to functionalize the magnetic nanoparticles with 3-(trimethoxysilyl) propyl methacrylate (TPM) and graft the microgel network on top of the nanoparticles. Thereby, the nanoparticles can be used as templates for the microgels [35, 40, 41], effectively creating a core-shell microgel with a solid, magnetic core, or multiple nanoparticles can be covalently bonded to the microgel, ensuring that they stay inside the network (Figure 2.3 C) [9, 42]. Both methods result in magnetic microgels without the possibility of leaking the magnetic nanoparticles. Last, Suzuki et al. have shown the in situ synthesis of magnetic nanoparticles inside a microgel network (Figure 2.3 D). For the microgel matrix, NIPAM and glycidyl methacrylate (GMA) were copolymerized and cross-linked with BIS, leading to a core-shell structure with predominantly GMA in the core. The nanoparticles were fabricated inside the microgel by functionalizing the GMA core with sulfonate groups and subsequent precipitation of iron oxide [38].

2.3.2 Anisotropic Magnetic Microgels as Model Systems

Microgels have frequently been proposed as model systems for a variety of systems, e.g. as model soft colloids in concentrated dispersions [43–45], or for biological systems like proteins [46, 47]. Anisotropic microgels are particularly interesting in this regard, as they can emulate anisotropic colloidal materials. The phase behavior of anisotropic nanomaterials is complex, and for many applications, controlling the ordering and packing of the particles is crucial [48, 49]. In simulations, Frenkel et al. have shown four distinct phases for ellipsoidal materials with an aspect ratio up to 3: isotropic, nematic, plastic and solid [50]. An advantage of thermoresponsive anisotropic microgels lies in their adjustable properties, such as softness and aspect ratio, enabling a single model system to accommodate a range of experimental parameters and, therefore, different phases depending on the temperature. Incorporating magnetic properties into anisotropic microgels presents additional benefits. External magnetic fields can be used to align the magnetic particles and facilitate nematic or smectic ordering, enhancing the control over phase behavior

and particle assembly [51]. This can be transferred to microgels. Additionally, the variable shell thickness of thermoresponsive microgels allows finetuning of other properties, including dipolar interactions, as dipolar interactions are ranged-dependent. This further expands their applicability and research potential.

Anisotropic magnetic microgels can be synthesized through a range of methods described in Section 2.3.1, especially using anisotropic MNPs as cores for the microgel synthesis [35, 40, 41] and the PRINT and SFL methods, described in Chapter 6 and 7, respectively.

2.4 Magnetic Microactuators

In the context of magnetic actuation for microscale materials, there are three distinct modes of action: deformation, translation and rotation. Deformation refers to the alteration in the shape of a material when subjected to an external magnetic field. This makes it useful for various applications, such as microgripper systems or mechanical triggers. At the macro scale, so-called magnetic shape memory polymers (MSMP) have been developed. These materials consist of magnetic components that enable bending when exposed to external magnetic fields through magnetic materials fixed to a non-magnetic anchor or differently magnetized local domains [52, 53]. Recently, efforts have been made to downscale comparable systems into microscale applications, resulting in several notable advancements. For instance, Lan et al. [54] demonstrated the fabrication of micro-sized shape memory polymer chains consisting of a polyurethane nickel composite, while Li et al. have shown the use of magnetic fields to influence the shape of Liquid crystal elastomer micro-structures [55]. Wang et al. [56] have fabricated magnetic micropillars that bend under the influence of a magnetic field, creating a microstructured stimuli-responsive "smart" surface (Figure 2.4 A). In the case of translational motion, the minimal case is applying a strong enough field gradient on a sample, thereby dragging magnetic materials toward the magnetic field (magnetophoresis) [57]. Thereby, no specific shape or distribution of the magnetic material is necessary, only a strong enough magnetic field to overcome the drag forces in the medium. Recent developments in the field of microrobotics have steered in a more complex direction, relying on microrollers or swimmers. Microrollers or surface rollers often work on the principle of magnetic spheres or rods, actuated by a rotating magnetic field (xz

plane), rolling along a surface [58], i.e. blood vessels [59]. For such systems, among others, magnetic Janus particles [60–62], Pickering emulsions [63] and nanorods/-tubes [64, 65] were developed for such applications. Rolling along a surface has an advantage over dragging in terms of the required forces (Figure 2.4 B).

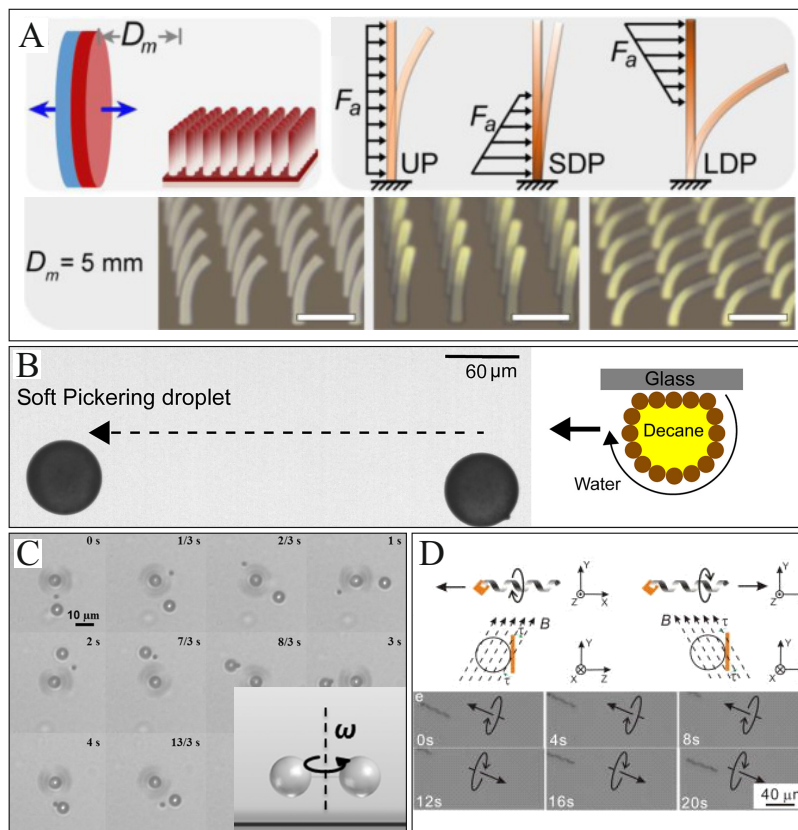


FIGURE 2.4: An overview of different microactuators: Deformation: A) magnetic micropillars filled with magnetic nanoparticles bend under an external magnetic field. The composite contained 15 vol.% nanofillers of SPIONs coated with functionalized silica shells ($\text{Fe}_3\text{O}_4@\text{SiO}_2$, average diameter of 30 nm). Scale bar = $20 \text{ }\mu\text{m}$. Reprinted with permission from Elsevier, *Extreme Mechanics Letters* [56]. Translation: B) Pickering droplet stabilized with $1 \text{ }\mu\text{m}$ polystyrene- Fe_3O_4 composite beads as microroller. Reprinted with permission from American Association for the Advancement of Science, *Science Advances* [63]. C) Artificial bacterial flagella driven by a rotating magnetic field. Reprinted with permission from American Chemical Society, *Chemical Reviews* [58]. Rotation: D) Dumbbell-shaped micro tweezer for contact-free trapping through rotation. The dumbbell particle consists of two polystyrene microbeads connected with a magnetic nickel nanowire. Reprinted with permission from John Wiley and Sons, *Advanced Functional Materials* [66].

Consequently, a weaker magnetic field can be employed when rolling. Magnetic actuation has also been applied to the development of so-called microswimmers, which rely on shape anisotropy or deformation for movement. Depending on the shape, magnetic material and deformability mechanism, there are different propulsion mechanisms possible. One of the most commonly used is the rotation of helical bodies [59, 67, 68]. These systems work on a system inspired by bacteria flagella movement and consist of a body often shaped like a screw and sometimes a "head" attached to it. Due to a rotational movement induced by a rotating magnetic field of either the body or the head, depending on which is magnetic, the cork-screw-like part of the microswimmer generates forward propulsion. An additional static magnetic field can be used for stirring in some cases (Figure 2.4 C, [58]).

The last type of magnetic actuation is a rotational actuation. While a rotation of magnetic materials in macroscale is nothing new and is used in a variety of applications already, i.e., magnetic stirrers, electro engines and others, microscale rotators are still a challenging field of development, with possible use cases in microrheology[69], microfluidics [70, 71] and contact-free motion [72]. The principle of rotating magnetic materials works similarly to microswimmers and microrollers as it also relies on rotating or alternating magnetic fields [69, 73]. In contrast, microscale rotators are stationary systems that are either fixed or confined in place or freely rotating around themselves. The shape can vary from spherical particles [74], assembled particles into an anisotropic shape [66, 75], rod-shaped probes [69, 73] to cylinder or propellor-shaped rotators. These are mostly actuated by a rotating magnetic field (xy plane), and their rotation speed is, among others, dependent on the balance between magnetic torque and the drag and friction forces (Figure 2.4 D).

These different actuators can be used for various applications, e.g., for biomedical applications such as drug delivery and cancer treatment.

2.5 Biomedical Applications

Biomedical applications are gaining significant interest in the biomedical field due to the aging populations, public health challenges and increasing cases of hard-to-treat diseases like cancer. Magnetic microgels have a wide range of potential applications in this field, some of which were briefly mentioned in

Section 2.4. In this section, these possibilities will be explored in greater detail. Magnetic microgels have a significant application in drug delivery systems. They work by incorporating drugs into the microgels, which can then be directed to specific areas in the body through magnetic guidance. This approach improves the effectiveness of therapy while also minimizing side effects by limiting exposure to healthy tissue [76]. The magnetic nanoparticles also allow for a collapse of thermosensitive hybrid microgels, leading to a remotely triggered and targeted release of the drugs [77–79].

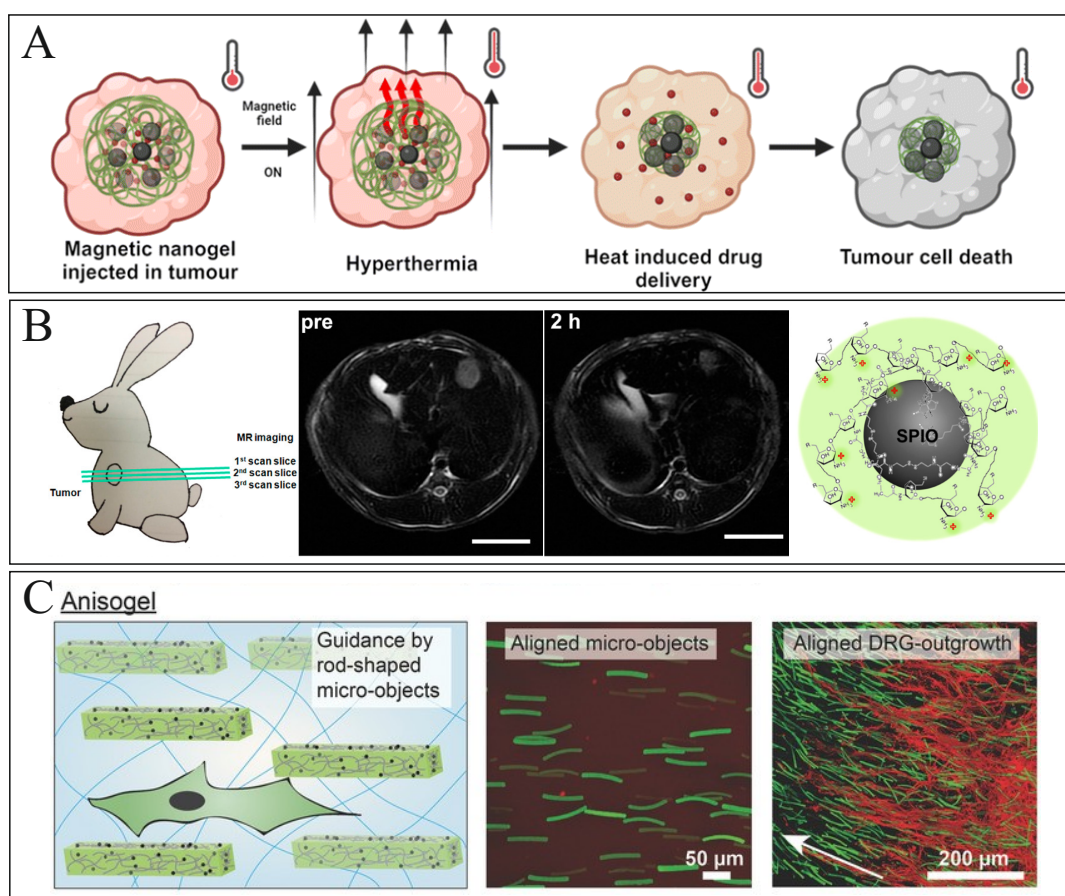


FIGURE 2.5: Biomedical applications of magnetic microgels: A) Schematic of a combined hyperthermia and drug therapy for cancer treatment. Reproduced with permission from Royal Society of Chemistry, Nanoscale [80]. B) Magnetic microgels used as contrast agents for Magnetic Resonance Imaging (MRI) enhancement. Reproduced with permission from American Chemical Society, ACS Nano [81]. C) Aligned magnetic microgel rods embedded within a hydrogel matrix that mimics the extracellular matrix form an Anisogel. This structure can be utilized to guide cell growth along the alignment of the microgels. Reprinted with permission from Wiley, Advanced Healthcare Materials [82].

Following the same principle, magnetic microgels are also investigated for magnetic hyperthermia therapy. In this context, exposure to an alternating magnetic field induces heat generation within the microgel, which can be harnessed to destroy cancer cells or bacteria (Figure 2.5 A) [80]. These magnetic microgels are designed with a hydrogel matrix that enhances biocompatibility by protecting the magnetic core from direct interactions with biological systems [83].

Additionally, magnetic microgels have significant applications in diagnostic imaging due to their magnetic properties. Magnetic nanoparticles are commonly used as contrast agents in Magnetic Resonance Imaging (MRI) because they enhance signal intensity, image quality, and resolution. Magnetic microgels can be engineered to mimic the properties of these contrast agents, enabling specific targeting of certain areas within the body. Wang et al. have advanced this technology by developing a multifunctional microgel system compatible with both ultrasonic and magnetic resonance imaging techniques (see Figure 2.5 B) [81]. This hybrid microgel consists of magnetic nanoparticles and enzymes (catalase and superoxide dismutase) encapsulated within a glycol chitosan matrix. The integrated enzymes are responsive to pathological stimuli (H_2O_2 , $\text{O}_2^{\bullet-}$), enabling catalytic reactions that generate oxygen bubbles and thereby increasing contrast in ultrasonic imaging. SPIONs incorporated into the microgel can be utilized for MRI, allowing the integration of both imaging modalities to enhance diagnostic capabilities.

Tissue engineering is a multidisciplinary field focused on developing functional tissues and organs to replace or repair damaged or diseased ones. Magnetic microgels have emerged as promising scaffolding materials in this area due to their unique properties, particularly their magnetic responsiveness. Instead of using scaffolds composed of large-scale hydrogels, the microgels are used as microscaled building blocks for tissue engineering scaffolds (Figure 2.5 C) [82, 84, 85]. The ability to manipulate magnetic microgels using external magnetic fields simplifies the creation of complex three-dimensional structures for tissue engineering applications. This is especially beneficial when working with cells that require specific microenvironments or arrangements, such as neuronal cells. Rose et al. have created an Anisogel by integrating magnetically aligned rod-shaped microgels with a hydrogel designed to mimic the extracellular matrix. These Anisogels have demonstrated the ability to direct cell growth along the aligned microgel rods. In this configuration, the microgels serve as barriers that do not support cell ingrowth, contrasting with the surrounding hydrogel [19, 37]. The magnetic properties

also allow for additional mechanic stimuli and release of therapeutic agents [86].

Magnetic microgels also have potential applications in water treatment and environmental remediation due to their high adsorption capacity and ease of separation using magnets. They can be utilized to remove heavy metals, pollutants and other contaminants from wastewater or soil [87, 88].

2.6 Scope of the Thesis

This thesis focuses on the complete size range of hybrid magnetic microgels (MMGs), from small ellipsoidal microgels measuring a few hundred nanometers to microgel rods sized 5x5x50 micrometers and complex-shaped impellers approximately 100 micrometers in diameter (Figure 2.6). The synthesis, conversion and characterization of ellipsoidal magnetic nanoparticles (MNPs) and their integration into microgels are studied to explore various applications. The resulting magnetic microgels exhibit unique properties that make them suitable for diverse purposes. A short overview of the methods used within this thesis and their theoretical background is given in Chapter 3.

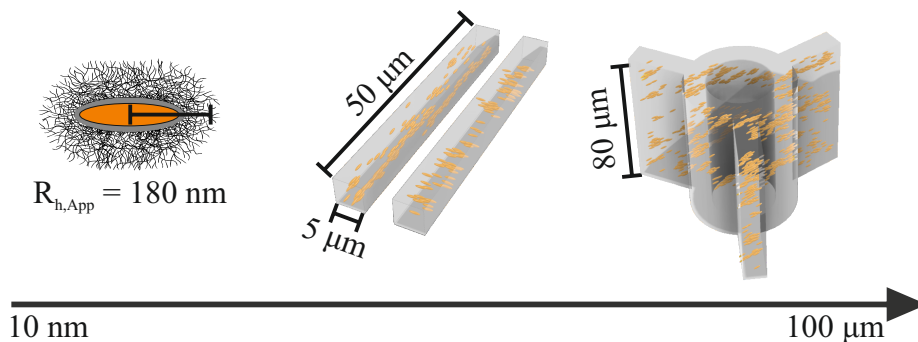


FIGURE 2.6: Schematic representation of the MMGs fabricated and studied in this thesis. Left to right: small ellipsoidal microgels, with a single nanoparticle core and a thermoresponsive PNIPAM shell, rod-shaped microgels with pre-programmed magnetic moments and impeller-shaped microgels fabricated via stop-flow lithography.

Chapter 4 focuses on the magnetic nanoparticles and sheds light on the synthesis, conversion and characterization of ellipsoidal iron-oxide nanoparticles, starting from weakly magnetic ellipsoidal hematite nanoparticles synthesized through a precipitation method. Subsequently, the conversion of

these nanoparticles into ferromagnetic maghemite MNPs is investigated, and the ellipsoidal MNPs and their dipolar self-assembly are characterized using electron microscopy and scattering methods. Depending on the non-magnetic shell (silica and microgel) around MNPs, the dipolar interactions between the particles and, therefore, their behavior under a magnetic field change significantly. Furthermore, Chapter 4 reports on the synthesis of a minimal magnetic microgel system consisting of silica-coated MNPs with a thermoresponsive PNIPAm microgel shell, allowing for finetuning magnetic dipolar interactions through swelling and deswelling the shell.

In Chapter 5, the phase behavior of small ellipsoidal MMGs, with sizes around a few hundred nanometers, in dense microgel dispersions is investigated in bulk and at the interface. The ellipsoidal MNP core facilitates easy detection in scattering and allows orientation tracking when exposed to an external magnetic field, providing valuable insights into the dynamics and phase behavior of microgels close to the glass transition. Therefore, SAXS measurements under static and rotating magnetic fields are conducted at different field strengths, probing the rotation and relaxation behavior of free, partly and fully arrested microgels.

Chapter 6 delves into the development of microgel scaffolds for tissue engineering for biomedical purposes, such as wound healing or drug testing devices. Therefore, the fabrication of rod-shaped magnetic microgels with pre-programmable magnetic properties is studied using particle replication in a non-wetting template (PRINT). It is revealed that the magnetic behavior of rod-shaped MMGs can be pre-programmed by incorporating and pre-aligning ellipsoidal MNPs during the synthesis, allowing the creation of multidirectional scaffolds to promote cell growth, making them promising candidates for controlled tissue development. The findings from this chapter also showcase a promising proof of concept, indicating the ability to align microgels within a dynamic magnetic field. This technique opens up the possibility of creating intricate 3D scaffolds with enhanced control and precision.

Finally, large complex-shaped magnetic microgels, produced in a continuous high throughput method, were studied in Chapter 7. The magnetic hybrid microgels were fabricated using stop-flow lithography (SFL), allowing every 2D shape to be elongated into the third dimension. This study involved the pre-alignment of MNPs in a magnetic field, followed by the cross-linking

of microgels around them. By applying a remote magnetic field, these MMGs can create a strong microscopic flow on demand. This capability opens up possibilities for applications in micro-robotics and lab-on-a-chip devices. For example, this chapter discusses the development of an active microfluidic device consisting of an impeller-shaped MMG fixed inside a microfluidic channel.

Chapter 3

Methods

3.1 Thermogravimetric Analysis (TGA)

This section provides a short introduction to thermogravimetric analysis based on the work of Prime et al. [86]. TGA is a powerful analytical technique used to study the thermal behavior of materials, particularly their decomposition or changes in mass with temperature. It involves heating a sample under controlled conditions and measuring its mass loss as a function of temperature. Typical temperature ranges from room temperature to 1000°C are possible, and the setup is usually coupled with a gas flowing through the furnace, varying from inert gases like nitrogen or argon to reducing (hydrogen) or oxidizing (oxygen or air) atmospheres. The TGA can provide valuable insights into the thermal stability, purity, composition, oxidation states and decomposition mechanisms of materials.

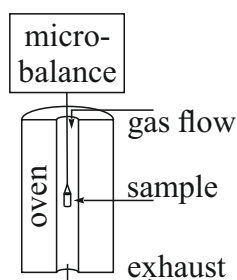


FIGURE 3.1: Schematic of a TGA device.

In this study, TGA was employed to precisely control the transformation of hematite (α -Fe₂O₃) into maghemite (γ -Fe₂O₃). Further details on the experimental procedure can be found in Chapter 4.

3.2 Scattering Methods

Determining the size, structure and dynamic behavior of small objects presents challenges, particularly as microscopy methods have limitations such as the diffraction limit and extended illumination times. However, scattering methods offer a viable solution, overcoming some of these limitations and providing valuable insights into various aspects of small-scale objects. In this section, the general principles of a range of scattering methods are described, detailing Dynamic Light Scattering (DLS), Small-Angle X-ray Scattering (SAXS) and Differential Dynamic Microscopy (DDM) [89–91].

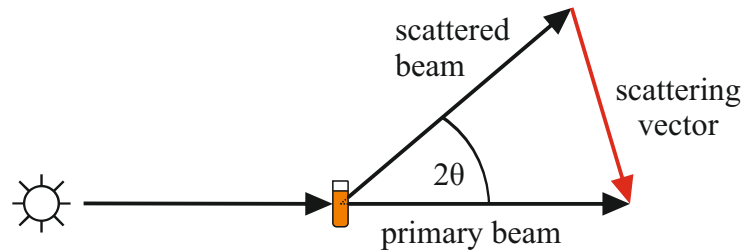


FIGURE 3.2: Schematic representation of scattering.

The minimal requirements for a scattering experiment are a coherent incident beam, a scattering medium and a detector. The incident beam can consist of light, neutrons or X-rays. Some of the incident beam passes through the sample (primary beam), while a part of it is scattered at the sample (secondary beam). Depending on the radiation used as the incident beam, the scattering is based on different interactions: Light scattering through variations of the refractive index or dielectric properties, X-rays through the electrons of the sample and neutrons scattered by the nuclei. The scattering vector q is defined as the difference between the scattered and the primary beam, and it depends on the wavelength λ of the incident beam, the reflective index of the medium n_0 as well as on the scattering angle 2θ (Equation 3.1).

$$q = \frac{4\pi n_0}{\lambda} \cdot \sin(\theta) \quad (3.1)$$

Depending on the scattering method used, the average scattering intensity either reveals structural information or information on the dynamic behavior. The following sections will provide detailed examples of both.

3.2.1 Dynamic Light Scattering (DLS)

Dynamic Light Scattering (DLS) works on the principle of intensity fluctuation of scattered light to determine the diffusive behavior of a sample. Therefore, the scattering intensity is measured time-dependently along a fixed scattering angle. The light scattering from a suspension of colloidal particles exhibits speckles due to interference between light scattered by individual particles. The intensity of the scattered light at any given point in the far field fluctuates randomly with time as the particle positions change due to Brownian diffusion. This signal contains information about the particle motions, particularly their speeds – the faster the particles diffuse, the more rapidly the intensity fluctuates. The information can be extracted from the intensity fluctuations from the time correlation function (Equation 3.2) [90],

$$\langle I(q, 0)I(q, \tau) \rangle \equiv \lim_{T \rightarrow \infty} \frac{1}{T} \int_0^T dt I(q, t) I(q, t + \tau) \quad (3.2)$$

with starting time t , lag time τ and the corresponding intensities $I(q, t)$ and $I(q, t + \tau)$ at a scattering vector q . The time correlation function of the scattered intensity is defined by

$$g^{(2)}(q, \tau) \equiv \frac{\langle I(q, t)I(q, t + \tau) \rangle}{\langle I(q) \rangle^2} \quad (3.3)$$

Considering the normalised time correlation function of the scattered field $g^{(1)}(q, \tau)$, the ‘Siegert relation’ can be derived (Equation 3.4).

$$g^{(2)}(q, \tau) = 1 + \beta [g^{(1)}(q, \tau)]^2 \quad (3.4)$$

with β being a correction factor for experimental setups. For ‘point detectors’, that detect areas as small as a single speckle $\beta \rightarrow 1$. For identical interacting spheres, the intermediate scattering function $f(q, t)$ is defined as equal to the field correlation function $g^{(1)}(q, \tau)$.

$$f(q, t) \equiv g^{(1)}(q, \tau) \quad (3.5)$$

For polydisperse spheres, the measured intermediate scattering function $f^M(q, \tau)$ is defined analogously to $f(q, \tau)$ in Equation 3.5. It can be described as the sum of intensity-weighted exponentials, each corresponding to a scattering object.

$$f^M(q, t) = \int dD P(D) e^{-Dq^2 \tau} \quad (3.6)$$

with the normalized intensity-weighted distribution of diffusion constants $P(D)$. Equation 3.6 can be resolved with the cumulant method [92], deriving f^M from a Taylor series (Equation 3.7).

$$\ln f^M(q, t) = -\bar{D}q^2\tau + \frac{1}{2}\left(\frac{\overline{D^2} - \bar{D}^2}{\bar{D}^2}\right)(\bar{D}q^2\tau)^2 + \dots \quad (3.7)$$

Considering narrow size distributions, the series is ended after the second cumulant and the mean diffusion coefficient \bar{D} can be determined through fitting with Equation 3.7. The diffusion coefficient is represented by the first cumulant, while the polydispersity can be determined by comparing both cumulants. Analog to ideal spheres, an apparent hydrodynamic radius $R_{H,app}$ can be calculated with the Stokes-Einstein equation (Equation 3.8).

$$R_{H,app} = \frac{k_B T}{6\pi\eta\bar{D}} \quad (3.8)$$

with the Boltzmann constant k_B , Temperature T and the viscosity of the solvent η . DLS alone is insufficient to determine the dimension of anisotropic particles, but it can be used to determine the quality of the dispersion if the particle dimensions are known.

3.2.2 Small-Angle X-Ray Scattering (SAXS)

Small-angle X-ray scattering (SAXS) is a well-established method for determining the structure of nanoparticles [90]. Analogous to light scattering, SAXS depends on the scattering of X-rays at the electrons of the sample. As evident from Equation 3.1, X-ray scattering can be used to resolve larger q ranges and, therefore, smaller size scales compared to light scattering due to its smaller wavelength ($\lambda \sim 0.1$ nm) [90].

The scattering intensity of a SAXS measurement can be defined as Equation 3.9,

$$I(q) = NV^2 \Delta\rho^2 P(q) S(q) \quad (3.9)$$

with the particle number density N , scattering volume V and scattering contrast $\Delta\rho$. Form factor $P(q)$ and structure factor $S(q)$ both contribute to the overall scattering intensity. The form factor $P(q)$ contains information on the internal structure of single uncorrelated particles, while $S(q)$ accounts for

the distribution of particles depending on their number density and inter-particle interactions.

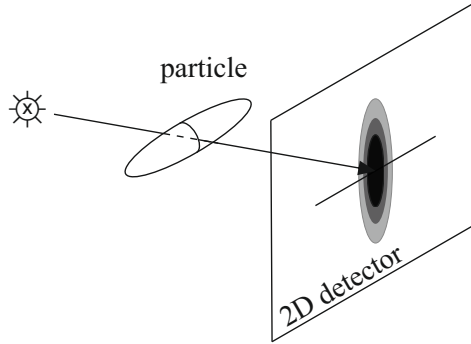


FIGURE 3.3: Schematic representation of small-angle X-ray scattering of ellipsoidal particles. Reproduced from "Small angle scattering of X-rays[93].

The form factor of an ellipsoid [94] can be described as

$$P(q) = \left[\Delta\rho V \frac{3(\sin qr - qr \cos qr)}{(qr)^3} \right]^2 \quad (3.10)$$

with scattering contrast $\Delta\rho$, volume V of the ellipsoid and

$$r = \left[R_{eq}^2 \sin^2 \alpha + R_{pol}^2 \cos^2 \alpha \right]^{1/3} \quad (3.11)$$

with the radii R_{pol} (polar) & R_{eq} (equatorial) and the angle α between R_{pol} and \vec{q} . The structure factor $S(q)$ can be defined as shown in Equation 3.12.

$$S(q) = \frac{1}{N} \sum_{j=1}^N \sum_{k=1}^N \langle e^{-iq(R_j - R_k)} \rangle \quad (3.12)$$

In the case of highly diluted systems, the structure factor is equal to 1 [90]. Experimentally, the structure factor can be determined through the ratio of two measurements, one highly diluted and the other the desired concentration.

$$S(q) = \frac{\langle I_S(q) \rangle_{conc}}{\langle I_S(q) \rangle_{dil}} \frac{N_{dil}}{N_{conc}} \quad (3.13)$$

Details on the experimental setups used for SAXS in this work can be found in the respective experimental Sections 4.2 and 5.2.

3.2.3 Differential Dynamic Microscopy (DDM)

Differential Dynamic Microscopy (DDM) is a recently developed method for investigating the dynamics of colloidal particles [95, 96], offering an alternative to traditional scattering techniques such as dynamic light scattering (DLS). Unlike those, DDM is executed on a relatively simple setup that comprises a standard microscope and a high-speed camera. This simplicity allows the utilization of this technique without extensive technical knowledge. Furthermore, DDM can be employed on turbid samples and samples under flow, making it suitable for studying anisotropic diffusion behaviors [30].

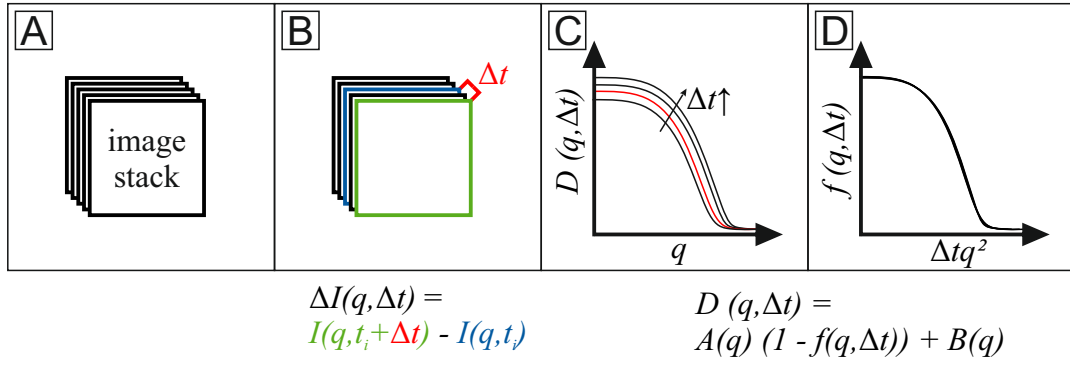


FIGURE 3.4: Schematic of the principle of DDM measurements. A) An image stack is recorded, and B) for each pixel, the difference is calculated depending on the time interval Δt . C) Fourier transformation and radial averaging yields in the DDM matrix $D(q, \Delta t)$. D) The intermediate scattering function $f(q, \Delta t)$ can be derived from the DDM Matrix dependent on Noise $B(q)$ and Amplitude $A(q)$.

Figure 3.4 illustrates the fundamental principles of Differential Dynamic Microscopy (DDM) measurements. To obtain meaningful data from this technique, a sequence of images is acquired and analyzed by comparing individual frames. The analysis hinges on calculating the intensity difference for each pixel between successive frames, as described by Equation 3.14 [91].

$$\Delta I(\vec{r}, t, \Delta t) = I(\vec{r}, t + \Delta t) - I(\vec{r}, t) \quad (3.14)$$

Here, $I(\vec{r}, t)$ represents the intensity of the pixel at a given spatial position \vec{r} and time instant t . By computing the difference in intensity between adjacent frames with a time interval Δt , we obtain the temporal contrast $\Delta I(\vec{r}, t, \Delta t)$.

Subsequently, the time-averaged 2D spatial Fourier transformation of the temporal contrast is calculated and denoted as the DDM matrix $D(q, \Delta t)$. This matrix can be expressed in terms of its amplitude $A(q)$, time-independent noise $B(q)$ and the intermediate scattering function $f(q, \Delta t)$ (as per Equation 3.16).

$$D(\vec{q}, \Delta t) = 2\langle |\hat{I}(\vec{q}, t)|^2 \rangle_t \left[1 - \frac{\langle \hat{I}^*(\vec{q}, t) \hat{I}(\vec{q}, t + \Delta t) \rangle_t}{\langle |\hat{I}^*(\vec{q}, t)|^2 \rangle_t} \right] \quad (3.15)$$

$$D(q, \Delta t) = A(q) [1 - f(q, \Delta t)] + B(q) \quad (3.16)$$

$A(q)$ and $B(q)$ can be determined by analyzing the behavior of $D(q, \Delta t)$ at short and long times. For short times, $\Delta t \rightarrow 0$, the system remains essentially unchanged and the correlation function f approaches $f(q, \Delta t \rightarrow 0) = 1$. In this case, $D(q, \Delta t \rightarrow 0)$ approximates $B(q)$, representing the time-independent noise or background signal. On the other hand, for long times, $\Delta t \rightarrow \infty$, the system becomes completely decorrelated and $D(q, \Delta t \rightarrow \infty)$ corresponds to $A(q) + B(q)$.

The analysis of the intermediate scattering function $f(q, \Delta t)$ depends on the system under investigation. For dilute Brownian particles, a cumulative analysis is typically employed. However, in some cases, a single exponential fit (Equation 3.17) does not consistently provide accurate results. Therefore, a stretched exponential function (Equation 3.18) can be used, which offers better flexibility for characterizing complex relaxation processes.

$$f(q, \Delta t) = e^{-\frac{\Delta t}{\tau}} \quad (3.17)$$

$$f(q, \Delta t) = e^{-\left(\frac{\Delta t}{\tau}\right)^\alpha} \quad (3.18)$$

with the stretching exponent α . The relaxation time τ , as defined in Equation 3.19, can be derived from the intermediate scattering function $f(q, \Delta t)$, and it is proportional to the diffusion coefficient D of the examined particles. The choice between a single exponential or stretched exponential fit depends on the specific system's behavior. It can significantly impact the accuracy of the results obtained from the DDM matrix analysis.

$$\tau = \frac{1}{Dq^2} \quad (3.19)$$

The methodology for calculating the DDM matrix $D(q, \Delta t)$ was adapted from the work provided by Germain, Leocmach and Gibaud [91] and conducted via DDMsoft [97].

3.3 Microscopy

Microscopy is a widely used imaging technique for examining and observing objects or structures that are too small to see with the naked eye. There are a variety of different microscopy methods for different sizes and materials. The most commonly used technique is bright field microscopy, in which the sample is illuminated from below with white light and can be viewed through an objective lens, allowing for high resolution when examining transparent or semi-transparent samples. With this method, the resolution is limited by the wavelength of visible light. This is described by the Abbe limit Equation 3.20 [98].

$$d = \frac{\lambda}{2 \cdot NA_{Obj}} \quad (3.20)$$

where d is the achievable resolution, defined as the minimum distance between two lines that can still be resolved as separate lines, and numerical aperture of the objective NA_{Obj} . There are a variety of techniques for imaging smaller objects, such as electron or confocal microscopy. These are described in the following sections.

3.3.1 Confocal Microscopy

Confocal microscopy represents a significant advancement in optical imaging technology, enabling high-resolution, three-dimensional visualizations. This technique improves image contrast and resolution by employing a confocal configuration often combined with fluorescence microscopy. This configuration ensures both the excitation and detection beams intersect at a single focal point within the sample, effectively rejecting out-of-focus light and improving image clarity.

In confocal microscopy, a focused laser beam is employed for excitation and detection. The laser beam passes through the objective lens to illuminate a small focal volume within the sample. Subsequently, the reflected or fluorescent light emitted from this volume is collected by a pinhole situated in the detection pathway, filtering out-of-focus light. Through scanning in xyz-directions, a 3D image is recorded. However, confocal microscopy does present some limitations, such as reduced field-of-view, longer acquisition times and photobleaching. The confocal technique achieves high resolution by using a narrow focus point, capturing only a small sample slice to limit background interference [99, 100].

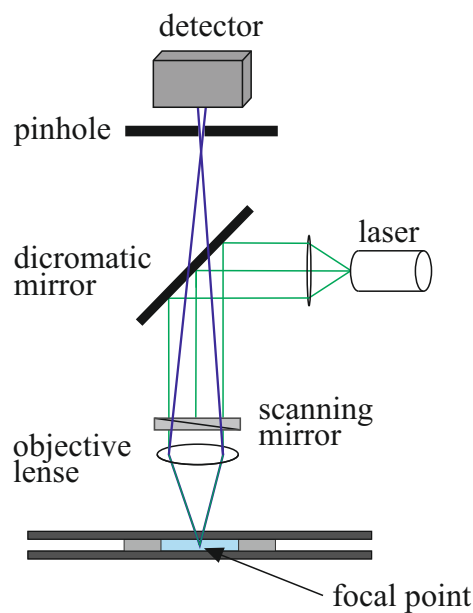


FIGURE 3.5: Schematic of the principle of confocal microscopy. Excitation light is colored in green and emission light in blue.

Details on the used setups can be found in the experimental section of the respective chapters.

3.3.2 Electron Microscopy

Electron microscopy (EM) represents a powerful tool for studying structures and materials beyond the reach of optical microscopy due to their dimensions and contrast. This imaging technique can achieve significantly higher resolution than its optical counterpart by employing an electron beam. Electrons have a smaller wavelength compared to visible light, leading to a higher

resolution (Abbe Limit, Equation 3.20). The two most common forms of electron microscopy are scanning electron microscopy (SEM) and transmission electron microscopy (TEM), each with unique applications and capabilities.

In SEM, a focused electron beam is raster-scanned across the surface of a sample, generating backscattering and secondary electrons collected by detectors. These electrons carry topographical information about the sample's surface, yielding high-resolution images of the sample's surface and, in the case of organic materials, the insides close to the surface. The resolution is in the low 10 nm range. SEM can be employed to image a wide range of samples, including metals, ceramics and polymers. As can be seen in the schematic (Figure 3.6 A), the electrons are produced and accelerated by an electron gun and an anode, and with condensing lenses and scanning coils, the electron beam is targeted onto the sample. In contrast to SEM, TEM employs a thin sample specimen with electrons passing through it to form an image. A focused electron beam is transmitted through the sample, and the diffracted electrons are collected by a projector lens and focussed onto an imaging detector. Thus, not only the surface but also the inner structure of the sample can be detected by TEM. For high-resolution TEM, a resolution below 0.1 nm can be achieved [98].

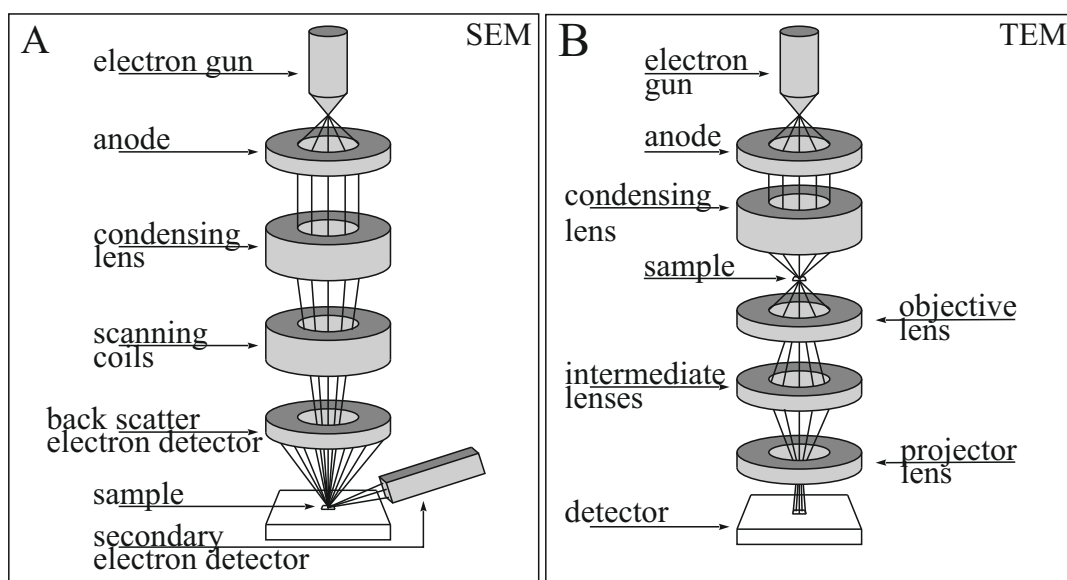


FIGURE 3.6: Schematic of the principle of A) scanning and B) transmission electron microscopy. Reproduced from [101, 102]

Further details on the different instruments used in this thesis are provided in the experimental sections of the chapters.

Chapter 4

Characterization and Self-Assembly of Anisotropic Hybrid Magnetic Microgels

4.1 Introduction

Magnetic microgels (MMGs) are nano- to micrometer-scaled hydrogels that exhibit magnetic properties primarily through the incorporation of magnetic nanoparticles (MNPs) [18, 31, 57]. These hybrid materials have garnered significant attention due to their unique properties and potential applications in various fields, including biomedicine and environmental technology [57, 103, 104]. Encasing MNPs within a soft polymer matrix creates a type of magnetic soft matter that is particularly beneficial for applications requiring enhanced biocompatibility or cellular interactions. A key strength of MMGs lies in their versatility: by tailoring the polymer network with specific monomers, MMGs can be functionalized with features such as thermo- or pH-responsiveness or to enhance their compatibility with cells and biomedical applications [18, 103].

The basic version of MMGs features a single magnetic nanoparticle as the core. These microgels enable the study of dipolar interactions between MNP cores and their self-assembly. As dipolar interactions are sensitive to the inter-particle distance [105], it is challenging to control their strength. To address this limitation, thermosensitive poly(N-isopropyl acrylamide) (PNIPAm) microgel shells are utilized to modulate the shell thickness, thereby influencing the inter-particle distance and, consequently, the strength of dipolar interactions [41, 106, 107].

Dagallier et al. have synthesized magnetic microgels using ellipsoidal hematite nanoparticles as iron oxide cores, exhibiting weakly magnetic moments perpendicular to the nanoparticle's long axis [41, 106]. These ellipsoidal hematite MNPs were prepared via a precipitation reaction and exhibit defined aspect ratios according to the procedure described by Ocaña et al. [108]. Consecutively, these nanoparticles were coated with silica before grafting thermoresponsive PNIPAm shells on top [41], creating magnetic microgels with tunable dimensions and aspect ratio. When subjected to a strong magnetic field (700 - 1000 mT), these microgels align according to their magnetic field but do not show dipolar interactions. Converting the nanoparticle core from hematite to maghemite enhances the magnetic strength, as demonstrated by Malik et al. [10]. This transformation alters the direction of the magnetic moment to align with the long axis of the ellipsoidal MNPs. Incorporating these maghemite nanoparticles into a PNIPAm microgel shell allows for studying thermally switchable dipolar assemblies.

The present chapter focuses on the preparation of ellipsoidal magnetic nanoparticles and the synthesis of a basic magnetic microgel system consisting of a single magnetic core encapsulated by a microgel shell. The study explores the process from preparing weakly magnetic ellipsoidal hematite nanoparticles to enhancing their magnetism through conversion to maghemite and, ultimately, the synthesis of a complete MMG system. Various characterization techniques are employed to investigate each step of this process, including thermogravimetric analysis (TGA) for assessing the conversion process of hematite nanoparticles to maghemite, electron microscopy (TEM & SEM) for determining the dimensions of individual ellipsoidal MNPs and observing the collective response of MNPs to magnetic fields. Dynamic light scattering (DLS) and differential dynamic microscopy (DDM) are employed to investigate the dynamic behavior of MNPs and MMGs, and small-angle X-ray scattering (SAXS) to study the structural organization of MNPs and MMGs through dipolar interactions. The results demonstrate an anisotropic hybrid microgel system with defined magnetic properties, where dipolar interactions can be tuned by the non-magnetic shell. In summary, this chapter details the synthesis, characterization and dipolar assembly inside a magnetic field of a core-shell MMG system.

4.2 Experimental Section

4.2.1 Materials

All materials in this section were used as provided by the respective supplier. Ammonia solution (28-30%), potassium peroxydisulfate (KPS), sodium dihydrogen phosphate monohydrate (NaH_2PO_4), tetra-ethyl orthosilicate (TEOS) and hydrochloric acid (HCl) (fuming, 37%) were acquired from Merck KGaA, Germany. *N, N'*-methylene bisacrylamide (BIS), *N*-isopropyl acrylamide (NI-PAm), polyvinylpyrrolidone (PVP) and tetramethylammonium hydroxide (TMAH) (25 wt%) were purchased at Sigma Aldrich, Germany.

4.2.2 Hematite Synthesis

The ellipsoidal hematite nanoparticles were prepared following a process previously described by Ocaña et al. [108]. Therefore, iron (III) perchlorate hydrate ($\text{Fe}(\text{ClO}_4)_3$) was dissolved in water with urea and sodium dihydrogen phosphate monohydrate (NaH_2PO_4). Ultrasonication ensured proper dissolution and mixing, and the closed bottle was heated to 98 °C for 24 h. The nanoparticles were purified by multifold centrifugation and solvent exchange. In this thesis, two different batches of hematite cores were used, one provided by Thiago Ito (H1) and the other by Anne Nickel (H2) [109]. The nanoparticle dimensions were assessed by electron microscopy and small-angle X-ray scattering. From TEM micrographs, around ~ 70-100 nanoparticles were measured to determine the dimensions. For H1, the TEM images were conducted after the conversions to maghemite, while H2 was measured directly after the nanoparticle synthesis. SAXS measurements on the core, core-shell and hollow shell were analyzed to support those measurements and precisely determine the long and short dimensions of the magnetic core and the thickness of the microgel shell using a polydisperse core-shell ellipsoid model.

4.2.3 Silica Coating

To stabilize and further functionalize the magnetic nanoparticles, a silica coating is applied following a two-step procedure, first described by Graf et al. [110] and conducted analog to previous publications [10, 17, 105]. First, the hematite cores dispersed in EtOH (23.5 ml, 2.13 wt%) were stabilized by adsorbing PVP at the surface of the nanoparticles. Therefore, 700 ml of a

0.12 wt% PVP (avg. MW: 40k) solution was added to the core dispersion while sonicating and stirring for 5 h and consecutively stirring for another 19 h without sonication. The stabilized cores were purified through fivefold centrifugation (90 min, 5000 rpm) and solvent exchange (1x H₂O & 4x EtOH). The silica coating is applied to the iron oxide cores in a second step. Therefore, 500 mg of the hematite cores stabilized by PVP are dispersed in a three-neck flask with 1055 ml of EtOH and 105 ml H₂O. Under sonication and stirring (overhead stirrer), 444 µl TMAH (25 %) was dropwise added to the dispersion. A mixture of 4.43 ml TEOS and 3 ml EtOH was added dropwise in three steps (each 1/3 of the total) after 30, 50, and 70 minutes, respectively. The mixture was sonicated for another 110 minutes and stirred only for the consecutive 21 h. The stabilized cores were purified through fivefold centrifugation (90 min, 5000 rpm) and solvent exchange (5x EtOH) and were concentrated to a volume of 45 ml. The silica coating was only applied for H2, as H1 was provided as a silica-coated freeze-dried powder (SCH1).

4.2.4 Transformation from Hematite to Maghemite

The conversion is a two-step procedure via the structure of magnetite and is conducted within a thermobalance.

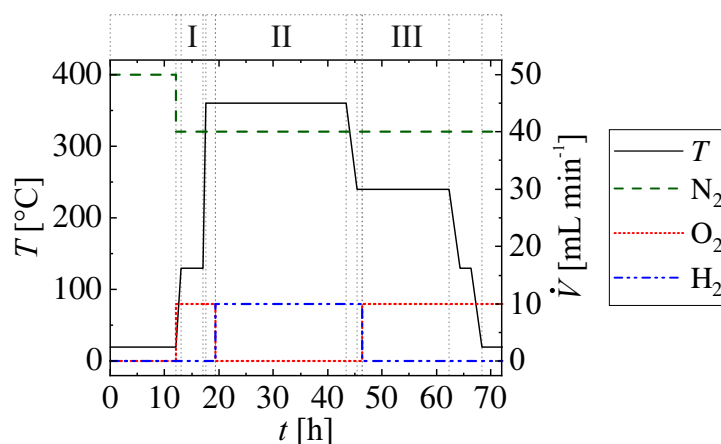


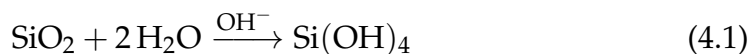
FIGURE 4.1: Gas flows and heat settings for the conversion process inside a thermobalance.

An Al₂O₃ TGA crucible was used for the process. SCH1 was provided as a freeze-dried powder, while SCH2 and SCH3 were dried at 80 °C in the oven. First, the silica-coated hematite particles are reduced to magnetite at 360 °C in a hydrogen atmosphere with nitrogen as carrier gas (N₂:H₂; 40:10 mL min⁻¹) for 24 h and consecutively re-oxidized to maghemite at 240 °C in an N₂:O₂

mixture of 40:10 ml min⁻¹ for 15 h (Figure 4.4). The conversion is conducted in a SETSYS 16/18 thermobalance for higher control over the conditions and to observe the mass loss of the different conversion steps separately. The thermobalance is connected to a gas mixing system consisting of multiple mass flow controllers.

4.2.5 Disolution of the Silica Shell

Especially for SCH1 and SCM1, respectively, the dissolution of the silica shell was necessary to properly disperse the particles, as they contain large aggregates after the conversion. Therefore, the silica coating was etched by adding 400 µL of 1 M NaOH solution per 5 mL of 1 wt% maghemite dispersion and mixing for one week — the silica dissolution proceeds according to the mechanism of a catalyzed hydrolysis reaction. Repeated centrifugation cycles with solvent exchange were conducted to purify the maghemite dispersion, first with ethanol and then with water.



4.2.6 Microgel Synthesis

The microgels were synthesized using a two-step process. First, the magnetic nanoparticles (SCM3) are functionalized with TPM. Therefore, 145.3 mg of SCM3 were dispersed in 23 mL ethanol through 15 mL ultra sonification and transferred into a 50 mL three-neck flask. 2.5 mL of ammonia solution was added under stirring with an overhead stirrer. After a dropwise addition of 0.39 mL MPS, the reaction solution was stirred for 24 h. Afterward, the solution was heated for 1 h to 80 °C. The functionalized MNPs were purified through repeated centrifugation with solvent exchange and redispersed in 3 mL ethanol. In the second step, the microgel was synthesized around the maghemite cores. The 3 mL functionalized nanoparticles were sonicated for 30 min before mixing with 402.3 mg NIPAm, and 26.4 mg BIS were dissolved in 150 mL of bidistilled water and 0.66 mg MRB dissolved in 15 mL. Another 60 mL of water was added to the three-neck flask. The reaction solution was degassed for 1 h with nitrogen gas while stirring at 250 rpm and heating to 60 °C. 31.3 mg KPS, used as the initiator, was dissolved in 10 mL H₂O and degassed for 1 h. After heating the reaction solution to 80 °C, the initiator

was dropwise added while stirring. After 4 h, the reaction was stopped by removing the heating. After adding the initiator, the solution changes color to a more milky orange, indicating the formation of microgels. The produced microgels were purified using repeated centrifugation.

4.2.7 Preparation Dipolar Chains

The alignment of the ellipsoidal nanoparticles to an external magnetic field was checked through SEM measurements. Therefore, field emission scanning electron microscopy micrographs were recorded of the dipolar chains formed by the ellipsoidal nanoparticles as shown in Figure 4.8 and 4.9. A droplet of the nanoparticle dispersion (0.05 wt%) was placed on top of a cleaned silica wafer, letting it dry under ambient conditions inside Halbach arrays of different strengths. Depending on the field strength, the ellipsoidal nanoparticles form dipolar chains that align strongly with the magnetic field. For scattering experiments on dipolar chains, nanoparticle dispersions were exposed to a magnetic field inside a custom-built sample holder.

4.2.8 Scanning Electron Microscopy

The samples were prepared by drying 20 μL of the batch on freshly cleaned silicon wafers at room conditions. The wafers were sonicated for 15 min in isopropanol and cleaned in air plasma for 15 min. For investigations of the influence of a magnetic field, the drying process was conducted inside Halbach arrays, creating different strong magnetic fields. The SEM measurements were performed using a JSM-7800F field emission scanning electron microscope (Jeol) with secondary electron (SE) and backscatter detectors (BSD). Acceleration voltages were varied from 5 – 15 keV depending on the desired contrast and penetration depth for soft matter composites.

4.2.9 Transmission Electron Microscopy

The TEM images were conducted on different instruments. For the MNPs, the TEM and EFTEM imaging were performed on a FEI Tecnai F20 instrument operated at 200 kV. Therefore, 10 μL of the diluted MNP dispersions was dropped on a Formvar-carbon-coated 3.05 mm Plano-EM 200 mesh copper grid and dried at ambient conditions.

The cryo-TEM images of the anisotropic magnetic microgels (SM-1) were

conducted at the Heinrich Heine University Düsseldorf. The samples (4 μ l) were dropped onto a copper grid (Lacey TEM Grids) and instantly freeze-dried using a Cryo Plunger Leica EM GP2 and liquid nitrogen to preserve the swollen state of the microgels. Consequently, the nanoparticles were imaged using a Jeol JEM-2100Plus (200 kV) with a Gatan OneView 4k Camera.

4.2.10 X-ray Diffractometry

To exclude the leftover hematite after the conversion to maghemite, X-ray Diffractometry (XRD) measurements were conducted on a D2 Phaser (Bruker) powder X-ray analyzer. To achieve a proper measurement with a very low sample amount, a special "Si low background" sample holder was used. A few droplets of 0.2 wt% bare nanoparticles in EtOH were dropped onto the silicon surface of the sample holder. The data analysis was conducted using "Match! - Phase Analysis using Powder Diffraction" [111].

4.2.11 Dynamic Light Scattering

In order to examine the size and distribution of magnetic microgels, dynamic light scattering experiments were carried out utilizing an advanced ALV 5000 goniometer equipped with a 633 nm laser, digital hardware correlator, and two sensitive avalanche photodiodes. A toluene bath was used in combination with an external programmable thermostat (Julabo F32) for temperature control. The samples were highly diluted for the DLS characterization at 20 °C to ensure accurate measurement results. Swelling curves were recorded from 20 °C to 50 °C and back down to 20 °C in incremental steps of 2 °C. The angular measurements ranged from 30 ° to 90 ° at 5 ° intervals, with a measurement duration of 1 minute at every angle. The diffusion coefficients were determined via cumulant analysis, whereby the second-order cumulant was plotted against q^2 , and the diffusion coefficient is the linear regressions' slope.

4.2.12 Differential Dynamic Microscopy

DDM measurements were performed using a Nikon TE 300 inverted microscope equipped with a FLIR Blackfly model FLIR-BFS-U3-04S2M-CS camera. For each measurement, image stacks of 10000 frames were recorded at a frame rate of 500 fps. The samples were prepared using 8 μ l of the sample enclosed between two glass slides separated by a spacer that is approximately

120 μm thick. The glass slides were thoroughly cleaned by ultrasonication in isopropanol for 15 minutes. The analysis was conducted with DDMsoft [97].

4.2.13 Small-Angle X-Ray Scattering

The SAXS measurements were conducted at the CoSAXS beamline at the MAX IV Laboratory in Lund, Sweden, with the Eiger2 4M detector at a distance of 14.8 m and a beam size of $150 \times 140 \mu\text{m}$ for the non-magnetic experiments and $150 \times 110 \mu\text{m}$ for the magnetic experiments (12.36 keV). The samples were filled into 1.5 mm thick quartz glass capillaries (mark tubes, Hilgenberg GmbH) and sealed with hot wax. For the magnetic SAXS experiments, a custom-developed sample holder setup (Figures A.1 & A.2) consisting of a 3D-printed base plate and a thermally controllable aluminum sample holder with attachable Halbach arrays was used. The capillaries for this holder were shortened to 30 mm after filling them. The data analysis is based on a data reduction script provided by the local contact adapted for 2D analysis and the core-shell ellipsoidal model of SASView [94] to fit the radially averaged SAXS curves.

4.3 Results and Discussion

4.3.1 Hematite Particles and Conversion to Maghemite

As a basis for the magnetic microgels studied in this work, magnetic nanoparticles (MNPs) of an ellipsoidal shape were used. Starting from ellipsoidal hematite particles, the nanoparticles were first silica-coated and consecutively converted to maghemite for more defined and stronger magnetic properties [10].

The two batches of hematite particles H1 and H2 have similar dimensions with the small axis $d_{\text{eq}} = 51.2 \pm 6.0 \text{ nm}$ and $56.0 \pm 7.7 \text{ nm}$ and a long axis $d_{\text{pol}} = 260 \pm 29 \text{ nm}$ and $248 \pm 43 \text{ nm}$, respectively. These values have been confirmed through SAXS measurements (Figure 4.3 & 4.7). Hematite (α - Fe_2O_3) is an antiferromagnetic material at room temperature with a rhombohedral lattice structure [112]. Ellipsoidal nanoparticles made from hematite exhibit a weak magnetic moment perpendicular to the short axis of the particles [10, 113] and do not form dipolar chains. In literature, a saturation magnetization of $0.12 \text{ Am}^2 \text{ kg}^{-1}$ [10] is reported for comparable

hematite nanoparticles. Maghemite (γ -Fe₂O₃), in contrast, is a ferromagnetic material with a spinel structure comparable to magnetite (Fe₃O₄). Ellipsoidal nanoparticles made from maghemite have a significantly higher magnetic saturation (72 Am² kg⁻¹ [10]), and the magnetic moment is fixed along the long axis of the nanoparticles (Figure 4.2). Maghemite nanoparticles form dipolar chains when exposed to a magnetic field.

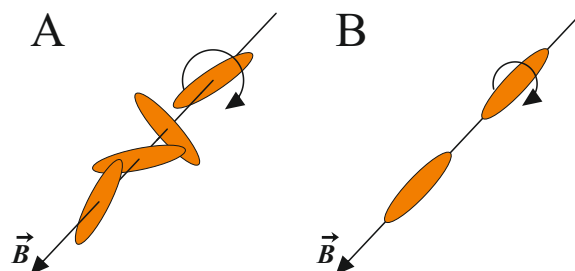


FIGURE 4.2: Schematic of ellipsoidal A) hematite and B) maghemite nanoparticles aligning parallel and perpendicular, respectively, to a magnetic field. Hematite nanoparticles can still rotate around the short axis, while the maghemite nanoparticles aligned with their long axis are "locked" in direction. This schematic does not show dipolar interactions, as hematite nanoparticles do not form dipolar chains, while maghemite nanoparticles exhibit complex dipolar interactions (Figure 4.8)

These MNPs have several advantages over hematite nanoparticles. On the one hand, the particles present a much stronger response to magnetic fields, allowing the use of less magnetic material while resulting in a similar magnetic response. On the other hand, the magnetic moment along the long axis allows for a fixed position of the nanoparticles in a magnetic field. At the same time, hematite ellipsoids can still rotate around their axis (Figure 4.2) [114].

For the conversion from hematite to maghemite, the nanoparticles are coated with a silica shell. The silica coating is applied following the method described by Graf et al. [110]. Therefore, the hematite cores are stabilized with PVP and subsequently coated with silica through the controlled addition of TEOS and TMAH.

The hematite batch H1 was provided as freeze-dried powder already with an applied silica coating (SCH1). These nanoparticles could not be redispersed with the silica shell intact, possibly because they were freeze-dried to store them. Consequently, SCH2 and SCH3 were dried in an oven before the conversion and could be redispersed afterward. For the second batch, the nanoparticles were coated, as detailed in the experimental section, in two

batches, SCH2 and SCH3. In the following, the bare hematite nanoparticles, before applying the silica coating, are called "H", silica-coated nanoparticles are described as "SCH" or "SCM", depending on whether the core consists of hematite or maghemite, and bare nanoparticles with a consequently etched silica shell are described as "ES_H" and "ES_M" (etched silica).

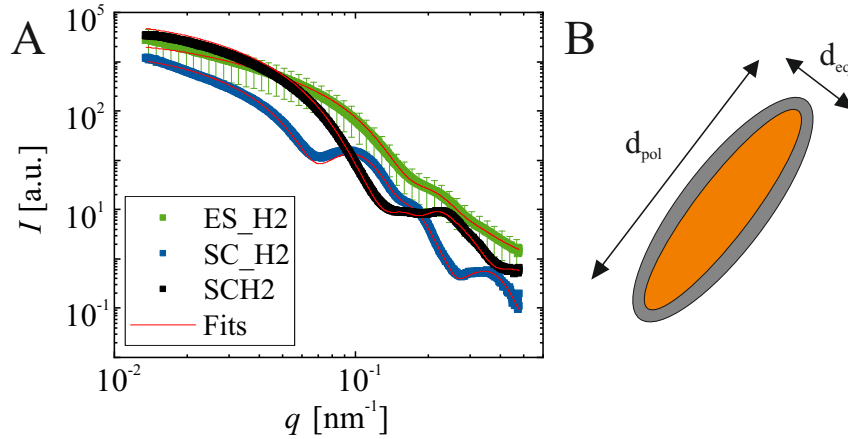


FIGURE 4.3: A) Scattering curves and respective fits with a core-shell ellipsoidal model [94] for bare hematite (ES_H2), hollow silica shells (SC_H2) and silica-coated hematite particles (SCH2). B) Schematic showing a silica-coated MNP.

Analogous to the measurements for the bare nanoparticles, the dimensions of SCH2 and SCH3 are determined. The silica shell is around 20 nm and 15 nm thick, respectively, and has seemingly a uniform thickness around the particles. To evaluate the core dimensions, small-angle X-ray scattering data was fitted using the core-shell ellipsoid model of Sasview [94]. The overview of the fit results can be seen in Table 4.1, and detailed fit parameters can be found in the appendix (Table A.1).

TABLE 4.1: Core dimensions of bare and silica-coated hematite MNPs determined by electron microscopy and SAXS fits (Schematic in Figure 4.3 B).

	ES_H2		SCH2		SCH3
	TEM	SAXS	TEM	SAXS	TEM
d_{eq} [nm]	56 ± 8	47	103 ± 9	99	87 ± 9
d_{pol} [nm]	248 ± 43	248	296 ± 43	284	274 ± 44
p []	4.4	5.3	3.2	2.9	3.2

The scattering data of the cores, the hollow silica coating and the complete particles were fitted using consistent sizes and densities in scattering

lengths (Figure 4.3 A). While slightly deviating, these are in good agreement with the measured values.

The maghemite nanoparticles are prepared by converting the silica-coated hematite ellipsoids to maghemite through a two-step procedure. First, the silica-coated hematite powder was heated to 130 °C and kept at this temperature for several hours (I) to completely remove the remaining water from the sample, indicated by a mass loss. Following a second heating period towards the reduction temperature (360 °C), an equilibration period under a $N_2:O_2$ atmosphere is used to burn all remnant organic contaminations.

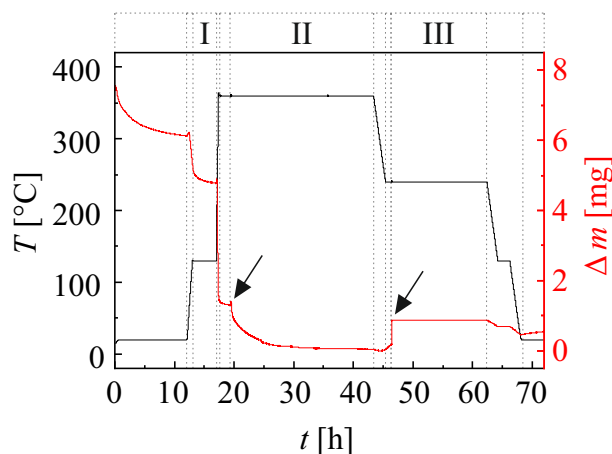
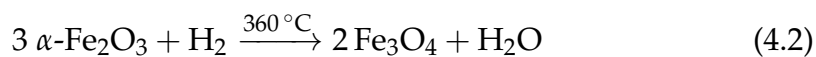


FIGURE 4.4: Exemplary representation of the oven heat profile (black) and mass changes (red) for the conversion process of SCH2/SCM2. The arrows indicate the start of the reduction (II) and reoxidation (III) period, respectively.

The reduction process (II) of hematite (α - Fe_2O_3) to magnetite (Fe_3O_4) is conducted at 360 °C with a $N_2:H_2$ gas flow of 40:10 $mL\ min^{-1}$. These conditions are maintained for 24 h to ensure the complete reduction of hematite to magnetite. Due to decreased oxygen content in the crystal structure, a mass loss was observed during the reduction. Completely converted silica-coated magnetite particles (with a magnetite/particle mass of roughly 40 %) are around 3 % lighter than the initial silica-coated hematite particles. The reduction reaction from hematite to magnetite is shown in Equation 4.2. Consecutively, the system is cooled down to 240 °C still under $N_2:H_2$ atmosphere to prevent reoxidation to hematite. The oxidation of magnetite to maghemite (γ - Fe_2O_3) is conducted at 240 °C in a 40:10 $mL\ min^{-1}$ $N_2:O_2$ gas flow. While

the oxidation reaction seems to be completed after a short time (III), a reaction time of 15 hours was set for this period to ensure complete oxidation. The oxidation reaction of magnetite to maghemite is shown in Equation 4.3.



The resulting maghemite nanoparticles are strongly magnetic and have a darker reddish-brown color compared to the bright orange-brown of hematite. The TEM images (Figure 4.5 B & C) show an evident change in the nanoparticle structure between hematite and maghemite. While maghemite can't be distinguished from magnetite in XRD measurements, an analysis performed on ES_M2 shows no traces of residual hematite after the conversion, with all peaks of the analyzed sample (Figure 4.5, black) matching those of the maghemite reference (blue) [111]. Additionally, specific peak positions of the hematite reference (green) are not reflected in the sample, confirming the absence of hematite and the successful conversion from hematite to maghemite. Collectively, it can be assumed that the conversion was successful and complete.

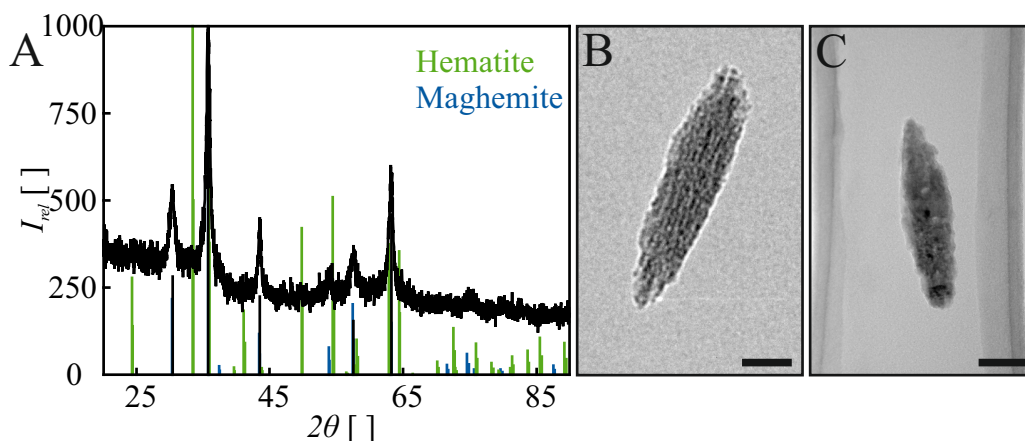


FIGURE 4.5: A) X-ray diffraction analysis of converted nanoparticles (black) shows no remaining hematite (green, reference) [111] after reduction and reoxidation and matches the pattern of maghemite (blue, reference) [111]. TEM micrographs of B) a hematite MNP (H2) and (C) a maghemite nanoparticle (ES_M1). Scale bar: 50 nm.

For SCM1, the redispersion of the silica-coated maghemite particles after the conversion was impossible, even through extensive ultrasonication. It can be assumed that the particles are backed together after the conversion

process. Redispersion was possible for SCM2 and SCM3, suggesting that the freeze-drying process of SCM1, in contrast to drying in an oven at 80 °C, altered the surface in a way that promoted irreversible aggregation during the conversion process. Nevertheless, to redisperse the magnetic nanoparticles, the silica shell was etched from the core in a catalyzed hydrolysis reaction by adding 1M NaOH. To confirm the full dissolution of the shell, EFTEM measurements were conducted, and the silicon and iron mappings were checked. The respective micrographs in Figure 4.6 clearly show a bare iron (oxide) nanoparticle with no leftover silica. For SCM2 and SCM3, the silica shell was etched only for a part of the MNP batch, while the majority were used as silica-coated MNPs.

TEM analysis of the maghemite nanoparticles confirms that the overall dimensions remain similar. However, the particle appears to be much rougher or porous (Figure 4.5 C & 4.6); this is reflected in the SAXS analysis (Figure 4.6).

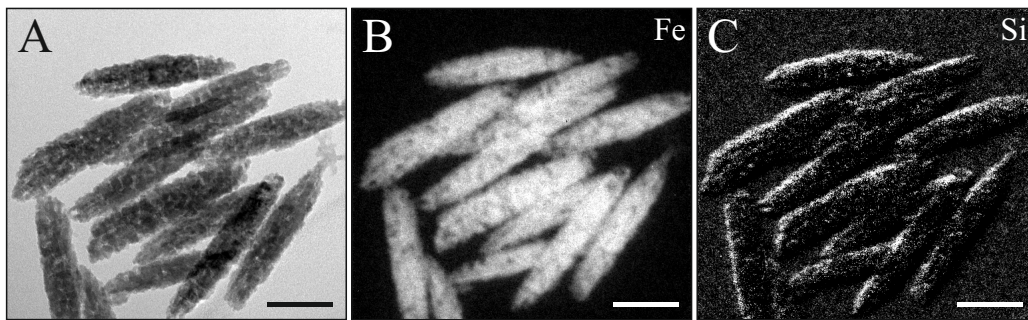


FIGURE 4.6: EFTEM micrographs of ES_M1 with A) normal TEM, B) energy filtered iron map, and C) silica map, the respective elements are indicated as brighter spots on these images.

Analogous to the SAXS experiments on hematite particles, experiments were conducted on bare ES_M1 particles to validate the dimensions determined from TEM images (Table 4.2).

TABLE 4.2: Core dimensions determined by electron microscopy and from SAXS fits for bare maghemite nanoparticles ES_M1.

	ES_M1	
	TEM	SAXS
d_{eq} [nm]	51 ± 6	49
d_{pol} [nm]	260 ± 29	260
p []	5.1	5.3

The SAXS measurement was done with a 0.2 wt% maghemite dispersion in water. For fitting the same ellipsoidal model of the SasView [94] was used. Still, unlike the measurements conducted on H2, the fit does not properly catch the data very well at high q values (Figure 4.7), possibly because of structural features within maghemite such as domains or pores. In this case, porous maghemite particles are assumed to improve the quality of the fit. Previous works have shown significant porosity for particles comparable to the used hematite precursor particles [113, 115]. Ellipsoidal pores with dimensions of $d_{\text{pol}} = 8$ nm and $d_{\text{eq}} = 3.5$ nm are modeled using SasView. Combined with an improved fit for lower q values, the porous system better represented the data. Furthermore, the model is very insensitive to the long axis of the ellipsoidal particles. Therefore, the long axis d_{pol} was fixed at 260 nm as determined from TEM.

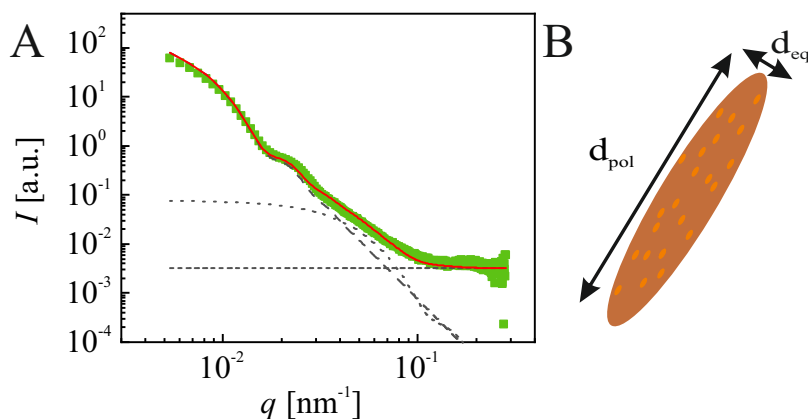


FIGURE 4.7: SAXS measurements of a 0.2 wt% dispersion of ellipsoidal maghemite particles ES_M1 (\square). The scattering curve was evaluated for ellipsoidal particles with ellipsoidal pores (—). In addition to ellipsoidal maghemite particles (---), ellipsoidal pores ($d_{\text{pol}} = 8$ nm & $d_{\text{eq}} = 3.5$ nm;), need to be considered (background (-----)). Jointly, these effects result in a modulation of ellipsoidal maghemite particles with ellipsoidal pores, agreeing with the experimental data.

DLS and DDM were used to check the dispersion of the different nanoparticle batches. For this purpose, theoretical diffusion coefficients were calculated from the determined dimensions and compared with the experimentally obtained values.

For ellipsoidal particles, theoretical isotropic diffusion coefficients can be calculated from the dimensions as described by Martchenko et al. [31] building on the work of Perrin [116] as the friction coefficients f_p for a prolate ellipsoid depends on the length d_{pol} and the width d_{eq} (Equation 4.4).

$$f_p = \frac{3\pi \cdot \eta_0 \cdot d_{\text{pol}} \sqrt{p^2 - 1}}{p \cdot \ln(p + \sqrt{p^2 - 1})} \quad (4.4)$$

with the solvent viscosity η_0 and the aspect ratio $p = d_{\text{pol}}/d_{\text{eq}}$

The Einstein relation gives the relation between friction coefficient and diffusion coefficient (Equation 4.5). By applying a weighted mean (Equation 4.6), the diffusion coefficients can be weighted for the volume of the measured particles.

$$D_T = \frac{k_B T}{f_p} \quad (4.5)$$

$$\langle D \rangle = \frac{\sum_i D_i \cdot V_i^2}{\sum_i V_i^2} \quad (4.6)$$

The bare hematite particles tend to aggregate strongly without stabilizing PVP, which, in turn, changes the diffusion coefficient. Therefore, only silica-coated and bare maghemite nanoparticle dispersions were checked this way. As the size of the nanoparticles is assumed to be equivalent for hematite and the corresponding converted maghemite nanoparticles, is the size determined from hematite TEM images used to compare with bare maghemite nanoparticles (Table 4.3).

TABLE 4.3: Diffusion coefficients, calculated from dimensions determined by TEM micrographs and measured with DLS at 20°C

[°C]	D_{cal} [$10^{-3} \text{ m}^2 \text{ s}^{-1}$]	D_{meas} [$10^{-3} \text{ m}^2 \text{ s}^{-1}$]
H1/ES_M1	3.70	3.65
H2/ES_M2	3.49	3.23
SCH2	2.52	2.40
SCM2	2.52	2.51
SCM3	2.82	2.46

The good agreement between the calculated and measured values confirms a proper dispersion of the MNP batches.

4.3.2 Dipolar Interactions

In literature, the magnetic moment of the ellipsoidal maghemite nanoparticles is assumed to point along the long axis. Using the saturation magnetization $\sigma_S = 72 \text{ Am}^2 \text{ kg}^{-1}$ [10] determined for similar MNPs, the magnetic moment μ can be estimated via $\mu = \sigma_S \cdot m$. This results in $\mu = 1.15 \cdot 10^{-15} \text{ Am}^2$ for maghemite MNPs with an average mass of $m_{\text{ES_M2}} = 1.6 \cdot 10^{-17} \text{ kg}$. The magnetic moments of the MNPs should preferably align homogeneously with the magnetic field to achieve the highest effect when incorporating magnetic nanoparticles in a microgel network. Still, when two MNPs are in close proximity, they can exhibit a dipolar interaction interfering with their orientation to a magnetic field. The interaction energy E_d of randomly distributed spherical nanoparticles is dependent on the distance d separating them and can be approximated with Equation 4.7 [117].

$$E_d \approx \frac{\mu_0 \cdot \mu^2}{4\pi \cdot d^3} \quad (4.7)$$

with the magnetic permeability in vacuum μ_0 . It has been shown that comparable magnetic nanoparticles exhibit a strong magnetic response and can form highly ordered dipolar chains at low magnetic fields in the range of 150 mT [118]. As the interaction energy depends on the distance between the MNPs, the dipolar interaction should be influenced by the silica-coating and, later on, by a microgel shell.

SEM micrographs of aqueous dispersion of ES_M1 and SCM2 dried under a homogenous magnetic field were recorded to determine the field dependence of the dipolar chain formation. For the SEM measurements, samples of 0.05 wt% nanoparticle solution were dried while exposed to a homogeneous magnetic field set by Halbach arrays of different strengths. As expected, the nanoparticles are increasingly self-assembling into dipolar chains with increasing field strength (Figure 4.8) and the orientation of the magnetic chains is in good agreement with the magnetic field orientation.

However, the alignment of the nanoparticles does not fully match the direction of the magnetic field, even at significantly higher field strengths. This suggests a complex interplay of close contact dipolar interactions. Even a weak field of 1 mT leads to some chain formation, confirming the high magnetic response of the MNPs. For higher B , nearly all nanoparticles assemble

into dipolar chains. At 10 mT, the nanoparticles inside the chains are mainly oriented parallel to the chain. With further increasing field strengths, the particles are increasingly arranged as side-to-side bundles packed together as chains. At high field strengths of 200 mT, the MNPs form dipolar chains from side-to-side stacked ribbons that partly twist around each other (Figure 4.8).

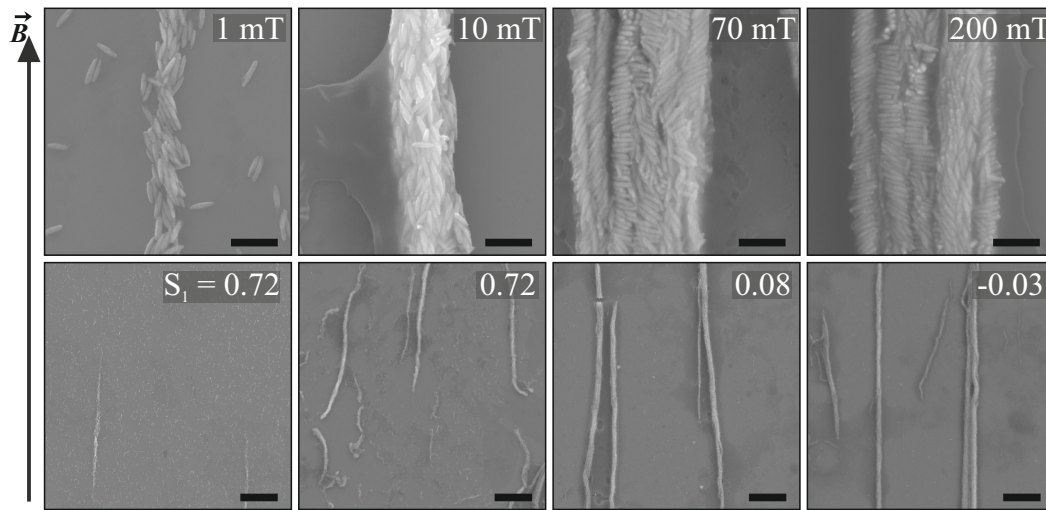


FIGURE 4.8: Dipolar F formed by bare ellipsoidal MNPs through dipolar interaction inside a magnetic field (1 - 200 mT). While the chains orient along the magnetic field lines, the orientation of the nanoparticles' alignment does not fully match the direction of the magnetic field, especially at higher field strength. Scale bars: upper row 500 nm; lower row 5 μ m.

We ascribe this assembly to the combination of the anisotropy of the particles with strong dipolar interactions. Interestingly, such an arrangement is somewhat reminiscent of a smectic assembly. Further investigation, including computer simulations, should be conducted to support this observation.

When silica-coated MNPs are subjected to a magnetic field, the chain types forming at higher field strengths are significantly different (Figure 4.9).

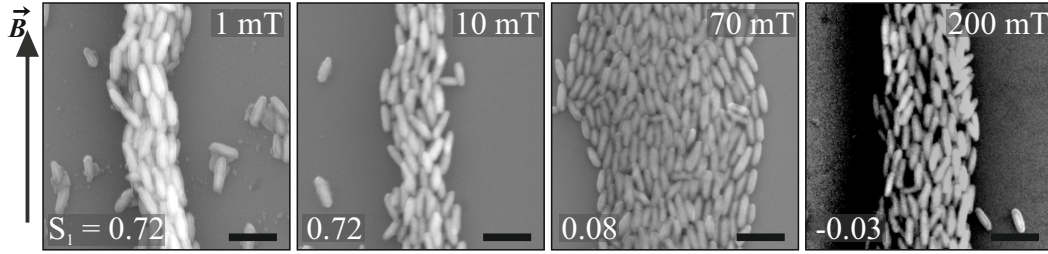


FIGURE 4.9: Dipolar chains formed by silica-coated ellipsoidal MNPs through dipolar interaction inside a magnetic field (1 - 200 mT). Chains and MNPs orient mostly along the magnetic field lines. Scale bars: 500 nm.

In this case, no side-to-side stacks are observable, and particles align with the long axis along the magnetic field and the chain direction. At higher field strengths above 70 mT, almost all MNPs are part of dipolar chains again. The changes are due to weaker dipolar interactions as the silica coating works as a non-magnetic spacer, increasing the distance between the magnetic cores. For low field strengths, the chains are similar to experiments with bare MNPs but with a clearer tendency to tip-to-tip ordering.

To quantify the change in the chain structure, the orientational order parameter S_1 is determined.

$$S_1 = \frac{3 \cdot \cos^2 \alpha - 1}{2} \quad (4.8)$$

For the order parameter calculation, the angle α between the ellipsoidal nanoparticles' long axis and the dipolar chains' orientation (as an indicator of the magnetic field direction) was measured for around 100 nanoparticles in one section of the chain. However, the overall order parameter might be different since the analysis is performed in the dried state on a surface and may be subjected to additional drying effects. Additionally, it was not possible to create a 3D representation of the nanoparticle arrangement within the chains. A first-order parameter was derived for bare (ES_M1) and silica-coated (SCM2) MNPs (Figure 4.10). For nanoparticles without silica-coating, a significant decrease in the order parameter can be observed between weak fields, $S_1 = 0.72$ for 1 and 10 mT, and higher field strengths, $S_1 = 0.08$ and $S_1 = -0.03$ for 70 and 200 mT, respectively. This indicates a better alignment to the magnetic field at lower field strengths. At the higher field strength, the

diminution of the first-order parameter is ascribed to the dipolar assembly of the maghemite nanoparticles into side-to-side stacks with ribbon-like long-range ordering. This effect is most likely related to a complex field-dependent dipolar self-assembly of the maghemite nanoparticles. In contrast, the silica-coated nanoparticles have a nearly constant order parameter $S_1 \approx 0.8 - 0.9$, corresponding to a good alignment to the magnetic field and the dipolar chains' orientation (Figure 4.10).

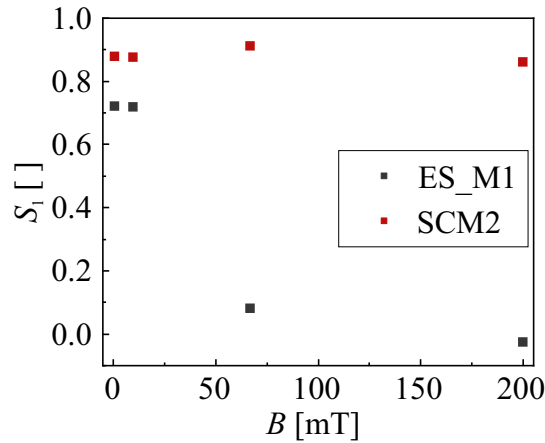


FIGURE 4.10: Dipolar interactions between magnetic nanoparticles. The orientational order parameter of bare (ES_M1, \blacksquare) and silica-coated (SCM2, \blacksquare) magnetic nanoparticles changes with the magnetic field strength.

In addition to the SEM measurements, a set of experiments in cross-polarization was conducted. In cross-polarization, the analyzer and polarizer are set up perpendicular to each other to ensure complete extinction of the light. Only additionally polarized light is detected through this setup (Figure A.4). The dipolar chains can polarize light depending on their orientation. When exposed to a rotating magnetic field of 70 mT, the dipolar chains rotate at a rotation speed up to the maximal motor speed of 90 rpm. The chain sizes depend on the field strength B , the exposure time, and the angular frequency ω_{MF} (in the case of a rotating magnetic field). Two Helmholtz coils were utilized for the cross-polarization experiments to create a rapidly switchable, homogeneous magnetic field. The linear polarizers were adjusted to maximize intensity when the dipolar nanoparticle chains were aligned with the magnetic field. Switching on the magnetic field leads to an increase in intensity if dipolar chains are formed. These experiments were conducted with weak magnetic fields between 0 and 4.5 mT, showing that chain formation already occurs for field strengths as low as 0.5 mT.

4.3.3 Microgel Synthesis

An MMG consisting of a single MNP core and a microgel shell around it can be considered the minimal model of an MMG system. How to create a microgel around a silica particle has been widely discussed in literature [17, 35, 119]. An established method is functionalizing the silica with TPM and subsequently performing the microgel synthesis according to the desired polymerization method (e.g., radical polymerization, ring-opening polymerization). In this case, the silica coating was functionalized using TPM, and a PNIPAm microgel shell was synthesized using a free radical precipitation polymerization with KPS as an initiator.

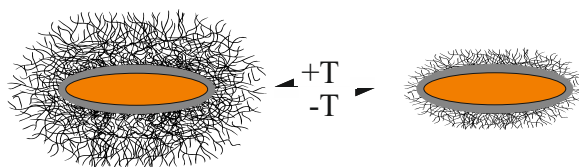


FIGURE 4.11: Schematic of a thermoresponsive hybrid microgel with an anisotropic magnetic nanoparticle as the core.

PNIPAm microgels are thermosensitive and swell and deswell with temperature. The microgel network collapses when the temperature increases above the volume phase transition temperature (VPTT), resulting in an overall decrease in particle size.

This process can generally be studied via dynamic light scattering, and the hydrodynamic radii can be calculated for spherical particles. In the case of anisotropic microgels, the Stokes-Einstein-Equation is no longer valid, only leading to an apparent hydrodynamic radii that gives an indication of the size but not the exact dimensions. Therefore, instead of R_H , the diffusion coefficients are used to represent the swelling curve (Figure 4.12 A). As a guide of the eye, the diffusion coefficients of the non-thermosensitive silica-coated nanoparticle cores calculated as described in Equation 4.4 - 4.5 are shown as well.

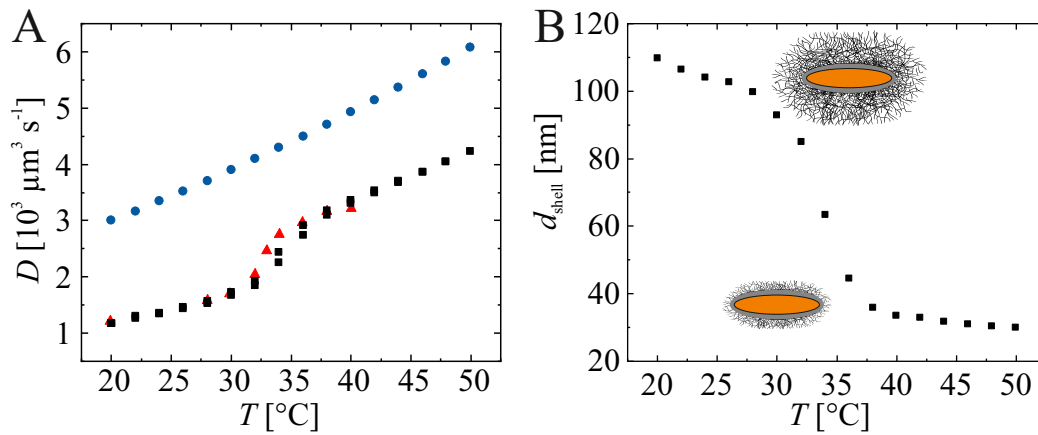


FIGURE 4.12: A) DLS (■) and DDM (▲) measurements of the swelling behavior of the thermoresponsive MMG SM-1 and calculated diffusion coefficients for the non-thermosensitive MNP core SCM3 (●). B) The swelling curve represents the thermoresponsive shell thickness d_{shell} estimated from the dimensions of the inorganic core SCM3 determined by TEM and the experimentally determined diffusion coefficients of the MMGs.

When combining theoretical and experimentally determined diffusion coefficients for MNP and SM-1, respectively, the microgel shell thickness can be estimated under the assumption of uniform shell thickness. In the swollen state, the microgel shell is 110 nm thick, and in the collapsed state, it is 30 nm thick. Using these values, the hybrid microgels measure between $d_{\text{pol}} \approx 494$ nm and $d_{\text{eq}} \approx 307$ nm in the swollen state at 20 $^\circ\text{C}$, and $d_{\text{pol}} \approx 334$ nm and $d_{\text{eq}} \approx 147$ nm in the collapsed state at 50 $^\circ\text{C}$, resulting in a swelling ratio Q of 6.1 (Equation 4.9). The aspect ratio changes from 1.6 to 2.3 between the swollen and the collapsed state.

$$Q = \frac{V_{20^\circ\text{C},\text{MMG}} - V_{\text{SCM}}}{V_{50^\circ\text{C},\text{MMG}} - V_{\text{SCM}}} \quad (4.9)$$

In addition to the DLS measurements, Cryo-TEM and AFM images were used to check the microgel shell around the MNP cores. The Cryo-TEM images show a slight shadow around the clearly visible cores. The dotted line in Figure 4.13 A indicates the calculated shell thickness in the swollen state.

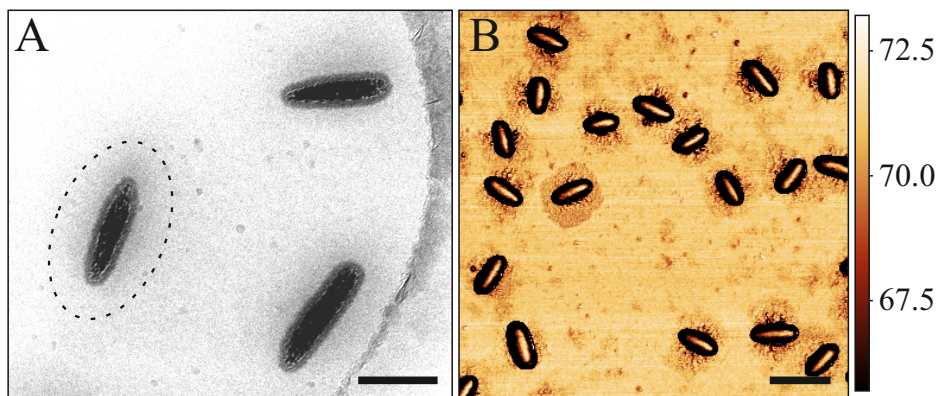


FIGURE 4.13: A) Cryo-TEM micrograph of SM-1, showing the silica-coated MNP core and a diffuse microgel shell. The calculated shell thickness is indicated by the dotted line. Scale bar: 200 nm. B) AFM phase image of SM-1, showing the MNP core and the spread microgel shell as a fried egg shape. Scale bar: 500 nm.

The shell dimensions cannot be determined from the Cryo-TEM images because the borders of the microgel cannot be clearly differentiated. In contrast to that, the AFM micrograph (Figure 4.13) depicts microgels adsorbed on a silica wafer exhibiting a fried egg shape with the nanoparticle core and the flattened microgel shell visible in the phase image. Neither of the methods clearly shows the shape of the MMGs but proves the core-shell structure of MNP and microgel shell.

The small-angle X-ray scattering of these MMGs is dominated by the inorganic core rather than the polymer shell due to the significantly higher electron density found in the core. This property allows the particles to serve as tracers for the entire microgel system, either as a numeric indicator to precisely determine the volume fraction [120] or, in the case of anisotropic cores, as director for the microgel orientation. Analogous to the fits used for ES_M1, the bare MNP cores (ES_M2) and the full microgel system (SM-1) can be fitted considering a core-shell ellipsoid model for maghemite and silica-coating and ellipsoidal pores for the high q region. The considered pores have dimensions of $d_{\text{eq}} = 19$ nm and $d_{\text{pol}} = 8$ nm. Analogous to the bare hematite particles (Table A.1), the maghemite cores have a short axis of $d_{\text{eq}} = 47$ nm and a long axis of $d_{\text{pol}} = 248$ nm with a silica coating thickness of ~ 20 nm.

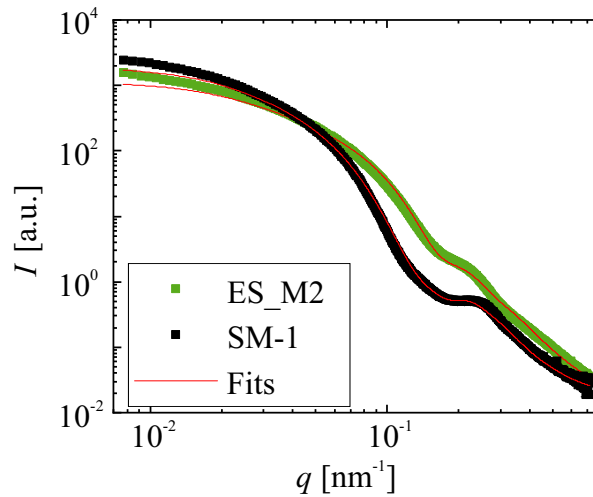


FIGURE 4.14: Small-angle X-ray scattering data of A) MNP core (ES_M2, green) and (B) MMG system (SM-1, black).

4.3.4 Magnetic Field directed Assembly

One of the underlying motivations for creating magnetic microgels is the possibility of aligning the MNP cores and, consequently, the MMGs inside a magnetic field. This property allows for a microgel assembly supported by magnetic fields. In the case of SM-1, when exposed to a magnetic field, the magnetic microgels behave similarly to their nanoparticle cores due to comparable magnetic properties; they align their long axis with the magnetic field. Analogous to the silica-coated MNPs, the dipolar interactions change with the shell due to thickness and repulsive interactions, leading to an increased distance between the magnetic cores. When exposed to a strong magnetic field, the microgels align, and some form small tip-to-tip dipolar chains, but the chains are significantly smaller than those formed by the nanoparticles. In dried SEM images (Figure 4.15 C), the microgel shells are not visible, but the orientation and structures formed by the MMGs can be observed. It is possible that part of the dipolar chains are forming during the drying process, as the microgel shell is shrinking, and therefore, the distance between the cores gets smaller. Additionally, the MMGs forming the dipolar chains tend to have larger cores (average volume $\bar{V} = 8.91 \pm 3.41 \cdot 10^4 \text{ nm}^3$) than the MMGs that are not part of a chain ($\bar{V} = 1.63 \pm 0.52 \cdot 10^5 \text{ nm}^3$). At the same time, the orientational order parameter of the chain MMGs ($S_1 = 0.98$) is slightly larger as well ($S_1 = 0.82$, free MMGs). This is consistent with the overall higher MNP volume, as the magnetic moment is influenced by the mass of the magnetic material, leading to a stronger magnetic response of

larger MNPs.

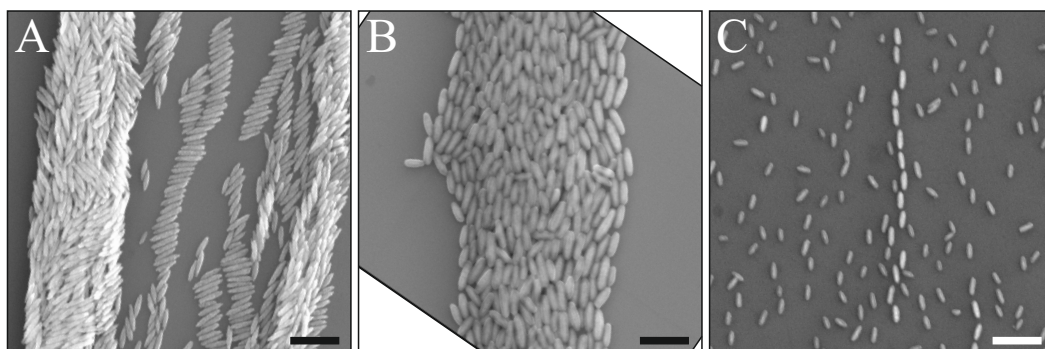


FIGURE 4.15: SEM micrographs of A) bare (ES_M3) and B) silica-coated maghemite nanoparticles (SCM3) and C) core-shell microgels (SM-1) exposed to a vertical magnetic field. Scale bars: 500 nm.

To get a more statistical view of the structure of the dipolar chain forming under a 280 mT magnetic field, SAXS measurements were conducted on bare and silica-coated microgels as well as the microgel system. Depending on the sample, the 2D scattering patterns show distinctive peaks marked with arrows (Figure 4.16). Due to the polydispersity of the particles, the peaks are somewhat smeared and broadened, especially as they are a 2D representation of a complex 3D structure. For all samples, the main pattern corresponds to an overall ellipsoidal shape aligned with the magnetic field as depicted in the schematic (Figure 4.16 D). The scattering pattern varies with the different shells around the magnetic nanoparticles, with the silica coating having a more pronounced effect on the intensity compared to the microgel shell due to its higher contribution to the X-ray scattering. All patterns exhibit structural peaks in the low q range, corresponding to the respective particle-particle order. In the case of the MNPs, the peaks align with a shifted tip-to-tip order. Furthermore, especially for bare MNPs, the peaks are broadened and approach a nematic phase pattern. The weaker 90° shifted ellipsoidal pattern may result from the side-by-side stacking of bare MNPs.

The silica-coated MNPs exhibit sharper, slightly shifted structure peaks and lack the cross-shaped pattern. Otherwise, the pattern is similar. For MMGs, the structure peaks correspond to a tip-to-tip arrangement of a distance of approximately $d = \frac{2\pi}{q_{max}^*} = 480$ nm. This distance is in reasonably good agreement with the full length of the long axis of the microgels, which is around 520 nm in the swollen state (core dimensions of SCH3 + shell thickness). This

distance is larger than observed in the dry-state SEM micrographs, as the microgel shell is swollen during the SAXS measurements and collapsed in the dry-state. This MMG system is, therefore, suitable for changing dipolar interactions based on the thickness of the shell. As additional experiments for the future, the scattering experiments should be conducted following the deswelling at a higher temperature, elaborating the distance dependence of dipolar interactions.

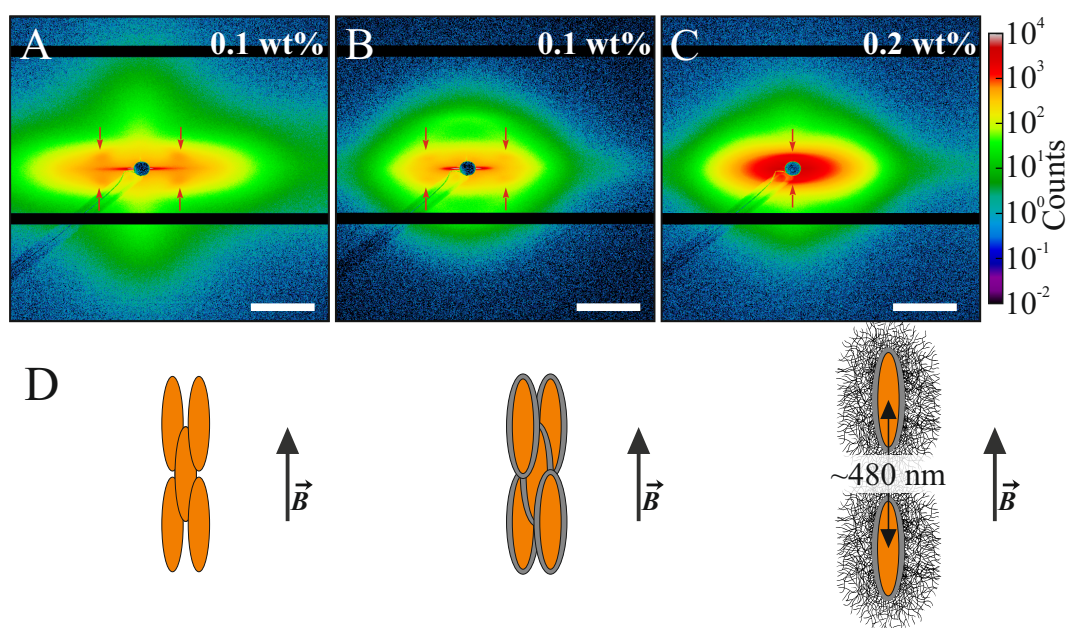


FIGURE 4.16: Scattering patterns of A) bare (ES_M3) and B) silica-coated maghemite nanoparticles (SCM3) and C) core-shell microgels (SM-1) exposed to a vertical magnetic field (280 mT) at 21 °C. The red arrows indicate the position of the structure peaks. Scale bars = 0.066 nm^{-1} . D) Schematics representing the structure as estimated from the structure peaks of the scattering patterns.

4.4 Summary and Outlook

This chapter delved into the characterization and self-assembly of magnetic microgels under relatively dilute conditions, with a particular focus on their core component – magnetic nanoparticles (MNPs). It outlined the synthesis and characterization processes for ellipsoidal MNPs, providing insights into their dimensions, magnetic properties and dipolar interactions. Subsequently, the synthesis of a minimal magnetic microgel system was described.

First, we investigated the synthesis and conversion process of ellipsoidal maghemite nanoparticles through various characterization methods. By employing a combination of imaging and scattering techniques, such as electron microscopy, dynamic light scattering and small-angle X-ray scattering, we determine the dimensions, dynamics and changes in the magnetic response of the different MNPs. Furthermore, we discuss how the conversion from hematite to maghemite necessitates the consideration of ellipsoidal pores in the SAXS evaluation of maghemite nanoparticles. This phenomenon is attributed to a change in the particle morphology through the conversion process.

Furthermore, when necessary for dispersion purposes, the dissolution of the silica coating on some MNPs was discussed. Freeze-drying silica-coated nanoparticles may alter the surface properties, making them more susceptible to aggregation at high temperatures. Drying the SCH particles in an oven at 80 °C instead of freeze-drying prevents irreversible aggregation during the conversion process.

Ellipsoidal MNPs have interesting dipolar properties when exposed to strong magnetic fields. Depending on the coating of the MNPs, the nature of the dipolar chains undergoes significant changes. While bare nanoparticles exhibit a predominantly tip-to-tip order below 10 mT, higher field strengths induce side-to-side stacks where the stacks remain aligned with the magnetic field. A difference is observed for silica-coated MNPs, in which the particles are nearly fully aligned with both the chains and the magnetic field.

Lastly, the synthesis of a hybrid magnetic microgel (MMG) system with an MNP core and a thermoresponsive PNIPAm microgel shell is described. These MMGs possess similar magnetic properties to the MNPs, except for their dipolar interactions, which are significantly weaker due to the thicker non-magnetic shell. Future experiments should use the thermoresponsiveness of the magnetic microgels to tune the shell thickness and analyze the influence of the dipolar interactions on self-assembly in greater detail.

In the light of this work, it will be interesting to study the influence of temperature in more detail. Therefore, MMGs with a thicker shell were synthesized at the end of this thesis and could be used to understand the transition from dipolar chains into individual particles and the particle distance at which dipolar interactions are completely suppressed. This system will be tested during the upcoming beamtime.

In conclusion, this chapter described the preparation and characterization of an intriguing small magnetic microgel system featuring a thermoresponsive shell that allows for tunable dipolar interactions between the magnetic nanoparticle cores. Such systems should be further developed in the future to emphasize their application as colloidal analogs of magnetic spins.

Chapter 5

Structure and Dynamics of Concentrated Magnetic Microgels under Static and Rotating Fields

5.1 Introduction

Microgels represent a class of soft colloidal systems that exhibit intricate phase behaviors and dynamics, which are significantly influenced by their chemical composition and inherent softness [13, 121, 122]. The level of softness in microgels determines their capacity to deform, interpenetrate, and contract at high volume fractions. However, the complexity of this phase behavior amplifies when dealing with anisotropic colloids. Magnetic core-shell microgels serve as an excellent model system for studying the intricacies of soft colloidal systems [41, 106] on top of their directional dipolar interactions. The application of magnetic fields allows for controlled alignment of these gels, especially within anisotropic structures [10].

Microgel phase diagrams have been studied mostly using scattering techniques, which probe their behavior across diverse length scales [121, 123]. These methods span from investigating individual conformations to examining spatial arrangements. By analyzing the jamming behavior in relation to microgel concentration, we can gain valuable insights into these complex systems. Jamming refers to the transition from a fluid-like state to a glass-like state within a disordered material, where the particles become incapable of diffusing individually [124, 125]. This phenomenon is widely observed in various colloidal and granular systems and exhibits significant complexity due to its non-equilibrium nature. Understanding jamming behavior in magnetic microgels can lead to advancements in fields such as soft matter physics, materials science, and biology, where the formation of jammed states

plays a crucial role.

Hybrid microgels with anisotropic cores offer several advantages, particularly in the study of jammed systems. The orientation of the core serves as a valuable indicator of whether the system has reached an arrested state. In their studies, Dagallier et al. [41, 106] explored the behavior of anisotropic magnetic microgels, which consisted of hematite (α -Fe₂O₃) cores coated with a thermoresponsive poly(N-isopropyl acrylamide) (PNIPAm) shell, within dense colloidal dispersions. The combination of the magnetic hematite core and the soft, temperature-sensitive PNIPAm shell enabled precise control over particle size and volume fraction, making it possible to investigate jamming transitions and the resulting arrested phases. When exposed to an external magnetic field, the hematite cores align with their long axis perpendicular to the field, and the system exhibits optical birefringence. These optical properties can serve as a direct probe of particle orientation and local ordering. As the effective volume fraction increases, the system undergoes a jamming transition, where the particles' rotational motion becomes hindered by elastic forces from interparticle contacts, leading to a metastable jammed state. Magnetic hybrid microgels offer an opportunity to explore the interplay between thermal and magnetic forces in determining the dynamics of anisotropic colloidal systems in dense phases, shedding light on the mechanisms behind jamming and arrested behavior. To further advance this research, substituting hematite with maghemite (γ -Fe₂O₃) nanoparticles can improve the magnetic properties of the MMGs while shifting their magnetic moment to align along the long axis of ellipsoidal maghemite nanoparticles (MNPs). This modification enhances the system's response to external magnetic fields [10, 40] and introduces magnetic field-induced dipolar interactions. As a result, the structure under a magnetic field becomes more defined, and the system becomes more dynamic when responding to moving magnetic fields. Another objective of this investigation is to examine the magnetic interactions within the microgels and explore the potential emergence of "spin glass" states. Spin glasses are characterized by disordered magnetic configurations that exhibit both spin disorder and structural disorder [126]. Understanding these configurations can provide valuable insights into the intricate behavior of anisotropic magnetic microgels, particularly in jammed states. This approach positions MMGs with anisotropic magnetic properties

as colloidal analogs of spin glasses, offering new opportunities for applications in materials science and engineering.

This chapter delves into the intricate properties of a dense system of anisotropic magnetic microgels, examining their phase behavior and dynamic properties through small-angle X-ray scattering and microscopy techniques. The core-shell microgel structure consists of ellipsoidal magnetic nanoparticles as the core and a crosslinked polymer network shell made of PNIPAm. The MNP core is encapsulated by the thermoresponsive shell. The phase behavior of this microgel system varies with microgel concentration and volume fraction, respectively. As the concentration increases, the system transitions from a dilute phase to plastic crystals, eventually reaching a glass state. By investigating the response of concentrated microgel systems to a rotating magnetic field, the jamming transition can be explored. Thereby, the anisotropic MNP core can act as an indicator of the microgel orientation during this process. Beyond bulk studies, proof-of-concept experiments were carried out at the air/water interface with and without applying a magnetic field. These complementary investigations provide valuable insights into the system's phase behavior and dynamics as a whole and the possibilities offered by the application of an external field to trigger phase transitions.

5.2 Experimental Section

5.2.1 SAXS

For the magnetic SAXS experiments, a custom-developed sample holder setup was used (Figure 5.1). The setup includes a 3D-printed base plate, a piezoelectric engine, attachable Halbach arrays of different strengths, and a sample holder (Figures A.1 & A.2). The piezoelectric engine allows for a maximal rotation rate of 90 rpm, and the setup is compatible with Halbach arrays with field strengths ranging from 1 - 70 mT. Details on the used Halbach arrays can be found in the Appendix. With this sample environment, static and dynamic magnetic fields can be applied. The SAXS measurements were conducted at the CoSAXS beamline at the MAX IV Laboratory in Lund, Sweden, with the Eiger2 4M detector at a distance of 14.8 m and a beam size of 150 x 140 μm for the nonmagnetic experiments and 150 x 110 μm for the magnetic experiments at a room temperature of 21 °C. The samples were filled into 1.5 mm thick quartz glass capillaries (mark tubes, Hilgenberg

GmbH). The detector images were background corrected with a capillary of pure water via a custom Python script provided by Pablo Mota-Santiago (Max IV Laboratory, Lund University). Further evaluations were conducted using custom-written Matlab scripts.

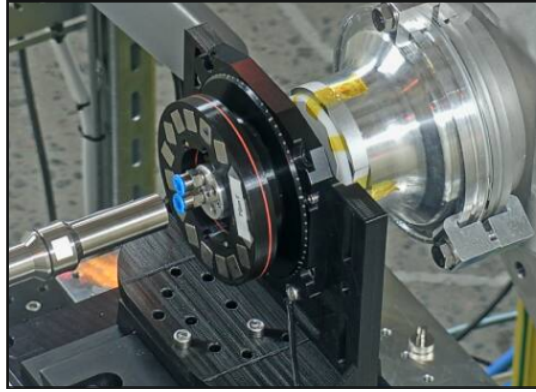


FIGURE 5.1: Custom-developed setup to conduct SAXS experiments under static and dynamic magnetic fields, consists of a base plate, a piezoelectric engine, attachable Halbach arrays of different strengths, and a thermostated sample holder.

5.2.2 Drying Cell

Controlled drying experiments were conducted in a drying cell consisting of a capillary (1 × 0.1 mm cross-section) and an attached reservoir (Figure 5.2 A). A 3D-printed well with saturated KCL solution was placed over the capillary tip for humidity control (relative humidity: 85% [127]).

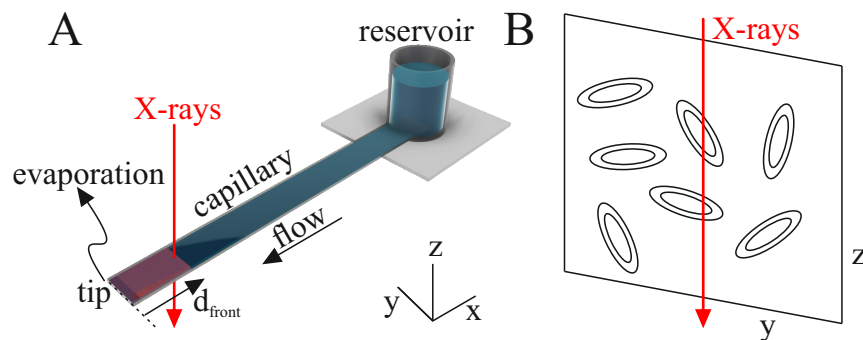


FIGURE 5.2: A) Schematic of a drying cell consisting of a 0.1 × 1 mm capillary attached to a reservoir. B) A schematic of microgels aligned in the yz-plane but without a preferred orientation in this plane. For simplicity, the SM-1 microgels are represented by their cores in this schematic.

200 μl of batch dispersions were filled into the reservoir and let to dry for a few hours overnight to reach a large enough accumulation of particles at the front of the capillary tip.

5.2.3 Experiments at the Air/Water Interface

To study the behavior of these microgels at an air/water interface, the particles were introduced to the interface by dropping 200 μl of an 80/20 water/isopropanol mixture (SM-1 batch concentration: 1 wt%) onto a cleaned water surface. Iridescence was used as an indicator for the formation of a monolayer. After equilibrating for 1.5 h, the particles were deposited onto a substrate by lifting the substrate through the surface. A linear dipper with a 3D-printed sample holder tilted upwards by 25° was used for this process. The silica wafer substrate was cleaned by ultrasonication for 2x 15 minutes in isopropanol. The substrate was lifted through the interface with a speed of 0.6 mm min^{-1} . SEM and AFM measurements were conducted to evaluate the structure of the monolayer.

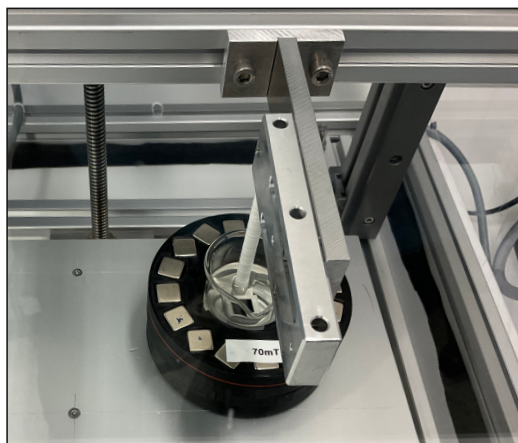


FIGURE 5.3: Setup for linear deposition of magnetic microgels adsorbed at an air/water interface. A Halbach Array is used to apply a homogeneous magnetic field of 70 mT at the interface.

5.2.4 Confocal Microscopy

Confocal microscopy was used to identify the crystal phase of the plastic crystals. As the sample did not crystallize in a "normal" confocal preparation, the quartz glass capillary filled with the microgel dispersion was investigated

using a Leica TP5 confocal microscope with a 545 nm HeNe Laser. The microgels were labeled with Rhodamine B.

5.2.5 SEM

The SEM measurements were performed using a JSM-7800F field emission scanning electron microscope (Jeol) with secondary electron (SE) and backscatter detectors (BSD) with acceleration voltages of 10 keV. The samples were prepared as described in the respective experimental section.

5.2.6 AFM

Images of the microgels deposited on a silicon wafer were recorded with atomic force microscopy on a Dimension Icon in close loop operation (Veeco Instruments Inc., software Nanoscope 9.4 (Bruker Corporation)). The measurements were performed in tapping mode using OTESPA tips (NanoAnd-More USA Corp., USA) with a nominal tip radius smaller than 7 nm (nominal spring constant: 26 N m^{-1} ; nominal resonance frequency: 300 kHz). The scan size of the images is $5 \times 5 \text{ }\mu\text{m}$ with a resolution of 514×514 pixels.

5.3 Results and Discussion

As established in Chapter 4, SM-1 is a strongly responding magnetic microgel system, with a silica-coated ellipsoidal magnetic nanoparticle as core and a thermoresponsive PNIPAm microgel shell. When studying the small-angle X-ray scattering pattern of such a microgel system, it is clear that the inorganic core dominates the results due to its significantly higher electron density compared to the microgel shell. Hereby, the anisotropic maghemite core can be used as a tracer for the orientation of the microgel.

5.3.1 Nematic Phases, Plastic Crystals and "Spin" Glasses

As the concentration of MMGs increases, the volume fraction of the system also rises, leading to alterations in both structural organization and packing density. For a concentration series of hard anisotropic colloids, nematic and smectic phases are reported in literature [128, 129]. The interactions between particles in microgels are more complex than those in hard colloids, as the polymer network can be compressed, entangled, or exhibit faceting at higher

concentrations. This added complexity makes ellipsoidal microgels, in particular, an intriguing subject to study. For SAXS measurements, the microgel system described in Chapter 4 was deionized using Amberlite ion exchange resin to maximize the electrostatic interactions and facilitate their assembly in defined structures. Different concentrations between 0.1 and 15 wt% were prepared. The anisotropic core dominates the small-angle X-ray scattering of this microgel system and, therefore, should provide an anisotropic pattern if the microgels are aligned in the same direction. With respect to the low aspect ratio estimated from DLS (~ 1.6) at 20°C, we do not expect the development of nematic or smectic phases unless the microgels are in an ultra-dense state. At all concentrations, the recorded SAXS patterns are isotropic in the absence of a magnetic field due to the random orientation of the microgels and their cores. As the concentration increases, the structure of the microgels transitions from a dilute state to a crystalline phase around 5 wt%, eventually reaching an arrested state at higher concentrations (see Figure 5.4). Beginning with a concentration of 3 wt%, a structure peak can be observed in the patterns, and this feature becomes more pronounced with increasing concentration, with multiple rings appearing at even higher concentrations.

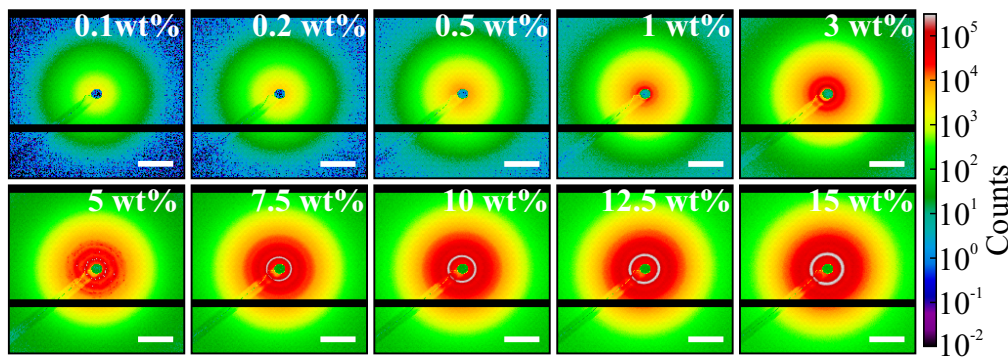


FIGURE 5.4: Micrographs showing the SAXS pattern of a concentration series of SM-1 (deionized) without magnetic field a concentration series 0.1 - 15 wt%. Scale bars: $5.4 \cdot 10^{-2} \text{ nm}^{-1}$.

At 5 wt% under deionized conditions, these microgels form plastic crystals, clearly visible from the SAXS pattern (Figure 5.5 D) and the sample capillary itself (Figure 5.5 A). With fluorescence confocal microscopy (Figure 5.5 B & C), the presence of local hexagonal crystals can be confirmed, but the sample lacks long-ranged crystalline order. This indicates a polycrystalline sample with small hexagonal domains, supported by the multiple reflexes in the SAXS

pattern. The deionization of the sample enhances the electrostatic repulsion, allowing the formation of local crystals. The formation of long-ranged crystalline structures might be hindered by the concentration, polydispersity of the microgel, or other nonideal conditions. Determined by the radial distribution function (Figure A.6, ImageJ macro [130]), the nearest neighbor distance is approximately 520 nm (Swollen Microgel: $d_{eq} = 307$ nm; $d_{pol} = 494$ nm). This value is in reasonable good agreement with the interparticle distance determined from the dipolar chains and the estimated particle dimensions, especially under deionized conditions (Table 5.1).

TABLE 5.1: Dimensions of the inorganic MNP core SCM3 and swollen and collapsed SM-1 magnetic microgels. The MMG dimensions are estimated from the MNP cores, and the shell thickness is determined from DLS data (Section 4.3.3).

	SCM3 [nm]	SM-1, 20°C [nm]	SM-1, 50°C [nm]
d_{eq}	87 ± 9	307	147
d_{pol}	274 ± 44	494	334

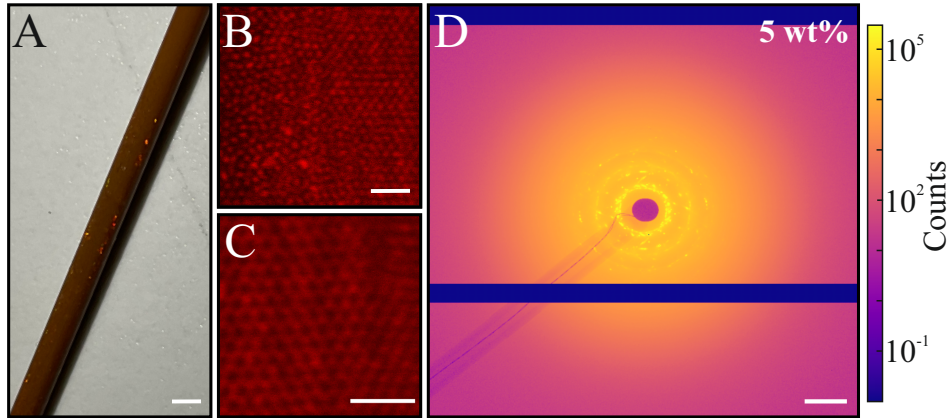


FIGURE 5.5: A) SAXS capillary with anisotropic magnetic microgels at 5 wt% with small crystalline "sparkles". Scale bar: 2 mm. B & C) Confocal microscopy images of the local hexagonal domains. Scale bars: 2 μ m. D) SAXS pattern of the 5wt % microgel dispersion. Scale bars: $5.4 \cdot 10^{-2} \text{ nm}^{-1}$.

To extract the scattering curves, the isotropic SAXS patterns in Figure 5.4 were radially averaged and normalized with the data of the diluted 0.1 wt% sample (Equation 5.1).

$$S(q) \sim \frac{I_c}{I_{0.1 \text{ wt\%}}} \cdot \frac{0.1}{c} \quad (5.1)$$

with the concentration c .

This representation of the structure factor enhances the curves' structural features, allowing for a more detailed analysis (Figure 5.6) of the peaks. When normalizing for the concentration as well, the curves converge to the same intensity. Following the increasing concentration, the curves show a higher structural peak but otherwise exhibit comparable characteristics, with the exception of the polycrystalline sample at 5 wt%. For this sample, the crystal reflexes overlay the structure factor. In addition, the curves shift towards higher intensity at higher concentrations, as more electrons in a denser dispersion scatter the incident X-rays. A Gaussian fit (Equation 5.2) was employed using a custom Matlab script to determine the position and characteristics of the structure peaks.

$$I_{q_{max}} = \frac{A}{B \cdot (2\pi)^{0.5}} \cdot e^{-\frac{(q-q_{max})^2}{2 \cdot B^2}} \quad (5.2)$$

with the peak position q_{max} , the intensity of the peak determined by $\frac{A}{B \cdot (2\pi)^{0.5}}$ and the relative width $\frac{B}{q_{max}}$. The structure peak develops at a concentration of 0.5 wt% and progressively shifts towards higher q ranges, indicating a more compressed system at higher concentrations. A detailed analysis of the peak characteristics can be found in the Appendix (Figure A.5).

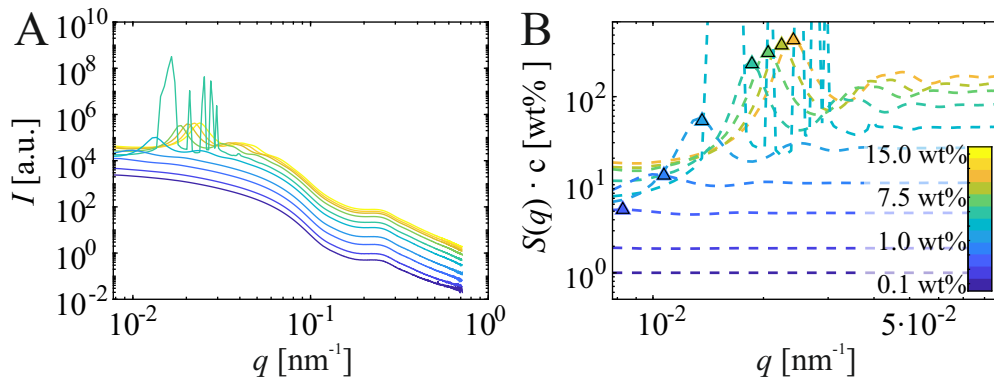


FIGURE 5.6: A) Radially averaged SAXS curves of the concentration series of small microgels (0.1 - 15 wt%). B) Structure factors derived from SAXS curves normalized by the sample with the highest dilution (0.1 wt%). Triangular markers indicate the position of the structure peak.

The peak characteristics confirm the initial impression that the structure peak shifts towards higher q values and increases in intensity according to the increase in volume fraction and concentration, respectively (Figure A.5). When deriving real space distances from the reciprocal structure peak with

$d_{\text{real}} = \frac{2 \cdot \pi}{q_{\text{max}}}$, the characteristic interparticle distance of colloidal particles can be estimated from the position of the scattering vector q . Generally, the interparticle distance decreases with increasing concentration due to the compressed microgel shell due to the increased number density and additional long-range interactions (Figure 5.7).

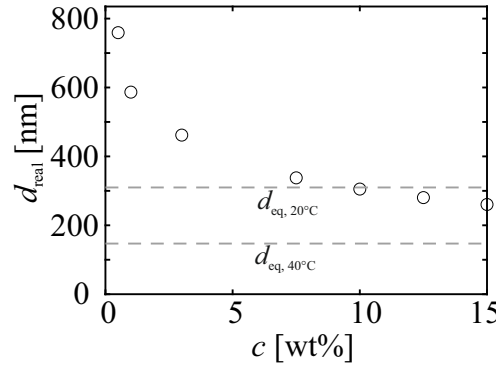


FIGURE 5.7: Real space interparticle distance correlated to the structure peaks. The dashed lines (---) indicate the dimensions of the short axis d_{eq} of SM-1 in the swollen (20°C) and collapsed (40°C) state.

Starting at 760 nm average distance between two particles for a highly dilute system, the particles are further compressed towards the glass transition, narrowing the distance towards the dimensions of the hard MNP core. At 15 wt%, the interparticle distance is 260 nm; when comparing the interparticle distance to the microgel dimensions (Table 5.1), it is smaller than the short axis of the microgel in the swollen state ($d_{\text{eq},20^\circ\text{C}} = 307$ nm). The results indicate that the microgels at this concentration are in contact with one another, likely forming a mixture of randomly oriented, partially collapsed, and possibly interpenetrated microgels. The SAXS experiments show isotropic patterns, suggesting that no nematic phase is present. Considering the aspect ratio of the microgels, a plastic crystal phase is expected.

To achieve a higher-ordered MMG system, additional effects, such as magnetic fields or flow, need to be considered. A magnetic field would allow the control of the orientation of the MNP core, and anisotropic particles tend to align under shear.

5.3.2 Structural Evolution of Anisotropic Microgels under Unidirectional Drying

In addition to the classical concentration series, a controlled drying experiment was performed. Thereby, the microgels were dried within a capillary attached to a reservoir (Figure 5.2) in a humidity control cell with saturated KCl solution (relative humidity: 85% [127]). The microgel concentration inside the reservoir was 1 wt%. As the solvent evaporates at the tip of the capillary, the sample is continuously transported through the capillary by the flow generated by the evaporation. Therefore, the microgels are consecutively accumulating at the tip, with a gradually decreasing concentration towards the reservoir until the diluted state is reached. With such a setup, a large concentration range can be covered with just one experiment.

In this experiment, the capillary was vertically placed into the X-ray beam, and multiple scans were performed every 20 μm along the capillary. As shown in Figure 5.8, the concentration increases with decreasing distance to the capillary tip, indicated by a higher scattering intensity at high q . Directly at the tip, there's a sharp transition in the intensity due to skin formation close to the air/liquid interface. This skin is defined by a lower water content and an increase in microgel packing [131]. In this case, the skin formation leads to closer-packed MNP cores and a distinct decrease in transmission. In the diluted phase, the patterns resemble the pattern for diluted concentrations in the previous experiment.

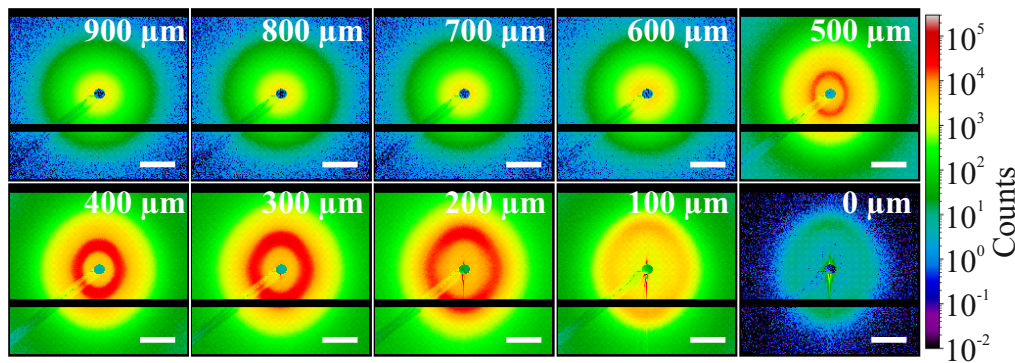


FIGURE 5.8: SAXS pattern of microgels concentrated in a drying cell. Distance d_{front} in μm from the capillary tip (Figure 5.2). Scale bars: $5.4 \cdot 10^{-2} \text{ nm}^{-1}$.

When entering the front ("front" is the area where the diluted flow is entering the aggregation phase), the particles are concentrated and more and more

compressed towards the tip, indicated by a marked increase in the q range of the structure peak. The SAXS patterns for the concentrated phase exhibit a weak anisotropy, indicating the alignment of the particles with their long axis parallel to the front (perpendicular to the flow). While the aspect ratio of the core - which dominates the scattering pattern - is around 3 (Chapter 4), close to the tip, the structure peak has an aspect ratio $p = \frac{q_{max,90^\circ}}{q_{max,180^\circ}}$ of around 1.5. This indicates that the microgels, while aligned with their long axis, can still rotate in the yz -plane (Figure 5.2 B). The overlay of particles randomly oriented in this plane results in an anisotropic pattern with an aspect ratio smaller than the particles themselves. For the scans closest to the front, the patterns show a more nematic order, with two peaks developing along the long axis of the anisotropic pattern.

The SAXS data of the drying cell experiments were treated as described in the previous section. The background correction was conducted with a scan of water in a drying cell and the normalization with the scan at 900 μm from the tip (Figure 5.9 B).

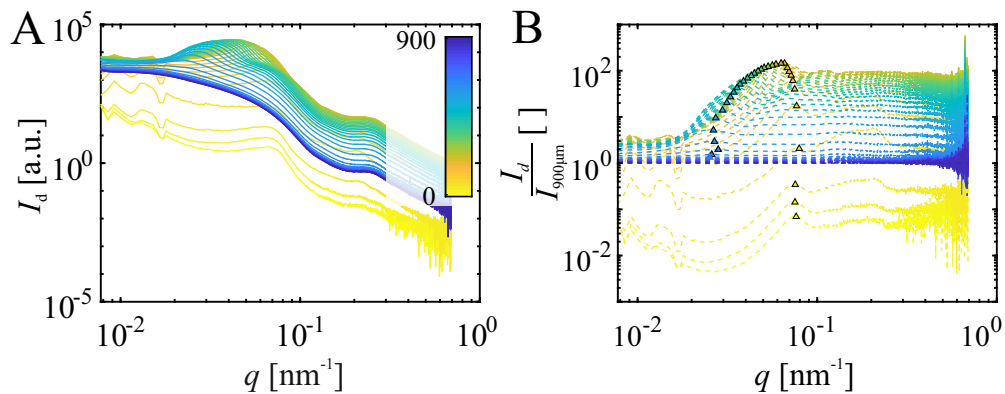


FIGURE 5.9: A) Background corrected SAXS curves of microgels concentrated in a drying cell. Distance in μm from the capillary tip. B) Structure peaks of microgels structuring under unidirectional drying. Triangular shapes indicate the peak position.

A distinct lack of a structure peak can be seen when comparing the diluted scattering curves (far from the tip) with the experiment above at the same concentration (1 wt%, Figure). There are several possible reasons for the observed differences. First, the flow may disrupt the ability of the microgels to structure themselves as they did in previous experiments. Second, the structuring observed in those earlier experiments might be enhanced by deionization, which increases the electrostatic interactions between the microgels. Additionally, it can be assumed that the environment of the drying

cell is not as clean as the quartz glass capillaries used in the previous experiments. As a result, impurities may weaken the electrostatic interactions among the microgels.

While the exact reasons for this discrepancy can't be resolved without further experiments, other trends observed from the concentration series are comparable in the drying experiments. The isotropic structure peak shifts towards higher q values closer to the tip, indicating an increasing compression of the microgels due to the rising microgel concentration. The structure factor follows a similar trend towards higher values until the absorption of the MNP core increases because of the dense packing of the inorganic cores of the microgels. This results in a distinct decrease in transmission and, consequently, a reduction of intensity. Therefore, the normalization fails for scans close to the tip (Figure 5.9 B).

In contrast to the scattering patterns of the concentration series earlier, the scans in the aggregated phase close to the tip show an anisotropy resulting from the unidirectional drying of the microgels in the yz -plane, leading to a perpendicular alignment to the flow direction. To further analyze the angle dependence, a 2D evaluation of the scattering data was conducted. Azimuthal splitting was performed, creating sectors comprising 1° slices of the detector image centered around the beam stop, as illustrated in Figure 5.10 A.

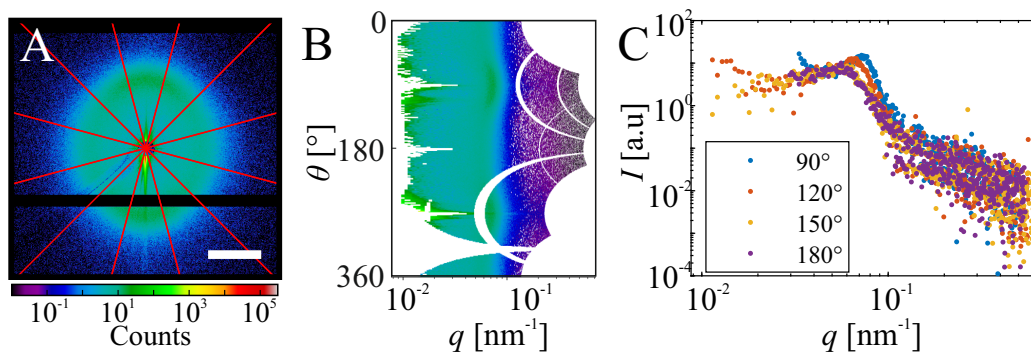


FIGURE 5.10: A) Schematic visualization of the azimuthal splitting of the SAXS pattern ($0 \mu\text{m}$) at the capillary tip with a binning of 30° (red lines). For the evaluation, a binning of 1° was used. Scale bar $5.4 \cdot 10^{-2} \text{ nm}^{-1}$. B) Sectorplot resulting from the azimuthal splitting, showing an angle-resolved SAXS pattern. C) SAXS curves derived via azimuthal splitting for 90° , 120° , 150° & 180° at the capillary tip.

These angle-dependent slices were consecutively radially averaged and can be plotted as a sector plot (Figure 5.10 B). From this sector plot, two

kinds of plots can now be extracted. First, the scattering curves for certain angles allow for the resolution of the angle-dependent structure peak, determining the average distance to the nearest neighboring microgel in a specific direction (Figure 5.10 C & 5.11). Second, the azimuthal plot at a particular q can be extracted, illustrating the anisotropy and orientation of the pattern (Figure 5.17). Exemplarily shown is the scan directly at the tip, with low intensity and narrow slicing, resulting in relatively noisy scattering curves. The q range available for the angle-dependent scattering curves depends on the mask and beamstop position as well as the sample position in the bottom left corner of the detector. The 90° and 180° sectors offer the largest q range and are therefore used in the following to compare the anisotropy of different patterns.

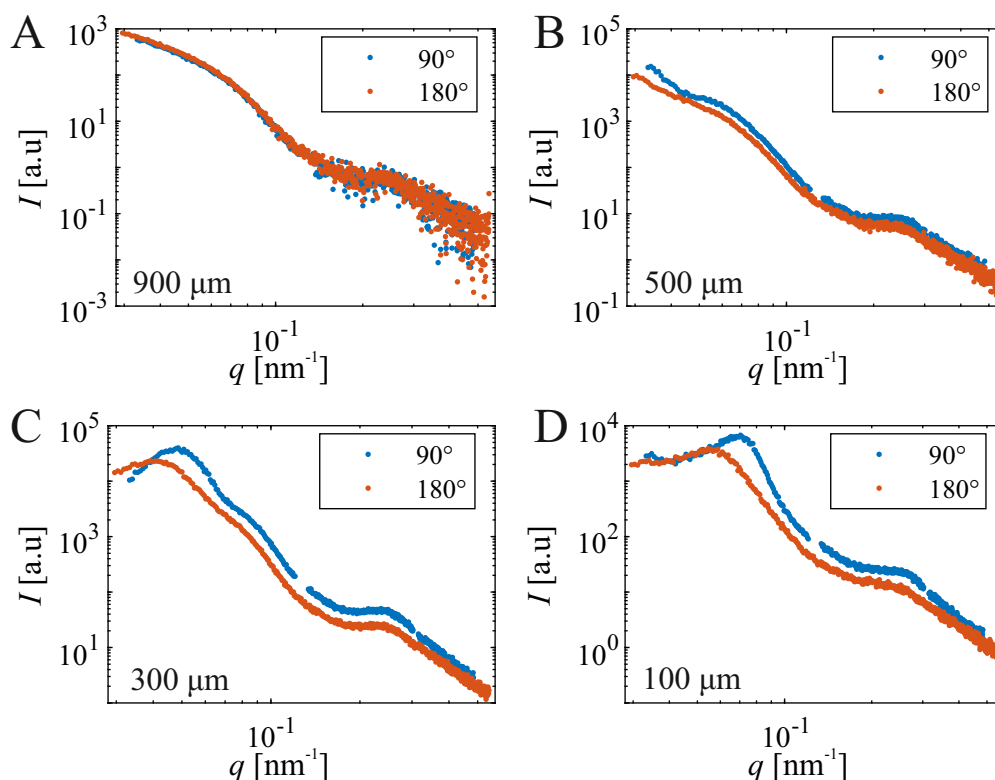


FIGURE 5.11: Azimuthal SAXS data for 90° & 180° for different distances d_{90° from the capillary tip, showing an increasing split between the major (90°) and minor (180°) axis of the scattering pattern.

For scans along the capillary, the angle-dependent scattering curves underline the observations described earlier, with splitting between the different axes increasing the higher the concentration. 90° represents the major axis

of the scattering pattern, showing a more distinct structure peak shifted towards higher q values compared to the minor axis because of the anisotropy (and alignment) of the microgels and their cores. Overlaying this split is the general shift towards the higher q due to increasing compressions in denser parts along the capillary.

The angle-dependent structure peak (90°) can be correlated to a real space interparticle distance d_{90° . This distance corresponds to the interparticle distance along the x-direction - along the capillary. As discussed earlier, the particles are compressed closer depending on the distance from the capillary tip. At the capillary tip, the particle distance is even slightly below the short axis of the magnetic cores, indicating a very dense packing. As the SAXS detector image shows a 2D representation of a three-dimensional structure, the structure peak might not perfectly correlate with the interparticle distance.

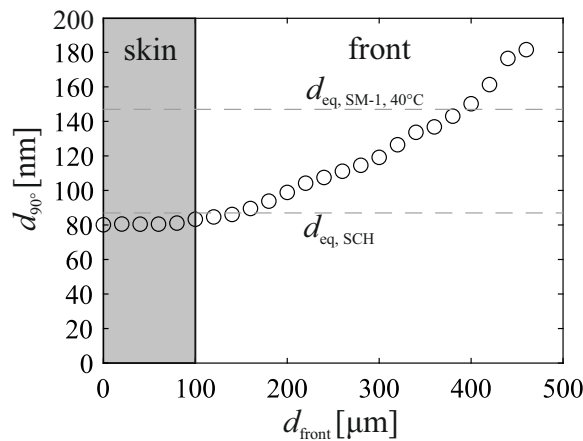


FIGURE 5.12: Interparticle distance at the 90° sector calculated from $q_{max,90^\circ}$, corresponding to a nematic arrangement in the x-direction (along the capillary). Directly at the air/water interface (0 - 100 nm), a very dense packing of microgels forms a skin defined by a significant decrease in scattering intensity. Followed by an accumulation area between 100 and 500 nm. In this area, the microgel packing decreases in the direction of the reservoir, as indicated by an increase in interparticle distance. Dotted lines indicate the short axis d_{eq} of the MNP core and the microgel in the collapsed state at 50°C .

The experiments in the drying cell show a nematic type of ordering close to the capillary tip and, therefore, are fundamentally different from the previous experiments. The nematic order can be seen as evidence of the compression of the microgel, reaching much higher volume fractions than the concentration series. While this order prevents us from using these experiments

to probe different concentrations comparable to the concentration series previously discussed, the formed structure is fascinating itself, and it allows the showcasing of the 2D analysis and the development of the structure peak as the particles align themselves perpendicular to the flow under unidirectional drying.

5.3.3 Static Magnetic Fields

One of the premises of this work was to use magnetic fields further to control the orientation and structuring of anisotropic microgels and test the metastability of the dispersion. Therefore, measurements with different magnetic fields were performed between 1 and 70 mT. These samples were exposed to the magnetic field at a custom-developed stage, as described in the experimental section. Under a static magnetic field, the microgels have been shown to align themselves with their long axis along the magnetic field, similar to the behavior of their magnetic cores (Chapter 4). It has been shown that the microgel shell weakens the dipolar interaction between the magnetic cores. As a result, the microgels can align within the field and only experience weak dipolar interactions below the volume phase transition temperature (VPTT). This is in contrast to the bare nanoparticles, which tend to form dipolar chains even in weak magnetic fields.

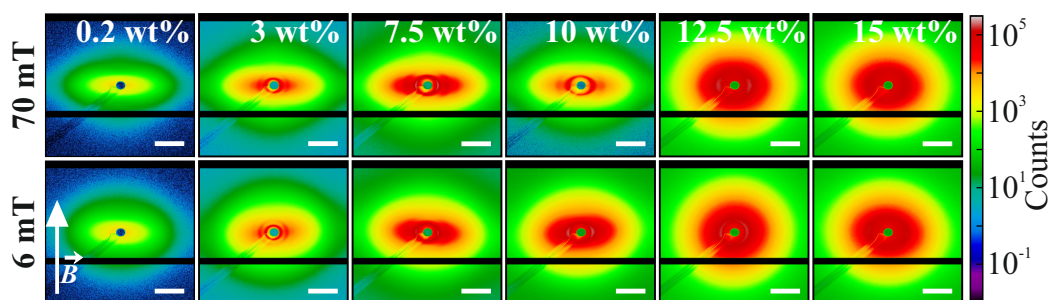


FIGURE 5.13: SAXS patterns recorded under static magnetic fields (6 and 70 mT) of SM-1 dispersions with concentrations between 0.2 - 15 wt%. Scale bars: $5.4 \cdot 10^{-2} \text{ nm}^{-1}$.

The field was applied vertically onto the sample, resulting in a horizontally projected anisotropy in reciprocal space. The SAXS pattern gives a first idea of the influence of the magnetic field on the microgels at concentrations between 0.2 and 15 wt%. The anisotropy of the diluted (0.2 & 15 wt%) and intermediate concentrated (7.5 & 10 wt%) samples increase significantly with

higher field strengths, showing a better alignment of the microgels with the magnetic field. With increasing concentration, the microgels get increasingly in contact, compress and possibly interpenetrate with each other, decreasing the effect of the magnetic field. The patterns of high-concentration samples are nearly isotropic, hinting at a possible arrested state. For weaker magnetic fields, a lower anisotropy can be observed, especially at lower concentrations, indicating secondary effects, such as increasing viscosity, interfering repulsive interactions, and Brownian motion. Additional dynamic experiments need to be conducted to probe the glass transition. In addition to the apparent anisotropy, the scattering patterns for intermediate concentrations show features indicating a nematic-like order.

The detector images were azimuthally split as described earlier, revealing a distinct split between the curves for 90° and 180° (Figure 5.14).

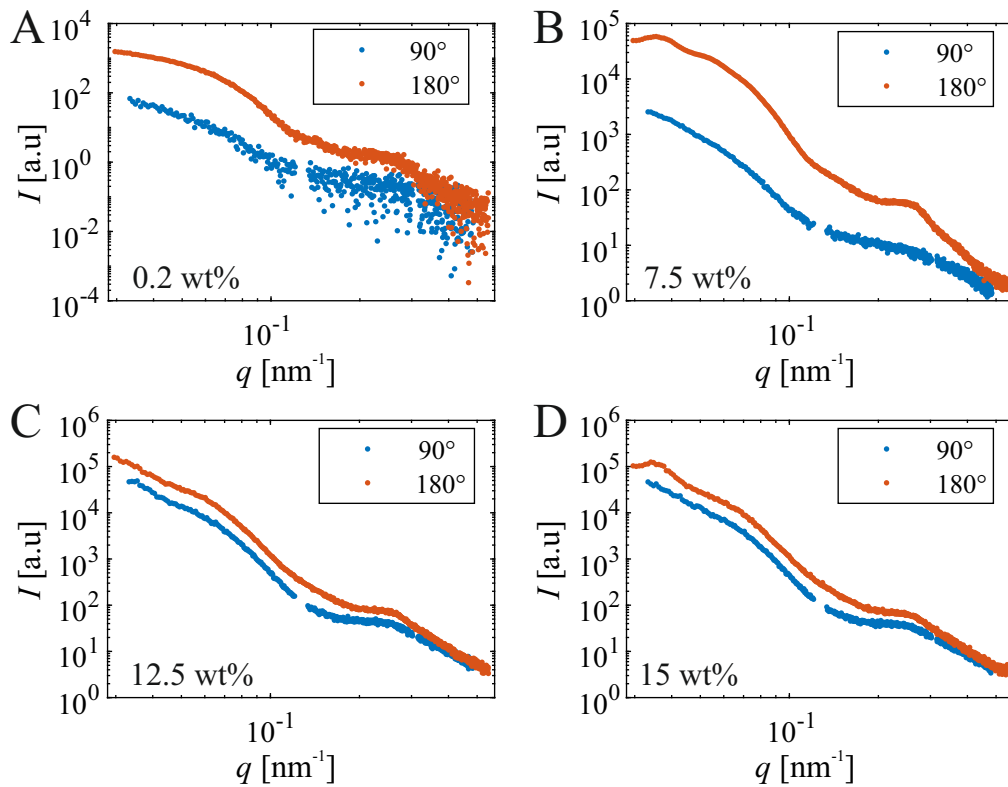


FIGURE 5.14: Azimuthal SAXS curves for 90° & 180° under a static magnetic field of selected concentrations (0.2, 7.5, 12.5 and 15 wt%). Showcasing the changing aspect ratio with increasing concentration.

This split underscores the anisotropy of the scattering pattern, which increases with concentration but decreases what we assume to be the glass

transition around 10 - 12 wt%. Furthermore, the split between the curves indicates the orientation of the microgel particles in response to the applied magnetic field.

At low concentrations, the microgels exhibit weak interactions. They are relatively free to rotate as the diffusion is faster than at higher concentrations, resulting in a lower anisotropy at weaker fields. However, as the concentration increases, the diffusions slow down, causing the microgels to orient more effectively along the magnetic field direction and increasing the apparent anisotropy.

However, for higher concentrations, the split between the particles almost disappears as expected for an isotropic state, indicating a possible arrested state where the particles are no longer able to rearrange themselves in response to the magnetic field or other stimuli. Surprisingly, for a concentration of 15 wt%, a small structural peak is visible despite almost no visible distinction. This peak could be due to the flow created while filling the capillary or a sign of "rattlers" moving freely within the arrested microgel matrix. These will be further discussed later in this chapter.

When normalizing the scattering intensity for the concentration c and the transmission I_T measured at the beam stop, the scattering curves can be overlaid onto a master curve, as scattering intensity for high q values is directly related to the number of scattering centers or particle count.

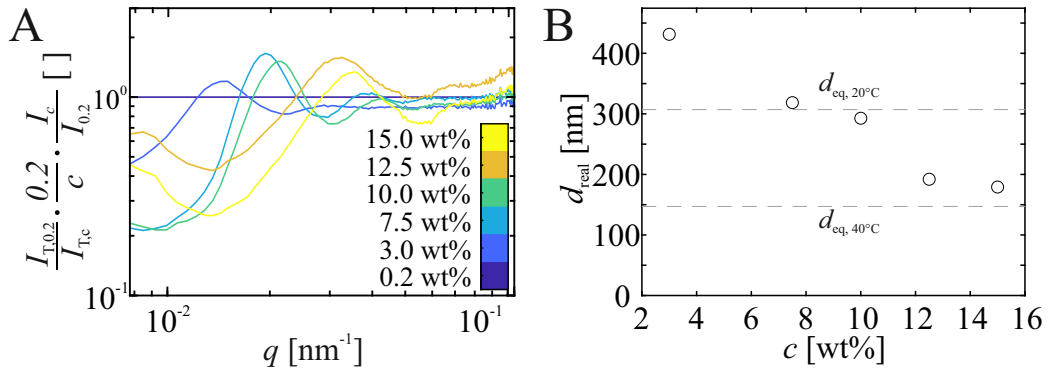


FIGURE 5.15: A) 180° angle-dependent structure factor for 0.2 to 15 wt% normalized by concentration and transmission. B) Real space interparticle distance d_{180° determined from the angle-dependent structure factors at 180°. The dotted lines indicate the short axis d_{eq} of the microgel in the swollen (20 °C) and collapsed state (50 °C).

As can be seen in Figure 5.15, the structure peak shifts towards higher q values as the system gets compressed with higher concentrations, and the

peak height increases for increasing concentrations but decreases again above 7.5 wt% indicating a decreased order due to approaching the glass transition. The real space distances can be estimated from the structure peak positions measured for the 180° section of the pattern. The distance decreases from approximately 460 nm at 3 wt% to 170 nm at 15 wt%. The short axis d_{eq} of the microgels is roughly 147 nm long in a fully compressed state and 307 nm in a swollen state (Table 5.1), the determined interparticle distances correlate to a significantly compressed side-to-side configuration.

Overall, static magnetic fields support orienting MMGs along the field lines. The anisotropy of the pattern increases with increasing concentration as the diffusion decreases. Close to the glass transition, the anisotropy decreases again as the dynamic of the microgels becomes arrested. These experiments give a rough estimate of the glass transition, but experiments studying the dynamic of dense microgels are needed for more detailed determination.

5.3.4 Dynamic Magnetic Fields

Response to Rotating Magnetic Field

To further study the phase behavior of dense microgel systems, the response to a rotating magnetic field was examined. Therefore, the microgels were actuated by rotating magnetic fields with four field strengths (1, 6, 36 & 70 mT) and two different rotating rates (5 and 50 rpm). The orientation of the microgels was recorded through SAXS with a frame rate of 0.1 and 0.01 fps, respectively (Figure 5.16 B).

To analyze the magnetic response, azimuthal splitting was performed as described in the previous section with a binning of 1° . For field strengths up to 70 mT and concentrations up to 10 wt%, the pattern's anisotropy allows the observation of the rotation. The azimuthal plots at $q = 0.048 \text{ nm}^{-1}$ between an angle of 0 and 300° were extracted to evaluate rotation type and rate automatically (Figure 5.16 B). The sector and q range were selected to avoid missing data due to the detector frames.

For a more detailed analysis, the maxima of the azimuthal plots (Figure 5.16 B) were determined. Therefore, part of the azimuthal plot was fitted with a Gaussian fit (Equation 5.3), allowing the analysis of both peak position and amplitude. In Figure 5.17, the scattering pattern correlating with time 0 s

in Figure 5.16 A is exemplarily analyzed to determine the peak position and rotation rate.

$$I(\theta, q) = A \cdot e^{-\frac{(\theta - \theta_p)^2}{2\sigma^2}} + B \quad (5.3)$$

with amplitude A , baseline B , and maxima position (and orientation of the pattern) θ_p .

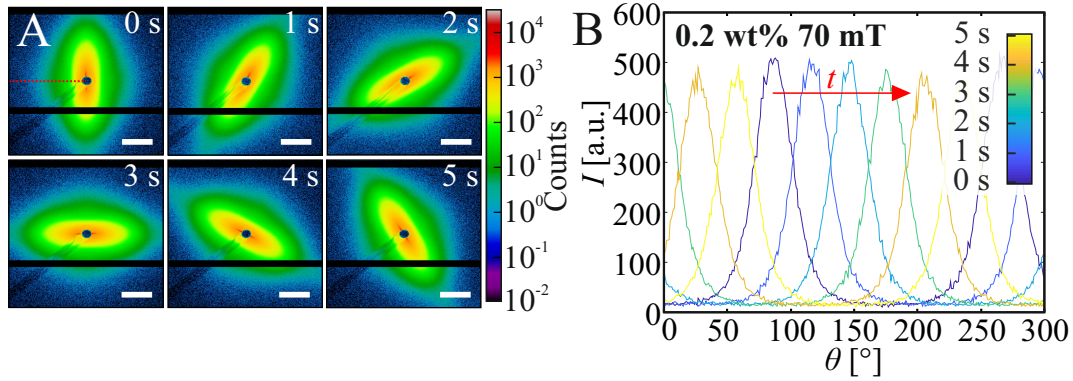


FIGURE 5.16: Example for the evaluation of a rotation experiment for a dilute sample (0.2 wt%, 50 rpm, 70 mT). A) Time laps of the rotating scattering pattern actuated by a rotating external magnetic field. Scale bars: $5.4 \cdot 10^{-2} \text{ nm}^{-1}$. B) Time-dependent azimuthal plots at $q = 0.048 \text{ nm}^{-1}$.

The peak position θ_{max} derived from the azimuthal plot fit (Figure 5.17 A) can be evaluated depending on the time that has passed since the start of the experiment. The rotation type and rate can be determined from the resulting orientation shift diagrams (Figure 5.17 B).

In the presented example, the rotation rate of 5 rpm leads to four full rotations within the recorded 50 s. The azimuthal plots reveal two maxima that are shifted by 180° because of the ellipsoidal shape of the pattern. Due to the limitations of the masking in the sector data, only the first peak of the azimuthal plot within the range of 60° to 240° was considered valid for analysis. Consequently, the orientation shift diagram (Figure 5.17 B) displays eight movements of the peak throughout the evaluation interval, corresponding to eight half rotations of the microgels through the observed detector area. These half rotations can be analyzed using a linear fit, where the slope indicates the resulting rotation rate of the microgel. For the diluted example system (0.2 wt%) actuated by a 70 mT field rotating with 5 rpm, the microgels rotate synchronously to the magnetic field with an average speed of 4.98 rpm.

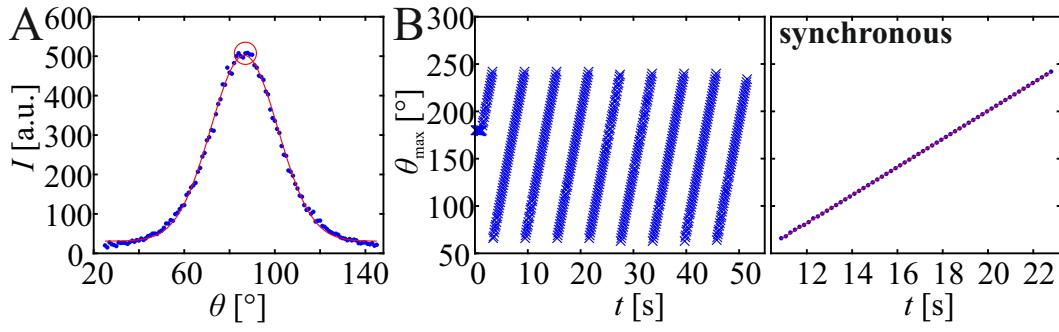


FIGURE 5.17: Example for the evaluation of a rotation experiment for a dilute sample (0.2 wt%, 5 rpm, 70 mT). A) Gaussian fit of a part of the azimuthal plot at $q = 0.048 \text{ nm}^{-1}$, allowing the extraction of the main orientation of the anisotropic scattering pattern and the amplitude that is correlated to the aspect ratio of the pattern. The red line indicates the Gaussian fit (Equation 5.3), and the red circle indicates the determined peak position. B) Time-resolved orientation shift of the rotating scattering pattern, represented by the shift of the peak position θ_{max} . A linear shift indicates a synchronous rotation with the external magnetic field; the slope of the fit (red line) represents the rotation rate, in this case, 4.98 rpm.

The rotation rate and type depend on a range of parameters, like the concentration of the sample dispersion, magnetic field strength, and, of course, rotation rate. In addition to a synchronous rotation, the microgels can asynchronously rotate or wiggle around a static orientation. In the case of an asynchronous rotation, the magnetic field rotates faster than the microgels can follow. For a ferromagnetic rod in a Newtonian liquid that is actuated by a constantly rotating magnetic field, the rotation of the particle can be described by the exerted viscous and magnetic torques (Equation 5.4) [73].

$$\gamma \left(\omega_{MF} - \frac{d\tilde{\zeta}}{dt} \right) = \mu B \cdot \sin \tilde{\zeta} \quad (5.4)$$

with magnetic field B , magnetic moment μ , angular frequency of the magnetic field ω_{MF} and the angle between the rod and the magnetic field $\tilde{\zeta}$. For an asynchronous rotation, the viscous torque dominates, leading to a slower rotation than the external magnetic field. As a consequence of this slower rotation, the magnetic field overtakes the microgel after some time, leading to a short period of fast backward movement, followed by a continued rotation in the direction of the magnetic field. This backtrack is represented by a brief decrease of θ_{max} in the orientation shift diagrams (Figure 5.18 A). This type of asynchronous rotation is called tumbling.

When the concentration of the microgels increases, the rotational dynamics change from synchronous to asynchronous and finally to a wiggling motion. It is important to note that this wiggling motion, strictly speaking, is not a rotational motion but an oscillation movement. The microgels are arrested for these samples and can't rotate anymore, even at high field strength. As seen in Figure 5.18 B, the orientation of the microgel oscillates by $\sim 30^\circ$ around a fixed average position. The wiggling is marked by a slow rotation in the same direction as the magnetic field and a faster "jump" backward when the magnetic field "overtakes" the main axis of the microgels.

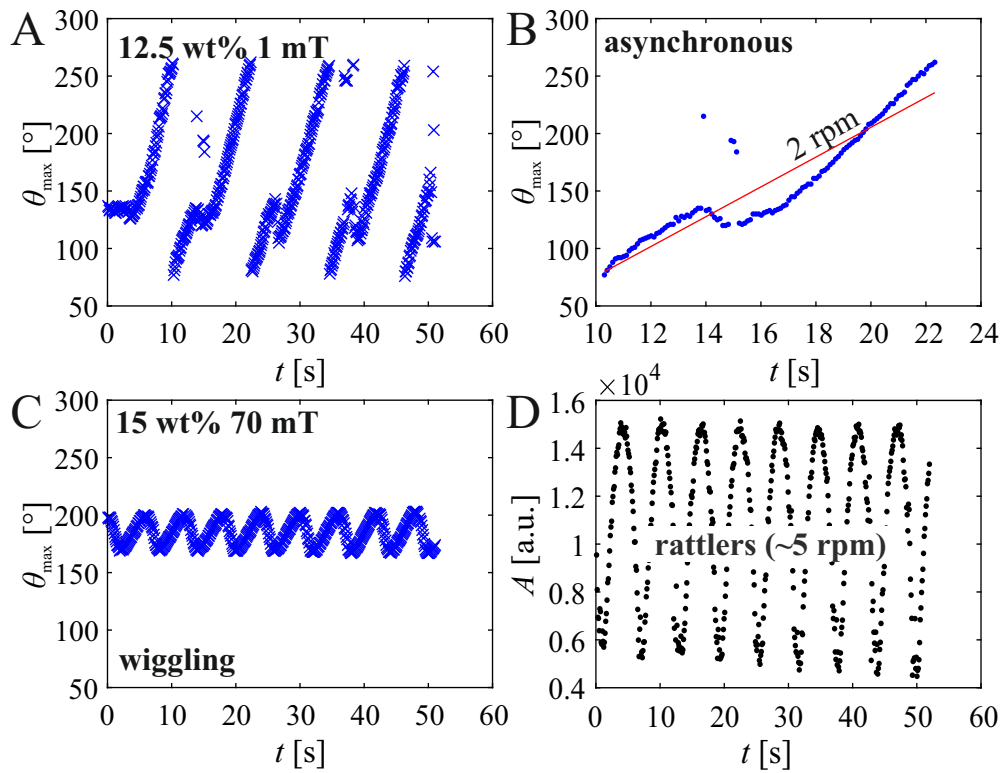


FIGURE 5.18: Example analysis for A/B) an asynchronous rotation (12.5 wt%, 1 mT, 5 rpm), and C/D) a wiggling motion (15 wt%, 70 mT, 5 rpm). The graphs represent the shift of maxima of the azimuthal plots within the range of 60° and 240° at $q = 0.048 \text{ nm}^{-1}$ in blue. The red line marks a linear fit representing the average rotation rate. D) Amplitude of the azimuthal plot for the wiggling system, showing a distinct oscillation with a frequency of ~ 5 rpm.

Notable for the 15 wt% samples (arrested system), although the peak shift only shows an oscillatory motion around the fixed orientation, the amplitude A derived from the fit (Equation 5.3) periodically fluctuates. The periodicity of this fluctuation is in agreement with the rotation rate of the magnetic field (~ 5 rpm), indicating the existence of free particles inside the arrested

microgel matrix (Figure 5.18 D). These so-called "rattlers" are caged by their arrested neighbors but have a higher degree of freedom compared to the arrested matrix [132, 133], allowing them to freely diffuse or, in this case, rotate with the magnetic field.

The average rotation rates and rotation modes depend not only on the concentration of the microgels but also on the applied field strengths and field rotation rates. A range of concentrations and field strengths need to be tested to determine the exact glass transition. Based on our estimations, the glass transition likely occurs between 12.5 and 15 wt%. The rotation rate starts to decrease at 12.5 wt%, indicating a partially arrested system. In Figure 5.19, the different rotation responses can be seen. In diluted systems, even a weak magnetic field of 1 mT enables the microgels to rotate along with the magnetic field (Figure 5.19 A). For 50 rpm, the experiments were only conducted at 70 mT (Figure 5.19 B), and the results follow the established trend, free rotation up until 12.5 wt% (comparable to 70 mT, 5 rpm) and a complete stop at 15 wt% showing no overall rotation.

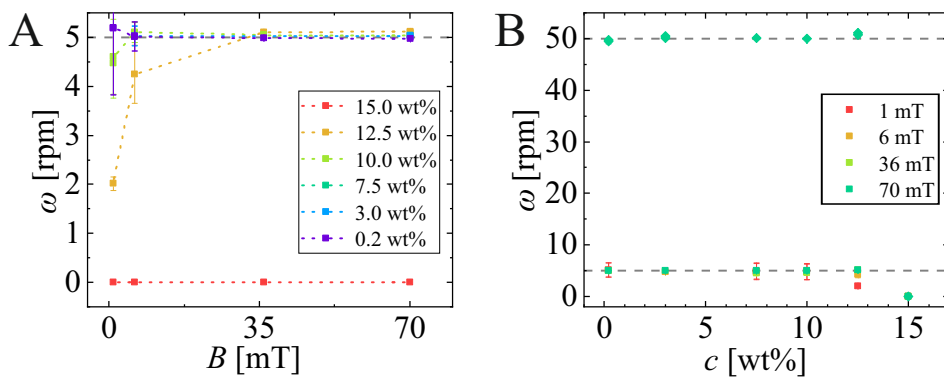


FIGURE 5.19: Determined overall rotation rates dependent on A) field strength and B) rotation rate, detailing the glass transition. At 15 wt%, the system is fully arrested, indicated by an overall rotation rate of 0 rpm. With decreasing concentration, the MMGs are increasingly dynamic, changing the rotation regime from arrested via asynchronous to a synchronous rotation starting around 10 wt%. The influence of the field strength can be observed most clearly at 12 wt%. With increasing field strength, the rotation regime changes from asynchronous (1 & 6 mT) to synchronous (36 & 70 mT).

When the particles are stuck in arrested systems, the rotation rate is 0 rpm. For samples near the glass transition, a decrease in the rotation rate is observed only for weaker magnetic fields, indicating that a strong magnetic torque can free the microgels while the particles are partly arrested. In these

partly arrested systems, a decrease in the aspect ratio can be observed during rotation. The anisotropy of the system arises from the relatively uniform alignment of the magnetic nanoparticle (MNP) cores. When the individual microgels rotate asynchronously at different speeds, the particles become oriented in various directions. As a result, the pattern becomes increasingly isotropic as the magnetic field continues to rotate.

These rotation experiments provided a good understanding of the glass transition and the dynamics approaching a glassy state. While an accurate determination of the transition requires additional concentrations, using the anisotropic core as a tracer for the dynamics of the microgels works quite well. Furthermore, the combined use of amplitude and peak position of the azimuthal plot allows us to confirm the presence of free "rattlers" within the arrested microgel matrix, indicating inhomogeneity in the degree of arrestment of this system.

90° Relaxation Experiments

In addition to the rotational experiments, sweep experiments were performed. These relaxation experiments are similar to the rotational experiments discussed in the previous section. However, instead of a continuous rotation at different speeds, a rapid (90 rpm) 90° shift of the magnetic field (70 mT) orientation is used in these experiments. Subsequently, the response (relaxation) of the microgel samples is observed and evaluated.

The evaluation was conducted analogous to the rotation experiments, extracting the peak shift and amplitude of the azimuthal plot. In the case of microgel samples that are diluted or semi-concentrated (up to 10 wt%), the scattering pattern and azimuthal plot display a quick and even relaxation of the entire pattern (Figure 5.20 A). A significant relaxation can also be observed for the intermediate state of 12.5 wt%. However, this relaxation is associated with a decreased aspect ratio, indicated by a change in the amplitude of the azimuthal plot. This decrease hints that the relaxation is not uniform, and the system might be partly arrested. Even denser microgel dispersions (15 wt%) no longer show an apparent effect on the magnetic impulse except for a slight decrease in the anisotropy of the scattering pattern (Figure 5.20 B). An in-detail analysis of the azimuthal plot reveals a frozen main pattern with a smaller anisotropy that decreases further during the relaxation progress due to a small secondary peak developing at 90°. Thus,

the system is not entirely arrested, or more precisely, some of the microgels within the arrested microgel matrix are still free to move. The relaxation process slows down with increasing concentration until the system is mainly arrested at 15 wt%. At this concentration, the main pattern no longer relaxes (Figure 5.20 B). Instead, a small peak develops during the 90° field rotation at a 90° shifted position. The presence of this additional peak indicates a heterogeneous arresting process, with caging effects that lead to free rattlers.

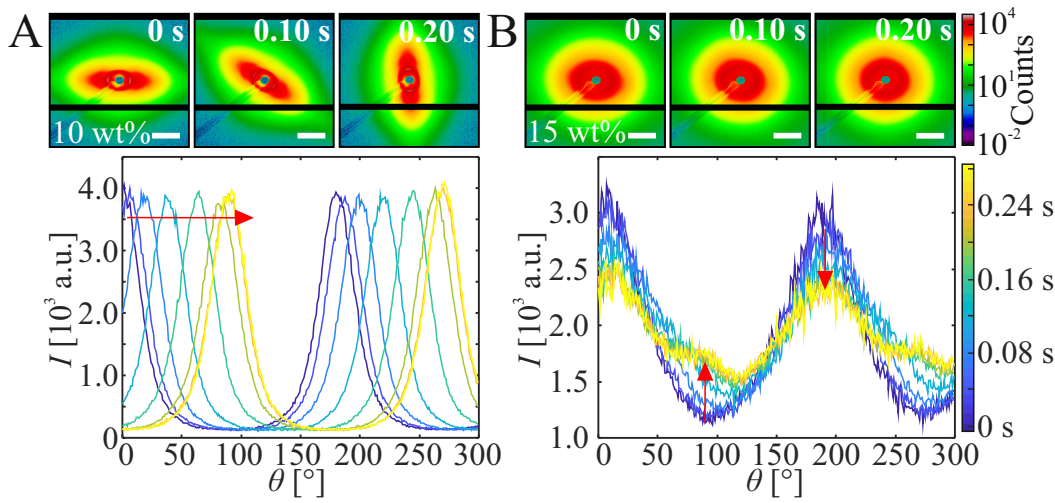


FIGURE 5.20: A) Upper: Time-lapse of the relaxation of a microgel system below the glass transition (10 wt%). SAXS pattern visualizing the free relaxation. Lower: Time-dependent evolution of the azimuthal plot at $q = 0.048 \text{ nm}^{-1}$, exhibiting a marked shift of the peak position θ_{max} (red arrow). B) Upper: Time-lapse of the (not) relaxation of an arrested microgel system (15 wt%). Lower: Time-dependent evolution of the azimuthal plot at $q = 0.048 \text{ nm}^{-1}$, exhibiting a marked decrease in the aspect ratio and the development of a secondary peak (red arrows).

The peak shift can be evaluated analogously to the analysis of the rotating pattern to determine the relaxation speed. The resulting relaxation curves for 7.5 - 12.5 wt% (Figure 5.21 A) exhibit the characteristic progression for relaxation progress. These systems relaxate within 0.23 - 0.27 s. For 15 wt%, the main pattern "wiggles" a bit, with the additional peak developing faster than the relaxation of the more dilute systems within ~ 0.17 s. The estimated rotation speed of the "rattlers" is ~ 88 rpm, very close to the 90 rpm incident field rotation, supporting the results of the rotation experiments. The results support that only a few particles are almost free to rotate, whereas the rest of the sample is arrested within this time scale. As a secondary evaluation, the peak shift analysis can be supported by evaluating the amplitude of the

azimuthal plots. For samples that are free to rotate (7.5 and 10 wt%), the amplitude remains constant throughout the entire measurement period. In contrast, the amplitude decreases for partly and mostly arrested systems (12.5 and 15 wt%). This decrease can be attributed to the fact that some of the microgels are moving while others are either stuck or moving at a different speed, which leads to a "smearing" of the pattern. The resulting relaxation speed for the arrested sample (15 wt%) correlates with the development of the secondary peak. For the sample that is partly arrested or at least close to the glass transition (12.5 wt%), there is a slight discrepancy in speed ~ 0.2 s vs. ~ 0.27 s. A reason for the discrepancy is that the amplitude is more sensitive to faster parts of the sample. At the same time, the peak position is a more collective value averaging over all microgels.

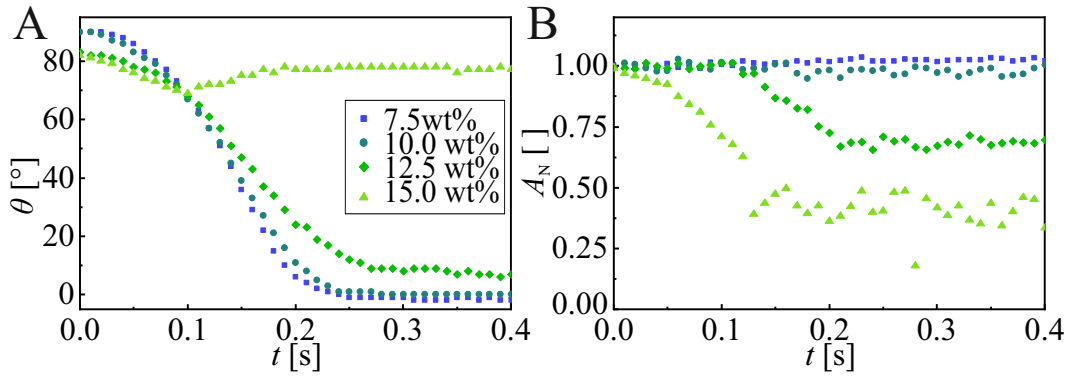


FIGURE 5.21: Relaxation process displayed as A) angular change of the peak position and B) amplitude of the azimuthal plot, respectively. In A), the decrease of the angle indicates a free system, while a decrease of the amplitude in B) indicates a - at least partly - arrested system.

In conclusion, the relaxation experiments can't entirely give the same results as the rotation experiments, as they were conducted at one field strength. However, the general results are comparable with the rotation experiments, supporting the impression that the microgels are partly arrested at 12.5 wt% and mostly arrested at 15 wt%. Apparent inhomogeneities hint at the existence of free rattlers inside the arrested microgel matrix.

5.3.5 Arrangement of Magnetic Microgels at the Air/Water Interface

Given the well-known surface activity of microgels [13, 35], experiments were carried out at the air/water interface to explore the behavior of the anisotropic MMGs in this environment. These experiments offer additional insights into the assembly of anisotropic magnetic microgels at the interface, where they are packed in a monolayer and serve as a proof-of-concept for using this MMG system as a micro tracer for probing the local dynamics at the interface or to create metasurfaces. For these experiments, the microgels were dispersed in an 80/20 mixture of isopropanol/water and dropped onto an air/water interface, allowing the microgel to spread and arrange at the interface. The amount of microgels added was selected so that a monolayer is formed at the interface, which is indicated by iridescence. The microgels were deposited onto a silicon wafer via a linear dipper moving through the interface to study the structure. During the whole experiment, a Halbach Array was used to apply a constant magnetic field onto the magnetic microgels, with the field direction parallel to the interface (Figure 5.3).

The microgels are mostly arranged in a hexagonal crystalline pattern analogous to the domains observed for 5 wt% in the bulk experiments (Figure 5.5). SEM images of these arrangements were analyzed using Matlab to create Voronoi diagrams, which reveal the number of neighbors for each microgel particle (Figure 5.22).

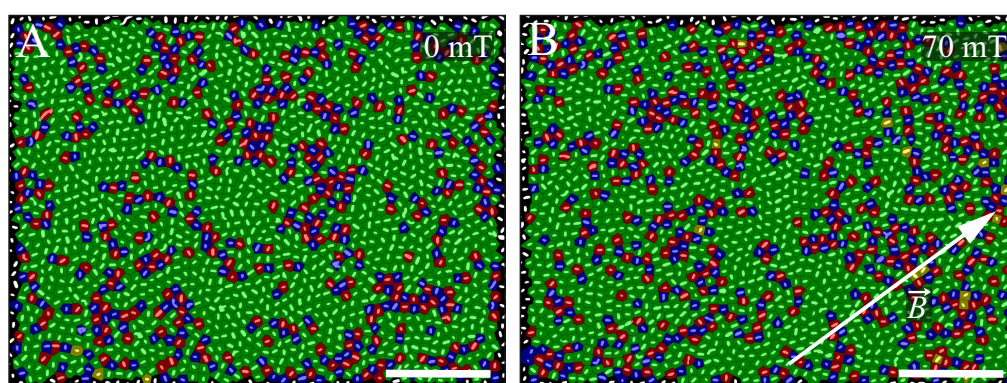


FIGURE 5.22: Voronoi diagrams of samples prepared at A) 0 mT and B) 70 mT, displaying the number of nearest neighbors. Green-colored areas indicate a hexagonal order with six neighbors; blue and red represent five and seven neighbors, and yellow for everything else. Scale bars: 5 μm .

Hexagonal patterns, representing six neighbors, were represented in green, while blue and red represented five and seven neighbors, respectively. All other neighbor numbers were colored in yellow. The Voronoi diagrams for 0 and 70 mT show mostly six-neighbor, hexagonal phases with defects in between. There is no obvious difference between samples prepared with and without a magnetic field, indicating that the presence of a magnetic field does not disturb the arrangement of microgels at the interface. Especially since no obvious dipolar chains were forming in the field.

On the other hand, the microgels couldn't fully align with the magnetic field during the 2 h equilibration time, possibly due to the spreading and interpenetration of the microgel shell or other effects. The orientational order parameter (Equation 4.10) shows a limited alignment with the magnetic field ($S_1 = 0.4$) compared to the random orientation for 0 mT ($S_1 = 0.1$). Possibilities to reach a better alignment with the magnetic field would be to increase the field strength or equilibration time or decrease the microgel concentration to either keep the microgels from hindering each other or "overpower" the retaining effects. In addition to the Voronoi diagrams, the radial distribution function of the SEM images was calculated via an ImageJ macro, showing four clear maxims, indicating a highly structured arrangement on a local level. There is no difference between field and no field, and the orientation of the magnetic core does not matter for this kind of structure.

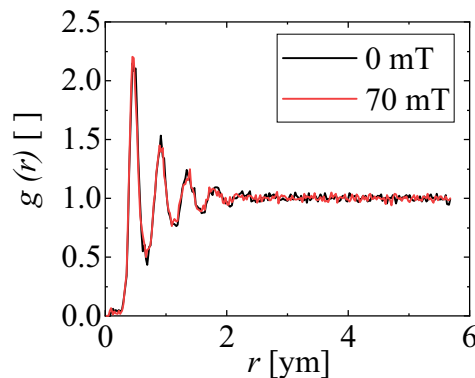


FIGURE 5.23: Radial distribution function of microgel depositions conducted under magnetic fields of 0 and 70 mT showing no significant differences in organization due to the magnetic field.

As a result, with some fine-tuning, it might be possible to use those particles as micro tracers at an interface. Additionally, it would be interesting to

perform such measurements in a Langmuir trough setup modified to apply a magnetic field while having precise control over the surface pressure.

5.4 Conclusion

In conclusion, this chapter on concentrated magnetic microgel dispersions highlights the significance of magnetic core-shell microgels. They can serve as an effective model system for exploring the complex phase behavior and dynamics within concentrated soft colloidal systems. By applying an external magnetic field, the magnetic core-shell microgels can be oriented in a preferred direction, significantly influencing their structural organization and interparticle interactions. This alignment allows for a more detailed investigation of the materials' behavior, revealing how the microgels interact with each other under different conditions, such as varying concentrations and field strengths.

Starting with the complex phase behavior of anisotropic microgels without a magnetic field, this chapter discusses the absence of clear nematic phases for standard SAXS measurements without aligning the MNPs in a unidirectional manner. Plastic crystals, on the other hand, do exist for this microgel system at 5 wt%, showing local crystalline domains but without long-range order. The concept of colloidal "spin glasses" was also introduced in this context. Spin glasses are in a glassy state with frozen magnetic moments, analogous to a colloidal glass from microgels with randomly oriented anisotropic MNPs [126]. For microgels, these states can form due to interparticle interactions at the glass transition and the presence of anisotropic MNPs. Further experiments studying the melting of such colloidal spin glasses should be conducted to evaluate the reversibility of the "freezing" of the "magnetic spins".

Consecutively, this chapter focused on structuring MMGs with two methods: magnetic fields and controlled drying. When subjected to flow, anisotropic microgels display structural changes due to their shape. In a drying cell setup, where fluid is withdrawn from the reservoir by evaporating at a capillary tip, anisotropic microgels self-assemble perpendicular to the capillary, forming strongly compressed nematic phases.

When exposed to a static magnetic field, the microgels align strongly with

the field orientation up to the glass transition, at which the "frozen" structure hinders the re-arrangement of the microgels. The interparticle distance of around 170 nm is smaller than the minor axis $d_{eq} = 307$ nm in a fully swollen state. This hints at a significantly compressed MMG system.

Static measurements alone were insufficient to precisely determine the glass transition point. To address this, dynamic SAXS measurements were conducted, providing a clearer picture of the transition from a freely rotating system to one nearly entirely arrested in a glassy state. By applying a dynamic magnetic field during the SAXS experiments, the behavior of the microgels could be monitored in real-time. This setup allowed for the differentiation between synchronous and asynchronous rotation regimes. In the case of asynchronous rotation or when the system reaches an entirely arrested state, SAXS revealed the characteristic signature of a glassy system, indicating a transition to a state where the microgels are immobilized and no longer able to rotate freely. Besides rotational experiments, the conducted relaxation experiments support the established glass transition but also show an interesting feature, as the aspect ratio of the scattering pattern decreases sharply with the 90° shift of the magnetic field, indicating free rotation of some particles inside the arrested microgel matrix. These "rattlers" are free to rotate at the maximum rotation rate, in stark contrast with the collective rotation at lower concentrations.

Lastly, proof-of-concept experiments at the air/water interface with and without magnetic revealed a highly structured arrangement on a local level, as evidenced by Voronoi diagrams and radial distribution functions derived from linear depositions. We observed no significant difference in the organization between field-aligned and non-aligned microgels, indicating that the orientation of the magnetic core does not influence this particular type of structural arrangement. However, we recorded a significant change in the order parameter. Despite limitations in achieving complete alignment with the magnetic field due to interpenetration and spreading effects, we have shown that anisotropic magnetic microgels hold great potential for further investigation. By fine-tuning experimental conditions, it may be possible to achieve stronger magnetic alignments and fully exploit the unique properties of magnetically actuable microgels at interfaces.

In summary, this chapter has offered important insights into the intricate phase behavior and dynamic properties of anisotropic magnetic microgels, enhancing our understanding of soft matter systems as a whole. It has highlighted the unique interactions and mechanisms at play in these anisotropic microgel systems. Future research directions will focus on exploring the potential applications of these microgels, particularly as micro tracers both in bulk materials and at interfaces, where their anisotropy and magnetic properties may offer unique advantages. Additionally, further investigation into the role of magnetic interactions within microgel glasses will be essential for understanding how these interactions influence their structural and dynamic behaviors. A deeper exploration of the interplay between particle orientation, structural formation, and dynamical response in anisotropic magnetic microgels will also be a key area of focus, providing valuable insights for developing new materials and advancing the field of soft condensed matter.

Chapter 6

Static and Dynamic Control of Rod-shaped Pre-programmed Magnetic Microgels

6.1 Introduction

Introducing magnetic properties into micron-scale building blocks is a way to introduce external control over different systems, ranging from micro-actuators possibly used in microfluidics [134, 135], via soft robotics [136] and implant development [137], to self-assembly for tissue engineering [32, 138]. In the field of tissue engineering and regenerative medicine, an increasing focus has been laid on cultivating cells inside 3D scaffolds to stimulate and guide cell growth in an unidirectional manner. Many different functional tissues need unidirectional cell structures to sustain their functions [139], for example, cardiac cells for a heartbeat [140, 141], cartilage either for reinforcement or reduced friction [142–144], and nerve cells for axon growth [145]. To support the formation of these unilateral structures, directional scaffolds can be used [11, 146]. Multiple approaches are possible to create such scaffolds, like using electrospun fibers [147, 148], structured hydrogels [149–151], or introducing magnetic properties into hydrogels or anisometric microgels inside Anisogels [19, 152]. The use of magnetic fields enables spatial manipulation of material building blocks after injection, artificially recreating the aligned extracellular matrix (ECM) naturally surrounding the cells [19, 37, 147, 148, 152].

Microgels are often proposed to be self-assembled into scaffolds in a bottom-up manner [147, 148, 153]. They consist of cross-linked polymer networks from nano- to micrometer size with a wide range of properties [13].

Depending on the used monomers or precursor molecules, cross-linking density, or possible filler materials, microgels can be softer or stiffer [13], stimuli-responsive [13, 19, 152, 154–156], and more or less permeable [157]. This diversity of controllable properties makes them an attractive choice for biotechnology applications, as they can be fine-tuned to deliver or capture certain molecules or mimic the cell environment [158].

Previous works have already shown the use of microgel building blocks to grow cells inside [159, 160], on the surface, or in between interlinked [161–164] or magnetically aligned microgels [18]. On the one hand, the rod shape of the microgels mimics the natural ECM filaments and allows for bigger and interconnected pores in the scaffold compared to materials consisting of spherical particles [18, 37, 82, 165]. On the other hand, magnetically aligned rod-shaped microgels can be immobilized inside a surrounding hydrogel, resulting in linear fibroblast and nerve growth both *ex vivo* [147, 148] and *in vivo* [37, 82]. The microgels are prepared via an in-mold polymerization technique based on particle replication in a non-wetting template (PRINT) from polyethylene glycol (PEG) mixed with superparamagnetic iron oxide nanoparticles (SPION) as a reactive filler [19, 37, 82, 152]. As SPIONs are superparamagnetic nanoparticles with a rotatable magnetic moment, the anisometry of the microgel rods, in combination with the interaction of the SPIONs, allows for the orientation of the rod-shaped microgels with their long axis along an external magnetic field, depending on their size and stiffness, the number of embedded SPIONs, the magnetic field strength, and the viscosity of the surrounding fluid [37, 82]. An additional advantage of these small microgels is their injectability, which enables bottom-up assembling after entering the body. However, so far, the applicability of this system is limited by the fact that microgel rods with SPION can only be oriented parallel to the magnetic field, while the design of more advanced tissues like cartilage [142–144] may require additional control over the orientation at different angles that could be achieved by mixing different-programmed microgels. Therefore, microgels, whose angle of alignment can be magnetically pre-programmed, can further provide new opportunities to structure biomaterial systems hierarchically.

In this chapter¹, ellipsoidal maghemite nanoparticles are employed to introduce variable magnetic properties into anisotropic magnetic microgels. α -Fe₂O₃ hematite nanoparticles were first converted into γ -Fe₂O₃ maghemite nanoparticles with ferrimagnetic properties at room temperature with a fixed magnetic moment oriented along their long axis [10]. Applying an external magnetic field onto these nanoparticles, they align themselves along the magnetic field. At a sufficiently strong magnetic field, the nanoparticles further form dipolar chains [10]. To integrate a specific magnetic moment into the microgels, the ellipsoidal nanoparticles are pre-aligned by applying a homogeneous magnetic field during the PRINT micro-fabrication of the microgels, as summarized in Figure 6.2. Herein, we report that the orientation and response of the microgels to the magnetic field can be efficiently controlled depending on the pre-alignment conditions of the ellipsoidal maghemite nanoparticles. The integration of the nanoparticles was investigated via scanning electron microscopy (SEM). The dynamic magnetic response of the rod-shaped PRINT microgels was analyzed based on their response to a rotating homogeneous magnetic field. Therefore, we adapted a bright field microscope with a custom-designed piezoelectric rotating stage fitted with circular Halbach arrays of different field strengths. Having demonstrated that the composite microgels could align parallel or perpendicular to the applied field, their applicability for tissue engineering was further tested under static and rotating magnetic fields. Hereby, the directional growth of fibroblasts within Anisogels is investigated, where 3D constructs containing a mixture of pre-programmed microgels with a parallel and perpendicular orientation lead to cell alignment in both directions.

¹This chapter is adapted with permission from Braunmiller, D. L., Babu, S., Gehlen, D. B., Seuß, M., Haraszti, T., Falkenstein, A., Eigen, J., De Laporte, L., & Cras-sous, J. J. Pre-Programmed Rod-Shaped Microgels to Create Multi-Directional Anisogels for 3D Tissue Engineering. *Advanced Functional Materials* **2022**, 32(50), 2202430. <https://doi.org/10.1002/adfm.202202430>. The experiments were designed by me and the other authors. I prepared and characterized the nanoparticles with the help of Andreas Falkenstein for the TGA experiments. The microgels were prepared by Susan Babu, David Gehlen, and Max Seuß, and the SEM images were recorded by Julian Eigen and analyzed by me. The Matlab and ImageJ routine I used to analyze the rotation of rod-shaped microgels was written by myself based on ImageJ plugins. Susan Babu conducted the preparation of the Anisogel and the cell culture experiments. Haraszti developed a code and performed the orientation analysis of cells and microgels in images of Anisogels. I wrote the manuscript jointly with Susan Babu, who focused on the parts concerning Anisogels. The manuscript was revised and corrected by all co-authors.

6.2 Experimental Section

6.2.1 Synthesis of the Ellipsoidal Magnetic Nanoparticles

The ellipsoidal maghemite nanoparticles were prepared by converting silica-coated hematite ellipsoids (SCH) to maghemite and dissolving the silica shell. The conversion was done in a SETSYS 16/18 thermobalance in a N_2/H_2 - and N_2/O_2 -atmosphere, respectively. The preparation of the maghemite nanoparticles is described in detail in Chapter 4. The SCH1 nanoparticles used in this work were freeze-dried before conversion to maghemite.

6.2.2 Preparation of Magnetic Rod-Shaped Microgels

The rod-shaped magnetic microgels discussed in this chapter were created using particle replication in a non-wetting template (PRINT, Figure 6.2). To fabricate the microgels, a precursor solution containing 20 μ l of PEG-DA (700 Da) along with a photoinitiator (Irgacure D 2959, 1 mol%), a fluorescent dye (methacryloxyethyl thiocarbamoyl rhodamine B, 0.5 wt%), and 80 μ l of ellipsoidal maghemite nanoparticles dispersed in PEG-OH (200 Da, 4.5 mg mL⁻¹) was applied to a PDMS template containing $5 \times 5 \times 50 \mu\text{m}^3$ molds and covered with PET film. The total concentration of PEG-DA in the precursor solution was 20 wt%. The excess of the precursor solution was removed by carefully lifting this film. The PEG-DA polymer chains were UV-cross-linked in a nitrogen atmosphere for one hour. For the microgel cross-linking, a 254 nm UV light was used at an intensity of 2.6 mW cm⁻². During the cross-linking time, a Halbach array was used to apply a magnetic field of 10 mT to pre-align the maghemite nanoparticles. The direction of the magnetic field was changed depending on the preferred alignment of the nanoparticles. For samples without pre-alignment, ellipsoidal nanoparticles were mixed into the precursor solution, but no field was applied. To harvest the microgel rods, a water-soluble poly(vinylpyrrolidone) adhesive was used to glue the PDMS molds with microgels to a glass slide, after which they were dried for four days at room temperature. Afterward, the microgel rods were removed from the glass slide after washing with water and purified through centrifugation and redispersion in water. The nanoparticle content of the microgels, determined by the ratio of maghemite to PEG-DA, was around 1.6 wt%. For control experiments, SPIONs (EMG 700, Ferrotec) were used to fabricate microgels in the same manner as those containing anisotropic nanoparticles.

6.2.3 Scanning Electron Microscopy

The samples were prepared by drying 20 μL of the batch on freshly cleaned silica wafers at room conditions. The wafers were sonicated for 15 minutes in isopropanol and were cleaned in air plasma for 15 minutes afterward. For investigations of the influence of a magnetic field, the drying process was conducted inside differently strong Halbach arrays. SEM measurements were performed using a JSM-7800F field emission scanning electron microscope (Jeol) for secondary electron (SE) micrographs and backscatter detector (BSD) micrographs. Acceleration voltages were varied from 5 – 15 keV depending on the desired penetration depth.

6.2.4 Magnetic Response Experiments

To study the magnetic response of the magnetic microgels, a Zeiss Axio-scope modified with a rotational stage driven by a piezoelectric engine PI-Line U651.03 (Figure 6.1) was used.

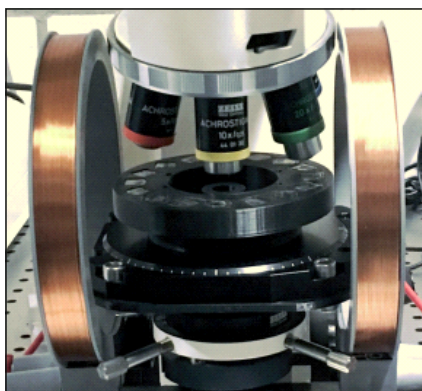


FIGURE 6.1: Experimental setup for experiments with magnetic fields consisting of a bright-field microscope equipped with a rotating stage holding a Halbach array. Alternatively, the Helmholtz coils can be used to apply weak static magnetic fields.

The magnetic field was applied by circular Halbach arrays (Figure A.3) consisting of different numbers and sizes of neodymium magnets. They can be mounted onto the stage to apply rotating or oscillating magnetic fields of varying field strengths (1 – 70 mT) and rotation frequencies (0.1 – 90 rpm). The microscope can also be fitted with two Helmholtz Coils, creating a

weak, static, homogenous field of 0 to 5 mT. For the experiments in cross-polarization, two linear polarizers were mounted before and after the sample with a 90° offset to ensure complete extinction of the transmitted light (Figure A.4).

The experiments involving dynamic control of the microgel rods were conducted using the magnetic setup described above. Glass slides were cleaned with isopropanol in an ultrasonic bath for 15 minutes and then treated with air plasma for 15 minutes. The sample was sealed within Secure-Seal spacers with wells of a diameter of 9 mm and a height of 0.12 mm and was directly placed inside the center of a Halbach array, and thereby, the microgel rods were oriented without letting them sediment to the glass surface. Consecutively, the magnetic field direction was changed by rotating the stage by 90° with a speed of 90 rpm. The microgels were recorded while re-orienting to the new field direction. With image analysis, the angular change of the rods is evaluated. The tracking of the rotation of the microgels is performed with ImageJ [130].

For experiments performed under a rotating magnetic field, the response experiments were conducted on rods next to a glass surface as the microgels sediment relatively fast. For each field strength and rotation frequency, a video of 3600 frames was recorded while rotating the magnetic field. The framerate was selected to correlate to the rotation frequency, resulting in one frame corresponding to 1° of rotation of the magnetic field. With image analysis (ImageJ), the angular change of the rods was evaluated, and the mean squared angular displacement was calculated. Tracking the microgels' rotation was performed with the 'Analyse Particles' function of ImageJ [130], and the Matlab routine was written for the computation and analysis of the mean squared angular displacement as described above.

6.2.5 Cell Culture in Anisogels

To prepare the Anisogel matrices, the MMGs were dispersed in an enzymatically cross-linked PEG hydrogel. The eight-arm star PEG-vinyl sulfones (sPEG-VS, 20 kDa) were conjugated with either a transglutaminase substrate (H-NQEQVSPLERCG-NH₂: Q-peptide) or a free primary amine (Ac-FKGGGPQGIWGQERCG-NH₂: K-peptide). The K-peptide can be degraded by cells due to a matrix metalloprotease (MMP) degradable sequence GPQG↓IWGQ. This allows cells to grow inside the Anisogel. The enzymatic

cross-linking of these conjugates was achieved by adding activated transglutaminase Factor XIII (FXIIIa) enzyme in the presence of a calcium buffer. The protocol for synthesizing star-PEG conjugates and activating Factor XIII was described in detail elsewhere [166].

The total concentration of peptide-functionalized PEG precursors in the Anisogel precursor solution was 1 wt/vol%. The two kinds of PEG-peptide conjugates were added at an equimolar concentration. The complex viscosity of the PEG precursor solution was measured to be 0.39 Pa s with a DHR3 Hybrid Rheometer (TA Instruments) using a 2° cone plate geometry with a diameter of 20 mm.

The encapsulation of pre-aligned microgel rods in a 3D hydrogel to form an Anisogel was achieved by first dispersing the microgels, along with L929 mouse fibroblast cells, in a cell culture medium (RPMI 1640, Gibco). A hydrogel precursor solution was then prepared by the addition of a 10X buffer (0.1 M CaCl₂, 0.5 M Tris, 1.1 M NaCl) and star-PEG conjugates of activated factor XIII substrate peptides to this dispersion [166]. The microgels constitute 1% of the total hydrogel volume in each of the parallel or perpendicular pre-programmed samples. In the condition where both types of microgels were present, as well as the control condition with microgels in the absence of a magnetic field, the total microgel concentration was 2 vol%. The cell concentration was kept at 700 cells μL^{-1} of the hydrogel. To enable cell attachment, a solution of Fibronectin (Sigma–Aldrich) in water was added to the precursor to achieve a final protein concentration of 1 μM in the hydrogel. To this precursor, an activated enzyme Factor XIII (CSL Behring GmbH, 1250 U FXIII) was added at a concentration of 50 U mL^{-1} . The precursor solution was then mixed well to disperse the microgels and cells homogeneously, and 10 μL of this solution was pipetted into each well of an Angiogenesis chamber (Ibidi) in the presence of a magnetic field (100 mT). The dispersion was then allowed to cross-link for 30 min at 37 °C in an incubator, with the magnets in place, while flipping the chamber back and forth every 5 min to prevent the settlement of microgels. After the gels were fully cross-linked, the magnets were removed, and 50 μL of RPMI medium was added to each of the wells.

The cells were cultured for four days with a media change done after every other day. After four days, the samples were washed three times using PBS for 30 min and then fixed using 4% paraformaldehyde for one hour with gentle shaking. After that, the samples were washed three times with PBS again,

and cells were permeabilized by incubation with 0.1% Triton X-100 solution for 30 min. After further washing with PBS, the cells were blocked with 4% bovine serum albumin solution for four hours. This was followed by the incubation with a conjugated primary antibody phalloidin 488 (Abcam 1:1000) overnight at 4 °C to visualize the actin filaments in cells. After washing three times with PBS, the samples were incubated with DAPI (1:1000). The samples were subsequently cleared three times with PBS and stored at 4°C. As control experiments, PEG hydrogels without a magnetic field and one without any microgels were prepared, showing a random distribution of microgels and cells, respectively.

For the experiments on Anisogels using a combination of rotating and static magnetic fields, a 50/50 mixture of microgel with a parallel and perpendicular orientation with a total concentration of 1 wt% was employed. The activated enzyme Factor XIII concentration was reduced to 10 U mL⁻¹ to slow down the cross-linking kinetics. A PDMS well was made by punching out holes using a 3.5 mm biopsy punch and sticking them on an Ibidi dish bottom using autoclaved vacuum grease. 10 µL of the precursor solution was deposited inside an already rotating magnetic field (10 rpm, 70 mT). After 4 minutes, the engine was stopped, and the gelation was allowed to proceed in the static field for 6 minutes. The Anisogel was fully cross-linked after 10 min. 3 mL of RPMI media were added to the petri dish for culture, which went on for four days.

6.2.6 Confocal Microscopy

The confocal microscopy images were captured using a Leica TCS SP8 confocal laser scanning microscope. The DAPI channel was visualized at a wavelength of 405 nm, the Phalloidin channel at 488 nm, and the microgels dyed with Rhodamine at 561 nm. Emission was detected using HyD detectors for DAPI and microgels, as well as PMT detectors for Phalloidin. A 100 µm thick z-stack was taken using a 10X dry objective from each sample, with four samples imaged per condition. The z-stacks were combined in ImageJ to create a single image per channel using the maximum intensity projection function. These projected images were processed in ImageJ to isolate the microgel signals by subtracting the Phalloidin signals from the Rhodamine channel. The resulting projected images of the microgel and actin channels were then separately analyzed for their orientation distribution.

The orientation of Anisogel and cell structures are analyzed using a highly elliptic 'Mexican hat' filter rotated to 20 angle values ζ between 0 and 180 degrees. The images undergo background subtraction using a normalized Gaussian (with a width of 10 pixels and a window size of 81 pixels) blurr. Negative pixel values were set to 0 and smoothed by applying a normalized Gaussian kernel filter with a width of 1.0 pixels (for microgels) or 1.5 pixels (for actin) and an 11-pixel window size. If the dynamic range of the image stack is high, the range is compressed by applying a $\frac{1}{2}$ power law to the intensity values (square root) before further processing. The applied 'Mexican hat' filter has a width of 10 pixels along its long axis and 1 pixel along its short axis. The window size is 61 x 61 pixels. The kernel is the second derivative of a Gaussian in both directions. The resulting images are collected in a 3D stack, where the z-axis represents the orientation angles. A maximum projection is applied along the z-axis to identify the local maxima, and then the corresponding angle is identified for each pixel (angle image). A threshold (using Otsu's method) is applied to the collected maximum intensities to identify pixels that belong to objects vs. those that are background. Orientation histograms are calculated only from the angle values of object pixels. A minimum of four different samples per condition are analyzed for their cellular and microgel alignment. These histograms show the distribution curves of cellular and microgel orientations, normalized against their respective total number of counts, plotted using Origin 2018b software.

6.3 Results and Discussion

6.3.1 Ellipsoidal Maghemite Nanoparticles

The ellipsoidal maghemite nanoparticles used as anisotropic magnetic fillers are obtained from converting silica-coated hematite nanoparticles into maghemite. The nanoparticles are then redispersed by etching the silica shell under alkaline conditions. The synthesis of the particles, their conversion, and redispersion are detailed in Chapter 4. For this chapter, the microgel batch M1 was used with an average dimension of the long axis $d_{\text{pol}} = 260 \pm 29$ nm and short axis $d_{\text{eq}} = 51 \pm 6$ nm. The stability of the maghemite aqueous dispersion was tested by using dynamic light scattering. The measured diffusion coefficient was compared to the expected value calculated based on the dimensions determined from the TEM analysis as proposed by Martchenko et al. (Equation 4.4 - 4.6) [31]. The apparent isotropic diffusion of $3.65 \mu\text{m}^2 \text{s}^{-1}$ at 25 °C (DLS) is in a close match with the calculated value of $3.73 \mu\text{m}^2 \text{s}^{-1}$ indicating for the proper dispersion of the maghemite. In literature, the magnetic moment of the ellipsoidal maghemite nanoparticles is assumed to point along the long axis [10]. It has been shown that comparable magnetite nanoparticles exhibit a strong magnetic response and can form highly ordered dipolar chains at low magnetic fields in the range of 150 mT [118]. As shown in the previous chapter, even a weak field of 1 mT leads to some chain formation. For higher B , nearly all nanoparticles assemble into dipolar chains, forming a complex dipolar chain structure with nanoparticles stacking side-to-side as well as tip-to-tip. At 10 mT, the nanoparticles inside the chains are mainly oriented parallel to the chain; therefore, this field strength is used to prepare the microgels in this chapter.

6.3.2 Preparation and Characterization of the Magnetic Microgel Rods via PRINT

The rod-shaped magnetic microgels are produced using PRINT, as schematically summarized in Figure 6.2. A PDMS template containing $5 \times 5 \times 50 \mu\text{m}^3$ cavities is filled with a precursor solution containing the ellipsoidal maghemite nanoparticles and linear polyethylene glycol diacrylate (PEG-DA) polymer chains. While applying a magnetic field of 10 mT on the template using a Halbach array, the PEG-DA polymer chains are UV-crosslinked. The direction of the magnetic field is set depending on the preferred alignment of the

nanoparticles. As a reference, microgels without pre-alignment are prepared by incorporating ellipsoidal nanoparticles, not applying a magnetic field during UV-curing. The nanoparticle content of the microgels, determined by the ratio of the maghemite content to polyethylene glycol diacrylate (PEG-DA), is 1.6 wt%. To harvest the microgel rods, a water-soluble adhesive was used to remove the microgels from the molds.

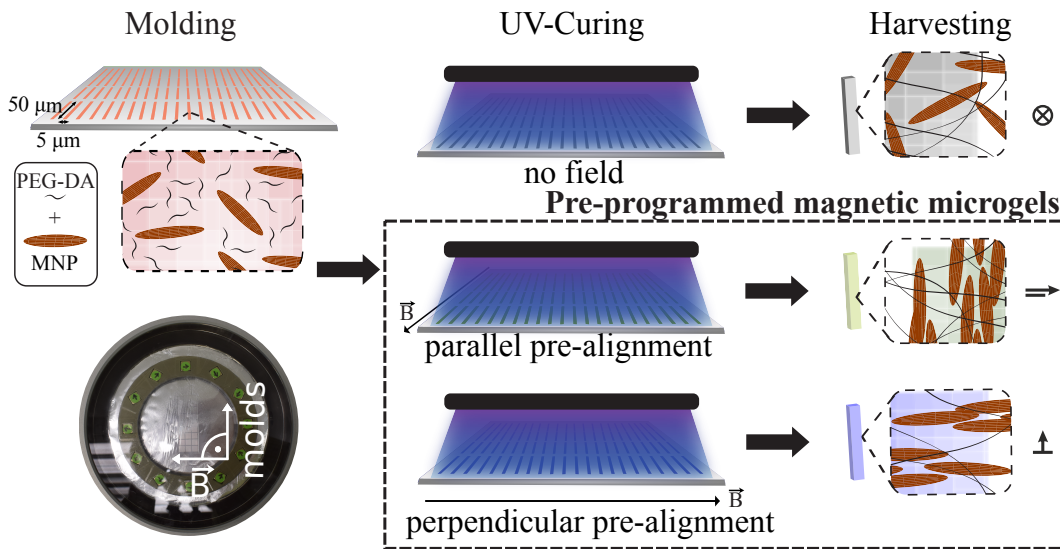


FIGURE 6.2: Fabrication of magnetic rod-shaped composite microgels via PRINT with different pre-alignment of the ellipsoidal nanoparticles. Step 1 - Molding: PDMS molds with micron-sized cavities, shown in the center of the photograph, are filled with the precursor solution containing PEG-DA, maghemite nanoparticles, and photoinitiator. Step 2 - UV-Curing: The dispersion is then cured with UV in the absence or presence of a homogeneous magnetic field set by a Halbach array (see photograph) applied either parallel or perpendicular to the rods' long axis. Step 3 - Harvesting: Following the pre-alignment conditions, three distinct systems are obtained after harvesting the cured composite microgel rods: "no field" microgels and parallel and perpendicular pre-programmed microgels.

To ensure the successful incorporation of the anisotropic magnetic nanoparticles into the PRINT microgels, SEM measurements were conducted. In the micrographs of the rod-shaped MMGs (Figure 6.3 A - F), the incorporated nanoparticles can clearly be seen, at least the ones close to the surface as the measurements were conducted in the dry state. Inside microgel rods prepared without a magnetic field (Figure 6.3 A, D), the nanoparticles are randomly distributed within the polymer network. For the MMGs cured under an applied magnetic field, the measurements (Figure 6.3 B, C, E, F) indicate that the weak magnetic field with a strength of 10 mT leads to dipolar chain formation in the direction of the magnetic field and therefore

a pre-alignment of the MNPs. A parallel field orientation to the long axis of the molds leads to dipolar chains following the entire length of the microgels (Figure 6.3 B, E), with the nanoparticles being mostly aligned with the magnetic field.

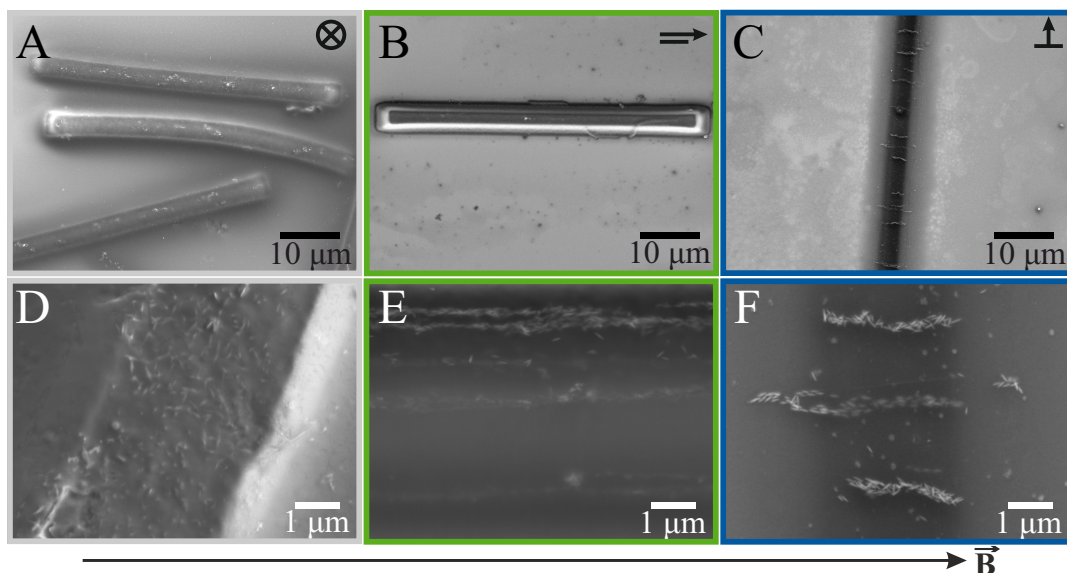


FIGURE 6.3: A - F) SEM micrographs of microgel rods with incorporated ellipsoidal maghemite nanoparticles. A, D) In the absence of magnetic pre-alignment, the nanoparticles are randomly distributed inside the microgels. The microgel rods with maghemites pre-aligned with a 10 mT magnetic field exhibit dipolar chains oriented either B, E) parallel or C, F) perpendicular to the microgel rod's long axis, depending on the synthesis conditions.

The perpendicular pre-alignment of the MNPs results in shorter dipolar chains perpendicular to the long axis of the rods (Figure 6.3 C, F). The length of the chains is determined by the mold size in the respective direction. The magnetic moment of the prepared microgel rods corresponds to the direction of the alignment of the dipolar chains. As these images were taken after removing the magnets, it confirms that the ellipsoidal maghemite nanoparticles and their assemblies into dipolar chains are fully integrated inside the cross-linked microgels. No significant disassembly of chains and nanoparticles inside the microgels was observed.

6.3.3 Static Control

The incorporation of ellipsoidal maghemite nanoparticles allows us to add variable magnetic properties to the microgels. Previous magnetic rod-shaped microgels with SPIONs as magnetic fillers only orient in one direction to the

magnetic field [19, 37, 82, 152], while the ellipsoidal nanoparticles enable the pre-programming of different orientations to the field (Figure 6.4). The dipolar chains formed by the maghemite nanoparticles align themselves along the magnetic field during PRINT fabrication and are fixed due to microgel cross-linking. Through this pre-alignment, the magnetic moment of the microgels can be pre-programmed.

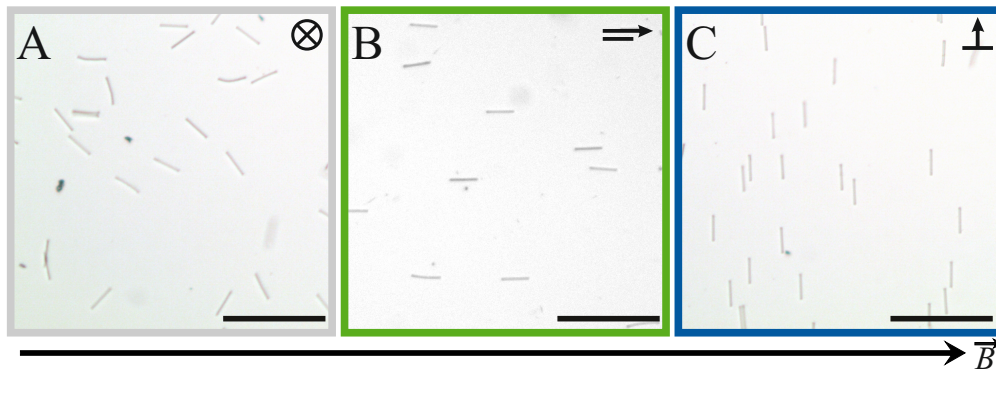


FIGURE 6.4: A - C) Magnetic microgel rods under a static horizontal magnetic field of 70 mT, with A) random, B) parallel and C) perpendicular pre-aligned nanoparticles. The pre-alignment of the nanoparticles determines the orientation of the rods in the magnetic field. Without pre-alignment, there is no uniform orientation. Scale bars = 200 μ m.

Without applying a magnetic pre-alignment during the PRINT synthesis (Figure 6.4 A), the microgel rods exhibit a random orientation to the applied static external magnetic field. The microgels containing maghemite nanoparticles pre-aligned parallel to the long axis of the microgel orient themselves parallel to the magnetic field (Figure 6.4 B). In contrast, a perpendicular pre-alignment leads to perpendicular microgel orientation (Figure 6.4 C). Following these results, we expect that any angle of alignment could be pre-programmed during the PRINT synthesis, leading to more or less defined microgel orientations.

While in water, dispersed SPIONs form strings along the magnetic field lines when exposed to a magnetic field of 10 mT and above (Figure A.8 A); it is unclear if these chains exhibit a combined magnetic moment along the direction of the strings. The individual SPIONs have a rotating magnetic moment in contrast to the fixed magnetic moment of the maghemite ellipsoids. Therefore, the resulting SPION-based microgels are magneto-responsive and orient parallel to a magnetic field [18]. While this property is retained for the microgels with pre-aligned SPIONs parallel or perpendicular to the long

axis of the microgel, the orientation of the magnetic microgels cannot be pre-programmed like with the ellipsoidal maghemite nanoparticles (Figure 6.5). This indicates that the SPION strings, as opposed to the maghemite dipolar chains, do not exhibit a fixed magnetic moment in the direction of their anisotropy.

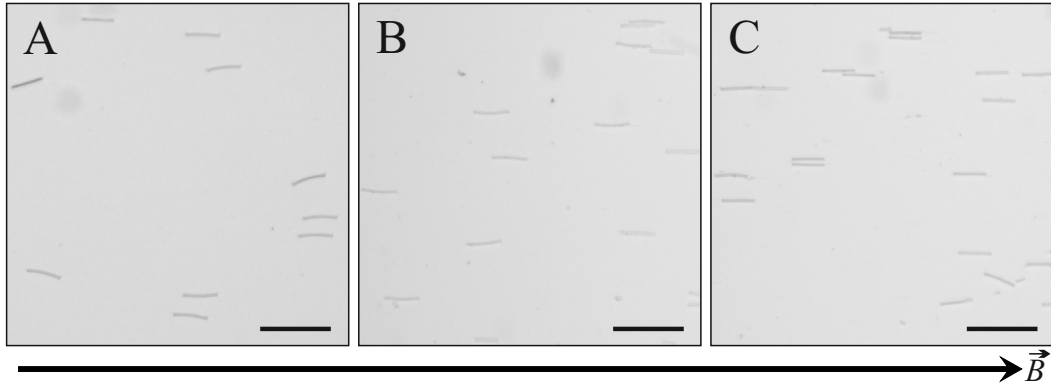


FIGURE 6.5: Magnetic microgel rods with incorporated SPIONs exposed to a static horizontal magnetic field of 70 mT. The pre-alignment field orientations are different: A) without, B) parallel, and C) perpendicular. These pre-alignment field orientations do not influence the orientation of the microgel rods. Scale bars = 100 μm .

6.3.4 Dynamic Control

In addition to controlling the static orientation of the MMGs, we can also manage how rod-shaped microgels respond to a dynamic magnetic field. When a ferromagnetic rod is immersed in a Newtonian liquid and subjected to a rotating magnetic field, its rotation is influenced by the viscous and magnetic torques acting on it. For a magnetic field B with a magnetic moment μ rotating at a constant angular frequency ω_{MF} , the corresponding equation of motion is the following [73],

$$\gamma \left(\omega_{MF} - \frac{d\alpha}{dt} \right) = \mu B \cdot \sin \alpha \quad (6.1)$$

where γ corresponds to the rotational drag coefficient, and α describes the angle between the direction of the magnetic field and the magnetic moment of the rod. When the magnetic torque dominates, the magnetic field and the rod rotate synchronously, and α remains constant. When the viscous torque dominates, α changes periodically, and the rod tumbles. The transition between

the synchronous and asynchronous regimes is determined by the critical angular frequency ω_c defined as [73]

$$\omega_c = \frac{\mu \cdot B}{\gamma} \quad (6.2)$$

ω_c increases with the magnetic moment μ of the microgels and the magnetic field strength B and is reduced for higher drag forces (drag coefficient γ). To characterize the magnetic response of the microgel rods, we performed different analyses under a dynamic magnetic field. At first, the microgel rods were oriented under a static magnetic field (70 mT) and consecutively forced to re-orient by swiftly changing the direction of the field by 90° at 90 rpm. The microgels change their orientation in response to the changed orientation of the magnetic field. On average, the microgels with pre-aligned maghemite nanoparticles inside change their orientation within 2 - 7 s (Figure 6.6).

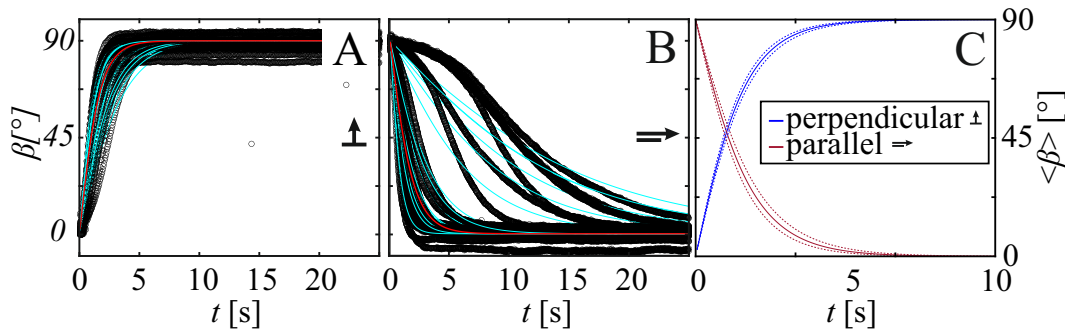


FIGURE 6.6: Time-resolved relaxation curves after a 90° shift of the magnetic field for microgels with A) perpendicular and B) parallel pre-alignment. The individual fits are indicated by the cyan lines, while the red lines indicate the mean fit derived from the fit parameters. C) Relaxation of the magnetic microgels after a quick rotation of the magnetic field by 90° . Displayed are mean curves derived from the relaxation curves of multiple microgels. The dashed lines indicate the standard errors.

The perpendicular pre-alignment leads to a slightly faster relaxation than the parallel one, but most of the microgels of both batches re-orient within this period. Furthermore, it should be noted that neither before nor after the field shift, all of the rods are perfectly oriented along the magnetic field but vary by a few degrees around the field directions. This also applied to both pre-alignment directions. The angular change of circa 30 microgels per batch was tracked. Depending on the pre-alignment, the orientation of the microgel rods defined by the angle $\beta(t)$ varies from 0 to 90° (parallel) or 90° to 0° (perpendicular). Using Equation 6.1 and 6.2, we derived the

following equations for the relaxation experiments:

- 90° to 0° (perpendicular pre-alignment):

$$\beta(t) = 2 \cdot \arctan(e^{-\omega_c \cdot t}) \quad (6.3)$$

- 0° to 90° (parallel pre-alignment):

$$\beta(t) = \frac{\pi}{2} - 2 \cdot \arctan(e^{-\omega_c \cdot t}) \quad (6.4)$$

The response of the individual microgels was fitted by the Equations 6.3 and 6.4 respectively, as shown in Figure 6.6. The mean value of ω_c determined from this analysis was 0.80 ± 0.08 and 0.91 ± 0.05 rad s⁻¹ for the parallel and perpendicular pre-alignment, respectively. The resulting relaxation curves using the average ω_c and Equations 6.3 and 6.4 are shown in Figure 6.6 C. Microgels without pre-aligned maghemite nanoparticles show no significant orientation change during this experiment; only a small angular change in the direction of the rotating magnetic field was observed. As shown in Figure 6.4 A, these rods do not orient uniformly under a static magnetic field, and the small rotational movement indicates that the rods still have a weak response to a changing rotating field. The relaxation experiments were also conducted on microgels with incorporated randomly distributed SPIONs. The rods show a wide range of relaxation times, but the mean reorientation time for those microgels is around 10 s, which is around twice as long as parallel maghemite microgel rods of a comparable size, shape, and nanoparticle content (Figure A.8). The relaxation experiments were analyzed considering paramagnetic rods; in this case, the following equation of motion applies [73]:

$$-\frac{d\alpha}{dt} = \omega_c \cdot \sin 2\alpha \quad (6.5)$$

Solving this equation, we obtain the following relation to describe the evolution of $\beta(t)$:

$$\beta(t) = \arctan(e^{-2\omega_c \cdot t - c_1}) \quad (6.6)$$

These show a slower relaxation process than pre-aligned maghemite microgels and have a mean ω_c of 0.40 ± 0.06 rad s⁻¹ (Figure A.8).

To determine the magnetization and the critical rotation frequency of the different magnetic microgels, experiments with a continuously rotating magnetic field were performed (Figure 6.7).

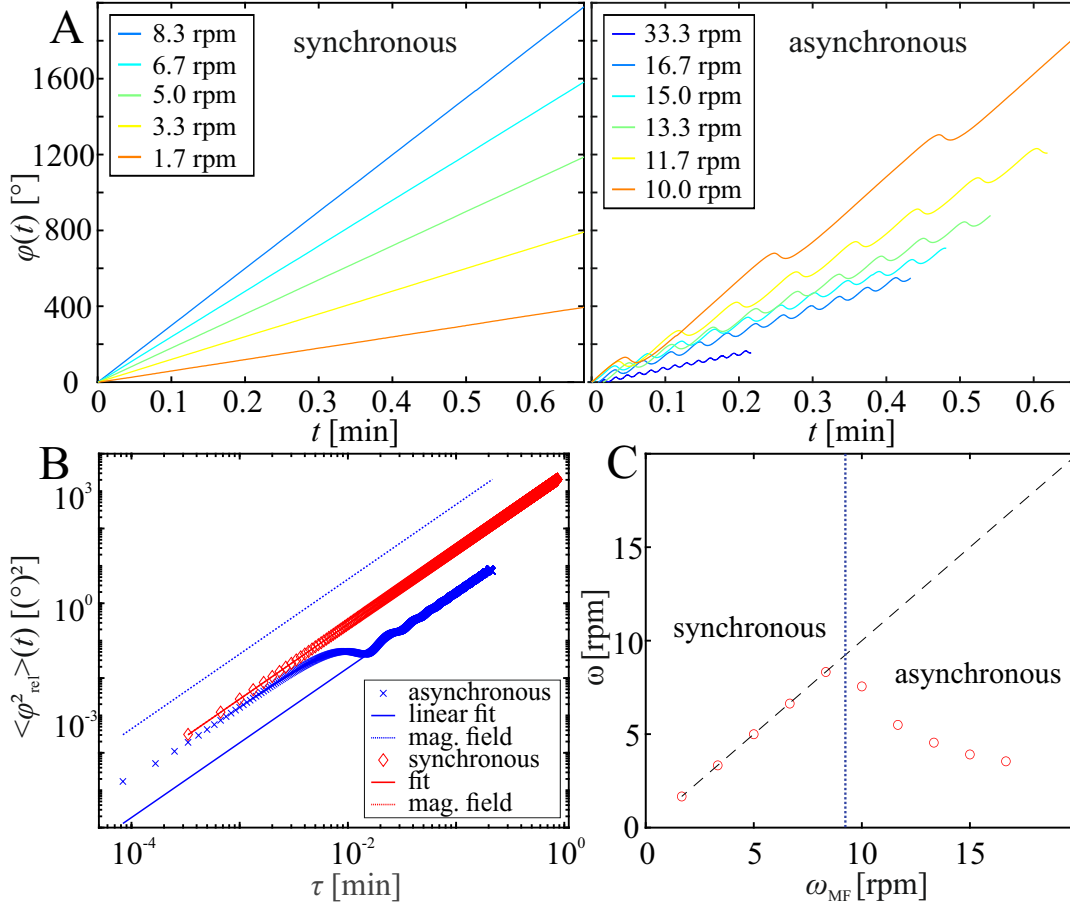


FIGURE 6.7: A) Cumulative angular displacement measured on a microgel with parallel magnetic pre-alignment at different field rotation frequencies ω_{MF} with a field of 70 mT within the synchronous (left) and asynchronous (right) regimes. B) An exemplary plot of the mean angular displacement for a rod rotating synchronously (red circles) and asynchronously (blue crosses). The solid lines correspond to the long-time average rotation frequency ω , while the dotted lines represent ω_{MF} . C) An exemplary plot of the dependence of ω on ω_{MF} (red circles) determined on one single microgel rod at 70 mT. Two rotation regimes can be identified: a synchronous rotation with $\omega = \omega_{MF}$ (dashed line) with a transition to an asynchronous rotation with $\omega < \omega_{MF}$ above ω_c (dotted line).

ω_c is the limit of the synchronous rotation regime, in which the rotation of motor and rod are synchronous but slightly offset [69, 73]. Above ω_c , in the asynchronous regime, the rods still show a rotational movement over long times, but due to the fast motor rotation frequency, they start to tumble. The synchronous rotation of the microgels is interrupted by a backward movement until the orientation of the pre-aligned maghemite chains corresponds

again with the orientation of the magnetic field. This results in an oscillating movement around the mean angular frequency. For the asynchronous regime, the cumulative angle change $\varphi(t)$ (Figure 6.7 A) shows oscillations with an increasing periodicity at higher ω_{MF} .

When the microgel rotation frequency ω increases in the synchronous regime with an increasing field rotation frequency ω_{MF} , for $\omega_{MF} > \omega_c$, ω decreases due to increasing tumbling. The long-time microgel rotation frequency ω can be calculated from the mean squared angular displacement $\langle \Delta\varphi^2 \rangle(\tau)$ for the synchronous and the asynchronous regime defined as

$$\langle \Delta\varphi^2 \rangle(\tau) = \langle |\varphi(t) - \varphi(t - \tau)|^2 \rangle \quad (6.7)$$

where τ refers to a specific time interval. Synchronous rotation of the microgel rods and the magnetic field orientation results in a linear dependence of $\langle \Delta\varphi^2 \rangle(\tau)$ against τ^2 (Figure 6.7 B). In the asynchronous regime, the periodicity of the tumbling motion correlates to the oscillation around the long-time rotation frequency of the microgels, represented by the dependence $\langle \Delta\varphi^2 \rangle(\tau) = \omega^2\tau^2$ at large τ in Figure 6.7 B (solid line). The fits in both regimes consider primarily longer τ for the determination of ω . While ω_{MF} (Figure 6.7 B, dotted lines) matches ω in the synchronous rotation regime, it deviates above the critical rotation frequency ω_c for the asynchronous regime. The critical rotation rate ω_c is experimentally determined from as the deviation point between ω_{MF} and ω (Figure 6.7 C, dotted line).

In order to establish the critical rotation frequency and the influence of pre-alignment, multiple experiments were conducted on three different microgel types at various values of B and ω_{MF} . The microgel rotation frequencies were determined using the method described above and by averaging more than 30 rods for each data point (Figure 6.8). Depending on the pre-alignment, the microgel rods respond differently. As established above, the microgels without a pre-alignment of the maghemite nanoparticles do not have a uniform orientation to a static magnetic field and only a minimal angular change when the magnet is quickly rotated by 90° . Interestingly, in a continuously rotating magnetic field, they can rotate with the field (Figure 6.8 A), but the different rods do not have a uniform orientation to the magnetic field, and the resulting rotation frequency does not depend on their orientation relative to the magnetic field. This corresponds to the absence of a

fixed magnetic moment. The rotation frequency ω of the microgels increases with increasing ω_{MF} and B . Although the rods do not show tumbling as an indication of the asynchronous regime, only rotation frequencies up to 1 rpm can be achieved when $\omega_{MF} > 1$ rpm for $B = 70$ mT. A more detailed understanding of the mechanisms has yet to be achieved. Similar to these results, an applied magnetic field strength of 6 to 36 mT leads to a maximum angular frequency of 0.1 rpm and 0.9 rpm, respectively. While there is a larger difference between 6 and 36 mT, the magnetic response is almost the same for 36 and 70 mT. This might indicate a magnetic saturation of the microgels at these field strengths.

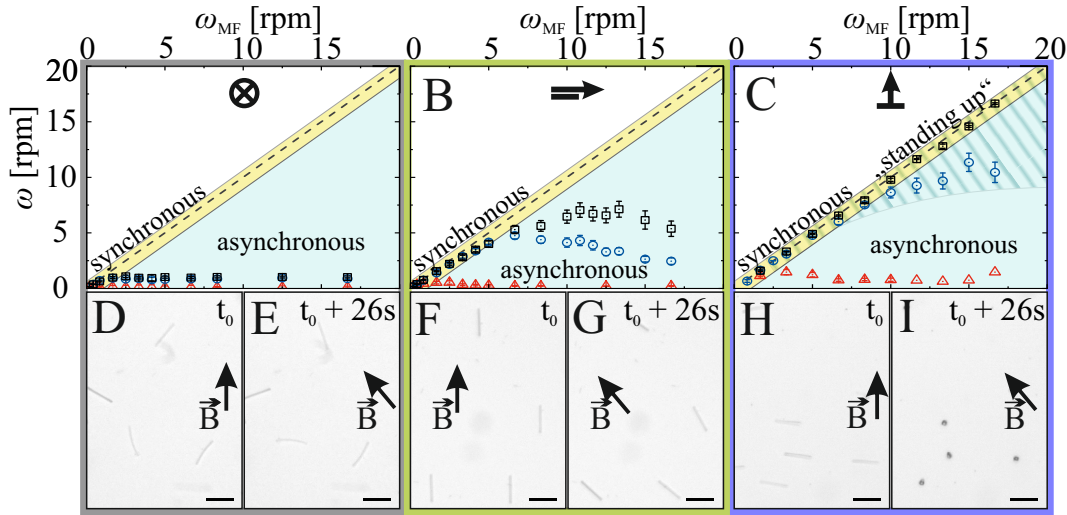


FIGURE 6.8: Resulting mean rotation frequencies ω of magnetic rod-shaped microgels determined for $B = 6$ mT (\triangle), 36 mT (\circ) and 70 mT (\square) for microgels A) without pre-alignment, B) parallel pre-alignment and C) perpendicular pre-alignment of the maghemite nanoparticles. Depending on the pre-alignment conditions, different rotation regimes can be observed at the different magnetic field strength B and rotation frequency ω_{MF} , i.e., the synchronous (blue areas) and asynchronous (yellow areas) regimes and an additional "standing up" regime in C) resulting from the dynamic reorientation orthogonal to the surface (hatched areas) starting at 3-4 rpm. D - I) Timestep snapshots of the different microgels, showing the non-uniform rotation (70 mT, 7 rpm; D, E) of microgels without pre-alignment, the uniform synchronous rotation with parallel pre-alignment (70 mT, 7 rpm; F, G), and the "standing up" of rods with perpendicular pre-alignment (70 mT, 15 rpm; H, I).

For microgel rods with a parallel pre-alignment, the magnetic response is significantly stronger than without a pre-alignment. The microgel rods show a synchronous or asynchronous rotation depending on ω_{MF} and B . For 36 and 70 mT, the rods mostly rotate synchronously up to 5 rpm

(0.5 rad s^{-1}), which is in reasonable agreement with the relaxation experiments ($\omega_c = 0.8 \text{ rad s}^{-1}$). With increasing ω_{MF} , the number of rods showing an asynchronous regime and the difference between ω and ω_{MF} increases. The influence of the field strength on the rotation frequency seems to be stronger in the asynchronous regime, as the rotation frequencies for 36 mT decrease faster with increasing ω_{MF} . For both field strengths, ω_c is in the order of 5 - 6 rpm, whereas for $B = 6 \text{ mT}$, it is lower than 1 rpm. The fact that ω_c is comparable at higher B is pointing once again to the saturation of the magnetic response. ω_c for 70 mT is significantly lower than with the relaxation experiments since the relaxation experiments are not conducted close to the glass and thus exhibit weaker frictional forces.

Rods with a perpendicular pre-alignment show a similar behavior up to $\omega_{MF} \approx 2 \text{ rpm}$ with the difference that for $B = 6 \text{ mT}$, the rods exhibit a stronger magnetic response than microgel rods with a parallel pre-alignment in agreement with our former observations on the relaxation experiments. At this field strength, the rods then start to rotate asynchronously. However, at higher B and ω_{MF} , we observe that the microgels rods start to "stand up". In contrast to rods with a parallel pre-alignment, which can only align the magnetic moment when positioned along the field, rods with a perpendicular pre-alignment simply require their long axis to be positioned perpendicular to the field. When deposited at the surface of the glass, it then results in the observed perpendicular alignment within the imaging plane under a static field. Upright rods rotating around the long axis exhibit a lower frictional torque than when they lay at the glass, which is one of the driving forces for them to stand up. The same observation was made when letting the rods sediment under a rotating magnetic field. It is interesting to note that such dynamic orientation behavior was already observed for hematite nanoparticles having a magnetic moment with their basal plane when subjected to a high-frequency alternating field [167]. Why they stand up from a flat conformation at the glass is still unclear and is the consequence of unbalanced forces exerted on the rotating rods. The latter may be related to hydrodynamic interactions with the surface of the glass and the slight bending of the rods. For $B = 70 \text{ mT}$, the rods rotate synchronously on the whole range of applied ω_{MF} with a transition from a planar rotation to an upwards rotation starting around 3 - 4 rpm, whereas for $B = 36 \text{ mT}$, a coexistence between a synchronous upward rotation and asynchronous planar rotation is observed at higher ω_{MF} . These results illustrate the importance of the pre-alignment

conditions to dynamically control the orientation of the microgel rods in the third dimension, offering extra control over their possible alignment.

6.3.5 Cell Culture in Anisogels

To explore the potential of these pre-aligned microgel rods in tissue engineering, Anisogels (soft hydrogels loaded with microgel particles) were prepared using microgels with maghemite particles aligned in parallel or perpendicular directions to the microgels' long axis as described in the Experimental Section. To prevent iron-cytotoxicity, a low concentration of nanoparticles is used inside each microgel, and the microgel content inside the Anisogels is only 1-2 vol%. Considering the precursor solution concentration in maghemite of 3.6 mg mL^{-1} , the maximum iron concentration is in the order of $72 \text{ } \mu\text{g mL}^{-1}$ for which a low cytotoxicity is expected [168–170]. Fibroblast cells were cultured in these Anisogels containing either parallelly or perpendicularly pre-programmed microgels or a combination of these two in equal amounts. As a control, cells were cultured in an Anisogel containing 2 vol% of randomly oriented microgels in the absence of an applied magnetic field. For each condition (Figure 6.9 A - D), at least four Anisogel samples were prepared.

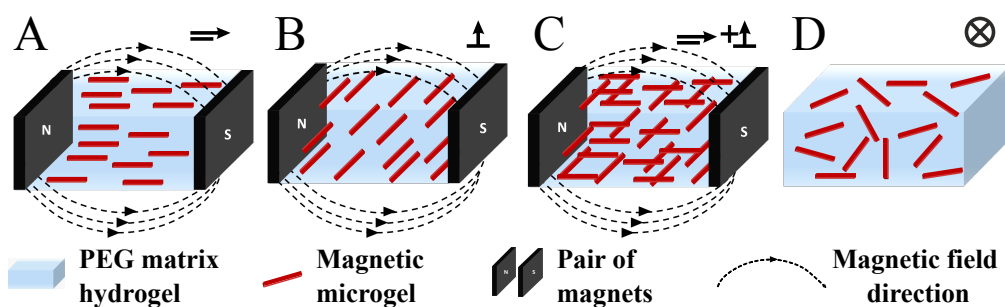


FIGURE 6.9: A - D) Schematics of Anisogels containing microgels pre-aligned in A) parallel, B) perpendicular, C) a combination of parallel and perpendicular directions, and D) a control hydrogel with randomly distributed microgels.

Cell growth was stopped and analyzed after four days with confocal microscopy (Figure 6.10). For this purpose, the microgels (red), cell nucleus (blue) and actin filaments (green) were fluorescently labeled. Figure 6.10 A - D presents 2D low magnification micrographs recorded for the different preparations, while Figure 6.10 E - H represents the corresponding 3D

reconstructions acquired at higher magnification. A closer look at the 3D reconstructions clearly confirmed that the microgels maintained their orientation within the Anisogels during the time of the culture (Figure 6.10 E - H). In all four Anisogel types, the cells grew equally well, and it can easily be seen from the low magnification micrographs that the orientation of cells in each preparation follows the microgel orientation. This first impression is verified by the analysis of the orientation of both microgels and cells, as shown in Figure 6.10 I - L.

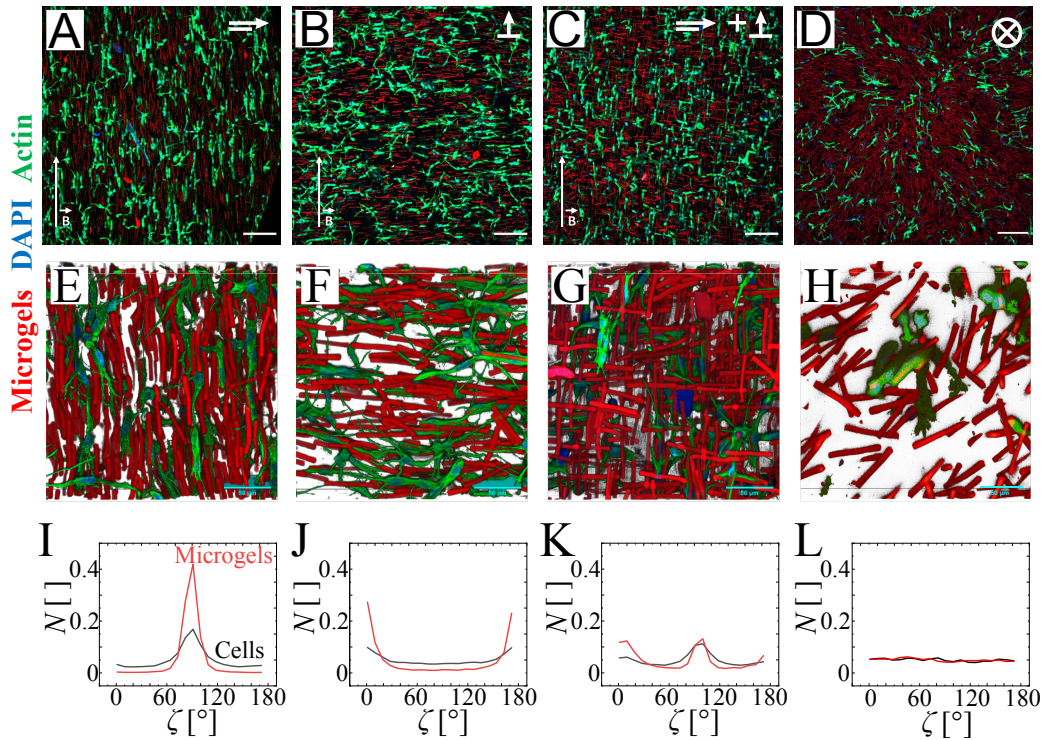


FIGURE 6.10: A - D) Confocal images of mouse fibroblast cells after four days of culture in the above Anisogel conditions. At least four samples were imaged per condition. Scale bars = 200 μm . E - H) 3D reconstructions of 50 μm thick stacks of the respective culture conditions were recorded at higher magnification. Scale bars = 50 μm . I - L) Plots of normalized angle distributions of cells and microgels in the different conditions, respectively, which prove that the cells grow in the direction(s) determined by the orientation of microgels present in the Anisogels.

The cells are sensitive to the anisotropy of the microgels and grow along the direction created by the Anisogel as opposed to the scenario in control samples (Figure 6.10 H, L), where the cells grow randomly in any direction (Figure 6.10 P). The randomly aligned microgels do not hinder cell growth. Instead, they allow cells to grow in all directions, similar to the control condition in the absence of microgels (see Figure A.9). This proves once

again the importance of microgel alignment in triggering an anisotropic cell response.

The Anisogels with parallel pre-aligned MNPs (Figure 6.10 A, E) exhibit a narrow distribution of their orientation (Figure 6.10 I), with cells consistently following the microgels' direction. Conversely, perpendicular alignment shows a less pronounced alignment for both microgels and cells (Figure 6.10 J). Indeed, these microgels could still rotate around their short axis during cross-linking of the surrounding matrix of the Anisogel, keeping their magnetic moment aligned to the field (Figure 6.10 B, F). Cells seem sensitive to this effect, and although they follow the orientation of the microgels, their orientation is less defined. The fact that most microgels appear to be mainly aligned parallel to the surface may be related to the influence of the substrate and the fact that the confocal micrographs are recorded 20 μm above the glass substrate. This additional degree of alignment can be considered an asset as it could allow the extension of the classical unidirectional cell growth observed in former Anisogels to planar growth.

For Figure 6.10 C,G,K), it is shown that the coexistence of both parallel and perpendicular pre-programmed microgels does not impede cell growth; instead, growth is dominant in both directions (Figure 6.10 O). This underscores the cells' ability to detect and respond to multiple directional cues within the same system, offering the potential for designing more complex tissue-engineered constructs.

Finally, by combining the dynamic experiments with the cell culture experiments, we were able to achieve the transition of a 2D scaffold into the 3rd dimension by subjecting a 50/50 mixture of perpendicularly and parallel pre-aligned microgels (1 vol%) to a rotating magnetic field (70 mT, 10 rpm) for 4 minutes followed by a static field for another 6 minutes during the gelation process (Figure 6.11 A). For these experiments, the concentration of the activation enzyme Factor XIII was decreased to slow down the gelation kinetics. The Anisogel was entirely arrested within 10 min. As a result of the rotating magnetic field, the perpendicularly pre-aligned microgels "stood up", pointing to the z-direction while the parallel microgels rotated in the xy-plane. After 4 minutes, the rotation of the magnetic field was stopped to allow the parallel pre-aligned microgels to orientate along the field, while the perpendicularly pre-aligned microgels maintained their upright configuration until the Anisogel was fully cross-linked after 10 min. The cells were allowed to grow

for 4 days and subsequently imaged by confocal fluorescence microscopy (Figure 6.11 B, C). While not all perpendicularly pre-aligned rods are perfectly upright, the two microgel orientations are clearly visible. It could also be seen that the cells grew in both directions, demonstrating the potential of our approach to create a 3D scaffold using a dynamic orientation control of the perpendicularly pre-aligned microgels and to realize assembly that could not be achieved with a simple static field.

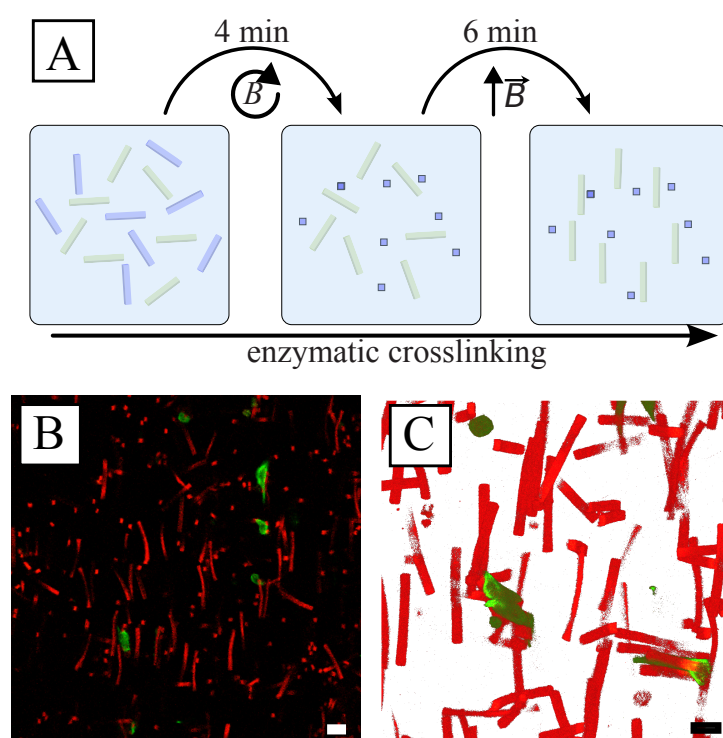


FIGURE 6.11: A) Schematics of the orientation of the microgel rods during the preparation of mixed Anisogels under the application of a rotating field (70 mT, 10 rpm) for 4 min leading to upright perpendicularly pre-aligned microgels (blue) and the subsequent orientation of the microgels with a parallel pre-alignment (green) along the field after the engine was stopped for 6 min until the end of the gelation. B) Confocal micrograph of the Anisogel after cell culture showing microgels alignment in the y- and z-directions (red) and the directional growth of fibroblasts (green). C) 3D reconstruction of 50 μm thick stacks recorded at a higher magnification. Scale bars = 30 μm .

To optimize the 3D microgel alignment, a systematic study of the gelation parameters is necessary, allowing for fine-tuning this process. In the future, a combination with 3D printing is envisioned for the creation of scaffolds able to recreate complex structures such as cartilage for which an upright configuration at the bottom and a planar configuration at the top is desired. In

vivo experiments have already demonstrated the in vivo applications of the Anisogels for spinal cord injuries with respect to their low cytotoxicity and fast gelation preventing dilution of the materials by body fluids [37]. The high magnetic susceptibility of the presented microgels allows their alignment at low magnetic fields that could be generated with electromagnets or Helmholtz coils.

6.4 Summary and Outlook

Having a high level of spatial control over biomaterial building blocks is crucial for building complex 3D scaffolds via a bottom-up approach. This chapter demonstrates that we can successfully incorporate ellipsoidal maghemite nanoparticles in a pre-aligned direction during PRINT. The pre-alignment enables us to pre-program the angle of orientation of anisometric magnetic microgels inside a static magnetic field and thus obtain microgels with a defined magnetic dipole. In contrast, previous rod-shaped microgels using paramagnetic SPIONs as magnetic fillers only orient parallel to the field lines, with or without SPION pre-alignment. Incorporating and pre-aligning ellipsoidal maghemite nanoparticles instead provide a higher degree of control over the orientation of the resulting magnetic microgel rods, depending on the predefined magnetic dipole orientation. Furthermore, the resulting microgels respond faster to a shifting magnetic field compared to SPION-loaded microgels with similar nanoparticle concentrations. Besides the static control of the orientation, we could demonstrate that the orientation can be altered dynamically by applying a rotating magnetic field, thereby extending the 2D orientation to the 3rd dimension. The presented magnetic rotational spectroscopy experiment provides a powerful tool to test the adhesive properties of the microgels with different substrates. Further on, the strategy developed for the synthesis of these ferromagnetic microgels can be extended to different materials, shapes and sizes for the design of multi-responsive actuators, devices and swimmers at the microscale bearing some potential for the design of therapeutic microbots for non-invasive surgical interventions [171]. For tissue engineering, mixtures of microgels with different polarizations were added inside an Anisogel, creating alignment in both parallel and perpendicular directions without hindering each other using static and dynamic orientation control. This led to cell alignment in both directions and opened the opportunity to orthogonally study multiple biochemicals and

mechanical and physical guiding cues in different directions and potentially selectively influence the growth of other cell types in co-culture. More significantly, static and dynamic control in combination with 3D printing may offer the possibility of quickly prototyping complex scaffolds with a stratified structure for functional tissue engineering.

Chapter 7

Complex-Shaped Magnetic Microgel Microactuators

7.1 Introduction

Metamaterials, a class of materials with anisotropic properties, have gained increased attention over the past years. These materials can go beyond a static function and provide a dynamic response over time by following a pre-programmed trajectory [172]. To achieve an architected structure, building blocks with diverse properties are integrated into a single unit or assembled in a superstructure, responding to diverse stimuli, comprising mechanical [173], optical [174], electrical [175] and magnetic responsiveness [176–179]. Aside from a static control over the position, these materials allow for spatio-temporal flow control. A whole new field of autonomous flow control was introduced through the pioneering work of Beebe et al. [180]. Previously published flow control devices range from pH-responsive hydrogel valves [180, 181] over guidable colloids [182, 183] to pumping approaches [70, 71, 184]. The ability to customize the materials is, therefore, of crucial importance.

In this respect, microgels are highly promising materials as they allow free-form fabrication and are highly tailorable in terms of mechanical and chemical properties and gradients thereof [13, 14, 185, 186]. Implementing magnetic responsiveness into microgels is of substantial interest, as the magnetic field can easily penetrate, e.g., tissue without adverse effects. As an example, the magnetic response of rod-shaped microgels can be used to remotely control their orientation during the scaffold build-up to guide cell growth [187]. Besides allowing the control of the structural assembly [19, 37], magnetic responsive building blocks are ultimately expected to provide the possibility to study mechanotransduction similar to light-responsive soft hydrogels [20].

Several examples of the incorporation of magnetic materials into hydrogels and microgels by various fabrication methods are reported in the literature. Anisometric magnetic microgels have been synthesized among other techniques by particle replication in a non-wetting template (PRINT) [19, 39, 187, 188], maskless lithography [189] and Stop-Flow Lithography (SFL) [190–192]. The incorporated magnetic materials are mainly based on iron oxide [193, 194], more precisely magnetite [188, 190] for example in the form of superparamagnetic iron oxide nanoparticles (SPIONs) [19], colloidal nanocrystal clusters [189] or ferrofluids [191]. The magnetic nanoparticles are often dispersed in the reaction mixture and integrated during the polymerization of the hydrogels [19, 187, 188]. Magnetic microgel rods loaded with SPIONs fabricated via PRINT were found to align exclusively along the magnetic field as a consequence of their shape anisotropy [37]. To pre-program the magnetic response and predefine the magnetic moment of the microgels, only a few studies have explored the possibility of fabricating anisometric microgels under the presence of an external magnetic field [39, 189, 195].

As shown in the previous chapter, magnetically pre-aligned ellipsoidal MNPs are a versatile alternative to more commonly used magnetic fillers such as SPIONs for controlling the orientation of microgels. These ellipsoidal MNPs exhibit a fixed magnetic moment expected along their major axis, in contrast to the freely rotating magnetic moment of the SPIONs [10, 18]. Therefore, when incorporated with a predefined orientation inside a microgel matrix, the microgel has a fixed overall magnetic moment corresponding to the alignment of the nanoparticles and dipolar chains they form. Due to their high magnetic response, permanent magnetic moment and anisotropic shape, ellipsoidal maghemite MNPs were therefore incorporated into PRINT rod-shaped microgels. This incorporation allowed for pre-programming their magnetic properties in 3D under static or rotating magnetic fields, where the magnetic properties depended directly on the nanoparticle orientation within the microgels (Chapter 6). However, PRINT is a batch process that allows the production of only a limited number of microgels simultaneously, while Stop-Flow Lithography is a high-throughput continuous method.

In this chapter¹, the fabrication of magnetic microgels via SFL is demonstrated, extending the maghemite-loaded rod-shaped microgels presented in Chapter 6 to complex-shaped microgels. For this purpose, pre-aligned ellipsoidal nanoparticles are incorporated into poly(ethylene glycol) diacrylate (PEG-DA) microgels during the polymerization in a homogeneous magnetic field created by a Halbach array. Magnetic microgels with different shapes and MNP content were synthesized. Their magnetic response was investigated under rotating magnetic fields to determine the influence of the microgel shape, the MNP content and the applied magnetic field, taking advantage of their optical properties. Finally, the applications of anisometric magnetic microgels as freely rotating actuators and fixed impellers inside a microfluidic device are assessed to demonstrate their potential for actuatable microfluidics.

7.2 Experimental Section

7.2.1 Synthesis and Characterization of Ellipsoidal Maghemite Nanoparticles

The synthesis of the ellipsoidal maghemite nanoparticles is a multi-step process of preparing ellipsoidal hematite nanoparticles of a specific size and aspect ratio following a procedure previously described by Ocaña et al. [108] and converting them to maghemite by reduction to magnetite and reoxidation at high temperatures. The preparation is explained in more detail in Chapter 4. The size of the nanoparticles reveals a long axis d_{pol} of 260 ± 29 nm and a short axis d_{eq} of 51 ± 6 nm. Previous works show that these nanoparticles exhibit a magnetic moment along their long axis and a saturation magnetization σ_S of around $72 \text{ A m}^2 \text{ kg}^{-1}$ [10]. These properties result in a strong

¹Steinbeck, L., Braunmiller, D. L., M. Wolff, H. J., Huettche, V., Wang, J., Wessling, M., Crassous, J. J., & Linkhorst, J. Magnetically Actuatable Complex-Shaped Microgels for Spatio-Temporal Flow Control. *Advanced Materials Technologies* **2023**, 8(14), 2300044. <https://doi.org/10.1002/admt.202300044>. The experiments were designed by me and the other authors. I prepared and characterized the nanoparticles with the help of Andreas Falkenstein for the TGA. The microgels were prepared by Lea Steinbeck, Hanna Wolff, and Vincent Huettche, and the SEM images were recorded by Julian Eigen and analyzed by me. The Matlab and ImageJ routine Julia Wang and I used to analyze the rotation of the microgels was written by myself based on ImageJ plugins. The fabrication of in-chip actuators was conducted and analyzed by Lea Steinbeck, Hanna Wolff, and Vincent Huettche. I wrote the manuscript jointly with Lea Steinbeck and Hanna Wolff, with them focussing on the fabrication of the microgels and in-chip systems. The manuscript was revised and corrected by all co-authors.

magnetic response and the formation of dipolar chains within a magnetic field. Further details on the nanoparticles and their response to magnetic fields are discussed in Chapter 4.

7.2.2 Fabrication of Microfluidic Chips

The masters for microfluidic chips were fabricated using dip-in laser lithography with a two-photon lithography printer (Photonic Professional GT Printer, Nanoscribe GmbH, Eggenstein-Leopoldshafen, Germany) [196]. Microfluidic chips were then cast from these masters using soft lithography techniques [197, 198]. Poly(dimethylsiloxane) (PDMS) (Dow Corning, Sylgard 184 plus curing agent, 10:1 (w/w)) was used as chip material, being poured onto the master and cured at 60 °C overnight. After detaching, the cured PDMS form was perforated to achieve tubing holes, washed by sonication in isopropanol, and dried at atmospheric conditions overnight. Afterward, the PDMS form was bonded on a PDMS-coated glass slide (VWR, 52 x 76 x 1 mm, cut to 25 x 25 x 1 mm, ~ 1 mm thick PDMS layer) by oxygen plasma activation of PDMS and the glass slide (TePla 100 Plasma System, PVA) [196]. The microfluidic channels for fabrication are 15 mm long (x-direction) and 900 μm (y-direction) wide.

7.2.3 Preparation of the Precursor Solution

The precursor solutions consist of linear poly(ethylene glycol) diacrylate polymer chains ($M_n = 575$ Da, with 400 - 600 ppm MEHQ as inhibitor, Sigma Aldrich), a photoinitiator lithium phenyl-2,4,6-trimethylbenzoylphosphinate (LAP) ($\geq 95\%$, Sigma-Aldrich), and a maghemite dispersion as solvent. Before addition, the MNP dispersion (batch conc.: 2 g L⁻¹) was ultrasonicated for 5 min.

For in-chip polymerization, a radical scavenger 4-methoxyphenole (MEHQ) (purity, $\geq 98\%$, Sigma-Aldrich) was prepared in a separate vial and added to the polymer/MNP mixture before mixing with the initiator.

7.2.4 Fabrication of Magnetic Microgels using SFL

Microgels were produced with precursor solutions consisting of 20 wt% PEG-DA, 0.5 wt% LAP, 0.08 wt% maghemite magnetic nanoparticles (MNPs),

and water. The microgel fabrication utilized the setup depicted in Figure 7.1 A, employing Stop-Flow Lithography (SFL) [185] with a Halbach array applying a magnetic field of 13 mT. A range of mask shapes and pattern diameters were employed, including circular rods (7 μm diameter), three-arm impellers (92 μm outer diameter), and snowflakes (100 μm outer diameter).

Polymerizations were carried out with different radiant powers and exposure times tailored to the mask patterns: rods (1280 mW, 50 ms), impellers (930 mW, 50 ms), and snowflakes (1280 mW, 60 ms). Furthermore, rod-shaped microgels were fabricated both with and without an applied magnetic field (13 mT), while impeller microgels were created with varying MNP contents (0.02 wt%, 0.04 wt%, and 0.16 wt%, in addition to the baseline 0.08 wt%).

Following fabrication, the resulting microgel dispersion was diluted with water in a 1:1 ratio to halt further reactions and was subsequently stored at 4 $^{\circ}\text{C}$.

7.2.5 Analysis of the Magnetic Response of Microgels

The prepared microgels were cleaned by repeated solvent exchange with water. Therefore, microgels were allowed to sediment for 30 min. The supernatant was removed and replaced with water. This procedure was repeated five times. To analyze the magnetic response of the microgels, experiments were conducted inside a rotating magnetic field. These were performed on a modified Axioscope (Carl Zeiss Microscopy Deutschland GmbH) with a rotational stage driven by a piezoelectric engine (PILine U651.03, Physik Instrumente (PI) GmbH & Co. KG). Custom made circular Halbach arrays consisting of different numbers and sizes of neodymium magnets can be mounted on the rotating stage and were used to apply the magnetic field (Figure A.3). With this setup, field strengths between 1 - 300 mT and rotation rates of 0.1 - 90 rpm are reached. Standard microscope glass slides (22 x 22 mm, VWR) used in the experiments were cleaned with isopropanol inside an ultrasonic bath for 15 min and treated in an ozone oven for an additional 15 min. The microgel batch (9 μL) is sealed with two Secure-SealTM Spacers (Invitrogen), creating a well (0.24 mm height, 9 mm diameter). To analyze the magnetic response, cross-polarization microscopy was performed on microgels exposed to a rotating magnetic field. Therefore, videos (3600 frames, 100 fps) were

recorded and analyzed regarding the intensity change caused by the magnetite chains inside the microgels. The image analysis was done with ImageJ [130] and a custom-written Matlab routine. For the mean values of ω_c , around 20 microgels were investigated.

7.2.6 Particle Tracking for Flow Manipulation

To track the flow generated by freely rotating microgels, hollow polystyrene particles [199] were used. The microgels were mixed in a ratio of 1:5 with the polystyrene particles (batch conc.: 0.09 wt%). The microgels were again actuated using a piezo-engine with an attached 70 mT Halbach Array rotating at rotation rates of 10, 20, and 30 rpm. Using a bright field microscope, 3600 frames were recorded at a rate of 100 fps. The image stack was then processed by considering the minimum intensity of each frame. Since the particles are dark, this enables direct imaging of their trajectories. The resulting processed micrographs were then inverted, and the LUT changed to better evidence the different tracer trajectories. For the detailed analysis, the polystyrene particles were tracked using the tracking software VW-H2MA (Keyence).

7.2.7 Scanning Electron Microscopy

The samples were prepared by drying 20 μL of the batch on freshly cleaned silica wafers at room temperature. The wafers were cleaned by ultrasonication in isopropanol for 15 minutes and then treated in an ozone oven for 15 minutes. Scanning electron microscopy (SEM) measurements were conducted using a JSM-7800F FESEM (Jeol). Secondary electron (SE) micrographs and backscattered electron (BSD) micrographs were captured at varying acceleration voltages ranging from 5 to 15 keV, depending on the desired penetration depth.

7.3 Results and Discussion

7.3.1 Magnetic Microgel Fabrication

The microgels prepared in this chapter are the largest fabricated as part of this thesis and, therefore, contain the highest amount of magnetic nanoparticles. According to the definition of the magnetic moment discussed in the previous chapter, this should result in a strong magnetic response suitable for microactuation.

To fabricate anisometric, magnetically actuable actuators and building blocks, ellipsoidal maghemite nanoparticles were integrated into complex-shaped PEG-DA microgels using Stop-Flow Lithography. Therefore, the MNPs (batch M1 as described in Chapter 4) were mixed into the microgel precursor solution and pumped into a microfluidic channel, where the flow was stopped for the illumination time. During the illumination time, the microgels were formed by cross-linking through UV light. After this stage, the flow was restarted to flush the produced microgels out of the channel. The shape and size of the microgels are determined by the mask that limits the illuminated area. During this phase, the magnetic nanoparticles (MNPs) are aligned by the magnetic field generated by a Halbach array, as illustrated schematically in Figure 7.1 A.

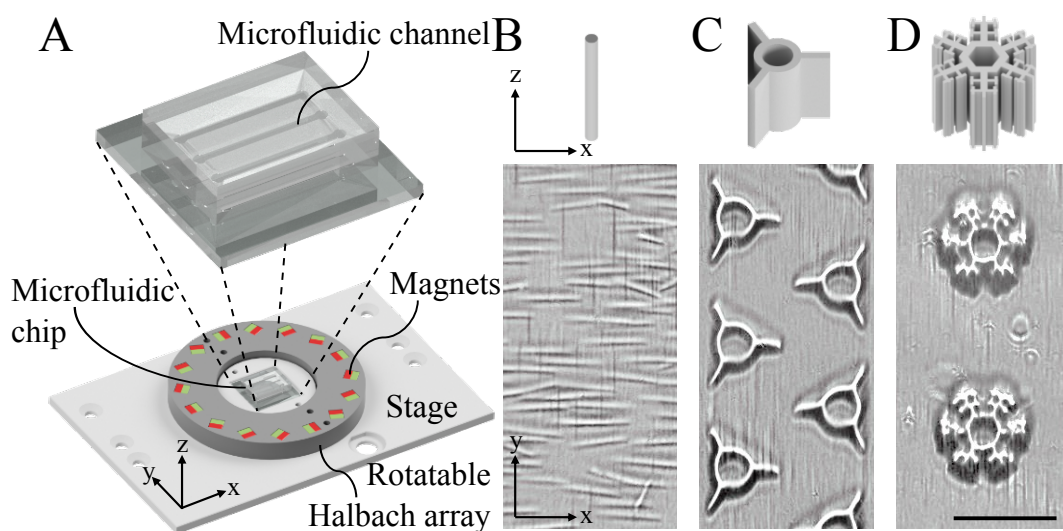


FIGURE 7.1: Fabrication of PEG-DA microgels with integrated maghemite nanoparticles. A) Setup of the microgel fabrication with the applied shapes and aligned ellipsoidal maghemite nanoparticles during microgel fabrication: B) rod, C) impeller, and D) snowflake-shaped microgels. Scale bar = 100 μm.

The microfluidic chip was positioned at the center of the Halbach array in all three dimensions to ensure a uniform magnetic field in the polymerization area. This setup allows for the control of the Halbach array's orientation, enabling the pre-programming of MNP alignment within the microfluidic channel. As a result, complex-shaped microgels with predefined magnetic moments can be mass-produced using this technique.

Using this method, rod-, impeller-, and snowflake-shaped microgels were produced (Figure 7.1 B - D). To show their shape in the micrograph, the rods were flipped and arranged to lie flat on the surface (xy-plane). Due to the still-applied magnetic field, the rod-shaped microgels align in the x-direction perpendicular to the field. This shows the successful pre-alignment of the MNPs inside the rods and in the precursor solution surrounding the rods, as visible in the micrograph as dark lines in the y-direction (indicating the field orientation). Impeller- and snowflake-shaped microgels also align as defined by their pre-programmed magnetic moment but stay upright due to their wider shape.

As discussed in the previous chapters, the pre-programmed magnetic moment is independent of the shape of the microgels but depends on the MNP pre-alignment within the microgels. In contrast to spherical nanoparticles, the ellipsoidal maghemite nanoparticles have a direction-dependent magnetic response (Chapter 4). Thus, by integrating ellipsoidal maghemite nanoparticles into the microgels, the direction of the magnetic moment of the microgels can be predefined by the applied magnetic field during fabrication. The rod-shaped microgels were fabricated with and without an applied magnetic field to investigate the influence of the maghemite alignment within the microgels. The snowflake-shaped microgels were fabricated with differing polymerization parameters to analyze the influence of fabrication conditions on the magnetic properties. For the impeller-shaped microgels, the MNP content was varied to test its effect on the microgels' magnetic moment.

The microgels prepared by SFL are significantly larger than the ones previously discussed in this thesis. The dimensions are obtained from bright field microscopy images (Figure 7.2). The cross-section is defined by the mask used for limiting the UV light, while the height is determined by the channel height. The snowflakes are with a length $l = 95 \pm 1 \mu\text{m}$, diameter $d = 87 \pm 1 \mu\text{m}$ and a height $h = 87 \pm 2 \mu\text{m}$ slightly larger than the impeller-shaped microgels ($l = 80 \pm 1 \mu\text{m}$, $d = 71 \pm 2 \mu\text{m}$ and $h = 95 \pm 3 \mu\text{m}$).

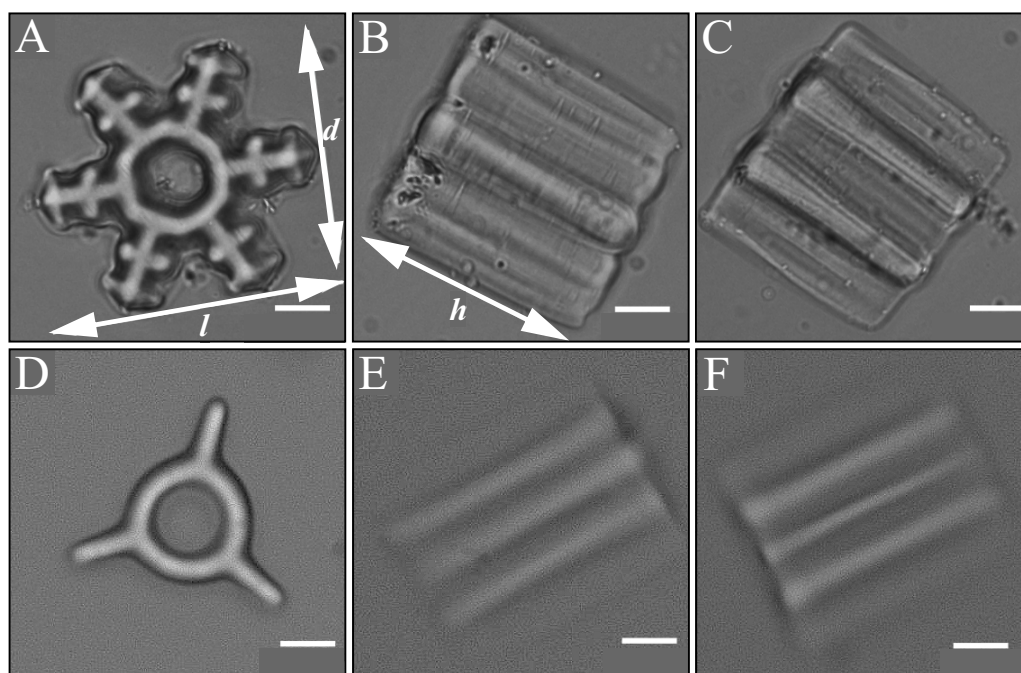


FIGURE 7.2: Bright field microscopy micrographs showing snowflake- and impeller-shaped microgels with different orientations. The microgels are A, D) upright and B, C, E, F) tilted to each side. Scale bars: $20 \mu\text{m}$.

To check the integration of ellipsoidal maghemite nanoparticles into the microgels, FESEM micrographs were recorded of impeller-shaped microgels shown in Figure 7.3. Therefore, the microgel batch ($20 \mu\text{l}$) was dried on a freshly cleaned silica wafer. The wafer was sonicated (15 min) in isopropanol and cleaned in an ozon oven (15 min) afterward. In these micrographs, the ellipsoidal nanoparticles can be observed in the near vicinity of the microgel surface and are found to be present as single nanoparticles coexisting with dipolar chains with only a few free particles at the substrate (see Figure 7.3 B, C).

Assembled into dipolar chains, the maghemites are not fully aligned along the chains but rather tend to associate side-by-side with a tilt with respect to the chain director, as reported in Chapter 4. The single particles, however, seem to have a preferential alignment along the chains. During drying, the microgels collapse, and their shape is not fully retained (see Figure 7.3 A, B).

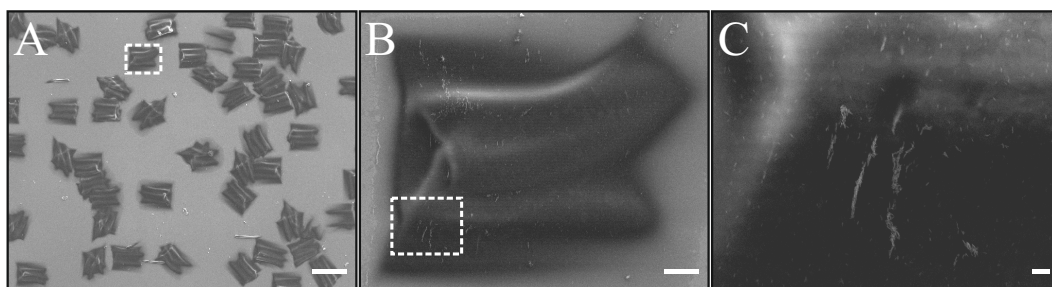


FIGURE 7.3: SEM micrographs of dried impeller-shaped microgels with incorporated ellipsoidal maghemite nanoparticles assembled into dipolar chains. Scale bars: A) 100 μm , B) 10 μm and C) 1 μm .

Therefore, the alignment of the chains is not fully representative of their orientation in a swollen microgel. Nevertheless, it can be concluded that the ellipsoidal nanoparticles are mostly integrated in microgels and oriented or assembled along the field applied during the fabrication.

7.3.2 Magnetic Responsiveness of Microgels

For these microgels, the magnetic response was analyzed based on their shape, the pre-alignment of the magnetic nanoparticles, the MNP content, and the strength of the magnetic field. The pre-alignment of the maghemite MNPs in the reaction solution plays a crucial role in allowing the microgels to rotate. The microgel rods that were created without aligning the MNPs, meaning they were fabricated without a magnetic field, did not uniformly align with a static magnetic field and only showed a weak magnetic response to dynamic fields. On the other hand, pre-aligning the nanoparticles significantly improved the magnetic response and allowed for the orientation of the microgels.

Considering a ferromagnetic system in a Newtonian fluid under a magnetic field rotating with the angular frequency ω , the equation of motion reads:

$$\gamma \left(\omega + \frac{d\alpha}{dt} \right) = \mu B \cdot \sin\alpha, \quad (7.1)$$

where γ is the drag coefficient, α the angle between the magnetic moment of the system μ and the applied field B . This expression describes the balance of the torques set by the rotation of the system in the fluid and the magnetic torque. The system rotates synchronously as long as $d\alpha/dt \approx 0$, which allows to define the critical angular frequency $\omega_c = \mu B \cdot \gamma^{-1}$. For $\omega > \omega_c$, the system can not continuously follow the field and start to tumble. Hence, the magnetic moment is not able to follow the field, and α becomes time-dependent. Measuring the field and angular frequency dependence of ω allows the characterization of the magnetic response of the particles.

An interesting feature of the incorporated nanoparticle chains can be used to determine the angular frequency of the microgels. As the dipolar chains formed by the MNPs (Chapter 4) polarize the light, the orientation of the chains can be determined using cross-polarization microscopy (Figure 7.4 A - D).

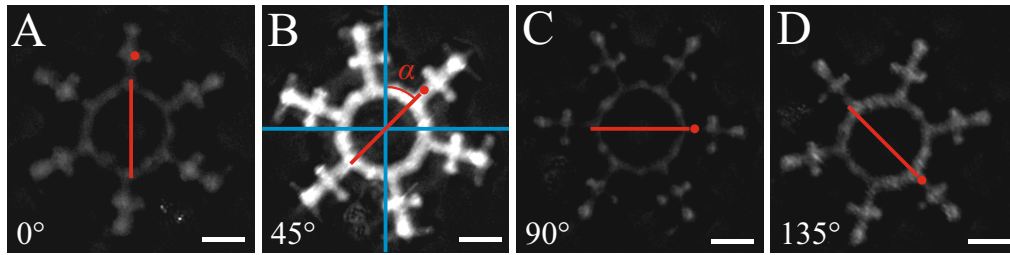


FIGURE 7.4: Optical analysis of light polarization via magnetic rotation of maghemite MNPs incorporated in snowflake-shaped microgels. A-D) Cross-polarization micrographs of a microgel with incorporated maghemite chains orientated at different angles θ to the polarizer. The transmitted intensity I changes depending on α . The blue lines indicate the orientation of the polarizer, and the red lines with the dot correspond to the orientations of the maghemite chains within the microgel. Scale bars: 20 μm .

Thereby, a linear polarizer and an analyzer, orientated perpendicular to each other, are positioned before and after the sample on a microscope. Light cannot pass through both without being polarized by the sample (Figure A.4). The intensity I_N of the transmitted light depends on the angle α

between the orientation of the polarizer and the dipolar chains (Figure 7.4 B). This feature is used to determine the angular frequency by the maxima of the intensity profile - a full rotation of the microgels with the entrapped maghemite chains is indicated by two larger and two smaller maxima (Figure 7.5 A). While working perfectly in the synchronous regime (Figure 7.5 B), in the asymmetric rotation regime, the intensity profile is influenced by the tumbling of the microgels (Figure 7.5 C). Depending on the degree of rattling, additional manual evaluation was performed.

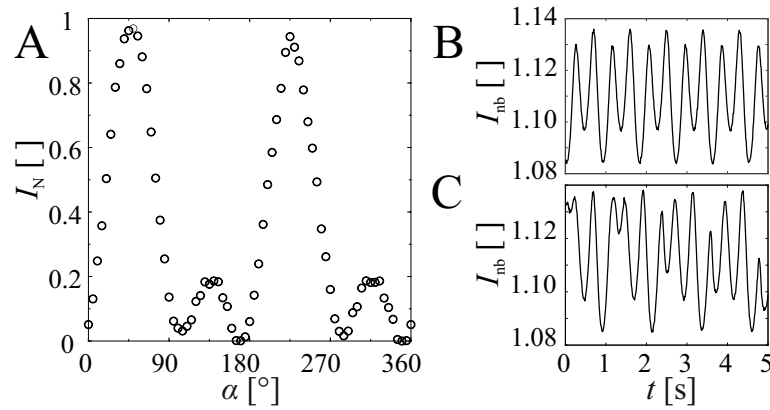


FIGURE 7.5: A) Intensity I_N profile of the rotating microgel normalized on the maximum and minimum intensity. A full rotation is indicated by two large and two small maxima at 45° (and 225°) and 135° (and 315°), respectively. B) Intensity profile of a synchronously rotating microgel with a motor speed f_{MF} and microgel rotation rate of 66.7 rpm. C) Intensity profile of an asynchronously rotating microgel with a motor speed f_{MF} of 73.3 rpm and a microgel rotation rate of 48.2 rpm. The additional intensity fluctuation is caused by a tumbling motion of the microgel. The intensity I_{nb} in B and C is normalized by the background of the image.

The rotation behavior of a single impeller-shaped microgel is exemplarily shown in Figure 7.6. With an increasing rotation rate of the magnetic field ω_{MF} , the rotation of the microgel ω increases linearly up to the critical rotation rate ω_c . This linear increase represents the synchronous rotation regime in which the microgel rotates synchronously with the magnetic field.

The angle ω between the magnetic torque of the microgel and the orientation of the magnetic field is constant. The rotation behavior changes above the critical rotation rate. At this point, the microgels start to tumble and, as a result, ω drops significantly below ω_{MF} . The friction and drag forces are greater than the magnetic torque in the asynchronous rotation regime ($\omega_{MF} > \omega_c$). This increases the angle α between the magnetic field and the magnetic moment. Before the magnetic field overtakes the magnetic moment,

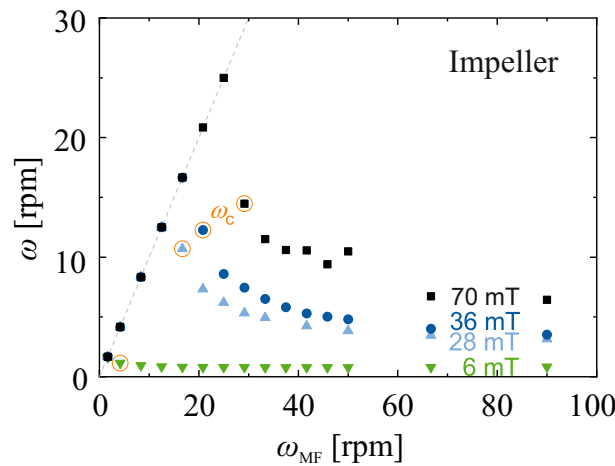


FIGURE 7.6: Magnetic response of a single impeller-shaped microgel in dependence on the rotation rate ω_{MF} and strength of the magnetic field. The critical rotation rate ω_c indicates the transition between the synchronous and the asynchronous rotation regime (○).

there is a change in the direction of the microgel rotation. When the magnetic field overtakes the magnetic moment of the microgel, another change in the direction of rotation leads to further rotation in the original direction. These back-and-forth oscillations are characteristic of the tumbling regime. The tumbling affects the rotational behavior, but the overall rotation proceeds in the direction of the magnetic field at a lower rate, which can be determined as described above.

7.3.3 Influence of Microgel Shape, MNP Content, and Magnetic Field Strength on the Magnetic Responsiveness

In addition to ω_{MF} , the magnetic response of the microgels depends on a variety of parameters, for example, magnetic field strength, MNP content, and shape of the microgels. In order to determine the average magnetic response, around 20 microgels are considered, and their mean rotation rates ω are summarized in Figure 7.8 & 7.9. Generally, the response of the different microgels shows larger variations from microgel to microgel for higher microgel rotation rates and field strengths as for the critical rotation rate. Possible reasons for this variation are different contact areas or gap sizes between microgel and glass surfaces, as different friction or shear forces influence the rotation

rates. Furthermore, there might be inhomogeneities in the nanospindle loadings inside the microgels due to unavoidable inhomogeneous chain formation during production. Accordingly, the critical rotation rate ω_c was not determined from the mean ω -values but rather from the individual data sets, as shown in Figure 7.6. The mean critical rotation rate $\omega_{C,m}$ was determined by evaluating the rotational behavior of individual microgels as described in the previous section. The distribution of ω_c varies strongly depending on the applied field strength, MNP content, and shape (Figure 7.7).

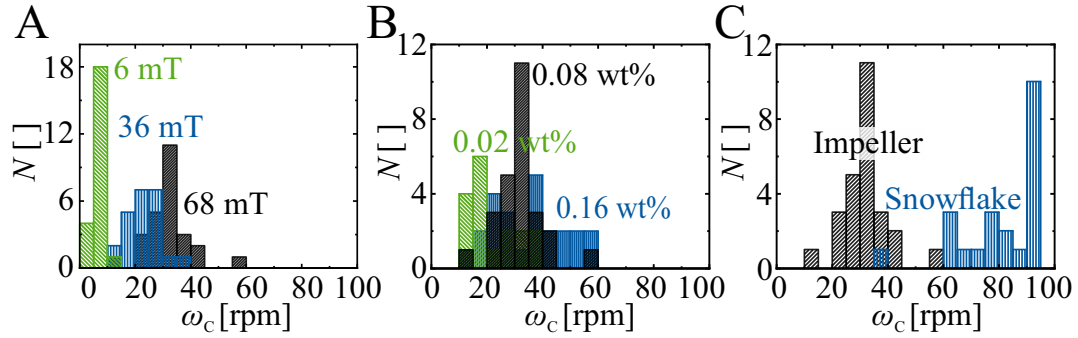


FIGURE 7.7: Distribution of critical rotation rates ω_c of individual microgels. Comparison for variations of A) field strength, B) nanoparticle content, and C) shape, respectively.

With an increasing magnetic field strength B , the mean rotation rate ω of impeller-shaped microgels with a maghemite loading of 0.08 wt% increases as shown in Figure 7.8 A. While the data for 6 mT exhibit the above-described linear increase of the rotation rate in the synchronous regime and a non-linear decrease in the asynchronous regime, the mean curves for higher field strengths show a more linear decrease. This linear decay is a result of the strong variation of ω_c for higher field strengths (Figure 7.7 A). The mean value of ω_c increases from 5.3 ± 0.3 rpm at 6 mT to 22.2 ± 1.3 rpm (36 mT) and 32.2 ± 1.8 rpm (70 mT), respectively. The rotation rate seems to reach a saturation value at some point above 70 mT, as the difference between 6 and 36 mT with 16.9 rpm is significantly larger than between 36 and 70 mT (10 rpm).

As the magnetic torque is directly dependent on the mass of the magnetic material in the microgels, a higher maghemite loading and a larger microgel shape are expected to increase the magnetic response of the composite microgels. The mean value of ω_c at 70 mT of impeller-shaped microgels increases from 21.5 ± 2.3 rpm with a nanoparticle content of 0.02 wt% to 32.2 ± 1.8 rpm (0.08 wt%) and 34.2 ± 2.8 rpm (0.16 wt%), respectively. While a higher MNP

content in the precursor solution increases the microgels' magnetic response, it also increases the inhomogeneity of the response to the magnetic field, as shown in Figure 7.8 B. The transition between the synchronous regime and asynchronous regime varies stronger for 0.16 wt% than for the lower contents (Figure 7.7 B). The higher contents might lead to a less defined chain structure inside the microgels, resulting in more inhomogeneous magnetic properties and a lower effect of the magnetic filler content with respect to the field.

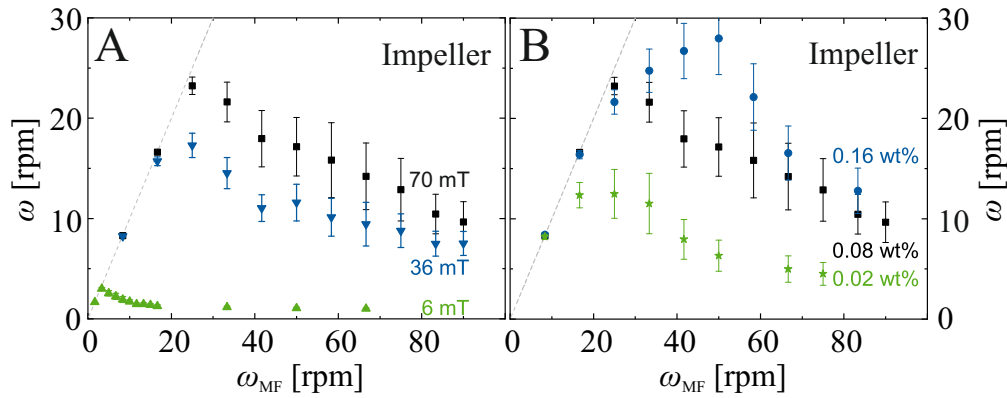


FIGURE 7.8: Mean magnetic response of the magnetic microgels ($n \approx 20$) measured as their microgel rotation rate ω as a function of the field rotation rate ω_{MF} , with regard to A) field strength and B) MNP content.

On the one hand, the shape of the produced microgels, as measured by their volume, influences the magnetic moment. On the other hand, the viscous torque, as well as friction and shear forces at the surface of the microgels, counteract the magnetic torque. For this investigation, impeller- and snowflake-shaped microgels with the same maghemite loading of 0.08 wt% are actuated with a magnetic field of 70 mT (Figure 7.9). The magnetic response of the snowflake-shaped microgels with a mean critical rotation rate at 79.8 ± 3.2 rpm is significantly higher than for impeller-shaped microgels ($\omega_c = 32.2 \pm 1.8$ rpm).

As the magnetic torque is proportional to the used magnetic material (Equation 7.1) and thus proportional to the volume of the nanoparticles, the magnetic response is expected to increase proportionally with the volume of the microgel. As the snowflake-shaped microgels have an estimated volume of $178 \pm 14 \cdot 10^3 \mu\text{m}^3$ and the impeller-shaped of $97 \pm 2 \cdot 10^3 \mu\text{m}^3$, this relates to a ratio of around 2:1 and an expected stronger magnetic response of the snowflakes. The magnetic torque is counteracted by the viscous torque and

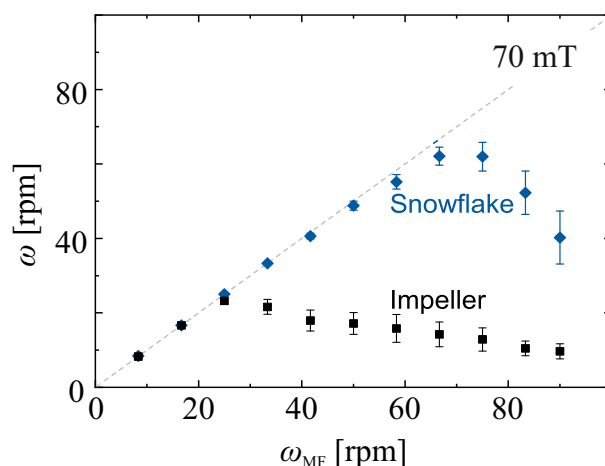


FIGURE 7.9: Mean magnetic response of the different shapes of magnetic microgels ($n \approx 20$) measured as their microgel rotation rate ω as a function of the field rotation rate ω_{MF}

the frictional and shear forces on the surface of the microgels. The snowflake-shaped microgels have a surface area on the bottom side of $2138 \pm 164 \mu\text{m}^2$, while the impeller-shaped microgels have a surface area of $1048 \pm 21 \mu\text{m}^2$, also suggesting a 2:1 ratio. Since the critical rotation rate is over two times higher for the snowflake-shaped microgels, the contribution of the magnetic torque is stronger than the friction forces. As neither of these forces nor the exact surface of complex shapes like snowflakes can be easily quantified, the influence of the shape cannot be clarified conclusively at this point.

7.3.4 Flow Manipulation with Actuated Microgels

After analyzing the factors influencing magnetic responsiveness, this section explores their potential as microactuators for mixing or pumping by examining the ability of freely rotating microgels to generate flow. The flow generated by single magnetic microgels was tested by adding a hollow polystyrene tracer to the surrounding solution. Details on the synthesis and characterization of these particles can be found in a previous study [199]. The impeller geometry was tested using bright field microscopy (see Figure 7.10 A). For this purpose, standing microgels rotating synchronously with the magnetic field were analyzed at different rotation rates, as shown in Figure 7.10 B - D. Three rotation rates were tested: 10, 20, and 30 rpm. Upon magnetic actuation of the microgel impellers, a large flow centered around the impellers was observed for a rotation rate of 30 rpm. The

generated flow was first directly evidenced by the projection of the tracer trajectories (Figure 7.10 B - D). The tracers were found to follow a circular trajectory, the tracers at the closest distance from the impellers exhibiting the largest displacement. Surprisingly, some small periodic oscillations were observed at the tracer paths of all the videos, possibly resulting from the hydrodynamic interaction generated by the particles. In literature, similar "sawtooth" trajectories were reported in the case of a synchronously rotating particle, generating a pulsed flow [200].

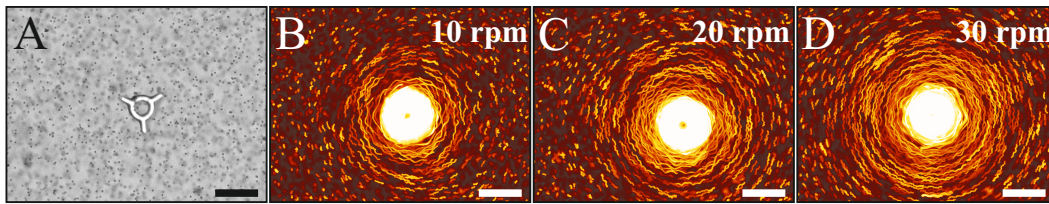


FIGURE 7.10: Impeller-shaped microgels actuated by a rotating magnetic field. The impellers rotate synchronously with the magnetic field in water dispersed with hollow polystyrene tracers. Scale bars = 100 μm . A) Bright-field micrograph snapshot of an impeller-shaped microgel dispersed with hollow polystyrene tracers. B - D) Corresponding inverted minimum intensity projections computed over 500 frames (5s) illustrate the tracer trajectories.

To properly study the behavior, the tracer positions over all frames were determined. Only the projected position of the particles in the plane corresponding to the coordinates $(x_i(t), y_i(t))$ were considered. The referential was set at the center of the impeller, and its position over time $(x_0(t) = 0, y_0(t) = 0)$ was followed by tracking the position of the impeller arms. After correcting the tracer positions for the position of the impeller center (Figure 7.11), the oscillations seen in the raw tracks are still visible. Therefore, the oscillations are not a product of the off-center rotation of the impeller.

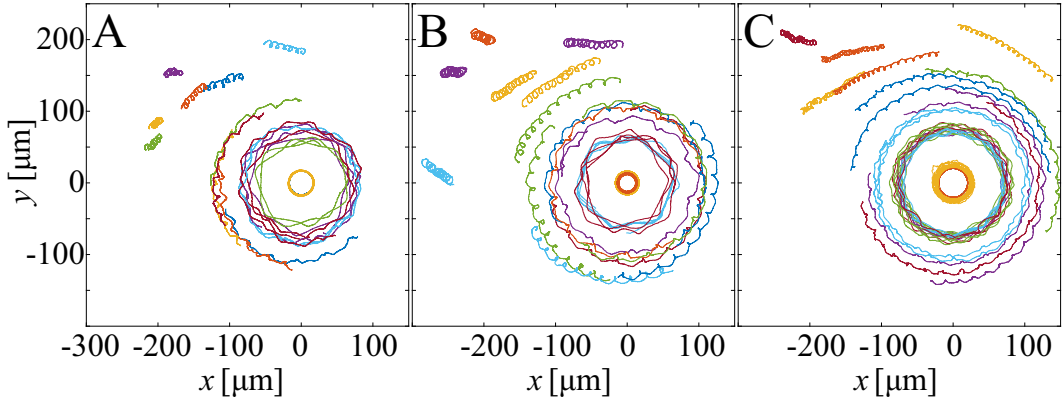


FIGURE 7.11: Corrected trackings of tracer particles around impellers rotating at A) 10 rpm, B) 20 rpm, and C) 30 rpm, respectively. The innermost tracers are attached to the microgel and, therefore, rotate at the same rate as the microgel and as the magnetic field.

The corrected tracer position can be described by the vector $\vec{r}(t)$ and its magnitude describes the distance between the tracer and the center of the impeller (Figure 7.12). It is given by:

$$r(t) = \sqrt{x(t)^2 + y(t)^2} \quad (7.2)$$

The tracer distance $r(t)$ changes periodically with the time due to the oscillations of the tracer. For large distances, the frequency of the oscillations matches the rotation of the impeller. In dependence on the rotation rate of the impeller, the oscillation frequencies of the tracers increase while still matching the rotation rate for large distances. Similar observations were made on rotating snowflakes.

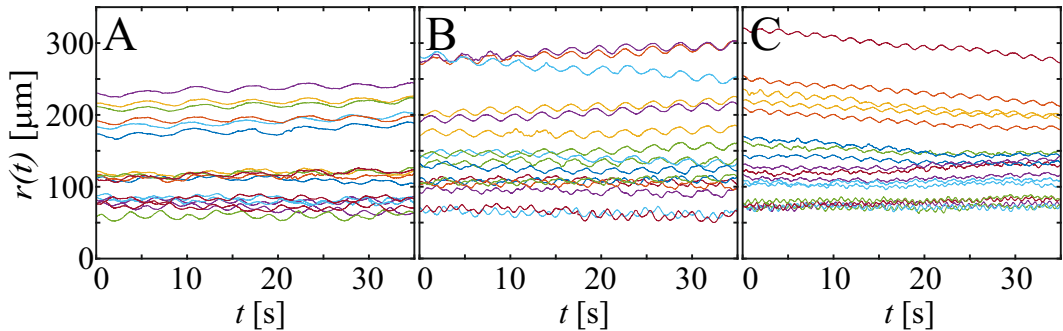


FIGURE 7.12: The distance $r(t)$ of the tracer particles is periodically fluctuating over the time for all used ω_{MF} A) 10 rpm, B) 20 rpm, and C) 30 rpm. The frequency for long distances corresponds to the impeller rotation rate.

The distance $p(t)$ a tracer moves in a time interval Δt can be described by the magnitude of the vector between the tracer position T_t and the new tracer position $T_{t+\Delta t}$.

$$p(t) = \sqrt{(x(t + \Delta t) - x(t))^2 + (y(t + \Delta t) - y(t))^2} \quad (7.3)$$

The relative angular displacement of the tracers after Δt is:

$$\delta = \arccos \frac{r(t)^2 + r(t + \Delta t)^2 - p(t)^2}{(2 \cdot r(t) \cdot r(t + \Delta t))} \quad (7.4)$$

The angular tracer velocity is then defined as:

$$\omega_T = \left\langle \frac{\delta}{\Delta t} \right\rangle \quad (7.5)$$

The average tracer velocity for about 15-20 tracers was calculated, which were located at different distances from the center of the impeller. Figure 7.13 shows the average tracer velocities ω_T over the distances of the tracers $r(t)$ for different magnetic field rotation rates. The angular velocity first quickly decreases to a distance of about 200 μm and then seems to become constant for all ω_{MF} .

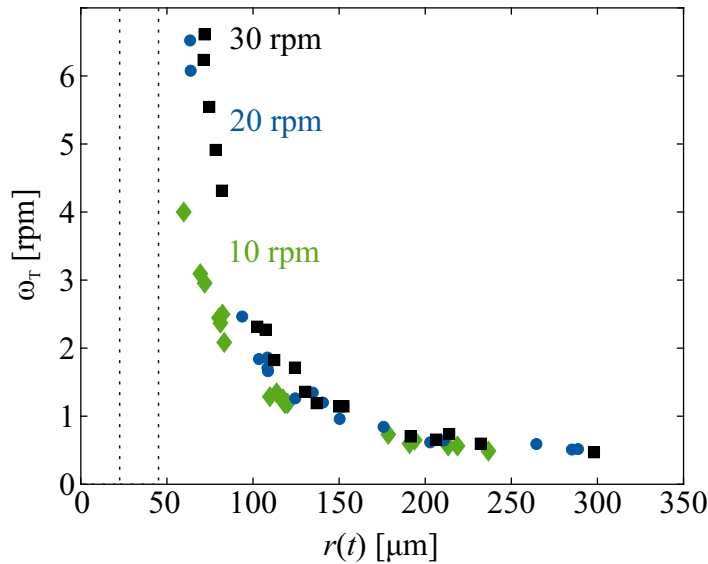


FIGURE 7.13: The average tracer velocity ω_T decreases strongly with the distance to the impeller center until a plateau is reached at 200 μm . Afterwards, ω_T stabilizes around 0.5 rpm for all used field rotation rates 10 rpm, 20 rpm, and 30 rpm. The dotted lines indicate the size of the body and the arms of the impeller, respectively.

While the 'sawtooth' tracer trajectories highlight complexities that require further study in future works, the strong local flow generated by the microgels demonstrates their potential and suggests possible applications as in-chip microactuators.

7.3.5 In-Chip Microactuator

The implementation of MMGs as in-chip impellers within a microfluidic chip was accomplished by directly integrating them via SFL around PDMS pillars. The pillars act as fixation points for the impellers, enabling their rotation around a fixed axis. To create a microfluidic chip with integrated impeller-shaped MMGs, we fabricated a PDMS microchannel featuring square lattice arrangements of pillars, as depicted in Figure 7.14 A.

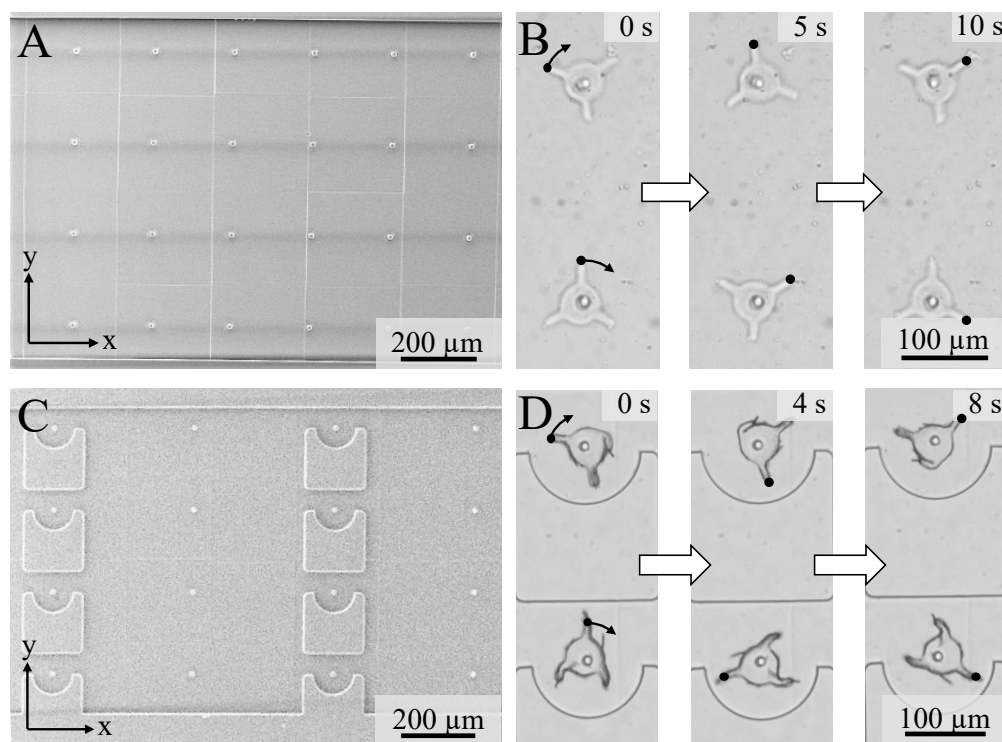


FIGURE 7.14: Actuable microfluidics and rotation analysis. A) SEM micrograph of the microfluidic channel with PDMS pillars. B) Time series of clockwise rotating impellers around pillars in-chip. C) SEM micrograph of the microfluidic pump housing. D) Incorporated impellers in housing showing a time series of clockwise in-chip rotation.

This design facilitates the fixation and rotation of the impellers around their axes while they remain inside the channel. The freedom of rotation

around the pillars was assured through the oxygen inhibition layer, hindering the cross-linking of the PEG-DA in the close vicinity of the PDMS. Furthermore, the system development is accomplished in a single step by positioning the magnetic microgels in any desired shape inside the chip following the microfluidic channel fabrication.

Additionally, we engineered an alternate microfluidic chip design to achieve both mixing and pumping functions (Figure 7.14 C). By reducing the number of pillars and integrating pump housings into every second row of the remaining pillars, alternating areas of pumping and mixing were generated within the channel. The fabrication process was carried out using the same technique for both designs. Impeller-shaped MMGs were successfully integrated into these pump housings. Despite higher PDMS content at pumping regions resulting in increased shear rates during fluid exchange, the impellers effectively rotated at up to 10 rpm — the same rotation rate as the magnetic field (Figure 7.14 D). The versatility of this novel active microfluidic system is illustrated by the combination of mixing and pumping functions, which can be easily adapted for various applications by modifying the microfluidic master design without additional fabrication process adjustments.

7.4 Summary and Outlook

In this chapter, a thorough investigation of large complex-shaped MMGs, their magnetic properties and their ability to be used for spatio-temporal flow control on the way to soft metamaterials is presented. By incorporating maghemite MNPs into a non-magnetic PEG-DA microgel matrix during the high throughput fabrication using Stop-Flow Lithography, highly magnetic hybrid microgels with pre-programmed magnetic properties were produced. Shape and size can be customized by the mask used in the setup, including but not limited to the snowflakes and impeller presented here. Employing an external magnetic field, a magnetic actuation of the microgels can be conducted, creating a fully remote controllable system.

To study the magnetic responsiveness of these microgels, experiments were conducted under a rotating magnetic field, examining how MNP alignment, microgel shape, MNP content, and magnetic field strength affected the actuation performance. Results revealed that microgels with pre-aligned MNPs exhibited significantly stronger magnetic responses

compared to those with non-aligned MNPs, highlighting the critical role of MNP alignment in enhancing microgel responsiveness to magnetic fields. While stronger magnetic field strengths and larger amounts of MNP tend to result in a stronger magnetic response, both parameters seem to reach a saturation value beyond which the improvement diminishes. The experiments have demonstrated that these microgels can act as local microactuators, generating strong flows when stimulated by a magnetic field, making them promising candidates for applications in microfluidics and micro-pumping. Building upon their magnetic responsiveness, these microgels were integrated into a functional microfluidic system by fabricating them around PDMS pillars fixed inside a microfluidic channel. On the one hand, the pillars work as a fixed rotation axis. On the other hand, it prevents the microgels from sticking to the pillars due to the oxygen inhibit layer preventing cross-linking of the polymer in the surrounding area. These magnetic microgel (MMG) microactuators can be remote-controlled to mix their surroundings, facilitating precise remote flow control.

The development of an active microfluidic system based on SFL-fabricated magnetic microgels represents a significant advancement in the field of lab-on-a-chip technologies and microsystems engineering. These magnetically responsive, biocompatible microstructures can be custom-designed in various elongated 2D shapes, opening up exciting possibilities for applications in tissue engineering. Future research should focus on assembling these magnetic microgels into scaffolds to investigate the impact of their inherent macroporosity and directionality on cell growth and responses to actuation patterns. Moreover, the ability to manipulate individual magnetic microgels in a rotating field at the single-microgel level paves the way for micro-scale mixing and the application of these structures in micro-rheometry, enabling the study of complex fluids. The potential applications of this technology extend beyond tissue engineering and include biomechanical analysis of proliferating tissues and other mechanobiological investigations. Additionally, the precise positioning of the microgel's axis of rotation within a microfluidic chip provides an opportunity to create more advanced designs incorporating movable and actuable elements for various applications, such as microfluidic valves, pumps, or particle sorting systems. The versatility and customizability of this platform offer significant potential for advancing research in numerous fields, including materials science, chemical engineering, biomedical engineering, and more.

Chapter 8

Summary and Outlook

This thesis explores the development and analysis of magnetic hybrid microgels (MMGs) with varied sizes and shapes, possessing pre-programmable magnetic properties. The research investigates these magnetic properties and their potential applications in a range of areas, including the anisotropic nanoparticle cores (Chapter 4), a colloidal magnetic microgel system (Chapters 4 and 5), rod-shaped microgels as building blocks for tissue engineering (Chapter 6), and large complex-shaped microgels as microactuators (Chapter 7).

8.1 Summary

In this thesis, ellipsoidal iron oxide nanoparticles were integrated into various microgel shells. The results show that these nanoparticles are excellent base materials for creating functional magnetic materials. It has been demonstrated that the magnetic nanoparticles (MNPs) used become highly magnetic when converted from hematite to maghemite and form dipolar chains when exposed to even a weak magnetic field. Depending on the magnetic field strength and the shell thickness, the dipolar interactions between the MNPs change. For bare MNPs, the dipolar interactions lead to complex ribbon-like assembly in magnetic fields. In contrast, silica-coated ones and MMGs form tip-to-tip chains with an increasing interparticle distance. In Chapter 4, a combination of imaging and scattering techniques, including transmission electron microscopy (TEM), dynamic light scattering (DLS), and small-angle X-ray scattering (SAXS), was employed to assess the dimensions, dynamics, and aspect ratios of the different components of silica-coated ellipsoidal MNPs. The synthesis of a magnetic hybrid microgel system with an MNP core and a thermoresponsive PNIPAm microgel shell was conducted, and the system was characterized. These MMGs possess

similar magnetic properties to the MNPs, except for their dipolar interactions, which are significantly weaker due to the thicker non-magnetic shell.

The significance of employing magnetic core-shell microgels as a model system to investigate the complex phase behavior and dynamics within concentrated soft colloidal systems has been demonstrated in Chapter 5. The application of magnetic fields facilitates the alignment of these microgels, leading to valuable insights into their structural organization and interactions. The phase behavior of anisotropic microgels in the absence of a magnetic field shows random orientation in both the diluted regime and beyond the glass transition, except in the case of plastic crystals that form at 5 wt%. These plastic crystals display local crystalline domains, though they lack long-range order. Consecutively, this chapter focused on structuring MMGs with two methods: magnetic fields and flow. When subjected to unidirectional drying, anisotropic microgels display structural changes due to their shape. In a drying cell setup, where fluid is withdrawn from the reservoir by evaporating at a capillary tip, anisotropic microgels self-assemble perpendicular to the flow, forming strongly compressed nematic phases.

Similar alignment can be achieved when exposed to a static magnetic field, as the microgels align strongly with the field orientation up to the glass transition, at which the "frozen" structure hinders the re-arrangement of the microgels due to interparticle contact and compression of the microgel shell. Dynamic SAXS measurements were conducted to determine the glass transition, leveraging the magnetic properties of the MNPs and their intrinsic anisotropy to determine the transition from a freely rotating system toward a fully arrested glass. When exposing the samples to a dynamic magnetic field, SAXS measurements were used to study the response of the microgels, allowing to differentiate between their rotation regimes. Rotation and relaxation experiments were used to determine the glass transition but also show an interesting feature, as the results indicate the free rotation of some particles inside the arrested microgel matrix. These "rattlers" are free to rotate at the maximum rotation rate, faster than the collective rotation at lower concentrations. In conclusion, small magnetic hybrid microgels hold great potential as tracer particles and probes, offering unique insights into local dynamics both in bulk and at surfaces, as well as serving as effective models for studying complex systems like colloidal spin glasses.

Advancing towards larger microgel systems, we have demonstrated that the ability to achieve a high level of spatial control over biomaterial building blocks is essential for constructing complex 3D scaffolds through a bottom-up approach. In Chapter 6, MMGs based on incorporated dipolar chains instead of single MNPs have been studied with pre-programmed magnetic properties. The pre-alignment of MNPs enables the predefining of the orientation of anisometric magnetic microgels inside a static magnetic field and, thus, obtaining microgels with a defined magnetic moment. This represents a significant advantage over comparable rod-shaped microgels using paramagnetic SPIONs as magnetic fillers, providing a higher degree of control over the microgel orientation and a faster response to a shifting magnetic field compared to SPION-loaded microgels with similar nanoparticle concentrations. Besides the static control of the orientation, we could demonstrate that the orientation can be altered dynamically by applying a rotating magnetic field, thereby extending the 2D orientation to the third dimension. For tissue engineering, mixtures of microgels with different polarizations were added inside an Anisogel, creating alignment in both parallel and perpendicular directions without hindering each other using static and dynamic orientation control. A natural extension of using MMGs as building blocks for bottom-up scaffolds in tissue engineering is their potential application in microactuation, where their responsiveness to external magnetic fields can be harnessed to induce controlled, dynamic movements for advanced biomedical devices.

At the upper end of the size scale of what can still be considered microgels, Chapter 7 provides an in-depth examination of complex-shaped MMGs and unveils a system enabling the manipulation and direction of fluid flow by remotely controlling their location and movement using an external magnetic field. Magnetic actuation of the microgels was achieved by integrating dipolar chains of MNPs into the precursor solution, followed by microfluidic fabrication using stop-flow lithography. The study systematically explored how various factors affect microgel actuation, including maghemite alignment, polymerization conditions, microgel shape, MNP content, and magnetic field strength. These findings establish a foundation for leveraging magnetic microgels in applications such as micrometer-scale stirring and mixing. When overcoming the adhesive forces of microgels, these MMGs provide a strong local flow creation, with proof of concept experiments of in-chip fabrications of integrated magnetic impeller-shaped

microgels to actively mix their surrounding fluid inside a microfluidic channel, thus enabling spatiotemporal flow control remotely actuated by a rotating magnetic field.

Overall, maghemite MNPs have proven to be a strong basis for the full range of hybrid magnetic microgels, allowing the pre-programming of static and dynamic properties of simple and complex, small and large microgels. The microgel shell allows the further functionalization and design of hybrid systems tailored for various applications.

8.2 Outlook

On the fundament of this thesis, further studies can explore a range of possible applications in a range of fields.

Using the thermoresponsiveness of small single-core MMGs, the shell thickness can be tuned to analyze the dipolar interaction in greater detail, as dipolar interactions are strongly sensitive to the distance between the MNPs. An intriguing outcome of this research could be defining the transition temperature at which dipolar chains transform into individual particles and understanding the particle distance at which dipolar interactions are completely suppressed. Through this knowledge, an MMG system could be derived that forms dipolar chains in the collapsed state above the VPTT, with the possibility of breaking the dipolar chains through swelling the microgel shell. To reach such a system, an MMG system with a thicker microgel shell should be synthesized, as the studied system does not provide fully separated Microgels for swollen microgels.

The concept of colloidal "spin glasses" was introduced in this context. Spin glasses exhibit a glassy state with frozen magnetic moments, analogous to a colloidal glass from microgels with randomly oriented anisotropic MNPs. In microgels, these states can form due to interparticle interactions at the jamming transition and the presence of anisotropic MNPs. Studying the melting of such colloidal spin glasses allows us to evaluate the reversibility of the "freezing" of the "magnetic spins", giving additional insights into the jamming behavior of microgels. The proof-of-concept experiments at the air/water interface should also be expanded.

These revealed a highly structured arrangement on a local level independent of the magnetic field. By fine-tuning experimental conditions, it may be possible to achieve stronger magnetic alignments and fully exploit the unique properties of magnetically actuable microgels at interfaces. Including exploring the potential applications of these particles as micro tracers at interfaces and in bulk, delving deeper into the role of magnetic interactions within microgel glasses, and investigating the relationship between orientation, structure and dynamics in anisotropic magnetic microgels.

Building on the findings from the colloidal magnetic microgels, the investigated rod-shaped MMGs hold significant promise for their applications in biomedicine and tissue engineering. The presented magnetic rotational

spectroscopy experiments provide a powerful tool to test the adhesive properties of the microgels with different substrates. While this thesis only briefly dips into three-dimensional scaffolds, it provides a basis for the development of bottom-up scaffolds for tissue. The combination of our new maghemite microgels and classical SPION microgels could be used to create complex scaffolds for cells growing in different directions comparable in natural tissues such as cartilage.

More significantly, static and dynamic control in combination with 3D printing may offer the possibility of quickly prototyping complex scaffolds with a stratified structure for functional tissue engineering. The mixing of differently pre-programmed microgels led to cell alignment in both directions and opens up the opportunity to orthogonally study multiple biochemicals and mechanical and physical guiding cues in different directions and potentially selectively influence the growth of different cell types in co-culture. Further on, the strategy developed for the synthesis of these pre-programmed MMGs can be extended to different materials, shapes, and sizes for the design of multi-responsive actuators, devices and swimmers at the microscale bearing some potential for the design of therapeutic microbots for non-invasive surgical interventions.

While the first two MMG systems developed in this thesis are produced in batch processes, SFL allows for the mass production of MMGs with pre-programmed magnetic properties. Magnetic microgels produced via SFL hold immense potential in microactuation, especially with the new technique of in-position fabrication, enabling the development of advanced microscale devices such as dynamic microfluidic pumps, valves, and particle sorting systems. These microgels can be precisely manipulated to create versatile, actuable elements in lab-on-a-chip technologies by leveraging their responsiveness to magnetic fields. Furthermore, their unique properties facilitate micro-scale mixing and rheometry, allowing researchers to study complex fluids and enhance biochemical processes. Beyond fluidics, magnetic microgels can be tailored for mechanobiological studies, offering new tools to investigate the biomechanics of proliferating tissues under controlled mechanical stimuli.

These materials' biocompatibility and ability to be custom-shaped into elongated two-dimensional forms make them excellent candidates for tissue engineering applications. For instance, these microgels can be assembled into

scaffolds with inherent macroporosity, enhance cell proliferation, and promote directional growth. These characteristics also allow researchers to explore how cells respond to various external actuation patterns, potentially revolutionizing how specialized tissues are developed in vitro. Additionally, magnetic microgels can play a crucial role in creating advanced metamaterials with adjustable mechanical and magnetic properties, opening up new avenues for innovation in bioengineering and materials science. This versatile technology effectively bridges fundamental research and practical applications in cutting-edge fields.

Bibliography

- (1) Kim, Y.; Zhao, X. Magnetic Soft Materials and Robots. *Chem. Rev.* **2022**, *122*, 5317–5364.
- (2) Szymczak, H.; Bassani, F.; Liedl, G. L.; Wyder, P. In *Encyclopedia of Condensed Matter Physics*; Elsevier: Oxford, 2005, pp 204–211.
- (3) Kim, Y.-K.; Noh, J.; Nayani, K.; Abbott, N. L. Soft matter from liquid crystals. *Soft Matter* **2019**, *15*, 6913–6929.
- (4) Rarokar, N.; Yadav, S.; Saoji, S.; Bramhe, P.; Agade, R.; Gurav, S.; Khedekar, P.; Subramaniyan, V.; Wong, L. S.; Kumarasamy, V. Magnetic nanosystem a tool for targeted delivery and diagnostic application: Current challenges and recent advancement. *Int. J. Pharm-X* **2024**, *7*, 100231.
- (5) Vangijzegem, T.; Lecomte, V.; Ternad, I.; Van Leuven, L.; Muller, R. N.; Stanicki, D.; Laurent, S. Superparamagnetic Iron Oxide Nanoparticles (SPION): From Fundamentals to State-of-the-Art Innovative Applications for Cancer Therapy. *Pharmaceutics* **2023**, *15*.
- (6) Hamley, I. W., *Introduction to Soft Matter*; John Wiley & Sons, Ltd: 2007.
- (7) Sheiko, S. S.; Vashahi, F.; Morgan, B. J.; Maw, M.; Dashtimoghadam, E.; Fahimipour, F.; Jacobs, M.; Keith, A. N.; Vatankhah-Varnosfaderani, M.; Dobrynin, A. V. Mechanically Diverse Gels with Equal Solvent Content. *ACS Cent. Sci.* **2022**, *8*, 845–852.
- (8) Backes, S.; Witt, M. U.; Roeben, E.; Kuhrts, L.; Aleed, S.; Schmidt, A. M.; von Klitzing, R. Loading of PNIPAM Based Microgels with CoFe₂O₄ Nanoparticles and Their Magnetic Response in Bulk and at Surfaces. *J. Phys. Chem. B* **2015**, *119*, 12129–12137.
- (9) Deng, Y.; Yang, W.; Wang, C.; Fu, S. A Novel Approach for Preparation of Thermoresponsive Polymer Magnetic Microspheres with Core–Shell Structure. *Adv. Mater.* **2003**, *15*, 1729–1732, (accessed 01/08/2024).
- (10) Malik, V.; Pal, A.; Pravaz, O.; Crassous, J. J.; Granville, S.; Grobety, B.; Hirt, A. M.; Dietsch, H.; Schurtenberger, P. Hybrid magnetic iron oxide nanoparticles with tunable field-directed self-assembly. *Nanoscale* **2017**, *9*, 14405–14413.
- (11) Agrawal, L.; Saidani, M.; Guillaud, L.; Terenzio, M. Development of 3D culture scaffolds for directional neuronal growth using 2-photon lithography. *Mater. Sci. Eng. C* **2021**, *131*, 112502.

- (12) Abid, N.; Khan, A. M.; Shujait, S.; Chaudhary, K.; Ikram, M.; Imran, M.; Haider, J.; Khan, M.; Khan, Q.; Maqbool, M. Synthesis of nano-materials using various top-down and bottom-up approaches, influencing factors, advantages, and disadvantages: A review. *Adv. Colloid. Interfac.* **2022**, *300*, 102597.
- (13) Karg, M.; Pich, A.; Hellweg, T.; Hoare, T.; Lyon, L. A.; Crassous, J. J.; Suzuki, D.; Gumerov, R. A.; Schneider, S.; Potemkin, I. I.; Richtering, W. Nanogels and Microgels: From Model Colloids to Applications, Recent Developments, and Future Trends. *Langmuir* **2019**, *35*, 6231–6255.
- (14) Plamper, F. A.; Richtering, W. Functional microgels and microgel systems. *Accounts Chem. Res.* **2017**, *50*, 131–140.
- (15) Alejo, T.; Andreu, V.; Mendoza, G.; Sebastian, V.; Arruebo, M. Controlled release of bupivacaine using hybrid thermoresponsive nanoparticles activated via photothermal heating. *J. Colloid. Interf. Sci.* **2018**, *523*, 234–244.
- (16) Schmitt, J.; Hartwig, C.; Crassous, J. J.; Mihut, A. M.; Schurtenberger, P.; Alfredsson, V. Anisotropic mesoporous silica/microgel core-shell responsive particles. *RSC Adv.* **2020**, *10*, 25393–25401.
- (17) Crassous, J. J.; Mihut, A. M.; Månsson, L. K.; Schurtenberger, P. Anisotropic responsive microgels with tuneable shape and interactions. *Nanoscale* **2015**, *7*, 15971–15982.
- (18) Rose, J. C.; Gehlen, D. B.; Omidinia-Anarkoli, A.; Fölster, M.; Haraszti, T.; Jaekel, E. E.; De Laporte, L. How Much Physical Guidance is Needed to Orient Growing Axons in 3D Hydrogels? *Adv. Healthc. Mater.* **2020**, *9*, 2000886.
- (19) Rose, J. C.; Cámara-Torres, M.; Rahimi, K.; Köhler, J.; Möller, M.; De Laporte, L. Nerve Cells Decide to Orient inside an Injectable Hydrogel with Minimal Structural Guidance. *Nano Lett.* **2017**, *17*, 3782–3791.
- (20) Chandorkar, Y.; Castro Nava, A.; Schweizerhof, S.; Van Dongen, M.; Haraszti, T.; Köhler, J.; Zhang, H.; Windoffer, R.; Mourran, A.; Möller, M.; De Laporte, L. Cellular responses to beating hydrogels to investigate mechanotransduction. *Nat. Commun.* **2019**, *10*, 1–13.
- (21) Zhang, H.; Mourran, A.; Möller, M. Dynamic Switching of Helical Microgel Ribbons. *Nano Lett.* **2017**, *17*, 2010–2014.
- (22) Lu, Y.; Mei, Y.; Ballauff, M.; Drechsler, M. Thermosensitive Core-Shell Particles as Carrier Systems for Metallic Nanoparticles. *J. Phys. Chem.* **2006**, *110*, 3930–3937, (accessed 01/08/2024).
- (23) Vescovo, R.; Becker, M.; Natile, M. M.; Canton, P.; Evangelisti, C.; Biffis, A. Microgels as Soluble Scaffolds for the Preparation of Noble Metal Nanoparticles Supported on Nanostructured Metal Oxides. *ACS Appl. Nano Mater.* **2021**, *4*, 8343–8351.

- (24) Wiberg, N., *Lehrbuch der Anorganischen Chemie*; De Gruyter: Berlin, Boston, 2008.
- (25) Bean, C. P.; Livingston, J. D. Superparamagnetism. *J. Appl. Phys.* **2009**, *30*, S120–S129.
- (26) Antwi-Baah, R.; Wang, Y.; Chen, X.; Liu, H.; Yu, K. Hybrid morphologies of paramagnetic manganese-based nanoparticles as theranostics. *Chem. Eng. J.* **2023**, *466*, 142970.
- (27) Hossain, S.; Hossain, S. Hyperthermia Using Magnetic Cobalt Ferrite Magnetoelectric Nanoparticles. *IEEE T. Magn.* **2022**, *58*, 1–6.
- (28) Masunga, N.; Mmesesi, O. K.; Kefeni, K. K.; Mamba, B. B. Recent advances in copper ferrite nanoparticles and nanocomposites synthesis, magnetic properties and application in water treatment: Review. *J. Environ. Chem. Eng.* **2019**, *7*, 103179.
- (29) Lisjak, D.; Mertelj, A. Anisotropic magnetic nanoparticles: A review of their properties, syntheses and potential applications. *Prog. Mater. Sci.* **2018**, *95*, 286–328.
- (30) Reufer, M.; Martinez, V. A.; Schurtenberger, P.; Poon, W. C. K. Differential Dynamic Microscopy for Anisotropic Colloidal Dynamics. *Langmuir* **2012**, *28*, 4618–4624.
- (31) Martchenko, I.; Dietsch, H.; Moitzi, C.; Schurtenberger, P. Hydrodynamic Properties of Magnetic Nanoparticles with Tunable Shape Anisotropy: Prediction and Experimental Verification. *J. Phys. Chem. B* **2011**, *115*, 14838–14845.
- (32) Gurkan, U. A.; Tasoglu, S.; Kavaz, D.; Demirel, M. C.; Demirci, U. Emerging Technologies for Assembly of Microscale Hydrogels. *Adv. Healthc. Mater.* **2012**, *1*, 149–158.
- (33) Campbell, S.; Maitland, D.; Hoare, T. Enhanced Pulsatile Drug Release from Injectable Magnetic Hydrogels with Embedded Thermosensitive Microgels. *ACS Macro Lett.* **2015**, *4*, 312–316.
- (34) Bhattacharya, S.; Eckert, F.; Boyko, V.; Pich, A. Temperature-, pH-, and Magnetic-Field-Sensitive Hybrid Microgels. *Small* **2007**, *3*, 650–657.
- (35) Nickel, A. C.; Kratzenberg, T.; Bochenek, S.; Schmidt, M. M.; Rudov, A. A.; Falkenstein, A.; Potemkin, I. I.; Crassous, J. J.; Richtering, W. Anisotropic Microgels Show Their Soft Side. *Langmuir* **2022**, *38*, 5063–5080.
- (36) Zhang, F.; Wang, C.-C. Preparation of P(NIPAM-co-AA) Microcontainers Surface-Anchored with Magnetic Nanoparticles. *Langmuir* **2009**, *25*, 8255–8262, (accessed 01/08/2024).
- (37) Rose, J. C.; Fölster, M.; Kivilip, L.; Gerardo-Nava, J. L.; Jaekel, E. E.; Gehlen, D. B.; Rohlf, W.; De Laporte, L. Predicting the orientation of magnetic microgel rods for soft anisotropic biomimetic hydrogels. *Polym. Chem.* **2020**, *11*, 496–507.

- (38) Suzuki, D.; Kawaguchi, H. Stimuli-sensitive core/shell template particles for immobilizing inorganic nanoparticles in the core. *Colloid. Polym. Sci.* **2006**, *284*, 1443–1451, (accessed 01/08/2024).
- (39) Nunes, J.; Herlihy, K. P.; Mair, L.; Superfine, R.; DeSimone, J. M. Multifunctional Shape and Size Specific Magneto-Polymer Composite Particles. *Nano Lett.* **2010**, *10*, 1113–1119.
- (40) Crassous, J. J.; Mihut, A. M.; Dietsch, H.; Pravaz, O.; Ackermann-Hirschi, L.; Hirt, A. M.; Schurtenberger, P. Advanced multiresponsive comploids: from design to possible applications. *Nanoscale* **2014**, *6*, 8726–8735.
- (41) Dagallier, C.; Dietsch, H.; Schurtenberger, P.; Scheffold, F. Thermoresponsive hybrid microgel particles with intrinsic optical and magnetic anisotropy. *Soft Matter* **2010**, *6*, 2174–2177.
- (42) Liu, C.; Guo, J.; Yang, W.; Hu, J.; Wang, C.; Fu, S. Magnetic mesoporous silica microspheres with thermo-sensitive polymer shell for controlled drug release. *J. Mater. Chem.* **2009**, *19*, 4764–4770.
- (43) Stieger, M.; Pedersen, J. S.; Lindner, P.; Richtering, W. Are Thermoresponsive Microgels Model Systems for Concentrated Colloidal Suspensions? A Rheology and Small-Angle Neutron Scattering Study. *Langmuir* **2004**, *20*, 7283–7292.
- (44) Crassous, J. J.; Siebenbürger, M.; Ballauff, M.; Drechsler, M.; Henrich, O.; Fuchs, M. Thermosensitive core-shell particles as model systems for studying the flow behavior of concentrated colloidal dispersions. *J. Chem. Phys.* **2006**, *125*, 204906.
- (45) Siebenbürger, M.; Fuchs, M.; Ballauff, M. Core-shell microgels as model colloids for rheological studies. *Soft Matter* **2012**, *8*, 4014–4024.
- (46) Nussbaum, N.; Bergfreund, J.; Vialetto, J.; Isa, L.; Fischer, P. Microgels as globular protein model systems. *Colloids Surf. B* **2022**, *217*, 112595.
- (47) Liao, W.; Zhang, Y.; Guan, Y.; Zhu, X. X. Fractal Structures of the Hydrogels Formed in Situ from Poly(N-isopropylacrylamide) Microgel Dispersions. *Langmuir* **2012**, *28*, 10873–10880.
- (48) Thorkelsson, K.; Bai, P.; Xu, T. Self-assembly and applications of anisotropic nanomaterials: A review. *Nano Today* **2015**, *10*, 48–66.
- (49) Li, D.; Jiang, R.-R.; Chen, S.-K.; Wu, J.-M.; Dong, X.; Wang, X.-L.; Wang, Y.-Z.; Song, F. Rapid, linear, and highly reliable structural-color switching enabled by thermal regulation of chiral nematic mesophases. *Chem. Eng. J.* **2023**, *453*, 139835.
- (50) Frenkel, D.; Mulder, B. M.; McTague, J. P. Phase Diagram of a System of Hard Ellipsoids. *Phys. Rev. Lett.* **1984**, *52*, 287–290.
- (51) Tang, J.; Fraden, S. Magnetic-field-induced isotropic-nematic phase transition in a colloidal suspension. *Phys. Rev. Lett.* **1993**, *71*, 3509–3512.

- (52) Dong, Y.; Wang, S.; Ke, Y.; Ding, L.; Zeng, X.; Magdassi, S.; Long, Y. 4D Printed Hydrogels: Fabrication, Materials, and Applications. *Adv. Mater. Technol.* **2020**, *5*, 2000034.
- (53) Khoo, M.; Liu, C. Micro magnetic silicone elastomer membrane actuator. *Sens. Actuators A: Phys.* **2001**, *89*, 259–266.
- (54) Lan, X.; Huang, W.; Leng, J. Shape Memory Effect in Micro-Sized Shape Memory Polymer Composite Chains. *App. Sci.* **2019**, *9*.
- (55) Li, S.; Librandi, G.; Yao, Y.; Richard, A. J.; Schneider-Yamamura, A.; Aizenberg, J.; Bertoldi, K. Controlling Liquid Crystal Orientations for Programmable Anisotropic Transformations in Cellular Microstructures. *Adv. Mater.* **2021**, *33*, 2105024.
- (56) Wang, Z.; Wang, K.; Tang, X. Heterogeneous magnetic micropillars for regulated bending actuation. *Extreme Mech. Lett.* **2020**, *38*, 100734.
- (57) Sung, B.; Kim, M.-H.; Abelman, L. Magnetic microgels and nanogels: Physical mechanisms and biomedical applications. *Bioeng. Transl. Med.* **2021**, *6*, e10190.
- (58) Zhou, H.; Mayorga-Martinez, C. C.; Pané, S.; Zhang, L.; Pumera, M. Magnetically Driven Micro and Nanorobots. *Chem. Rev.* **2021**, *121*, 4999–5041.
- (59) Ghosh, A.; Xu, W.; Gupta, N.; Gracias, D. H. Active matter therapeutics. *Nano Today* **2020**, *31*, 100836.
- (60) Alapan, Y.; Bozuyuk, U.; Erkoç, P.; Karacakol, A. C.; Sitti, M. Multifunctional surface microrollers for targeted cargo delivery in physiological blood flow. *Sci. Robot.* **2020**, *5*, eaba5726.
- (61) Driscoll, M.; Delmotte, B.; Youssef, M.; Sacanna, S.; Donev, A.; Chaikin, P. Unstable fronts and motile structures formed by microrollers. *Nat. Phys.* **2017**, *13*, 375–379.
- (62) Kim, S.-H.; Sim, J. Y.; Lim, J.-M.; Yang, S.-M. Magneto-responsive Microparticles with Nanoscopic Surface Structures for Remote-Controlled Locomotion. *Angew. Chem., Int. Ed.* **2010**, *49*, 3786–3790.
- (63) Gao, Y.; Sprinkle, B.; Springer, E.; Marr, D. W. M.; Wu, N. Rolling of soft microbots with tunable traction. *Sci. Adv.* **2023**, *9*, eadg0919.
- (64) Mair, L. O.; Evans, B. A.; Nacev, A.; Stepanov, P. Y.; Hilaman, R.; Chowdhury, S.; Jafari, S.; Wang, W.; Shapiro, B.; Weinberg, I. N. Magnetic microkayaks: propulsion of microrods precessing near a surface by kilohertz frequency, rotating magnetic fields. *Nanoscale* **2017**, *9*, 3375–3381.
- (65) Lin, Z.; Fan, X.; Sun, M.; Gao, C.; He, Q.; Xie, H. Magnetically Actuated Peanut Colloid Motors for Cell Manipulation and Patterning. *ACS Nano* **2018**, *12*, 2539–2545.

- (66) Zhou, Q.; Petit, T.; Choi, H.; Nelson, B. J.; Zhang, L. Dumbbell Fluidic Tweezers for Dynamical Trapping and Selective Transport of Microobjects. *Advanced Functional Materials* **2016**, *27*.
- (67) Zhang, L.; Abbott, J. J.; Dong, L.; Kratochvil, B. E.; Bell, D.; Nelson, B. J. Artificial bacterial flagella: Fabrication and magnetic control. *Appl. Phys. Lett.* **2009**, *94*, 064107.
- (68) Wang, X.; Chen, X.-Z.; Alcântara, C. C. J.; Sevim, S.; Hoop, M.; Terzopoulou, A.; de Marco, C.; Hu, C.; de Mello, A. J.; Falcão, P.; Furukawa, S.; Nelson, B. J.; Puigmartí-Luis, J.; Pané, S. MOFBOTS: Metal-Organic-Framework-Based Biomedical Micro-robots. *Adv. Mater.* **2019**, *31*, 1901592.
- (69) Frka-Petesic, B.; Erglis, K.; Berret, J. F.; Cebers, A.; Dupuis, V.; Fresnais, J.; Sandre, O.; Perzynski, R. Dynamics of paramagnetic nanostructured rods under rotating field. *J. Magn. Magn. Mater.* **2011**, *323*, 1309–1313.
- (70) Maruo, S.; Inoue, H. Optically driven micropump produced by three-dimensional two-photon microfabrication. *Appl. Phys. Lett.* **2006**, *89*, 144101.
- (71) Lei, K. F.; Law, W. C.; Suen, Y.-K.; Li, W. J.; Yam, Y.; Ho, H. P.; Kong, S.-K. A vortex pump-based optically-transparent microfluidic platform for biotech and medical applications. *Proc. Inst. Mech. Eng. Part H J. Eng. Med.* **2007**, *221*, 129–141.
- (72) Ebrahimi, N. et al. Magnetic Actuation Methods in Bio/Soft Robotics. *Adv. Funct. Mater.* **2021**, *31*, 2005137.
- (73) Kornev, K. G.; Gu, Y.; Aprelev, P.; Tokarev, A. In *Magnetic Characterization Techniques for Nanomaterials*, Kumar, C. S., Ed.; Springer: Berlin, Heidelberg, 2017.
- (74) Petit, T.; Zhang, L.; Peyer, K. E.; Kratochvil, B. E.; Nelson, B. J. Selective Trapping and Manipulation of Microscale Objects Using Mobile Microvortices. *Nano Lett.* **2012**, *12*, 156–160.
- (75) Van Reenen, A.; de Jong, A. M.; den Toonder, J. M. J.; Prins, M. W. J. Integrated lab-on-chip biosensing systems based on magnetic particle actuation - a comprehensive review. *Lab Chip* **2014**, *14*, 1966–1986.
- (76) Schuerle, S.; Soleimany, A. P.; Yeh, T.; Anand, G. M.; Häberli, M.; Fleming, H. E.; Mirkhani, N.; Qiu, F.; Hauert, S.; Wang, X.; Nelson, B. J.; Bhatia, S. N. Synthetic and living micropropellers for convection-enhanced nanoparticle transport. *Sci. Adv.* **2019**, *5*, eaav4803.
- (77) Regmi, R.; Bhattarai, S. R.; Sudakar, C.; Wani, A. S.; Cunningham, R.; Vaishnav, P. P.; Naik, R.; Oupicky, D.; Lawes, G. Hyperthermia controlled rapid drug release from thermosensitive magnetic microgels. *J. Mater. Chem.* **2010**, *20*, 6158–6163.

- (78) Cazares-Cortes, E.; Espinosa, A.; Guigner, J.-M.; Michel, A.; Grif-fete, N.; Wilhelm, C.; Ménager, C. Doxorubicin Intracellular Remote Release from Biocompatible Oligo(ethylene glycol) Methyl Ether Methacrylate-Based Magnetic Nanogels Triggered by Magnetic Hyperthermia. *ACS Appl. Mater. Interfaces* **2017**, *9*, 25775–25788.
- (79) Shin, B. Y.; Cha, B. G.; Jeong, J. H.; Kim, J. Injectable Macroporous Ferrogel Microbeads with a High Structural Stability for Magnetically Actuated Drug Delivery. *ACS Appl. Mater. Interfaces* **2017**, *9*, 31372–31380.
- (80) Patri, S.; Thanh, N. T. K.; Kamaly, N. Magnetic iron oxide nanogels for combined hyperthermia and drug delivery for cancer treatment. *Nanoscale* **2024**, *16*, 15446–15464.
- (81) Wang, X.; Niu, D.; Li, P.; Wu, Q.; Bo, X.; Liu, B.; Bao, S.; Su, T.; Xu, H.; Wang, Q. Dual-Enzyme-Loaded Multifunctional Hybrid Nanogel System for Pathological Responsive Ultrasound Imaging and T2-Weighted Magnetic Resonance Imaging. *ACS Nano* **2015**, *9*, 5646–5656.
- (82) Rose, J. C.; De Laporte, L. Hierarchical Design of Tissue Regenerative Constructs. *Adv. Healthc. Mater.* **2018**, *7*, 1701067.
- (83) Liu, Z.; Tan, X.; Huang, Y.; Li, W.; Yang, N.; Yuan, R.; Cheng, Q.; Liu, L.; Ge, L. Microwave absorption-based magnetic liquid metal nano-missiles for thermodynamic/ immunological cascade hepatoma therapy. *Chem. Eng. J.* **2023**, *471*, 144688.
- (84) Xu, F.; Wu, C.-a. M.; Rengarajan, V.; Finley, T. D.; Keles, H. O.; Sung, Y.; Li, B.; Gurkan, U. A.; Demirci, U. Three-Dimensional Magnetic Assembly of Microscale Hydrogels. *Adv. Mater.* **2011**, *23*, 4254–4260.
- (85) Tasoglu, S.; Yu, C. H.; Gungordu, H. I.; Guven, S.; Vural, T.; Demirci, U. Guided and magnetic self-assembly of tunable magnetoceptive gels. *Nat. Commun.* **2014**, *5*, 4702.
- (86) Prime, R. B.; Bair, H. E.; Vyazovkin, S.; Gallagher, P. K.; Riga, A., *Thermogravimetric Analysis (TGA)*, 2009, pp 241–317.
- (87) Jiang, L.; Liu, P. Novel Magnetic Fly Ash/Poly(acrylic acid) Composite Microgel for Selective Adsorption of Pb(II) Ion: Synthesis and Evaluation. *Ind. Eng. Chem. Res.* **2014**, *53*, 2924–2931.
- (88) Ur Rehman, S.; Khan, A. R.; Sahiner, M.; Sengel, S. B.; Aktas, N.; Siddiq, M.; Sahiner, N. Removal of arsenate and dichromate ions from different aqueous media by amine based p(TAEA-co-GDE) microgels. *J. Environ. Manage.* **2017**, *197*, 631–641.
- (89) Schärftl, W., *Light Scattering from Polymer Solutions and Nanoparticle Dispersions*; Springer Berlin Heidelberg: 2007.
- (90) *Neutrons, X-rays and light, Scattering methods applied to soft condensed matter*, Transferred to digital print.; Lindner, P., Ed.; North-Holland delta series; Elsevier: Amsterdam [u.a.], 2006; 541 pp.

-
- (91) Germain, D.; Leocmach, M.; Gibaud, T. Differential dynamic microscopy to characterize Brownian motion and bacteria motility. *Am. J. Phys.* **2016**, *84*, 202–210.
- (92) Koppel, D. E. Analysis of Macromolecular Polydispersity in Intensity Correlation Spectroscopy: The Method of Cumulants. *J. Chem. Phys.* **2003**, *57*, 4814–4820.
- (93) Guinier, A.; Fournet, G., *Small angle scattering of X-rays*; John Wiley and Son: 1955.
- (94) Sasview, 2024, <http://www.sasview.org/>.
- (95) Cerbino, R.; Trappe, V. Differential Dynamic Microscopy: Probing Wave Vector Dependent Dynamics with a Microscope. *Phys. Rev. Lett.* **2008**, *100*, 188102.
- (96) Giavazzi, F.; Brogioli, D.; Trappe, V.; Bellini, T.; Cerbino, R. Scattering information obtained by optical microscopy: Differential dynamic microscopy and beyond. *Phys. Rev. E* **2009**, *80*, 031403.
- (97) Dux Frederic; Crassous, J. J. DDMSOft, 2021.
- (98) Linnemann, A.; Köhl, S., *Grundlagen der Licht- und Elektronenmikroskopie*, 1. Auflage; Ulmer: Stuttgart, Deutschland, 2017, p 397.
- (99) Mertz, J., *Introduction to Optical Microscopy*, 2nd ed.; Cambridge University Press: 2019.
- (100) Cremer, C. Lichtmikroskopie unterhalb des Abbe-Limits. Lokalisationsmikroskopie. *Physik in unserer Zeit* **2011**, *42*, 21–29.
- (101) Mhadhbi, M., *Electron Microscopy*, 2022.
- (102) Michler, G. H., *Electron microscopy of polymers*; Springer Laboratory; Springer: Berlin, 2010; 473 pp.
- (103) Fernández-Barbero, A.; Suárez, I. J.; Sierra-Martín, B.; Fernández-Nieves, A.; de las Nieves, F. J.; Marquez, M.; Rubio-Retama, J.; López-Cabarcos, E. Gels and microgels for nanotechnological applications. *Adv. Colloid. Interfac.* **2009**, *147-148*, 88–108.
- (104) Qian, J.; Zhou, L.; Yang, X.; Hua, D.; Wu, N. Prussian blue analogue functionalized magnetic microgels with ionized chitosan for the cleaning of cesium-contaminated clay. *J. Hazard. Mater.* **2020**, *386*, 121965.
- (105) Martchenko, I.; Crassous, J. J.; Mihut, A. M.; Bialik, E.; Hirt, A. M.; Rufier, C.; Menzel, A.; Dietsch, H.; Linse, P.; Schurtenberger, P. Anisotropic magnetic particles in a magnetic field. *Soft Matter* **2016**, *12*, 8755–8767.
- (106) Dagallier, C.; Cardinaux, F.; Dietsch, H.; Scheffold, F. Magnetic orientation of soft particles in a jammed solid. *Soft Matter* **2012**, *8*, 4067.

- (107) Martin, J. E.; Venturini, E.; Odinek, J.; Anderson, R. A. Anisotropic magnetism in field-structured composites. *Phys. Rev. E* **2000**, *61*, 2818–2830, (accessed 12/18/2023).
- (108) Ocaña, M.; Morales, M. P.; Serna, C. J. Homogeneous Precipitation of Uniform α -Fe₂O₃ Particles from Iron Salts Solutions in the Presence of Urea. *J. Colloid Interf. Sci.* **1999**, *212*, 317–323.
- (109) Nickel, A. C. Anisotropic Microgels: From Synthesis to Features in 2 and 3 Dimensions, Ph.D. Thesis, RWTH Aachen University, 2022.
- (110) Graf, C.; Vossen, D. L. J.; Imhof, A.; van Blaaderen, A. A General Method To Coat Colloidal Particles with Silica. *Langmuir* **2003**, *19*, 6693–6700.
- (111) Match! - Phase Analysis using Powder Diffraction, Kreuzherrenstr. 102, 53227 Bonn, Germany, <https://www.crystalimpact.com/match/>.
- (112) R. M. Cornell, U. S., *The Iron Oxides: Structure, Properties, Reactions, Occurences and Uses*, 2nd ed.; Wiley-VCH Verlag GmbH: 2003.
- (113) Reufer, M.; Dietsch, H.; Gasser, U.; Hirt, A.; Menzel, A.; Schurtenberger, P. Morphology and Orientational Behavior of Silica-Coated Spindle-Type Hematite Particles in a Magnetic Field Probed by Small-Angle X-ray Scattering. *J. Phys. Chem.* **2010**, *114*, 4763–4769.
- (114) Pal, A.; Martinez, V. A.; Ito, T. H.; Arlt, J.; Crassous, J. J.; Poon, W. C. K.; Schurtenberger, P. Anisotropic dynamics and kinetic arrest of dense colloidal ellipsoids in the presence of an external field studied by differential dynamic microscopy. *Sci. Adv.* **2024**, *6*, eaaw9733.
- (115) Martchenko, I. Magnetic colloidal ellipsoids, Ph.D. Thesis, Universität Freiburg in der Schweiz, 2014.
- (116) Perrin, F. Mouvement Brownien d'un ellipsoïde (II). Rotation libre et dépolarisation des fluorescences. Translation et diffusion de molécules ellipsoïdales. *J. Phys. Radium* **1936**, *7*, 1–11.
- (117) Mørup, S.; Hansen, M. F.; Frandsen, C. Magnetic interactions between nanoparticles. *Beilstein J. Nanotechnol.* **2010**, *1*, 182–190.
- (118) Li, Z.; Qian, C.; Xu, W.; Zhu, C.; Yin, Y. Coupling morphological and magnetic anisotropy for assembling tetragonal colloidal crystals. *Sci. Adv.* **2021**, *7*, eabh1289.
- (119) Karg, M.; Wellert, S.; Pastoriza-Santos, I.; Lapp, A.; Liz-Marzán, L. M.; Hellweg, T. Thermoresponsive core-shell microgels with silica nanoparticle cores: size, structure, and volume phase transition of the polymer shell. *Phys. Chem. Chem. Phys.* **2008**, *10*, 6708–6716.
- (120) Hildebrandt, M.; Lazarev, S.; Pérez, J.; Vartanyants, I. A.; Meijer, J.-M.; Karg, M. SAXS Investigation of Core-Shell Microgels with High Scattering Contrast Cores: Access to Structure Factor and Volume Fraction. *Macromolecules* **2022**, *55*, 2959–2969.

-
- (121) Scotti, A.; Schulte, M. F.; Lopez, C. G.; Crassous, J. J.; Bochenek, S.; Richtering, W. How Softness Matters in Soft Nanogels and Nanogel Assemblies. *Chem. Rev.* **2022**, *122*, 11675–11700.
- (122) Dai, Z.; Ngai, T. Microgel particles: The structure-property relationships and their biomedical applications. *J. Polym. Sci. Part A: Polym. Chem.* **2013**, *51*, 2995–3003.
- (123) Wang, H.; Wu, X.; Zhu, Z.; Liu, C. S.; Zhang, Z. Revisit to phase diagram of poly(N-isopropylacrylamide) microgel suspensions by mechanical spectroscopy. *J. Chem. Phys.* **2014**, *140*, 024908.
- (124) Coulais, C.; Candelier, R.; Dauchot, O. The glass and jamming transitions in dense granular matter. *AIP Conf. Proc.* **2013**, *1542*, 25–31.
- (125) Purnomo, E. H.; van den Ende, D.; Vanapalli, S. A.; Mugele, F. Glass Transition and Aging in Dense Suspensions of Thermosensitive Microgel Particles. *PRL* **2008**, *101*, 238301.
- (126) Binder, K.; Young, A. P. Spin glasses: Experimental facts, theoretical concepts, and open questions. *Rev. Mod. Phys.* **1986**, *58*, 801–976.
- (127) Greenspan, L. Humidity fixed points of binary saturated aqueous solutions. *J. Res. NBS A: Phys. Chem.* **1977**, *81A*, 89.
- (128) Dierking, I.; Al-Zangana, S. Lyotropic Liquid Crystal Phases from Anisotropic Nanomaterials. *Nanomaterials* **2017**, *7*, 305.
- (129) Bolhuis, P.; Frenkel, D. Tracing the phase boundaries of hard spherocylinders. *The Journal of Chemical Physics* **1997**, *106*, 666–687.
- (130) Abramoff, M.; Magalhães, P.; Ram, S. J. Image Processing with ImageJ. *Biophotonics Int.* **2003**, *11*, 36–42.
- (131) Roger, K.; Crassous, J. J. How the interplay of molecular and colloidal scales controls drying of microgel dispersions. *Proc. Natl. Acad. Sci. U.S.A.* **2021**, *118*.
- (132) Torquato, S.; Stillinger, F. H. Multiplicity of Generation, Selection, and Classification Procedures for Jammed Hard-Particle Packings. *J. Phys. Chem. B* **2001**, *105*, 11849–11853.
- (133) Giacco, F.; de Arcangelis, L.; Pica Ciamarra, M.; Lippiello, E. Rattler-induced aging dynamics in jammed granular systems. *Soft Matter* **2017**, *13*, 9132–9137.
- (134) Fulcrand, R.; Jugieu, D.; Escriba, C.; Bancaud, A.; Bourrier, D.; Boukabache, A.; Gué, A. M. Development of a flexible microfluidic system integrating magnetic micro-actuators for trapping biological species. *J. Micromech. Microeng.* **2009**, *19*, 105019.
- (135) Jung, J. H.; Han, C.; Lee, S. A.; Kim, J.; Yang, C. Microfluidic-integrated laser-controlled microactuators with on-chip microscopy imaging functionality. *Lab Chip* **2014**, *14*, 3781–3789.

- (136) Decroly, G.; Toncheva, A.; Blanc, L.; Raquez, J.-M.; Lessinnes, T.; Delchambre, A.; Lambert, P. Programmable Stimuli-Responsive Actuators for Complex Motions in Soft Robotics: Concept, Design and Challenges. *Actuators* **2020**, *9*, 131.
- (137) Lee, S. A.; Lee, H.; Pinney, J. R.; Khialeeva, E.; Bergsneider, M.; Judy, J. W. Development of microfabricated magnetic actuators for removing cellular occlusion. *J. Micromech. Microeng.* **2011**, *21*, 054006.
- (138) Guven, S.; Chen, P.; Inci, F.; Tasoglu, S.; Erkmen, B.; Demirci, U. Multiscale assembly for tissue engineering and regenerative medicine. *Trends Biotechnol.* **2015**, *33*, 269–279.
- (139) Place, E. S.; Evans, N. D.; Stevens, M. M. Complexity in biomaterials for tissue engineering. *Nat. Mater.* **2009**, *8*, 457–70.
- (140) Engelmayer, G. C.; Cheng, M.; Bettinger, C. J.; Borenstein, J. T.; Langer, R.; Freed, L. E. Accordion-like honeycombs for tissue engineering of cardiac anisotropy. *Nat. Mater.* **2008**, *7*, 1003–1010.
- (141) Hirt, M. N.; Hansen, A.; Eschenhagen, T. Cardiac Tissue Engineering. *Circ. Res.* **2014**, *114*, 354–367.
- (142) Sun, Y.; You, Y.; Jiang, W.; Wang, B.; Wu, Q.; Dai, K. 3D bioprinting dual-factor releasing and gradient-structured constructs ready to implant for anisotropic cartilage regeneration. *Sci. Adv.* **2020**, *6*, eaay1422.
- (143) Şenol, M. S.; Özer, H. In *Comparative Kinesiology of the Human Body*, Angin, S., Şimşek, I. E., Eds.; Academic Press: 2020, pp 91–100.
- (144) Madeira, C.; Santhagunam, A.; Salgueiro, J. B.; Cabral, J. M. S. Advanced cell therapies for articular cartilage regeneration. *Trends Biotechnol.* **2015**, *33*, 35–42.
- (145) Corey, J. M.; Lin, D. Y.; Mycek, K. B.; Chen, Q.; Samuel, S.; Feldman, E. L.; Martin, D. C. Aligned electrospun nanofibers specify the direction of dorsal root ganglia neurite growth. *J. Biomed. Mater. Res. A* **2007**, *83A*, 636–645.
- (146) Basurto, I. M.; Mora, M. T.; Gardner, G. M.; Christ, G. J.; Caliar, S. R. Aligned and electrically conductive 3D collagen scaffolds for skeletal muscle tissue engineering. *Biomater. Sci.* **2021**, *9*, 4040–4053.
- (147) Johnson, C. D. L.; Ganguly, D.; Zuidema, J. M.; Cardinal, T. J.; Ziemba, A. M.; Kearns, K. R.; McCarthy, S. M.; Thompson, D. M.; Ramanath, G.; Borca-Tasciuc, D. A.; Dutz, S.; Gilbert, R. J. Injectable, Magnetically Orienting Electrospun Fiber Conduits for Neuron Guidance. *ACS Appl. Mater. Interfaces* **2019**, *11*, 356–372.
- (148) Omidinia-Anarkoli, A.; Boesveld, S.; Tuvshindorj, U.; Rose, J. C.; Haraszti, T.; De Laporte, L. An Injectable Hybrid Hydrogel with Oriented Short Fibers Induces Unidirectional Growth of Functional Nerve Cells. *Small* **2017**, *13*, 1702207.

- (149) Berns, E. J.; Sur, S.; Pan, L.; Goldberger, J. E.; Suresh, S.; Zhang, S.; Kessler, J. A.; Stupp, S. I. Aligned neurite outgrowth and directed cell migration in self-assembled monodomain gels. *Biomaterials* **2014**, *35*, 185–95.
- (150) Sheikhi, A.; de Rutte, J.; Haghniaz, R.; Akouissi, O.; Sohrabi, A.; Di Carlo, D.; Khademhosseini, A. Microfluidic-enabled bottom-up hydrogels from annealable naturally-derived protein microbeads. *Biomaterials* **2019**, *192*, 560–568.
- (151) Truong, N. F.; Kurt, E.; Tahmizyan, N.; Leshner-Pérez, S. C.; Chen, M.; Darling, N. J.; Xi, W.; Segura, T. Microporous annealed particle hydrogel stiffness, void space size, and adhesion properties impact cell proliferation, cell spreading, and gene transfer. *Acta Biomater.* **2019**, *94*, 160–172.
- (152) Rose, J. C.; Gehlen, D. B.; Haraszti, T.; Köhler, J.; Licht, C. J.; De Laporte, L. Biofunctionalized aligned microgels provide 3D cell guidance to mimic complex tissue matrices. *Biomaterials* **2018**, *163*, 128–141.
- (153) Du, Y.; Lo, E.; Ali, S.; Khademhosseini, A. Directed assembly of cell-laden microgels for fabrication of 3D tissue constructs. *Proc. Natl. Acad. Sci.* **2008**, *105*, 9522–9527.
- (154) Zhang, H.; Koens, L.; Lauga, E.; Mourran, A.; Möller, M. A Light-Driven Microgel Rotor. *Small* **2019**, *15*, 1903379.
- (155) Özbaş, Z.; Özkahraman, B.; Bal Öztürk, A. Controlled release profile of 5-fluorouracil loaded P(AAM-co-NVP-co-DEAEMA) microgel prepared via free radical precipitation polymerization. *Polym. Bull.* **2018**, *75*, 3053–3067.
- (156) Minina, E. S.; Sánchez, P. A.; Likos, C. N.; Kantorovich, S. S. The influence of the magnetic filler concentration on the properties of a microgel particle: Zero-field case. *J. Magn. Magn. Mater.* **2018**, *459*, 226–230.
- (157) Schmid, A. J.; Dubbert, J.; Rudov, A. A.; Pedersen, J. S.; Lindner, P.; Karg, M.; Potemkin, I. I.; Richtering, W. Multi-Shell Hollow Nanogels with Responsive Shell Permeability. *Sci. Rep.* **2016**, *6*, 22736.
- (158) Kittel, Y.; Kuehne, A. J. C.; De Laporte, L. Translating Therapeutic Microgels into Clinical Applications. *Adv. Healthc. Mater.* **2021**, *11*, e2101989.
- (159) Guerzoni, L. P. B.; Rose, J. C.; Gehlen, D. B.; Jans, A.; Haraszti, T.; Wessling, M.; Kuehne, A. J. C.; De Laporte, L. Cell Encapsulation in Soft, Anisometric Poly(ethylene) Glycol Microgels Using a Novel Radical-Free Microfluidic System. *Small* **2019**, *15*, 1900692.

- (160) Guerzoni, L. P. B.; Tsukamoto, Y.; Gehlen, D. B.; Rommel, D.; Haraszti, T.; Akashi, M.; De Laporte, L. A Layer-by-Layer Single-Cell Coating Technique To Produce Injectable Beating Mini Heart Tissues via Microfluidics. *Biomacromolecules* **2019**, *20*, 3746–3754.
- (161) Rommel, D.; Mork, M.; Vedaraman, S.; Bastard, C.; Guerzoni, L. P. B.; Kittel, Y.; Vinokur, R.; Born, N.; Haraszti, T.; De Laporte, L. Functionalized Microgel Rods Interlinked into Soft Macroporous Structures for 3D Cell Culture. *Adv. Sci.* **2022**, *9*, 2103554.
- (162) Qazi, T. H.; Wu, J.; Muir, V. G.; Weintraub, S.; Gullbrand, S. E.; Lee, D.; Issadore, D.; Burdick, J. A. Anisotropic Rod-Shaped Particles Influence Injectable Granular Hydrogel Properties and Cell Invasion. *Adv. Mater.* **2022**, *34*, 2109194.
- (163) Daly, A. C.; Riley, L.; Segura, T.; Burdick, J. A. Hydrogel microparticles for biomedical applications. *Nat. Rev. Mater.* **2020**, *5*, 20–43.
- (164) Griffin, D. R.; Weaver, W. M.; Scumpia, P. O.; Di Carlo, D.; Segura, T. Accelerated wound healing by injectable microporous gel scaffolds assembled from annealed building blocks. *Nat. Mater.* **2015**, *14*, 737.
- (165) Kim, J.; Staunton, J. R.; Tanner, K. Independent Control of Topography for 3D Patterning of the ECM Microenvironment. *Adv. Mater.* **2016**, *28*, 132–137.
- (166) Licht, C.; Rose, J. C.; Anarkoli, A. O.; Blondel, D.; Roccio, M.; Haraszti, T.; Gehlen, D. B.; Hubbell, J. A.; Lutolf, M. P.; De Laporte, L. Synthetic 3D PEG-Anisogel Tailored with Fibronectin Fragments Induce Aligned Nerve Extension. *Biomacromolecules* **2019**, *20*, 4075–4087.
- (167) Hoffelner, D.; Kundt, M.; Schmidt, A. M.; Kentzinger, E.; Bender, P.; Disch, S. Directing the orientational alignment of anisotropic magnetic nanoparticles using dynamic magnetic fields. *Faraday Discuss.* **2015**, *181*, 449–461.
- (168) Karlsson, H. L.; Cronholm, P.; Gustafsson, J.; Möller, L. Copper Oxide Nanoparticles Are Highly Toxic: A Comparison between Metal Oxide Nanoparticles and Carbon Nanotubes. *Chem. Res. Toxicol.* **2008**, *21*, 1726–1732.
- (169) Karlsson, H. L.; Gustafsson, J.; Cronholm, P.; Möller, L. Size-dependent toxicity of metal oxide particles—A comparison between nano- and micrometer size. *Toxicol. Lett.* **2009**, *188*, 112–118.
- (170) Singh, N.; Jenkins, G. J. S.; Asadi, R.; Doak, S. H. Potential toxicity of superparamagnetic iron oxide nanoparticles (SPION). *Nano Rev.* **2010**, *1*, 5358.
- (171) Wang, L.; Meng, Z.; Chen, Y.; Zheng, Y. Engineering Magnetic Micro/Nanorobots for Versatile Biomedical Applications. *Adv. Intell. Syst.* **2021**, *3*, 2000267.

- (172) Xia, X.; Spadaccini, C. M.; Greer, J. R. Responsive materials architected in space and time. *Nat. Rev. Mater.* **2022**, *7*, 683–701.
- (173) Jackson, J. A.; Messner, M. C.; Dudukovic, N. A.; Smith, W. L.; Bekker, L.; Moran, B.; Golobic, A. M.; Pascall, A. J.; Duoss, E. B.; Loh, K. J., et al. Field responsive mechanical metamaterials. *Sci. Adv.* **2018**, *4*, eaau6419.
- (174) Aubret, A.; Martinet, Q.; Palacci, J. Metamachines of pluripotent colloids. *Nat. Commun.* **2021**, *12*, 1–9.
- (175) Han, D.; Farino, C.; Yang, C.; Scott, T.; Browe, D.; Choi, W.; Freeman, J. W.; Lee, H. Soft robotic manipulation and locomotion with a 3D printed electroactive hydrogel. *ACS Appl. Mater. Interfaces* **2018**, *10*, 17512–17518.
- (176) Cui, J.; Huang, T.-Y.; Luo, Z.; Testa, P.; Gu, H.; Chen, X.-Z.; Nelson, B. J.; Heyderman, L. J. Nanomagnetic encoding of shape-morphing micromachines. *Nature* **2019**, *575*, 164–168.
- (177) Schmidt, A. M. Electromagnetic activation of shape memory polymer networks containing magnetic nanoparticles. *Macromol. Rapid Commun.* **2006**, *27*, 1168–1172.
- (178) Ze, Q.; Kuang, X.; Wu, S.; Wong, J.; Montgomery, S. M.; Zhang, R.; Kovitz, J. M.; Yang, F.; Qi, H. J.; Zhao, R. Magnetic shape memory polymers with integrated multifunctional shape manipulation. *Adv. Mater.* **2020**, *32*, 1906657.
- (179) Xu, T.; Zhang, J.; Salehizadeh, M.; Onaizah, O.; Diller, E. Millimeter-scale flexible robots with programmable three-dimensional magnetization and motions. *Sci. Robot.* **2019**, *4*, eaav4494.
- (180) Beebe, D. J.; Moore, J. S.; Bauer, J. M.; Yu, Q.; Liu, R. H.; Devadoss, C.; Jo, B. H. Functional hydrogel structures for autonomous flow control inside microfluidic channels. *Nature* **2000**, *404*, 588–590.
- (181) Eddington, D. T.; Beebe, D. J. Flow control with hydrogels. *Adv. Drug Deliver. Rev.* **2004**, *56*, 199–210.
- (182) Terray, A.; Oakey, J.; Marr, D. W. Microfluidic control using colloidal devices. *Science* **2002**, *296*, 1841–1844.
- (183) Han, K.; Shields IV, C. W.; Diwakar, N. M.; Bharti, B.; López, G. P.; Velev, O. D. Sequence-encoded colloidal origami and microbot assemblies from patchy magnetic cubes. *Sci. Adv.* **2017**, *3*, e1701108.
- (184) Matteucci, M.; Perennes, F.; Marmiroli, B.; Miotti, P.; Vaccari, L.; Gosparini, A.; Turchet, A.; Di Fabrizio, E. Compact micropumping system based on LIGA fabricated microparts. *Microelectronic Eng.* **2006**, *83*, 1288–1290.
- (185) Wolff, H. J.; Linkhorst, J.; Göttlich, T.; Savinsky, J.; Krüger, A. J.; de Laporte, L.; Wessling, M. Soft temperature-responsive microgels of complex shape in stop-flow lithography. *Lab Chip* **2020**, *20*, 285–295.

- (186) Weigel, N.; Li, Y.; Thiele, J.; Fery, A. From microfluidics to hierarchical hydrogel materials. *Curr. Opin. Colloid In.* **2023**, *64*, 101673.
- (187) Babu, S.; Chen, I.; Vedaraman, S.; Gerardo-Nava, J.; Licht, C.; Kittel, Y.; Haraszti, T.; Di Russo, J.; De Laporte, L. How do the Local Physical, Biochemical, and Mechanical Properties of an Injectable Synthetic Anisotropic Hydrogel Affect Oriented Nerve Growth? *Adv. Funct. Mater.* **2022**, 2202468.
- (188) Oberdick, S. D.; Zabow, G. Patterned Surface Energy in Elastomeric Molds as a Generalized Approach to Polymer Particle Fabrication. *ACS Appl. Polym. Mater.* **2020**, *2*, 846–852.
- (189) Lee, H.; Kim, J.; Kim, H.; Kim, J.; Kwon, S. Colour-barcoded magnetic microparticles for multiplexed bioassays. *Nat. Mater.* **2010**, *9*, 745–749.
- (190) Suh, S. K.; Chapin, S. C.; Hatton, T. A.; Doyle, P. S. Synthesis of magnetic hydrogel microparticles for bioassays and tweezer manipulation in microwells. *Microfluid. Nanofluid.* **2012**, *13*, 665–674.
- (191) Hakimi, N.; Tsai, S. S.; Cheng, C.-H.; Hwang, D. K. One-step two-dimensional microfluidics-based synthesis of three-dimensional particles. *Adv. Mater.* **2014**, *26*, 1393–1398.
- (192) Suh, S. K.; Yuet, K.; Hwang, D. K.; Bong, K. W.; Doyle, P. S.; Hatton, T. A. Synthesis of nonspherical superparamagnetic particles: in situ coprecipitation of magnetic nanoparticles in microgels prepared by stop-flow lithography. *J. Am. Chem. Soc.* **2012**, *134*, 7337–7343.
- (193) Sanchez, L. M.; Actis, D. G.; Gonzalez, J. S.; Zélis, P. M.; Alvarez, V. A. Effect of PAA-coated magnetic nanoparticles on the performance of PVA-based hydrogels developed to be used as environmental remediation devices. *J. Nanopart. Res.* **2019**, *21*, 64.
- (194) Deufflhard, M.; Eberbeck, D.; Hietschold, P.; Wilharm, N.; Mühlberger, M.; Friedrich, R. P.; Alexiou, C.; Mayr, S. G. Magnetically responsive composites: electron beam assisted magnetic nanoparticle arrest in gelatin hydrogels for bioactuation. *Phys. Chem. Chem. Phys.* **2019**, *21*, 14654–14662.
- (195) Saadli, M.; Braunmiller, D. L.; Mourran, A.; Crassous, J. J. Thermally and Magnetically Programmable Hydrogel Microactuators. *Small* **2023**, *19*, 2207035.
- (196) Lölsberg, J.; Linkhorst, J.; Cinar, A.; Jans, A.; Kuehne, A. J.; Wessling, M. 3D nanofabrication inside rapid prototyped microfluidic channels showcased by wet-spinning of single micrometre fibres. *Lab Chip* **2018**, *18*, 1341–1348.
- (197) Kim, P.; Kwon, K. W.; Park, M. C.; Lee, S. H.; Kim, S. M.; Suh, K. Y. Soft lithography for microfluidics: a review. *BioChip J.* **2008**, *2*, 1–11.
- (198) Xia, Y.; Whitesides, G. M. Soft lithography. *Angew. Chem., Int. Ed.* **1998**, *37*, 550–575.

- (199) Cautela, J.; Stenqvist, B.; Schillén, K.; Belić, D.; Månsson, L. K.; Hagemans, F.; Seuss, M.; Fery, A.; Crassous, J. J.; Galantini, L. Supracolloidal Atomium. *ACS Nano* **2020**, *14*, 15748–15756.
- (200) Svetlizky, I.; Roichman, Y. Spatial Crossover Between Far-From-Equilibrium and Near-Equilibrium Dynamics in Locally Driven Suspensions. *Phys. Rev. Lett.* **2021**, *127*, 038003.
- (201) Halbach, K. Design of permanent multipole magnets with oriented rare earth cobalt material. *Nucl. Instrum. Methods* **1980**, *169*, 1–10.
- (202) Choi, J.; Yoo, J. Design of a Halbach Magnet Array Based on Optimization Techniques. *IEEE T. Magn.* **2008**, *44*, 2361–2366.
- (203) Halbach, K. Application of permanent magnets in accelerators and electron storage rings (invited). *J. Appl. Phys.* **1985**, *57*, 3605–3608.
- (204) Supermagnete.de, Web Page, 2019, <https://www.supermagnete.de/eng/faq/How-do-you-calculate-the-magnetic-flux-density>.

Appendix

Magnetic Sample Environment for the CoSAXS Beamline

A custom-developed sample environment was used for the magnetic SAXS experiments at the CoSAXS beamline. The setup includes a 3D-printed base plate, a piezoelectric engine, attachable Halbach arrays of different strengths, and a sample holder (Figures A.1 & A.2).

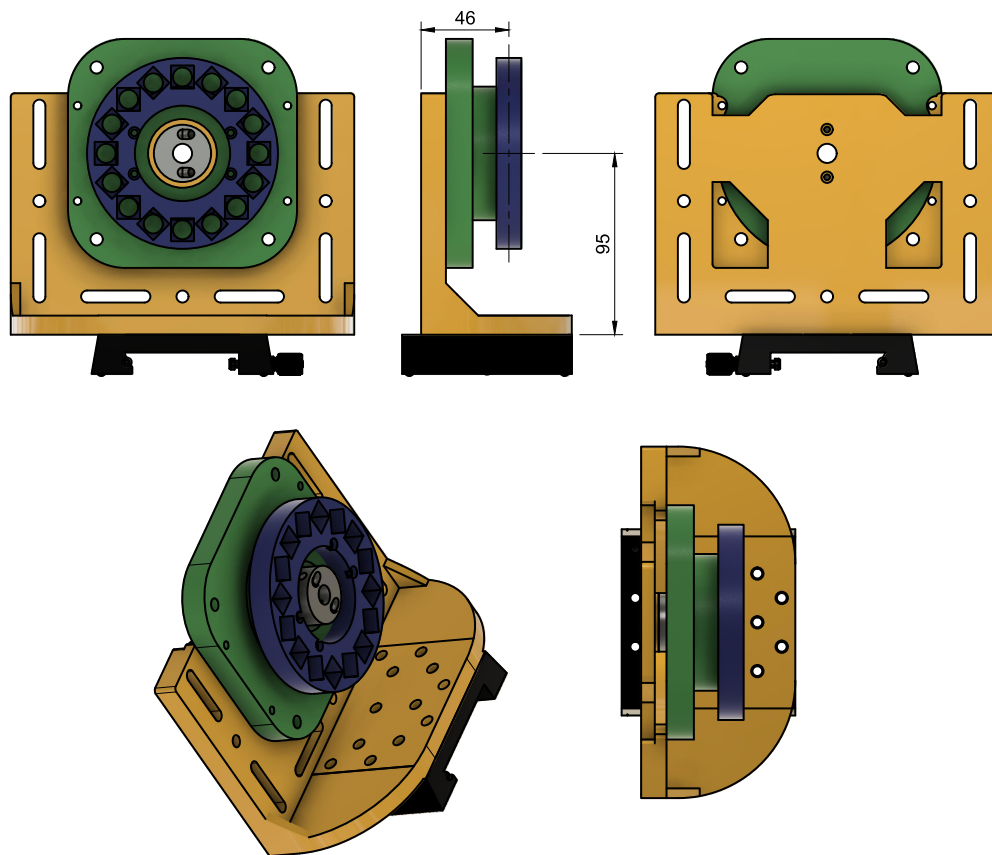


FIGURE A.1: A 3D model of the setup used on the CoSAXS beamline at Max IV Laboratory is presented. The setup includes a 3D-printed baseplate (yellow), a piezoelectric engine PILine U651.03 (green), and a thermostated sample holder made of aluminum (grey). It can be equipped with circular Halbach arrays of varying strengths (blue). All measurements are provided in millimeters.

The piezoelectric engine allows for a maximal rotation rate of 90 rpm, and the setup is compatible with Halbach arrays with field strengths ranging from 1 - 70 mT. Details on the used Halbach arrays can be found in the Appendix. With this sample environment, static and dynamic magnetic fields can be applied.

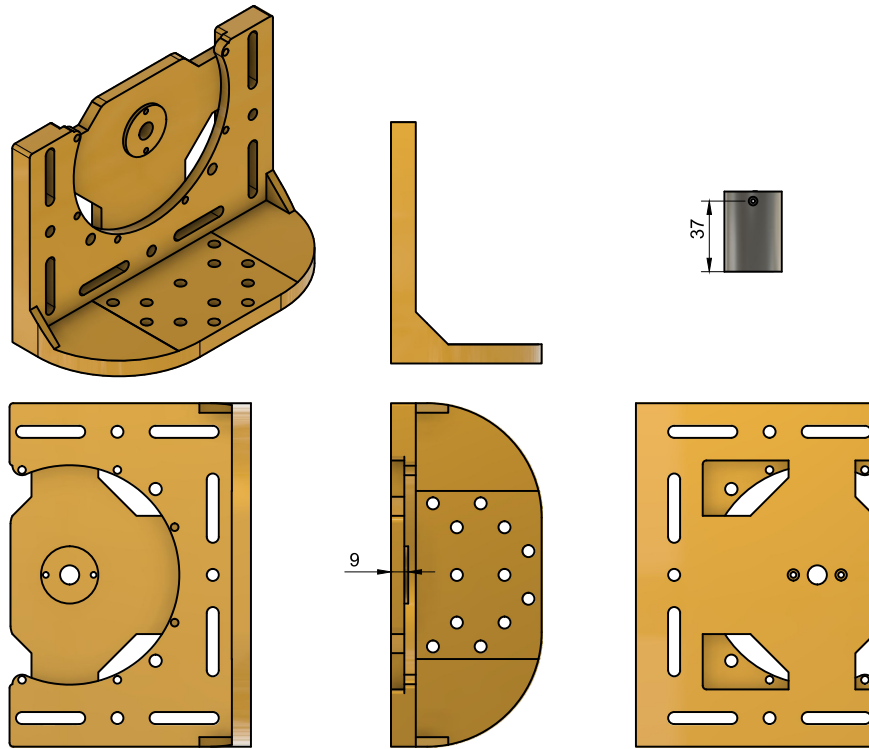


FIGURE A.2: Detailed view of the baseplate designed for the CoSAXS beamline. All measurements are provided in millimeters.

Halbach Arrays

Halbach arrays provide an efficient and cost-effective means of generating homogeneous magnetic fields from weak individual magnets. Additionally, their modular design enables a lightweight and flexible setup for creating magnetic fields. There are several types of Halbach arrays, including linear and circular configurations, which differ in their arrangement of magnets. As demonstrated in Figure A.3, the strategic placement of small cubic magnets can create a stronger, homogeneous magnetic field at the center of the array. This phenomenon is attributed to the design of the Halbach array, strengthening the magnetic flux density on the inside of the array while weakening it on the other side [201–203].

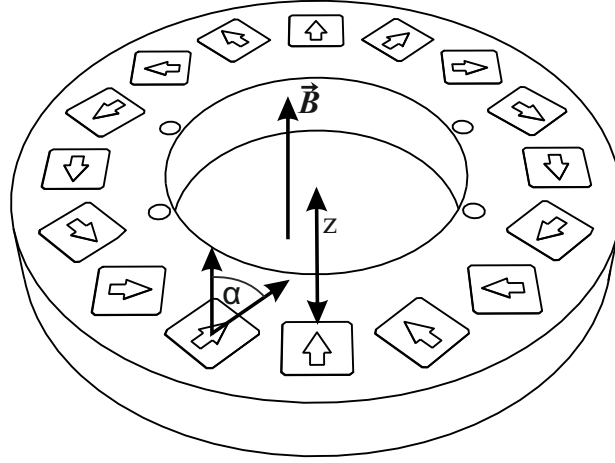


FIGURE A.3: Schematic of circular Halbach Arrays made up of individual cubic magnets, each with an orientation angle α position at a distance z from the array's center.

The magnetic flux density H of such a Halbach array is dependent on the magnetic remanence B_r , the magnetic flux density of the single cubic magnets B_{1M} and the geometric factor f_{Geo} (Equation A.1).

$$H = B_r \cdot B_{1M} \cdot f_{Geo} \quad (A.1)$$

The magnetic flux density of a single magnet at a given distance z from the magnet is influenced by its shape and size. When dealing with cubic magnets that have an edge length a_M the magnetic field generated by a single magnet located at the center of the array can be derived (see Equation A.2) [204].

$$B_{1M} = \frac{B_r}{\pi} \left[\arctan \left(\frac{2a_M}{2z\sqrt{4z^2 + 2a_M^2}} \right) - \arctan \left(\frac{2a_M}{2(a_M+z)\sqrt{4(a_M+z)^2 + 2a_M^2}} \right) \right] \quad (A.2)$$

When considering the building type and magnet orientation, a geometric factor f_{Geo} is applied to account for their impact on the magnetic field. For the specific configuration employed in this study, f_{Geo} can be calculated using Equation A.3, which relates the number of magnets N and their angular orientation α . The arrangement of individual magnets plays a pivotal role in shaping the homogeneity and strength of the magnetic field at the array's center.

$$f_{Geo} = \sum_{i=1}^N \cos(\alpha_i) \quad (A.3)$$

The casings of the Halbach arrays were 3D printed using polylactic acid (PLA) with an Anycubic i3 Mega printer, incorporating cubic neodymium magnets coated in nickel-copper of varying sizes.

Crosspolarisation Setup

Aligned ellipsoidal maghemite particles can polarize light based on their orientation. This property allows for the investigation of maghemite particle alignment through simple cross-polarization experiments. In this setup, two polarizers are positioned before and after the sample. Light can pass through the first polarizer only if it is polarized in a specific direction, meaning that only linearly polarized light enters the sample. The second polarizer is oriented at a 90-degree angle relative to the first polarizer, preventing direct transmission through the combined polarization setup. As a result, only light that is additionally polarized by the sample can be detected.

The intensity of the transmitted light varies according to the orientation of the maghemite particles. The system is calibrated using a standard maghemite sample and a 70 mT Halbach array, which is designed to achieve maximum intensity at 0 degrees (aligned parallel to the magnetic field generated by the Helmholtz coils).

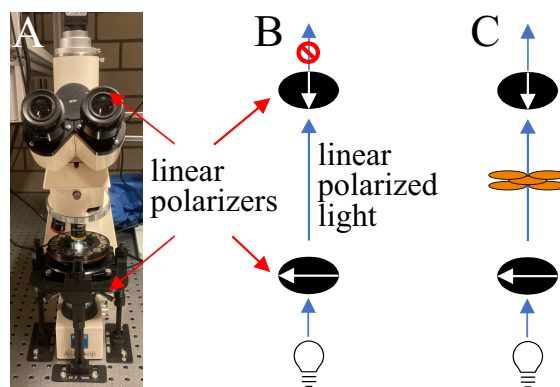


FIGURE A.4: A) Setup for cross-polarization microscopy experiments combined with a rotational Halbach array for rotational magnetic fields. B) With a 90° offset between two linear polarisers, light passing through both is blocked by the second polariser. C) When aligned nanoparticles additionally polarise linear polarised light, it is not blocked by the second polariser, allowing the use of the intensity to track the orientation of the particle alignment.

SasView Fitting Parameter

Detailed fitting parameter corresponding to SasView Fits, displayed in chapter 4.

TABLE A.1: SasView fit parameter for a core-shell ellipsoid for Figure 4.3

	ES_H	SC_H	SCH
scale	5.99E-04	1.13E-03	1.44E-03
background	0.73	0.01	0.25
r_eq	233	233	233
x_core	5.33	5.33	5.33
thick_shell	0	263	263
x_polar_shell	0.00	0.70	0.70
sld_core	43.2	9.42	43.2
sld_shell	9.42	21.2	21.2
sld_solvent	9.42	9.42	9.42
radius_equat_core.width	0.16	0.18	0.18
radius_equat_core.nsigmas	1	1	1
radius_equat_core.npts	0	0	0
x_core.width	0.16	0.18	0.18
x_core.nsigmas	1	1	1
x_core.npts	0	0	0
thick_shell.width	0.0125	0	0.1
thick_shell.nsigmas	1	1	1
thick_shell.npts	0	0	0
x_polar_shell.width	0.0125	0	0
x_polar_shell.nsigmas	1	1	1
x_polar_shell.npts	0	0	0

TABLE A.2: SasView fit parameter for Figure 4.14

	ES_M	Pores	SM-1
scale	3.34e-05	3.45e-06	7.38e-05
background	0	0	0
r_eq	233	95	233
x_core	5.33	0.42	5.33
thick_shell	0	0	230
x_polar_shell	0	0	0.8
sld_core	39.9	9.42	39.9
sld_shell	9.42	0	17
sld_solvent	9.42	17	9.42
radius_equat_core.width	0.15	0.15	0.18
radius_equat_core.nsigmas	1	1	1
radius_equat_core.npts	0	0	0
x_core.width	0.15	0.15	0.18
x_core.nsigmas	1	1	1
x_core.npts	0	0	0
thick_shell.width	0	0	0.1
thick_shell.nsigmas	1	1	1
thick_shell.npts	0	0	0
x_polar_shell.width	0	0	0
x_polar_shell.nsigmas	1	1	1
x_polar_shell.npts	0	0	0

Concentration Series without Magnetic Field

Detailed peak characteristics are determined by fitting the structure peak with a Gaussian fit (Equation 5.2) for the concentration series 0.1 - 15 wt%.

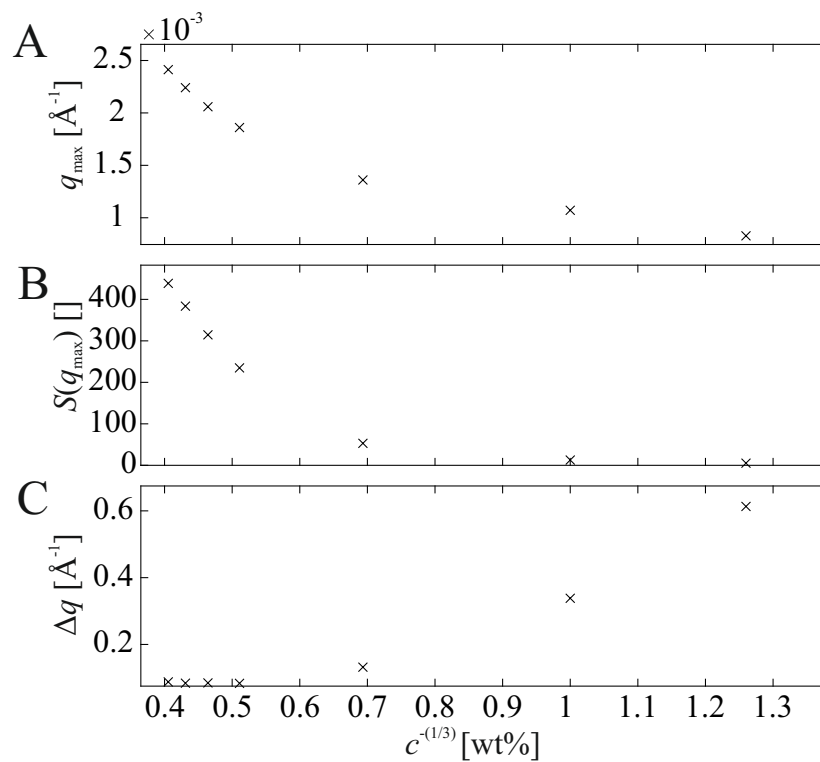


FIGURE A.5: Detailed peak characteristics of the structure peak changing with concentration: A) Peak position, B) intensity of the structure peak $S(q_{\max})$ and C) structure peak width.

Radial distribution function derived from confocal images of plastic crystals containing 5 wt% deionized magnetic microgel.

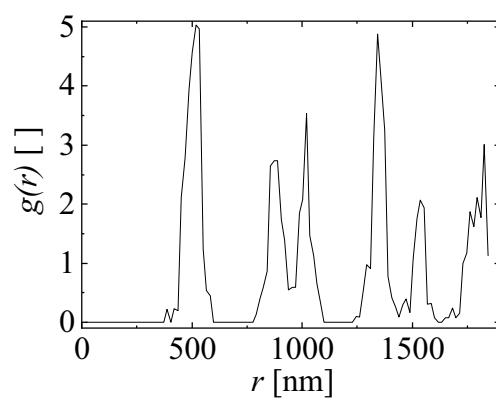


FIGURE A.6: The radial distribution function of SM-1 microgels crystalising at 5 wt% (deionized).

Drying Cell Experiments

Detailed peak characteristics are determined by fitting the structure peak with a Gaussian fit (Equation 5.2) for the drying cell at the distance d_{front} from the capillary tip.

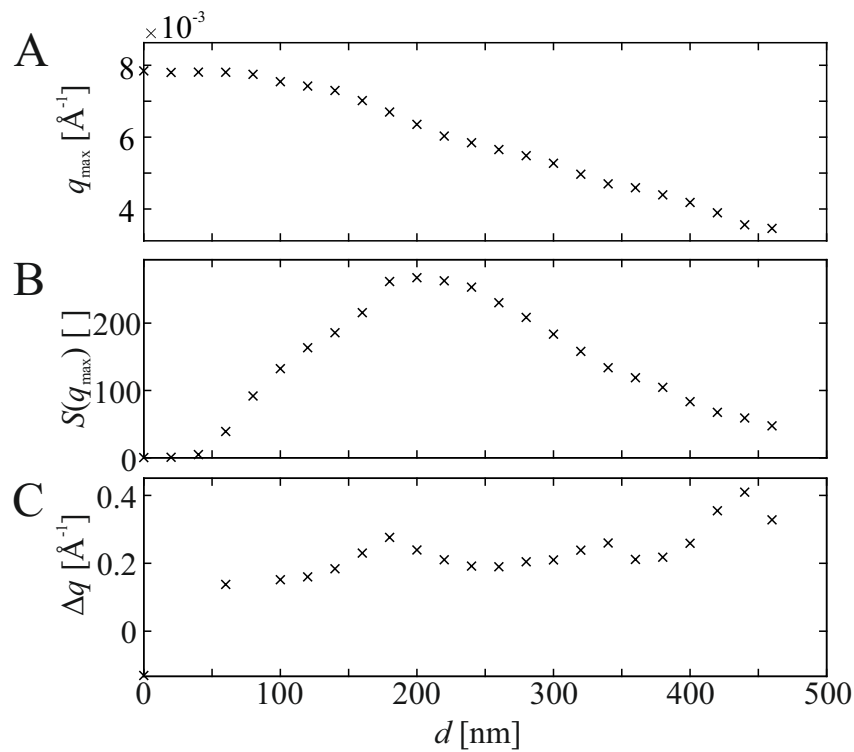


FIGURE A.7: Characteristics of the structure peak determined from fit data, visualizing the A) peak position, B) intensity of the structure peak $S(q_{\text{max}})$, and C) peak width in dependence of the distance from the capillary tip.

Relaxation Experiments using with Microgels with incorporated SPIONs

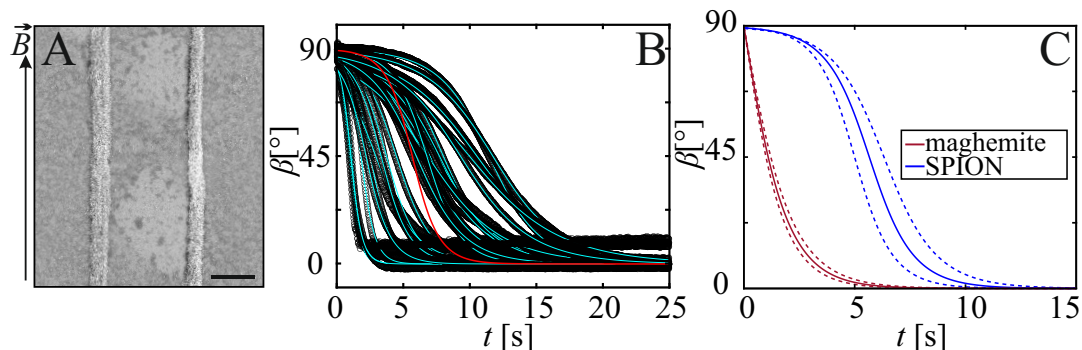


FIGURE A.8: A) SEM image of SPIONs forming strings in water along the field lines and dried under a 70 mT magnetic field. Scale bar = 5 μm . B) Time-resolved relaxation curves after a 90° shift of the magnetic field for microgels and rods with randomly distributed SPIONs. The individual fits are indicated by the cyan lines, while the red lines indicate the mean fit derived from the fit parameters. C) The mean fit curves are used to indicate the relaxation process of magnetic microgel based on SPIONs and ellipsoidal maghemite nanoparticles. When comparing microgels with the same weight content of nanoparticles, the maghemite-based materials show a faster re-orientation. The dashed lines indicate the standard errors.

Cell Culture in the Absence of Rod-Shaped Microgels

As an additional control, an Anisogel completely without rod-shaped microgels was prepared. When analyzing as discussed in Chapter 6, no preferred orientation of the cell growth could be detected, indicating an omnidirectional cell growth without the directional properties of the microgels.

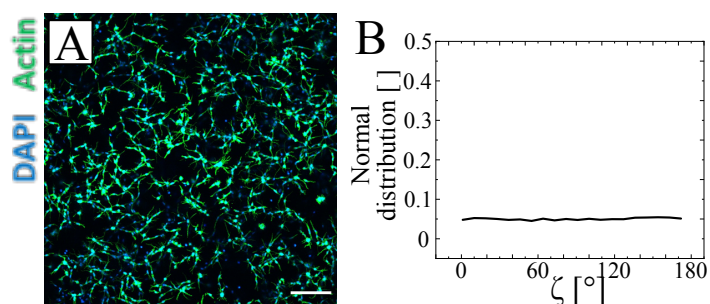


FIGURE A.9: A) Confocal micrograph of mouse fibroblasts after 4 days of culture in PEG hydrogel in the absence of any microgels. Scale bar = 200 μm . B) The orientation distribution plot of cells in PEG hydrogel shows a random distribution of cells.

Acknowledgements

I have to thank many people who have joined me on my way to this day:

First and foremost, I would like to express my gratitude to Jérôme for the opportunity to conduct this work under his supervision. I am also thankful for the discussions we had and the support I received throughout the years, including attending various conferences. I would like to extend my thanks to Prof. Laura De Laporte for her collaboration and for agreeing to be the second reviewer of my thesis. I also have to thank all of my cooperation partners who worked alongside me, helping to overcome countless challenges. Additionally, I appreciate the students I had the privilege of mentoring during a part of their own academic journeys.

Additionally, there are:

The AK Crassous, with Nabanita, Meriem, Alan and Chandeswar. Thanks for sharing ideas, knowledge and time in the basement and elsewhere.

Anne and Christian, with whom I got used to my PhD time at the IPC and survived the first Corona lockdown with important Zoom after-work beers, it is indeed sad that we never got to sit in the same office again afterward.

Timon, who joined me in office 223 and to whom I was able to show the joys and agonies of 3D printing.

Christian and Tom, for the regular expulsion of invaders, if necessary, by sinking the game board in accordance with the rules.

Steffen, who told me at the bar one night about the new junior professor at the IPC, who I could ask for my last research internship.

Anish for the talks during the more difficult time while writing the thesis.

All the others of the Lunch/Mensa/Not-Mensa/Dönerstag/Baclava-Day gang as it changed over the years. And everyone who ever joined an after-work beer at the IPC.

Johannes, Matthias and Sandy, with whom I still meet (digitally) almost every week for boardgame night, even after the flat share was dissolved and everyone except me moved away from Aachen.

And of course, my family for the support over all my studies, whether be it through asking how it is going, or decidedly NOT asking.

I want to thank so many more who do not fit in here because I have decided to limit myself to a single page. Thank you for everything.

As the wise saying goes: "So long, and thanks for all the fish."

xxx

Conferences

Poster Contribution

- 2021 35th Conference of the European Colloid & Interface Society
- 2022 17th Zsigmondy Colloquium
- 2022 51. Hauptversammlung der Kolloid-Gesellschaft
- 2024 Microgels

Oral Contribution

- 2020 16th Zsigmondy Colloquium
- 2021 Nordic Rheology Conference & Nordic Polymer Days
- 2022 European Student Colloid Conference
- 2022 36th Conference of the European Colloid & Interface Society
- 2023 ACS Fall Meeting
- 2023 37th Conference of the European Colloid & Interface Society
- 2024 19th Zsigmondy Colloquium

Supervised Students

2020	Anna Meyer	Research student, <i>Probing the Orientational Diffusion of Anisotropic Magnetic Colloids Using Differential Dynamic Microscopy</i>
2021	Julia Wang	Bachelor thesis, <i>Complex-Shaped Photolithographed Magnetic Microgels under Rotating Magnetic Field</i>
2022	Yannick Nußbaum	Research student, <i>Self-assembly of PNIPAm microparticles based on controlled drying</i>
2023	Yannick Nußbaum	Master thesis, <i>Probing the phase behavior of responsive microgels using unidirectional drying</i>
2023	Martin Fischer	Research student, <i>Probing complex dynamics with anisotropic magnetic microgels</i>

Curriculum Vitae

Personal Data

Name: Dominik Lukas Braunmiller
Date of birth: 19.07.1994
Place of birth: Oberndorf bei Salzburg
Nationality: German

Education

2019 - Present Doctorate candidate (RWTH Aachen University)
2016 - 2019 Master of Science in Chemistry (RWTH Aachen University)
2012 - 2016 Bachelor of Science in Chemistry (RWTH Aachen University)
2012 Abitur, Rupert-Ness-Gymnasium

Eidestattliche Erklärung

Dominik Lukas Braunmiller erklärt hiermit, dass diese Dissertation und die darin dargelegten Inhalte die eigenen sind und selbstständig, als Ergebnis der eigenen originären Forschung, generiert wurden.

Hiermit erkläre ich an Eides statt

1. Diese Arbeit wurde vollständig oder größtenteils in der Phase als Doktorand dieser Fakultät und Universität angefertigt;
2. Sofern irgendein Bestandteil dieser Dissertation zuvor für einen akademischen Abschluss oder eine andere Qualifikation an dieser oder einer anderen Institution verwendet wurde, wurde dies klar angezeigt;
3. Wenn immer andere eigene- oder Veröffentlichungen Dritter herangezogen wurden, wurden diese klar benannt;
4. Wenn aus anderen eigenen- oder Veröffentlichungen Dritter zitiert wurde, wurde stets die Quelle hierfür angegeben. Diese Dissertation ist vollständig meine eigene Arbeit, mit der Ausnahme solcher Zitate;
5. Alle wesentlichen Quellen von Unterstützung wurden benannt;
6. Wenn immer ein Teil dieser Dissertation auf der Zusammenarbeit mit anderen basiert, wurde von mir klar gekennzeichnet, was von anderen und was von mir selbst erarbeitet wurde;
7. Teile dieser Arbeit wurden zuvor veröffentlicht und zwar in:
 - Braunmiller, D. L., Babu, S., Gehlen, D. B., Seuß, M., Haraszti, T., Falkenstein, A., Eigen, J., De Laporte, L., & Crassous, J. J. Pre-Programmed Rod-Shaped Microgels to Create Multi-Directional Anisogels for 3D Tissue Engineering. *Advanced Functional Materials* **2022**, 32(50), 2202430.
 - Steinbeck, L., Braunmiller, D. L., M. Wolff, H. J., Huettche, V., Wang, J., Wessling, M., Crassous, J. J., & Linkhorst, J. Magnetically Actuable Complex-Shaped Microgels for Spatio-Temporal Flow Control. *Advanced Materials Technologies* **2023**, 8(14), 2300044.